الجمهوريــة الجزائريــة الديمقراطيــة الشعبيــة

République Algérienne Démocratique et Populaire

و البحث العلمي وزارة التعليم العالي

Ministère de l'Enseignement Supérieur et de la Recherche Scientifique

Université MUSTAPHA Stambouli

Mascara

جامعة مصطفى اسطمبولي

معسكر

Faculté des sciences exactes

Département de physique

THESE de DOCTORAT

Spécialité : Matériaux et énergie photovoltaïque

Intitulée

L'effet de la balance de charges sur les performances des Matériaux photovoltaïques

Présentée par : M^{elle} LARBI Rekia

Le 29/01/2025

Devant le jury :

Président	**Riane Houaria**	Professeur	U. de Mascara
Examinateur	**Baadj Salim**	MCA	USTO-MB
Examinateur	**Dahou Fatima Zohra**	Professeur	U. de Mascara
Directeur de thèse	**Sahnoun Omar**	MCA	U. de Mascara
Co-directeur de thèse	**Sahnoun Mohammed**	Professeur	U. de Mascara

Année Universitaire : 2024-2025

الجمهوريــة الجزائريــة الديمقراطيــة الشعبيــة
People's Democratic Republic of Algeria
و البحث العلمي وزارة التعليم العالي
Ministry of Higher Education and Scientific Research

University MUSTAPHA Stambouli
Mascara

جامعة مصطفى اسطمبولي
معسكر

Faculty of Exact Sciences
Department of Physics

DOCTORAL THESIS

Specialty: Materials and photovoltaic energy

Title

The effect of charge balance on the performance of photovoltaic materials

Presented by : Miss. LARBI Rekia

Defended on : 29/01/2025

In front of the jury :

President	**Riane Houaria**	Professor	U. of Mascara
Examiner	**Baadj Salim**	MCA	USTO-MB
Examiner	**Dahou Fatima Zohra**	Professor	U. of Mascara
Supervisor	**Sahnoun Omar**	MCA	U. of Mascara
Co-supervisor	**Sahnoun Mohammed**	Professor	U. of Mascara

Academic Year : 2024-2025

Table of contents

General introduction…….. 01

Chapter I: Ferroelectricity in Perovskites for Photovoltaics

I-1. Introduction……..09

I-2. Overview of Perovskites……10

I-2.1. Classification of Perovskites……..10

I-2.1.1. Presentation of simple perovskite ……10

I-2.1.2 Hybrid organic_inorganic perovskite……12

I-2.1.3 Double Perovskites…….....14

I-2.1.4 Halide Double Perovskite Material……15

I-2.1.4.1 Indium In(I) and Bismuth Bi(III) halide double perovskite….18

I-2.1.5 Hybrid Halide Double Perovskite……..19

I-2.2. Working principle of perovskite solar cells……20

I-2.3 Recent Advances in Perovskites Ferroelectric Materials for Photovoltaic Applications……23

I-2.4 Evolution of Perovskite Solar Cells……24

I-3 Energy: the case for Renewables and Photovoltaics ……27

I-3.1 The Photovoltaic effect ……28

I-3.2 The Schockley-Queisser limit……30

I-3.3. General Photovoltaic properties: Voc, Jsc, FF and efficiency……...31

I-4. SLME……35

I-5. Ferroelectric photovoltaic……37

I-5.1. Ferroelectric material……37

I-5.2 The perovskite ferroelectric……39

I-5.3 Photovoltaic effect in the perovskite ferroelectric oxides……..40

I-6 Classical PV effect in p-n junction……40

I-7 Bulk photovoltaic effect (BPVE)……41

I-8 Factors affecting PV properties in FE……43
I-8.1 Polarization……43
I-8.2 Defects……45
I-8.3 Bandgap engineering……46
I-9 the ferroelectric switching barrier……47
I-10 Formal Description of the Berry-Phase Theory……48
I-11 Wannier representation and Berry Phase……51
I-12 Conclusion ……53
Bibiography……54

Chapter II: Calculation methods and Formalisms

II.1 Introduction……68
II.1.1 The Schrödinger Equation……69
II.1.2 the different approximations of the Schrödinger equation……71
II.1.2.1 The Born-Oppenheimer approximation……71
II.1.2.2 The Hartree approximation……71
II.1.2.3 The Hartree-Fock Approximation……73
II.2 Density Functional Theory……74
II.2.1. the Electron density……74
II.2.2. The Thomas-Fermi approximation……75
II.2.3. The Hohenberg-Kohn Theorems……75

II.2.4. The Kohn-Sham Equations……76

II.2.5. The Exchange-Correlation Functionals……77

II.2.6 Solving The Kohn-Sham Equations……78

II.3. Approximations used in DFT……79

II.3.1. The local density approximation LDA……79

II.3.2. Generalized Gradient Approximation GGA……81

II.3.3. Modified Becke-Johnson potential (mBJ)……82

II.4 Spin-orbit coupling……83

II.4.1. Intrinsic Spin-orbit Coupling……83

II.4.2. Dresselhaus-type Spin-orbit Coupling: Bulk Inversion Asymmetry ……86

II.4.3 Rashba-type Spin-orbit Coupling: Structure Inversion Asymmetry ……87

II.5. The linearized augmented plane wave method (FP-LAPW)……90

II.5.1.Introduction……90

II.4.2. The APW method……90

II.4.3. La méthode FP-LAPW……92

II.6. WIEN2K code……93

II.6.1. Initialization ……93

II.6.2. Self-Consistent Field (SCF)……93

II.6.3. Calculations and determination of properties……93

II.7 Conclusion ……94

Bibiography……94

Chapter III: Switchable photovoltaic properties in ferroelectric Lead-Free Bismuth Halide Double Perovskites

III.1 Introduction……102

III-2 Lead-Free Halide Double Perovskite Materials Toward Green and Stable Optoelectronic Applications……106

III-3 Computational methods……107

III-4 Main calculated results……108

III-4.1 Structural properties and stability structural parameters……108

III-3.2 Band structure and density of states ……110

III.3.3 Effective mass tensor……116

III-3.4 Electron localization function ELF and Chemical bonding……117

III-3.5 Binding energies of the excitons ……120

III-3.6 The spin texture ……120

III-3.7 Optical properties……125

III-3.8 Photovoltaic (PV) Characteristics ……132

III-3.9. Spontaneous polarization ……137

III-3.10. Linear bulk photovoltaic effect……138

III-4. CONCLUSION AND OUTLOOK……140

Bibiography……142

Chapter IV: Assessing the performance of SFPbI3 from DFT and SLME calculations for photovoltaic applications

IV-1 Introduction……147

IV-2 The bulk Rashba effect……149

IV-3 Methodology……150

IV-4 Results and Discussion……152

IV-4.1 Stability and Structural Properties……152

IV-4.2. Electronic Structure……153

IV-4.3 Optical properties ……160

IV-4.4 Ferroelectric Properties……164

IV-4.5. Photovoltaic Properties……165

IV-5 Implications for Photovoltaic and Spintronic Applications……169

IV-5.1. Electronic properties……170

IV-5.2. Optical properties ……173

IV-5.3. Solar cell parameters……175

IV-5 Conclusion ……177

Bibiography……177

Chapter V : Photoconversion efficiency of polar double Iodide perovskite (CsRb)(GeSn)I6

V-1. Introduction……184

V-2. Computational Method……186

V-3. Results and Discussion……187

V-3.1. Structural properties……187

V-3.2. Electronic Structure and Optical Properties……188

V-3.3. Photovoltaic Performance……194

V-3.4. Ferroelectric Properties……198

V-4. Conclusion……200

Bibiography……201

General conclusion ……206

List of figures

FigureI.1:	Evolution of photovoltaic solar cells	10
FigureI.2:	Diagram illustrating the unit cell of a generic perovskite crystal structure on the left, along with a view of the BX_3 octahedra, to the right. Diagram of The idealised cubic perovskite crystal structure.	11
FigureI.3:	General crystal structure of $CH_3NH_3PbX_3$ perovskite.	13
FigureI.4:	The diagram illustrates two different device architectures: meso-structured and planar. In the meso-structured device, an Al2O3 scaffold is used to minimize pinholes in the MAPbI3 layer, whereas the planar device relies on the deposition process to create a seamless MAPbI3 film. In this example, the Spiro-OMeTAD layer extracts holes, while compact TiO_2 removes electrons from the perovskite layer.	14
FigureI.5:	The double perovskite structure. Two divalent cations at the B-site of the AB(II)X3 perovskite structure (left) are replaced with a monovalent and a trivalent cation to form the double perovskite A2B(I)B_(III)X6 structure (right).The two types of octahedra in the double perovskite remain corner-sharing. When the B(I) and B_(III) cations are ordered in a rock-salt.	18
FigureI.6:	Charge transport channels in perovskite solar cells (a) using mesoporous medium (b) planar perovskite structure	21
FigureI.7:	A Energy band levels diagram and charge transport processes of electrons and holes in perovskite solar cells. The arrows (1-7) indicate the direction of the charge transfer. The blue circle represents the electrons with a white minus sign, and the holes are the purple circles with a white plus sign. (FTO-Fluorine –doped Tin Oxide coated glass).	22
FigureI.8:	Graph showing the rise in power conversion efficiency (PCE) of Perovskite Solar cells.	24
FigureI.9:	Numbers of publications with the topic on perovskite solar cells (PSCs) from 2015 to 2024. The publication data is adapted from ISI web of science database.	26
FigureI.10:	Chart depicting the record cell efficiencies for multiple materials families, published as of the end of 2024. This plot is courtesy of National Renewable Energy Laboratory (NREL), Golden, CO Available from: https://www.nrel.gov/pv.	26
FigureI.11:	Representation of photoexcitation of an electron (green circle) in direct and indirect semiconductors. The electronic transition in each case is represented by the black arrow, while the incident photon is represented by the purple and a phonon, providing the change in	29

momentum for an indirect transition, by the brown arrow respectively.

FigureI.12: The Shockley Queisser limit for a single junction solar cell, given as a function of cell efficiency against band gap of the absorber layer. 31

FigureI.13: J(V) curve for a hypothetical solar cell, marked by a red line, with the positions of Jsc and Voc marked. The fill factor, FF, is represented by the ratio of the areas of the blue rectangle (defined by Jsc and Voc) and the pink rectangle (defined by the point of maximal power output, at (JMP,VMP)). 34

FigureI.14: Flow chart of 32 crystal classes. 38

FigureI.15: Ferroelectric ABO3 perovskite structure in a) cubic phase above Tc, b) tetragonal phase below Tc for up and down polarization states. 38

FigureI.16: Typical P-E hysteresis loop of a ferroelectric material below its Curie temperature (Tc). Above Tc, the crystal has no spontaneous polarization. 38

FigureI.17: Photovoltaic effect schematics in a) a semiconductor p-n junction and b) ferroelectric based capacitor device. 41

FigureI.18: Schematic illustrating the photoexcitation processes in (a) centrosymmetr ic crystal and (b) non-centrosymmetr ic crystal. 42

FigureI.19: Various perovskite oxides with their bandgap. 46

FigureI.20: One-dimensional chain of alternating cations (pink postively charged ion cores) and anions (green positively charged ion cores with their associated negatively charged valence electron cloud). 52

FigureII.1: Illustration of the self-consistent field (SCF) procedure for solving the Kohn-sham equations where cc represents a suitably selected convergence criterion. 79

FigureII.2: A schematic overview of the effective term of the Rashba-type spin-orbit coupling originating from an electric field. The z-component of the real spin is indicated by an arrow at each orbital. 89

FigureII.3: Muffin-tin potential. 91

FigureIII.1: Schematic illustration of the transformation from APbX3 to A2M(I)M(III)X6 or A2M(IV)X6, where two toxic Pb2+ ions are substituted by combining M+ and M3+ ions (or M4+ ion). "□" denotes M-site vacancy. BB Elements of M-location cations with M+ and M3+ in the periodic table for halide double perovskites. When any M-site elements are localized at IA or IIIA groups of the periodic table, the materials have direct bandgaps. 107

FigureIII.2: Crystal structure of Rhombehedral of double perovskites (a) Cs2InBiBr6 and (b) Cs2InBiCl6. 109

FigureIII.3: Total energy versus volume. 109

FigureIII.4: The calculated band structures of Cs2InBiCl6, and Cs2InBiBr6 using GGA-PBE. 111

FigureIII.5: The calculated band structures of Cs2InBiCl6, and Cs2InBiBr6 using TB-mBJ with and without SOC. 114

FigureIII.6:	Calculated total densities of states TDOS for R3m Cs2InBiX6. And parsial densities of statesPDOS within Tb-mBj with and without spin orbit coupling SOC.	115
FigureIII.7:	Rashba spin splitting (with SOC) on the energy bands in Cs2InBiCl6 and Cs2InBiBr6.	116
FigureIII.8:	Electron localization function ELF for (a)Cs2InBiCl6 and (b) Cs2InBiBr6.	119
FigureIII.9:	2D plot of the spin texture of Cs2InBiBr6	121
FigureIII.10:	2D plot of the spin texture of Cs2InBiCl6.	123
FigureIII.11:	The dependence of the The average real part ε1(ω) of dielectric fonction of double perovskites on energy of incident photons.	126
FigureIII.12:	The dependence of the average imaginary part ε2(ω) of dielectric fonction of double perovskites on energy of incident photons.	127
FigureIII.13:	The dependence of the average refractive index n(ω) of double perovskites on energy of incident photons.	128
FigureIII.14:	The dependence of the average extinction coefficient k(ω) of double perovskites on energy of incident photons.	129
FigureIII.15:	The dependence of the Energy loss function L (ω) of double perovskites on energy of incident photons.	130
FigureIII.16:	The dependence of the reflectivity R(ω) of double perovskites on energy of incident photons.	130
FigureIII.17:	The dependence of the absorption α (ω) of (a) Cs2InBiCl6 and (b) Cs2InBiBr6 on energy of incident photons.	131
FigureIII.18:	The dependence of the optical conductivity σ(ω) of double perovskites on energy of incident photons.	132
FigureIII.19:	Photocurrent density as a function of the forward bias voltage for (a) Cs2InBiCl6 and (b) Cs2InBiBr6.	134
FigureIII.20:	The Open circuit voltage Voc as function of thickness forCs 2InBiCl6 and Cs2InBiBr6.	135
FigureIII.21:	The Fill factor FF as function of thickness for Cs2InBiCl6 and Cs2InBiBr6.	135
FigureIII.22:	The short circuit photo-current density as function of thickness for Cs2InBiCl6 and Cs2InBiBr6.	136
FigureIII.23:	Calculated efficiency through SLME versus thickness .	137
FigureIII.24:	Shift current response σzzZ vs incident photon energy for Cs2InBiCl6 and Cs2InBiBr6 structures with the three methods.	140
FigureIV.1:	The energy bands and spin orientations in a semiconductor material affected by Spin-Orbit Coupling (SOC) and Rashba SOC.	150
FigureIV.2:	Ball-and-stick model illustrating the rhombohedral crystal structure of SF_3PbI_3.	151
FigureIV.3:	The total-energy versus volume optimization for the SF3PbI3	152

	compound.	
FigureIV.4:	Electronic band structures of SF_3PbI_3 in high symmetry directions.	153
FigureIV.5:	Electronic band structure of SF_3PbI_3 showing Rashba spin splitting.	155
FigureIV.6:	Partial Density of States (PDOS) and Total Density of States (TDOS) for SF_3PbI_3 calculated using the modified Becke-Johnson (mBJ) potential with spin-orbit coupling (SOC).	158
FigureIV.7:	Charge density distribution map of SF3PbI3.	159
FigureIV.8:	The real dielectric functions ε1(ω) of SF_3PbI_3 as a function of energy, displaying anisotropic optical properties with distinct absorption coefficients (αxx and αzz) in the xx and zz directions.	160
FigureIV.9:	The real dielectric functions ε2(ω) of SF_3PbI_3 as a function of energy, displaying anisotropic optical properties with distinct absorption coefficients (αxx and αzz) in the xx and zz directions.	161
FigureIV.10:	Absorption spectra of SF_3PbI_3 as a function of energy, displaying anisotropic optical properties with distinct absorption coefficients (αxx and αzz) in the xx and zz directions.	162
FigureIV.11:	Refractive index n(ω) of SF_3PbI_3 as a function of energy, displaying anisotropic optical properties with distinct absorption coefficients (αxx and αzz) in the xx and zz directions.	163
FigureIV.12:	The effect of off-center displacements of Pb, I, and S atoms on the total energy and spontaneous polarization in SF_3PbI_3.	165
FigureIV.13:	Current density-voltage (J-V) characteristics of SF_3PbI_3 solar cells for various thicknesses (10 µm to 100 µm).	166
FigureIV.14:	Variation of short circuit current density (JSC) and open circuit voltage (VOC) with the thickness of SF_3PbI_3-based photovoltaic devices.	167
FigureIV.15:	Variation of Fill Factor (FF) and Spectroscopic Limited Maximum Efficiency (SLME) with thickness of SF_3PbI_3-based photovoltaic devices	168
FigureIV.16:	The calculated band structures using mBJ without and with SOC for studies compounds	172
FigureIV.17:	Electronic band structure of studies compounds showing Rashba spin splitting	173
FigureIV.18:	Absorption spectra of studies compounds as a function of energy, displaying anisotropic optical properties with distinct absorption coefficients (αxx and αzz) in the xx and zz directions.	174
FigureIV.19:	open circuit voltage (VOC) and short circuit current density (Jsc) with thickness of studies compounds.	177
FigureIV.20:	Variation of Fill Factor (FF) and Spectroscopic Limited Maximum Efficiency (SLME) with thickness of studies compounds .	177
FigureV.1:	(a) Atomic arrangement of the double perovskite $(CsRb)(SnGe)I_6$. (b) Energy-volume relationship demonstrating the stability of $(CsRb)(SnGe)I_6$ in its optimized configuration.	188

FigureV.2: Band structure of (CsRb)(SnGe)I_6 along high-symmetry directions in the Brillouin zone. (b) Partial densities of states (PDOS) illustrating electronic transitions near the Fermi level. 189

FigureV.3: Absorption coefficient (α) for (CsRb)(SnGe)I_6, demonstrating its efficient light absorption capability across a broad spectrum. 193

FigureV.4: Simulated J-V characteristics for (CsRb)(SnGe)I_6 as a function of absorber layer thickness (L = 50 µm), highlighting the optimal thickness for maximizing short-circuit current density (Jsc). 197

List of tables

Table.I.1:	Photovoltaic parameters of the PSCs .	25
Table.I.2:	Summary of bandgap of different perovskite oxides	47
Table.III.1:	Lattice constants, volume and atomic fractional coordinates of the Cs_2InBiX_6 (space group R3m)	108
Table.III.2:	Calculated electronic band gaps (eV).	110
Table.III.3:	Rashba parameters for band-splitting at Γ point for Cs2InBiCl6and Cs2InBiBr6 compounds.	112
Table.III.4:	Calculated hole (m^*_h) and electron (m^*_e) effective masses (in units of electron mass rest, m_0) of the compound at **Γ** points of the Brillouin zone. $\left\| m^*_h(ii) \right\|$ and $m^*_e(ii)$ are the average values of the diagonal components of hole and electron effective mass tensor, i.e., $m^*ii = (m^*_{xx} + m^*_{yy} + m^*_{zz})/3$.	117
Table.III.5:	The bond length (Å) and bond angles (degree) of doubles perovskites .	118
Table.III.6.	The Bader charge distribution of the Cs_2InBiX_6 compounds.	119
Table.III.7:	The average of zero-frequency values of the real part of dielectric function, refractive index, and first onset of the imaginary part of dielectric function.	125
Table.III.8:	Calculated optical constants for Cs2InBiCl6 and Cs2InBiBr6: absorption coefficient α(ω);extinction coefficient $k(\omega)$; optical conductivity σ(ω).	131
Table.III.9:	A comparative table listing on Solar cell parameters of Cs2InBiCl6 and Cs2InBiBr6 at T = 293.15 K. Here *J-V* and *P–V* parameters of perovskites are calculated at L = 50 μm thickness. by different exchange correlation potentials.	133
Table.III.10:	shift current σ_{zzZ}(μA/V ^{2}) of Cs2InBiCl6 and Cs2InBiBr6.	140
Table.IV.1:	Calculated lattice parameters a(Å) and c(Å) , volume of the unit cell V (Å^3), Bulk modulus B (GPa) and its first pressure derivative B‘, and the formation energy E_f(eV) of SF_3PbI_3 system. The hexagonal lattice parameters a and c were derived from the rhombohedral lattice parameter a_r and angle α.	153

Table.IV.2:	Calculated band gaps compared with other theoretical values (eV) for SF3PbI3.	154
Table.IV.3:	Rashba parameters α (eVÅ) for band-splitting at R and M point in R3m phase of SF_3PbI_3.	155
Table.IV.4:	Effective masses of electrons and holes along high-symmetry directions (longitudinal and transverse) for SF_3PbI_3, under the GGA + mBJ and mBJ + SOC computational methods.	157
Table.IV.5:	Solar cell parameters of SF_3PbI_3 at T = 300 K. Here P–V characteristics of perovskite are calculated at L = 70 μm thickness in case of SLME approach.	169
Table.IV.6:	Effects of Off-Center Displacements of Pb, I, and S Atoms in SF_3PbI_3 on Spontaneous Polarization, Rashba Parameters, and SLME. The results correspond to changes in the polarization state.	169
Table.V.1:	The calculated effective mass, volume deformation potentials, and carrier mobilities for $(CsRb)(SnGe)I_6$ compared with some other materials.	192
Table.V.2:	Photovoltaic parameters for $(CsRb)(SnGe)I_6$ at L = 50 μm compared with other materials from literature references.	198

ACKNOWLEDGEMENTS

I would like to express my sincere and deepest gratitude to my principal supervisor *Dr. Omar SAHNOUN* for giving me the opportunity to conduct this research as well as his continuous support, excellent motivation and constructive guideline throughout my PhD. He always provided quick feedback and it helped me a lot to progress smoothly in this research journey to reach my goal.

I would also like to convey my gratitude to my associate supervisor *Professor Mohammed SAHNOUN* for his support and feedback during my PhD candidature. The critical and constructive feedback from his is appreciated and it helped me to improve my level.

I am very grateful to *RIANE Houaria*, Professor at the University of Mascara, who gave me the honor of chairing the jury for this thesis.

I express my gratitude to *Dr .BAADJ Salim* at the University of USTO-MB, and *to DAHOU Fatima Zohra*, Professor at the University of Mascara who have agreed to devote their time to the expertise of this thesis. I would like also to express my gratitude to them for their participation in the jury.

I am very grateful to all former and present members of our research group, forproviding me with help, support and friendship. Especially, I would like to thank Pr G. KAVAK BALCI, Dr I.Candan, Dr A. AISSA, N.Chalil , and N.H. Mokhefi, for their great help and supportive suggestions.

Finally, I would like to express my deepest gratitude to my parents for theirunconditional love, constant support and encouragement.

Abstract

Renewable energy sources offer the only sustainable means to meet the growing global energy demand while minimizing contributions to anthropogenic climate change and environmental harm. Photovoltaics provide a way to capture the vast solar radiation that reaches the Earth daily and convert it directly into electricity. However, their widespread adoption has historically been limited by high production and deployment costs. Perovskite materials have attracted significant interest over the past decade for their potential in high-efficiency photovoltaic devices. Their chemical and structural flexibility allows materials scientists and engineers to tailor their properties to meet the specific requirements of various applications.

In this thesis we use *ab initio* methods to explore the fundamental distortions in various structures and their corresponding optoelectronic properties. The research focuses on a selection of perovskites compound that are either central to current international photovoltaic studies or have the potential to emerge as significant materials in the field. The study addresses some of the key challenges facing current photovoltaic technologies and examines how newly developed materials, such as halide perovskites, have driven the search for alternatives that combine high efficiency with affordability, scalability, and flexibility for solar cell production. Specifically, this work investigates the $Cs_2InBi(Br,Cl)_6$, SF_3PbI_3, and $(CsRb)(SnGe)I_6$ perovskite compounds. Through the calculation of their electronic and optical properties, are able to assess their viability and potential as absorbers within photovoltaic devices.

Keywords: Simple Perovskites Halides, Double Perovskites, electronic ,Optical and photovoltaic Properties, ferroelectric Properties , DFT.

Résumé:

Les énergies renouvelables sont la seule solution durable qui puisse répondre à la demande mondiale croissante en énergie sans accroître considérablement le changement climatique anthropique et la destruction de notre environnement. Le photovoltaïque peut exploiter la grande quantité de rayonnement solaire qui atteint la Terre chaque jour en convertissant directement en électricité, mais les coûts de production et de déploiement à grande échelle ont été historiquement élevés. Les matériaux de perovskite ont reçu

Abstract

l'attention qu'ils méritent au cours de la dernière décennie en raison de leurs applications potentielles dans les dispositifs photovoltaïques à haute efficacité. Leur flexibilité chimique et spatiale offre aux scientifiques et aux ingénieurs de matériaux la possibilité d'adapter les propriétés de ce matériau aux applications souhaitées. Dans ce travail de recherche, en utilisant la méthode des ondes planes augmentées linéarisées avec un potentiel total (FP-LAPW) dans le cadre de la théorie de la fonctionnelle de la densité (DFT) implémentée dans le code Wien2k. pour décrire les propriétés structurales, électroniques et les propriétés optiques associées qui se produisent dans une série de structures. Les travaux de Cette thèse ont examiné un certain composés de structure pérovskite qui sont soit à la pointe de la recherche photovoltaïque internationale actuelle, soit qui devraient devenir l'un de ces matériaux émergents. Dans Cette étude, nous examinons certains des défis actuels auxquels sont confrontées les technologies photovoltaïques et comment les matériaux récemment développés, tels que les halides perovskites, ont inspire la recherche de matériaux qui pourraient être utilisés pour fournir des cellules solaires efficaces, peu coûteuses, produites à grande échelle et flexibles. Plus précisément, ce travail étudie les composés perovskites $Cs_2InBi(Br,Cl)_6$, SF_3PbI_3 et $(CsRb)(SnGe)I_6$. Grâce au calcul de leurs propriétés électroniques et optiques, nous sommes en mesure d'évaluer leur viabilité et leur potentiel en tant qu'absorbeurs dans les dispositifs photovoltaïques.

Mots Clés: Halides perovskites simple, perovskites doubles, Propriétés électroniques, optiques et photovoltaïques, Propriétés ferroelectrique , DFT.

ملخّص :الطاقة المتجددة هي الحل المستدام الوحيد الذي يمكنه تلبية الطلب العالمي المتزايد على الطاقة دون حدوث زيادة كبيرة في تغير المناخ الناتج عن الأنشطة البشرية وتدمير بيئتنا. يمكن للخلايا الكهروضوئية الاستفادة من الكمية الكبيرة من الإشعاع الشمسي الذي يصل إلى الأرض كل يوم عن طريق تحويلها مباشرة إلى كهرباء، ولكن تكاليف الإنتاج والنشر على نطاق واسع كانت مرتفعة . حظيت مواد البيروفسكايت بالاهتمام الذي تستحقه على مدار العقد الماضي نظرًا لتطبيقاتها المحتملة في الأجهزة الكهروضوئية عالية الكفاءة. توفر مرونتها الكيميائية والمكانيكية لعلماء ومهندسي المواد القدرة على تخصيص خصائص هذه المواد للتطبيقات المطلوبة.

تم في هذا البحث، استخدام طريقة الامواج المستوية المتزايدة خطيا مع الكمون الكلي (FP-LAPW) في سياق نظرية الكثافة الوظيفية (DFT) المنفذة في برنامج Wien2k لوصف الخصائص الهيكلية والإلكترونية والبصرية المرتبطة بها والتي تحدث في سلسلة من الهياكل. تناولت هذه الأطروحة بعض مركبات بنية البيروفسكايت التي تعد إما في طليعة الأبحاث

Abstract

الكهروضوئية الدولية الحالية أو من المتوقع أن تصبح واحدة من هذه المواد الناشئة. في هذه الدراسة، ونحن نستعرض بعض التحديات التي تواجه حاليا تكنولوجيا الضوئية وكيف ألهمت المواد التي تم تطويرها مؤخرًا، مثل هاليد البيروفسكايت، البحث عن مواد يمكن استخدامها لتوفير خلايا شمسية فعالة وغير مكلفة وواسعة النطاق ومرنة . وبشكل أكثر تحديدًا، يدرس هذا العمل مركبات البيروفسكايت $Cs_2InBi(Br,Cl)_6$ ، SF_3PbI_3 و $(CsRb)(SnGe)I_6$ من خلال حساب خصائصها الإلكترونية والبصرية،حيث يمكننا تقييم جدوىها وإمكاناتها كامتصاصات للأجهزة الكهروضوئية.

الكلمات المفتاحية:
هاليدات البيروفسكايت البسيطة ، هاليدات بيروفسكايت مزدوجة، الخصائص الإلكترونية ،الضوئية والكهروضوئية ، الخواص الفيروالكترونية،DFT .

General Introduction

The production of usable energy has historically driven technological and societal progress, starting with early innovations like fire and water mills for food processing and evolving to the massive global electricity usage that powers today's industries and devices. As the world's population and development increase, the demand for energy continues to rise. By 2050, with the global population anticipated to exceed 9 billion, energy consumption is expected to at least double, growing from 13.5 TW in 2001 to 27.6 TW, according to projections by the US and EU[1,2]. From the latter half of the 20th century into the 21st, it has become clear that while rising energy demands could be satisfied by depleting natural gas, oil, and coal reserves, doing so would worsen the impacts of human-induced global warming and ocean acidification. These effects threaten ecosystems, food production, and various natural and human systems [3]. To prevent such consequences and align with governmental and international emissions goals, transitioning from fossil fuels to renewable energy sources is crucial. Among these, wind and solar energy stand out as low-carbon options, offering significant advantages without the high initial costs or hazardous waste associated with nuclear fission reactors, making them some of the most promising and rapidly growing alternatives [2].

Solar energy holds immense potential to fulfill humanity's long-term energy needs, with the sun emitting around 3.86×10^{26} watts of power. Remarkably, the energy the sun provides in just 80 minutes is equivalent to the total annual energy consumption of the entire planet, highlighting its vast potential for harnessing power. However, significant hurdles remain, including economic, geopolitical, and technological challenges, particularly in efficiently capturing and utilizing sunlight for energy production. The concept of photovoltaics emerged from Alexandre-Edmond Becquerel's discovery of the photovoltaic effect in the late 1800s [4]. Although he could not explain the phenomenon, major advancements followed in the early 1900s, including Albert Einstein's quantum explanation of the photoelectric effect in 1905. This breakthrough laid the foundation for a century of research in photovoltaics, ultimately leading to the creation of the first modern silicon solar cell by Chapin and colleagues in the mid-20th century [5].

General Introduction

Photovoltaic (PV) technology, which converts light into electricity, is an evolving field with devices known as solar cells operating under this principle. The development of solar cells is categorized into three generations: wafer-based silicon solar cells, thin-film solar cells, and organic solar cells [6,7]. Organic solar cells include dye-sensitized solar cells (DSSCs) [8], organic PVs [9], inorganic cells [10], and quantum dot solar cells [11]. Third-generation PV technologies offer high photoconversion efficiency at lower manufacturing costs, presenting a promising alternative to traditional silicon-based solar cells [12]. First-generation technologies initially had low photoconversion efficiencies of around 9.2–13%. Decades of research have since improved efficiency, approaching the Shockley-Queisser limit [13]. In light of the global energy crisis, advanced solar technologies with higher efficiencies are being explored as alternatives to conventional cells [14]. Perovskite solar cells (PSCs), discovered by Lev Perovski in 2009, are part of the third generation and evolved from DSSCs. Initially, PSCs achieved a photoconversion efficiency of 3.8% [15], which has since surged to 22% within a short span [16]. This rapid improvement has garnered significant research interest. PSCs are notable for their flexibility, lightweight nature, and semi-transparency, enabling a wide range of applications. These characteristics offer opportunities for researchers and engineers to fine-tune their properties for maximum utility [17].

PSCs are considered strong candidates to replace silicon solar cells due to their rapid efficiency growth. However, challenges remain, including degradation caused by moisture, temperature, and UV light, and the use of toxic lead (Pb) in methylammonium lead halides [15,18]. Efforts are underway to develop lead-free alternatives and enhance the stability of the perovskite layer [19]. Despite these hurdles, PSCs are regarded as a future-forward technology. Researchers are working to improve their photoconversion efficiency, stability, and lifespan while exploring synergies with other technologies [20, 21]. PSCs can also operate across various wavelength spectra, enhancing their versatility. With a theoretical efficiency of approximately 31% for MA lead iodide [22], perovskites are efficient, cost-effective, and easy to synthesize. Their unique structure allows researchers to optimize their physical, optical, and electrical properties. Recently, halide double perovskites have been proposed as stable and environmentally friendly alternatives to lead-based perovskites. These materials replace toxic lead ions with combinations of monovalent and trivalent ions or tetravalent ions and vacancies, maintaining the charge balance of traditional perovskites.

This innovation further highlights the potential of perovskite technology to drive the future of renewable energy.

Furthermore, Ferroelectric perovskites hold significant promise for photovoltaic (PV) applications [23] due to their high open-circuit voltage and switchable photovoltaic effect. The switchability of the bulk photovoltaic effect (BPVE) in ferroelectrics extends their use beyond energy generation. In these materials, the direction of ferroelectric polarization can control the sign of the photocurrent, theoretically enabling complete (100%) switchability of the photocurrent with polarization. This feature opens the door to innovative applications like photo-ferroelectric memory devices. Previous studies have shown that photocurrent behavior mirrors a ferroelectric hysteresis loop, highlighting a direct correlation between the photocurrent and electrically poled polarization in various ferroelectric materials [24]. Ferroelectric halide perovskites are attracting interest due to their distinctive characteristics and possible uses. Research has demonstrated adjustable electronic structures, low-threshold lasing, potential in light-emitting diodes, ferroelectric properties, p-n junction formation, anion diffusion mechanisms, pressure-induced phase transitions, large polarons, and topological polarons in these materials [25]. These discoveries are significant for the progress of research and technology in the realm of halide perovskites [26].

In recent years, the bulk photovoltaic effect (BPE) in ferroelectric perovskite materials has attracted significant attention for its potential applications in photovoltaics and solar energy conversion. Wang et al. [27] proposed a band engineering approach by substituting Zn^{2+} for Nb^{5+} in $KNbO_3$ to design semiconductor perovskite ferroelectrics for photovoltaic purposes. Panda et al. [28] highlighted the potential of Bi5+-doped ferroelectric perovskite materials like $PbBaBiNbO_6$ for the BPE, attributing the reduced activation energy to the low-lying empty states of the Bi atom. Shafir et al. [29] investigated the cosubstitution of Mo and Ti for Nb in $KNbO_3$, resulting in a promising absorber material for photovoltaic applications utilizing the BPE. Additionally, recent studies have explored the BPE in various ferroelectric materials beyond traditional perovskite oxides. Li et al. [30] reported an enhanced BPE in two-dimensional ferroelectric $CuInP_2S_6$, showing a significant increase in photocurrent density compared to conventional bulk perovskite oxides. Zhao et al. [31] observed the emergence of the BPE in anion-ordered perovskite $MASbSI_2$ with spontaneous out-of-plane ferroelectricity, expanding the understanding of BPE mechanisms in different material systems. Furthermore, the potential of ferroelectric materials for circularly polarized light

(CPL) detection has been explored by [32], emphasizing the robust spin-dependent anisotropy of CPL detection in layered hybrid perovskite ferroelectrics with a significant BPE. Chalil et al. [33] presented theoretical calculations of the photovoltaic properties of $CsGeI_3$, an inorganic germanium halide perovskite, demonstrating the relationship between ferroelectric and photovoltaic properties for solar energy conversion. In conclusion, the literature review showcases the diverse strategies and materials being studied to harness the bulk photovoltaic effect in ferroelectric perovskite materials, indicating potential advancements in photovoltaics and solar energy conversion applications.

In this work, we use ab initio methods to describe the ferroelectric and Rashba effect effect that appear in a series of polar compounds and their associated optoelectronic properties. These materials are either at the forefront of current international research in photovoltaics or promise to become suitable candidates for it. Much of this research is pushing our understanding of the intrinsic properties that materials need to perform well as solar absorbers; indeed with the increased resources and developed theories available to computational chemists of today, accurate theoretical prediction of such properties, and even other properties difficult to examine through experiment, of complex compounds and structures is becoming possible. As such research has the potential to develop cheaper, non-toxic materials with less stringent manufacturing requirements and efficiencies that match or exceed those of current records, new directions in photovoltaic technologies are opening up, including exible cells based on plastic substrates or roll-to-roll printable solar cells, as well as ferroelectric bulk photovoltaic effect.

After this general introduction which attempts to situate our research work in its global context, the remainder of this thesis manuscript is organized as follows:

The first chapter presents a set of definitions and basic concepts necessary for understanding the rest of this thesis. It describes the latest technology concerning perovskite structure materials. Then, in the form of a literature review, it focuses on the photovoltaic characteristics of these materials.

The second chapter introduces the theoretical framework of our research. It explains the bases of the different calculation methods used during this work. It details the methods based on DFT, the different approximations used for the exchange-correlation energy, as well as the FP-LAPW method. It describes, in a second part, the Wien2k calculation code

which allowed us to simulate the different structural, electronic and optical properties of the perovskite materials studied.

In the first results chapter we complete a rigorous exploration of the geometric structures, electronic structures and optical parameters and SLME relevant to photovoltaic applications as well as the origin of the ferroelectricity is discussed of noncentrosymmetrical Cesium halide double-perovskites Cs2InBiCl6 and $Cs_2InBiBr_6$. We also explored the effects of Spin-Orbit coupling and the type of exchange-correlation functional that was used on the accuracy of our results.

In the second results chapter we present a comprehensive first-principles study on SF_3PbI_3, a promising member of the stable polar halide perovskite family. Using density functional theory calculations, we investigate its electronic band structure, optical and ferroelectric properties, and photovoltaic characteristics. We find that, SF_3PbI_3 exhibits strong spin-orbit coupling, attributed to the heavy elements within its structure, potentially leading to Rashba splitting near the electron band extrema. Furthermore, we explore the fascinating phenomenon of distortion-induced polarization switching within SF_3PbI_3.

In the third results chapter We investigates the electronic and optical properties of the polar $(CsRb)(GeSn)I_6$ material using first-principles density functional theory (DFT). Our results demonstrate that $(CsRb)(GeSn)I_6$ exhibits a direct bandgap and high absorption coefficient, making it an excellent candidate for optoelectronic applications. Furthermore, we assess its photovoltaic performance using the Spectroscopic Limited Maximum Efficiency (SLME) model.

Finally, we provide a general conclusion and insights into perspectives.

Bibliography

[1] Peter, L. M. (2011). Towards sustainable photovoltaics: the search for new materials. Philosophical Transactions of the Royal Society A: Mathematical, Physical and Engineering Sciences, 369(1942), 1840-1856.

[2] Lewis, N. S., & Nocera, D. G. (2006). Powering the planet: Chemical challenges in solar energy utilization. Proceedings of the National Academy of Sciences, 103(43), 15729-15735.

[3] Field, C. B., & Barros, V. R. (Eds.). (2014). Climate change 2014–Impacts, adaptation and vulnerability: Regional aspects. Cambridge University Press.

[4] Chodos, A., Ouellette, J., & Tretkoff, E. (2009). This month in physics history. American Physical Society News, 18(4), 5-7.

[5] Chapin, D. M., Fuller, C. S., & Pearson, G. L. (1954). A new silicon p-n junction photocell for converting solar radiation into electrical power. Journal of applied physics, 25(5), 676.

[6] Kazmerski, L. L. (1997). Photovoltaics: A review of cell and module technologies. Renewable and sustainable energy reviews, 1(1-2), 71-170.

[7] Parida, B., Iniyan, S., & Goic, R. (2011). A review of solar photovoltaic technologies. Renewable and sustainable energy reviews, 15(3), 1625-1636.

[8] Grätzel, M. (2003). Dye-sensitized solar cells. Journal of photochemistry and photobiology C: Photochemistry Reviews, 4(2), 145-153.

[9] Brabec, C. J. (2004). Organic photovoltaics: technology and market. Solar energy materials and solar cells, 83(2-3), 273-292.

[10] Miles, R. W., Zoppi, G., & Forbes, I. (2007). Inorganic photovoltaic cells. Materials today, 10(11), 20-27.

[11] Salant, A., Shalom, M., Hod, I., Faust, A., Zaban, A., & Banin, U. (2010). Quantum dot sensitized solar cells with improved efficiency prepared using electrophoretic deposition. Acs Nano, 4(10), 5962-5968.

[12] Green, M. A., Ho-Baillie, A., & Snaith, H. J. (2014). The emergence of perovskite solar cells. Nature photonics, 8(7), 506-514.

[13] Shockley, W., & Queisser, H. (2018). Detailed balance limit of efficiency of p–n junction solar cells. In Renewable energy (pp. Vol2_35-Vol2_54). Routledge.

[14] Yang, W. S., Noh, J. H., Jeon, N. J., Kim, Y. C., Ryu, S., Seo, J., & Seok, S. I. (2015). High-performance photovoltaic perovskite layers fabricated through intramolecular exchange. Science, 348(6240), 1234-1237.

[15] Grätzel, M. (2014). The light and shade of perovskite solar cells. Nature materials, 13(9), 838-842.

[16] Ciro, J., Betancur, R., Mesa, S., & Jaramillo, F. (2017). High performance perovskite solar cells fabricated under high relative humidity conditions. Solar Energy Materials and Solar Cells, 163, 38-42.

[17] Bailie, C. D., Christoforo, M. G., Mailoa, J. P., Bowring, A. R., Unger, E. L., Nguyen, W. H., ... & McGehee, M. D. (2015). Semi-transparent perovskite solar cells for tandems with silicon and CIGS. Energy & Environmental Science, 8(3), 956-963.

[18] Jung, H. S., & Park, N. G. (2015). Perovskite solar cells: from materials to devices. small, 11(1), 10-25.

[19] Azpiroz, J. M., Mosconi, E., Bisquert, J., & De Angelis, F. (2015). Defect migration in methylammonium lead iodide and its role in perovskite solar cell operation. Energy & Environmental Science, 8(7), 2118-2127.

[20] Snaith, H. J. (2013). Perovskites: the emergence of a new era for low-cost, high-efficiency solar cells. The journal of physical chemistry letters, 4(21), 3623-3630.

[21] Niu, G., Guo, X., & Wang, L. (2015). Review of recent progress in chemical stability of perovskite solar cells. Journal of Materials Chemistry A, 3(17), 8970-8980.

[22] Sha, W. E., Ren, X., Chen, L., & Choy, W. C. (2015). The efficiency limit of CH3NH3PbI3 perovskite solar cells. Applied Physics Letters, 106(22).

[23] Han, X., Ji, Y., & Yang, Y. (2022). Ferroelectric photovoltaic materials and devices. Advanced Functional Materials, 32(14), 2109625.

[24] Tan, L. Z., Zheng, F., Young, S. M., Wang, F., Liu, S., & Rappe, A. M. (2016). Shift current bulk photovoltaic effect in polar materials—hybrid and oxide perovskites and beyond. Npj Computational Materials, 2(1), 1-12.

[25] Zhu, X. (2019, August). Ferroelectric polarons in lead halide perovskites. In ABSTRACTS OF PAPERS OF THE AMERICAN CHEMICAL SOCIETY (Vol. 258). 1155 16TH ST, NW, WASHINGTON, DC 20036 USA: AMER CHEMICAL SOC.

[26] Zhang, L., Wang, K., Lin, Y., & Zou, B. (2020). Pressure effects on the electronic and optical properties in low-dimensional metal halide perovskites. The Journal of Physical Chemistry Letters, 11(12), 4693-4701.

[27] Wang, F., Grinberg, I., & Rappe, A. M. (2014). Semiconducting ferroelectric photovoltaics through Zn2+ doping into KNbO3 and polarization rotation. Physical Review B, 89(23), 235105.

[28] Panda, N., Parida, B. N., Padhee, R., & Choudhary, R. N. P. (2015). Dielectric and electrical properties of the double perovskite PbBaBiNbO 6. Journal of Electronic Materials, 44, 4275-4282.

[29] Shafir, O., Bai, Y., Juuti, J., & Grinberg, I. (2020). Visible-light-absorbing potassium niobate titanate-molybdate ferroelectrics. Physical Review Applied, 14(4), 044052.

[30] Li, Y., Fu, J., Mao, X., Chen, C., Liu, H., Gong, M., & Zeng, H. (2021). Enhanced bulk photovoltaic effect in two-dimensional ferroelectric CuInP2S6. Nature communications, 12(1), 5896.

[31] Zhao, M., Wang, H., Gou, G., Ding, X., & Sun, J. (2021). Emergence of bulk photovoltaic effect in anion-ordered perovskite sulfur diiodide MASbSI2 with spontaneous out-of-plane ferroelectricity. Materials Today Physics, 21, 100459.

[32] Li, X., Wu, F., Yao, Y., Wu, W., Ji, C., Li, L., ... & Liu, X. (2022). Robust spin-dependent anisotropy of circularly polarized light detection from achiral layered hybrid perovskite ferroelectric crystals. Journal of the American Chemical Society, 144(31), 14031-14036.

[33] Chelil, N., Sahnoun, M., Benhalima, Z., Larbi, R., & Eldin, S. M. (2023). Insights into the relationship between ferroelectric and photovoltaic properties in CsGeI 3 for solar energy conversion. RSC advances, 13(3), 1955-1963.

Chapter I :
Ferroelectricity in Perovskites for Photovoltaics

Chapter I Ferroelectricity in Perovskites for Photovoltaics

I-1. Introduction

Gustav Rose first discovered the perovskite structure in the Ural Mountains of Russia in 1839. The structure is named after the scientist Lev Perovski[1]. The earliest material identified with this structure was $CaTiO_3$, and since then, thousands of similar structures have been found. Perovskite compounds are generally represented by the chemical formula ABX_3, where A and B are cations and X is an anion. The B-site cations are smaller and more electronegative, while the A-site cations are typically larger, electropositive metals, often including alkaline earth or rare earth ions such as Pb^{2+}, Bi^{3+}, Sr^{2+}, Ca^{2+}, and La^{3+}. B-site ions can be transition metals from the 3d, 4d, and 5d series, such as Cr^{3+}, Ru^{4+}, and Os^{3+}, respectively. X-site anions include O^{2-}, F^{-}, Cl^{-}, Br^{-}, N^{3-}, and S^{2-}. The coordination numbers of A and B-sites are 12 and 6, respectively. Ideal perovskites exhibit cubic symmetry and belong to the space group Pm-3m. Deviations from this ideal structure can result in various structural variations. Perovskite oxides are essential in fundamental research and have numerous applications, including use as lithium ion and proton conductors. They are also employed in devices such as lasers and light-emitting diodes (LEDs). Perovskites possess valuable properties like superconductivity, magnetoresistance, and ionic conductivity, making them highly significant in microelectronics and telecommunications [2].

Due to their combination of optical, electronic, and magnetic properties, as well as their tunability and processability, perovskites have long attracted the attention of researchers in both science and technology. Recently, perovskites have emerged as a revolutionary class of materials with exceptional properties for a wide range of optoelectronic applications, including lighting, lasing, and photon detection, with a particular emphasis on photovoltaics. Researchers are particularly interested in perovskite solar cells (PSCs) because of their high theoretical photoelectric conversion efficiency, tunable band gap, low production cost, and easy fabrication process.

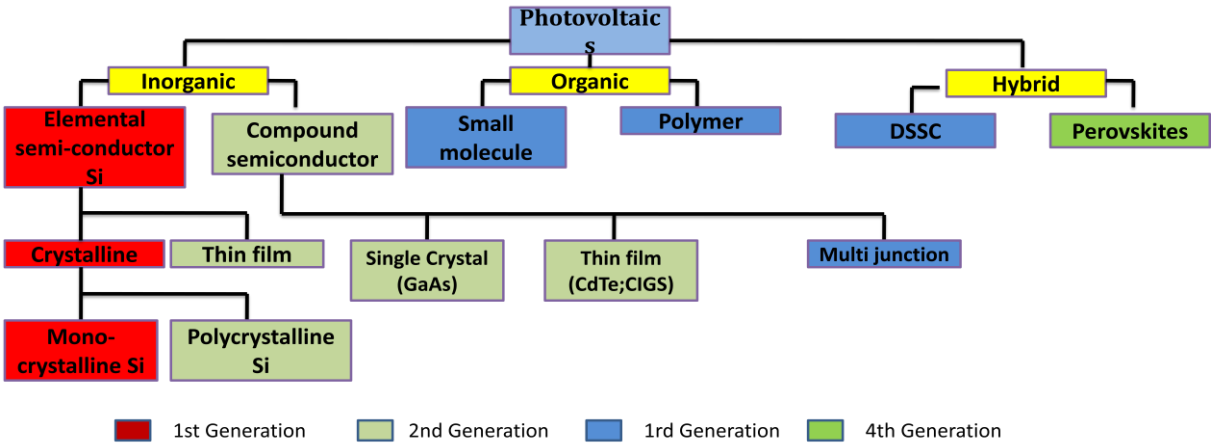

Figure I-1 : Evolution of photovoltaic solar cells[3]

I-2. Overview of Perovskites

Charge balancing in the formal stoichiometry of perovskites (ABX_3) can be achieved in several ways. Perovskites are mainly classified into two types based on their constituents: metal oxide perovskites and metal halide perovskites. In metal oxide perovskites, the combined valence of the two metal cations must equal six. These perovskites can have compositions such as I-V-O_3, II-IV-O_3, and III-III-O_3, containing elements from groups I, II, III, and IV (e.g., $KTaO_3$, $CaCrO_3$, and $GdFeO_3$). The anions in perovskites can be substituted to create a variety of materials, including oxyhalides, oxynitrides, sulfides, and selenides[4].

Metal halide perovskites have a composition of I-II-VII_3, where the two cations must have a combined valence of three [5]. It is noted that halide perovskites generally have lower ionization potentials compared to metal oxide perovskites[6].

I-2.1. Classification of Perovskites

I-2.1.1. Presentation of simple perovskite :

The term 'perovskite' is used to describe any material that has the crystal structure of CaTiO3 and belongs to a large family of structures. Generally, the perovskite structure is represented by the formula ABX3, as depicted in Figure I-1. Any compound with an ABX3 stoichiometry and the same crystal structure, or a structure that results from a distortion of the ideal cubic perovskite structure, is considered perovskite-like. Often, even if used incorrectly, it is simply referred to as perovskite. In the ideal scenario, the A cations are

located at the corners of the cubic or nearly cubic unit cell, while the B cations are at the center of the unit cell, coordinated with the X anions in an octahedral manner (typically oxygen or halogens) at the face-centered positions. Due to the various options for A, B, and X ions, there are numerous potential perovskite materials, although the structure will only be stable for specific combinations of ionic radii[7]. One notable feature of perovskites is their flexibility in composition and structure, allowing for the adjustment of their properties through the substitution of elements at the A, B, or X sites for different applications. Various perovskite materials, including metal oxide-based and halide perovskites, have been extensively researched for a range of device applications.

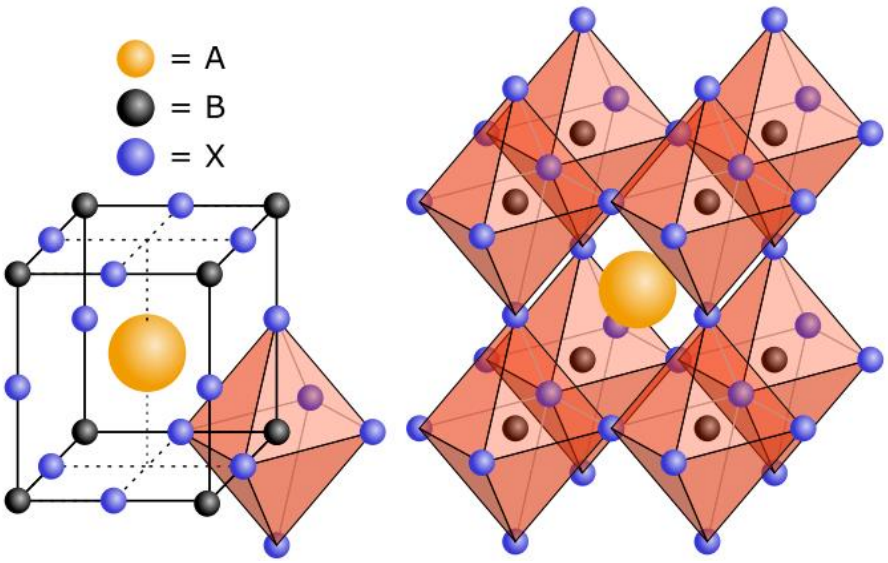

Figure I-2: Diagram illustrating the unit cell of a generic perovskite crystal structure on the left, along with a view of the BX3 octahedra, to the right. Diagram of The idealised cubic perovskite crystal structure[7].

I-2.1.2 Hybrid organic-inorganic perovskites

Hybrid organic-inorganic perovskites (HOIPs) have a stoichiometry of AMX3, where A represents the organic cation, M represents the metal ion, and X represents the halide (refer to Figure I-2) [9]. The most commonly studied HOIP is methylammonium lead iodide, (CH3NH3)PbI3. Other HOIPs have been explored, including those containing formamidinium (FA1) cations instead of methylammonium (MA1), Br2 or Cl2 instead of I2, and Sn21 instead of Pb21, as well as mixtures of these components [10]. HOIPs display a diverse range of structures. For example, MAPbI3 is orthorhombic (space group Pnma) below 165K when MA1 dipoles are aligned, transitions to a tetragonal phase (I4/mcm) at 165K when MA1 gains rotational freedom, and further transitions to a cubic phase (Pm3m) at 327K when MA1 dipoles are disordered [11]. The PbI6 octahedra can distort significantly even in the cubic phase, providing bulk flexibility in these materials [12]. In 1893, all-inorganic alkali-metal lead and tin halide perovskites were first synthesized, and their crystallographic structures were determined in 1958 by Christian Møller, who observed their photoconductivity [13]. The first HOIP, methylammonium lead iodide (MAPbI3), was created by Dieter Weber in 1978, and the optoelectronic properties of these materials were studied in the early 1990s by Mitzi et al [14].

Initially, HOIPs were introduced in the photovoltaic field as a light-absorbing dye in dye-sensitized solar cells (DSSCs) rather than as a primary active material. The first liquid hybrid perovskite DSSC was created in 2009, achieving a power conversion efficiency (PCE) of 3.8% [15]. In 2012, Lee et al. and Kim et al. developed solid-state HOIP active material photovoltaics using MAPbI3 and MAPbIxCl12x, respectively, with PCEs ranging from 8% to 10%. These advancements surpassed the performance of the best known solid-state DSSCs and many organic photovoltaic materials at that time [16]. Since then, the efficiency of HOIP photovoltaics has steadily improved, with the current device efficiency record standing at 22.1%. This places HOIP photovoltaics in competition with other highly efficient photovoltaic technologies such as CIGS, CdTe, and crystalline silicon [17-19].

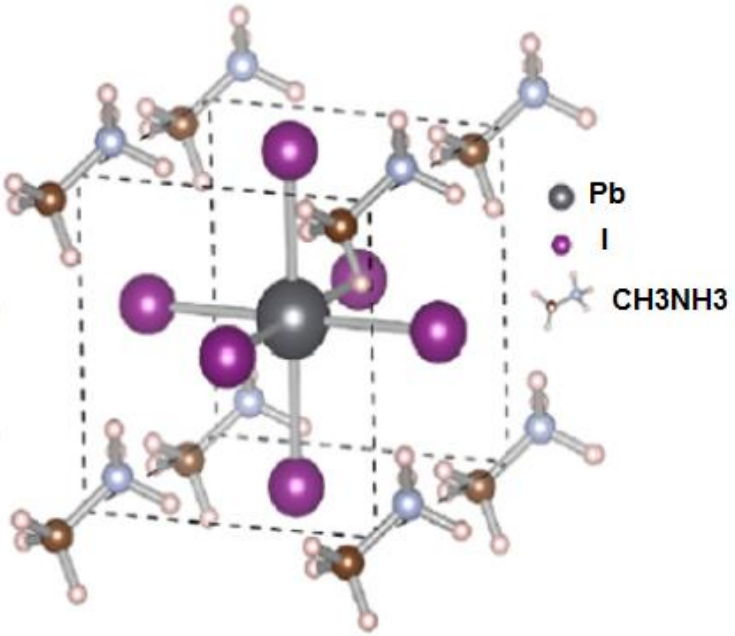

Figure I-3: General crystal structure of $CH3NH_3PbX_3$ perovskite [20].

The potential of HOIP materials for photovoltaic applications is undeniably significant. According to the Shockley-Queisser limit, single-junction HOIPs have a theoretical potential power conversion efficiency (PCE) of nearly 30% [21]. HOIP-based devices have the capability to surpass this limit through the use of tandem cell architectures. Recent studies by Catchpole et al. have shown PCE values of 26.4% in a tandem cell incorporating HOIP and silicon as active layers. The high efficiency of HOIPs is attributed to their unusually low electron-hole recombination rates, even in low temperature solution-processed devices with high bulk defect densities. The band gap of MAPbI3 is well-suited for photovoltaic applications at 1.55 eV and can be adjusted through doping or substitution with different organic cations or halides [22]. Excitons in HOIPs have low binding energies, such as 0.03 eV for MAPbI3, allowing them to dissociate into free carriers at room temperature. HOIPs also exhibit ambipolar charge transport properties with high electron and hole mobilities, on the order of 10^1 $cm^2/V/s$ for MAPbI3, and long carrier diffusion lengths ranging from 100 to 1000 nm—significantly longer than the film thickness required for full optical absorption[23].

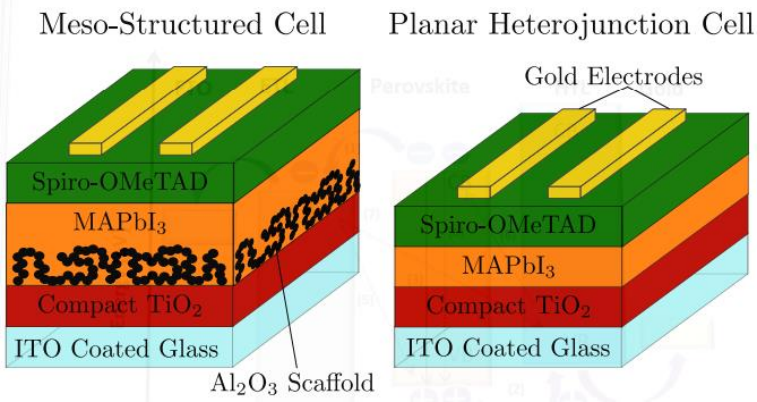

Figure I-4: The diagram illustrates two different device architectures: meso-structured and planar. In the meso-structured device, an Al2O3 scaffold is used to minimize pinholes in the MAPbI3 layer, whereas the planar device relies on the deposition process to create a seamless MAPbI3 film. In this example, the Spiro-OMeTAD layer extracts holes, while compact TiO2 removes electrons from the perovskite layer[24].

I-2.1.3 Double Perovskites

It is known that there are numerous compounds with the perovskite structure due to the ability of any of its three sites to undergo chemical replacement. Both cations and anions can be substituted in various ways. In perovskite, multiple cations can be used in either the A-site or B-site, and they can be arranged randomly or systematically. The different sizes and charges of the two cations often determine the ordering. Both A and B-site cations are known to exhibit ordering, although the methods they use can vary greatly. The most common type of ordering involves a rock-salt structure with a 1:1 ratio of B-site cations, resulting in a perovskite composition of A2BB'X6. Another type of perovskite, AA'BB'O6, features ordered A and A' cations stacked on top of each other, and ordered B and B' cations arranged according to rock salt[25,26]. The tolerance factor (t) provides a relationship between different cations and anions in double perovskites DPs[26], and is expressed as:

$$t = \frac{r_A + r_O}{\sqrt{2}\left(\frac{r_A}{2} + \frac{r_{BI}}{2} + r_O\right)} \quad (1)$$

where r_A, r_B, r_{B0} represent different radii of ions and r_0 represents radius of oxygen. The DPs having structure A_2BB_0O6 are found by doping one of the ion at B sites with another B0 ion. These types of compound are well studied experimentally and theoretically because of their unusual and alluring characteristics.

DPs with the structure A_2BB0O_6 have significant applications in the field of spintronics due to their unique properties[27]. Spintronic devices utilize both the charge and spin of electrons, resulting in more efficient memory devices in modern technology [28]. Experimental research has been conducted on the magnetic characteristics, crystal structure, and crystal development of 5d DPs oxides. Discoveries such as room-temperature CMR and half metallicity in $Sr_2FeMoO_6$and Sr_2FeReO_6[29,30], multi ferroicity in Bi_2NiMnO_6[31], and magneto dielectricity in La2NiMnO6[32] have led to intensive research in DPs. Recent studies are focused on understanding the different behavior of 3d-4d (5d) containing DPs with significant spin polarisability[33]. AA'BB'O6 perovskites may become unstable if there is a significant size imbalance in the A site cations. The rock-salt arrangement sequence in $A_2BB'O_6$ perovskite allows for significant size mismatches among the cations, as discovered by Ward et al. in 1961. The A and A' layers must have identical lateral dimensions. The DPs structure has double the unit cell of the perovskite structure, with 12-coordinate A-sites and 6-coordinate B-sites. The unique properties of these DPs result from the combination of electronically more localized 3d ions with more delocalized 4d or 5d ions.

I-2.1.4 Halide Double Perovskite Materials

Inorganic Halide Double Perovskites like Cs2AgBiX6 have garnered attention for their potential as substitutes for lead halide perovskites in solar energy applications. The inorganic halide double perovskite Cs2NaAmCl6 was first synthesized in 1968 by evaporating a solution of HCl containing cations until dry[34]. Subsequently, a few more all-inorganic halide double perovskites (Cs2NaM(III)Cl6) were created using the same method[35]. At that time, the ferroelectric phase transition in all-inorganic halide double perovskites[36] was of particular interest, as seen in the cooling of $Cs_2NaBiCl_2$[36].

In the past two years, there has been a growing interest in halide double perovskites as an alternative to lead halide perovskites. In 2016, three separate research groups simultaneously introduced Cs_2AgBiX_6 (X=Cl or Br) as a promising option for light absorption in the visible spectrum[37-39]. Woodward et al. found bandgaps of 2.19 eV and 2.77 eV for Cs2AgBiBr6 and $Cs_2AgBiCl_6$, respectively, through diffuse reflectance measurements[37]. While both compounds are stable in air, Cs2AgBiBr6 degrades over time when exposed to ambient air and light. Karunadasa et al[39] successfully synthesized a highly stable Cs2AgBiBr6 single crystal with an indirect bandgap of 1.95 eV and a photoluminescence

lifetime of approximately 660 ns, showing promise for photovoltaic applications. Giustino et al [56]designed and created $Cs_2AgBiCl_6$ with bandgaps ranging from 1.95 to 3.04 eV. Karunadasa et al [39] also experimented with incorporating Tl as a dilute impurity into Cs2AgBiBr6 single crystals, resulting in $Cs2(Ag_{1-a}Bi_{1-b})Tl_xBr_6$ with low indirect and direct bandgaps of 1.40 and 1.57 eV respectively.Significantly, time-resolved photoconductivity measurements show that the alloyed material contains long-lived carriers with microsecond lifetimes, indicating potential for efficient carrier extraction in a solar cell [40]. This alloyed perovskite is the first halide double perovskite to exhibit comparable bandgap and carrier lifetime to $CH_3NH_3PbI_3$, but unfortunately, the presence of Tl remains toxic . In 2017, Yan et al [41] utilized Cs2AgBiBr6 as a host to adjust the bandgap by alloying In3+ and Sb3+. The $Cs_2Ag(Bi_{1-x}M_x)Br_6$ (M=In, Sb) system can accommodate up to 75% In3+ to increase the bandgap, and up to 37.5% Sb3+ to decrease the bandgap, allowing for a bandgap modulation of approximately 0.41 eV through the introduction of these two metals, with the smallest bandgap value of 1.86 eV for $Cs2Ag(Bi_{0.625}Sb_{0.375})Br_6$. Band structure calculations reveal that the different atomic configurations of Sb and In lead to opposite directions of bandgap shifts upon substitution. Similarly, McQueen et al [42] employed an alloy strategy to design indirect and direct bandgap transitions. The synthesized $Cs_2AgSbCl_6$ and $Cs_2AgInCl_6$ single crystals exhibit indirect and direct bandgaps, respectively. By increasing the Sb composition x in $Cs2AgSb_xIn_{1-x}Cl6$, the compounds transition gradually from direct to indirect bandgap. Subsequently, Giustino et al determined that $Cs_2InAgCl_6$ has a direct bandgap of 3.3 eV and is photosensitive, changing reversibly from white to orange under UV light. However, $Cs_2InAgCl_6$ has a wide bandgap that limits its application in the visible region.

In 2018, Nag et al demonstrated the enhancement of visible-light emission in direct bandgap Cs2AgInCl6 by introducing Mn2+ ions . The Cs2AgInCl6 host absorbs UV light and transfers the excitation energy to Mn d electrons. The Bohr radii for X-site in perovskites increase gradually from F to I elements, leading to tighter binding and larger bandgaps .Typically, the X elements in halide double perovskites are Cl or Br, resulting in relatively large bandgaps. Gamelin et al synthesized Cs2AgBiX6 (X=Cl, Br) colloidal nanocrystals using a hot injection method, which were then converted to new materials such as Cs2AgBiI6 with a narrow bandgap of approximately 1.75 eV through anion exchange [43]. Ma et al [44] recently reported the synthesis of Cs2NaBiI6, a novel halide double perovskite material, and

characterized its crystal structure using XRD and XPS tests, as well as its optical properties through UV-Vis absorption spectra. Cs2NaBiI6 possesses a low direct bandgap of 1.66 eV and demonstrates high stability against moisture and oxygen in ambient air. Zhang et al [45,46] have theoretically designed a series of all-inorganic halide double perovskites through first-principles calculations over the past two years. A total of sixty-four candidate materials were screened for photovoltaic functionality, resulting in the identification of 11 Sb- and Bi-based optimal materials with intrinsic thermodynamic stability, suitable bandgaps, small carrier effective masses, and low exciton binding energies as promising photovoltaic materials. Materials containing monovalent ions Tl+ or In+ exhibit direct bandgaps, with Cs2InSbCl6 and Cs2InBiCl6 having a bandgap of approximately 1.0 eV, showing theoretical maximum performance comparable to CH3NH3PbI3.However ,Tl remains toxic and In+ is prone to spontaneous oxidation into In^{3+}[47].

They conducted a study where they designed trivalent In3+ ions with monovalent Ag+ or Cu+ ions to explore halide double perovskites [46]. Notable examples include Rb2CuInCl6, Rb2AgInBr6, and Cs2AgInBr6, which have direct bandgaps of 1.36, 1.46, and 1.50 eV, respectively, and theoretical spectroscopic limited maximal efficiency comparable to $CH_3NH_3PbI_3$. Another type of halide double perovskite, known as vacancy-ordered $A_2M(IV)X_6$ (M(IV)=Sn, Ti, Pd, Te, etc.), has also been identified, offering direct bandgaps, intrinsic stability, and low toxicity [48]. In 2014, Kanatzidis et al. [49] prepared Cs_2SnI_6 microcrystal by a hot-injection method. In recent years, researchers have successfully prepared Cs_2SnI_6 [50] and Cs_2PdBr_6[53] nanocrystals with controlled shapes and sizes, demonstrating high stability and intriguing optical properties. The bandgap of the Cs_2SnI_6 was found to be varied in the range of 1.36–1.67 eV. Quantum confinement effect has been observed for the nanoparticles of dimension below 8 nm. In 2018, Tang et al. [51] fabricated Bi-doped Cs_2SnCl_6 single crystals, where the photoluminescence was observed from Bi3+ ions. In 2017, Snaith et al. [52] reported Cs2PdBr6 single crystal, which exhibits long-lived photoluminescence, direct bandgap of 1.6 eV and long-term stability. Additionally, Ti-based vacancy-ordered halide double perovskites have been synthesized, with the bandgap tunable from 1.02 to 1.78 eV, showcasing ultrastability and excellent optical absorption properties [53].

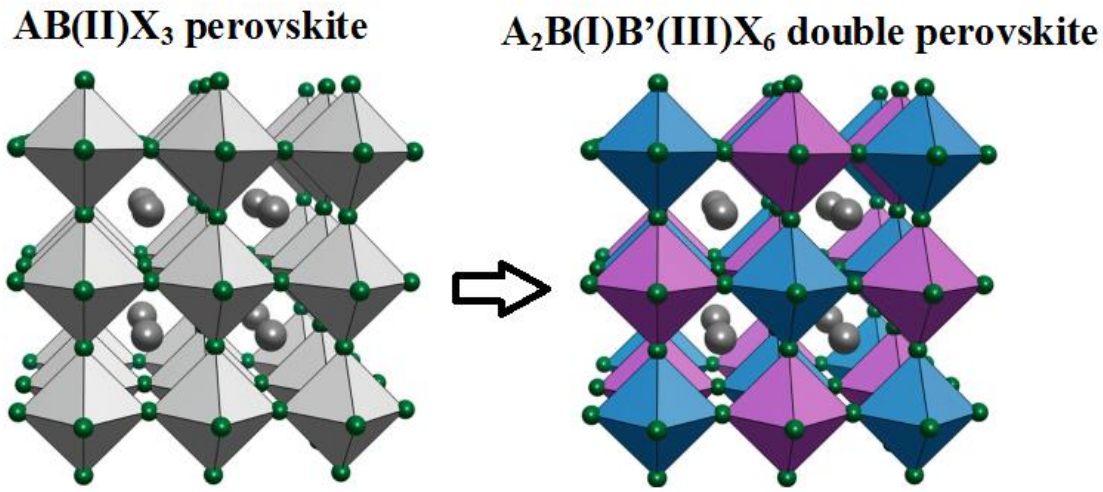

Figure I-5: The double perovskite structure. Two divalent cations at the B-site of the AB(II)X3 perovskite structure (left) are replaced with a monovalent and a trivalent cation to form the double perovskite A2B(I)B-(III)X6 structure (right). The two types of octahedra in the double perovskite remain corner-sharing. When the B(I) and B(III) cations are ordered in a rock-salt[54]

I-2.1.4.1 Indium In(I) and Bismuth Bi(III) halide double perovskites.

The newly discussed double perovskites in previous sections show either indirect band gaps or non-dispersive bands at the band edges. In an effort to develop high-quality lead-free semiconducting halide perovskites, Volonakis et al. [55] revisited the split-cation design principles using +1 and +3 cations. They proposed that an ideal double perovskite should have cations with the same valence configuration as Pb2+, which means the cations should have (i) filled s-orbitals, (ii) vacant p-orbitals, and (iii) a filled d-shell far from the band edge. For the monovalent cation, the choices are limited to alkali metals, noble metals, and Group III elements (boron group). However, only Group III elements have both filled s-orbitals and vacant p-orbitals in their +1 oxidation state, and among them, only In and Tl are stable as +1 cations. Since Tl is toxic, In+ becomes the sole candidate for the monovalent B-site cation. For the trivalent B-site cation, options include pnictogens, some transition metals like Sc, Y, Cu, and Au (known to form elpasolites [56]), as well as Group III elements in their +3 oxidation state, lanthanides, and actinides. Among these, only the pnictogens meet the criteria (i)–(iii). However, N and P are too small to coordinate six halogens in an octahedral structure, and As is toxic, leaving Sb3+ and Bi3+ as the only viable options. Based on this

reasoning, Volonakis et al. [55] concluded that the most promising replacements for lead are double perovskites using In(I)/Sb(III) and In(I)/Bi(III). Building on this idea, the authors assessed the stability of hypothetical compounds A2InPnX6 (where A = K, Rb, Cs; Pn = Sb, Bi; and X = F, Cl, Br, I) using Goldschmidt tolerance factor analysis and decomposition energy calculations from DFT and the Materials Project Database [57]. Their findings revealed that most compounds are unstable with respect to decomposition, consistent with previous research by Xiao et al. [58]. However, Cs2InBiBr6 was found to be only marginally unstable, with a decomposition energy of 1 meV per formula unit, falling within the uncertainty range of the computational method. This result suggests that Cs2InBiBr6, or a similar compound, could potentially be synthesized.

Volonakis et al. [55] also observed that the stability of double perovskites correlates with the size of the A-site cation, with larger A-site cations making the compounds less prone to decomposition. As a result, they proposed that In(I)/Bi(III) halide double perovskites could be synthesized using large organic cations like CH_3NH^{3+} and $CH(NH_2)^{2+}$.

I-2.1.5 Hybrid Halide Double Perovskite

To our knowledge, nine hybrid halide double perovskites have been synthesized, including (MA)2KBiCl6 , $(MA)_2TlBiBr_6$, $(MA)_2AgBiBr_6$, $(MA)_2AgSbI_6$, $(MA)_2AgBiI_6$, $(MA)_2KGdCl_6$, $(MA)_2KYCl_6$, $(MA)_2AgInBr_6$, and $(MA)_2SnI_6$. In 2016, the first hybrid halide double perovskite, (MA)2KBiCl6, was synthesized by evaporating an HCl solution to dryness . Density functional theory screening of (MA)2MBiX6 (where M=K, Cu, Ag, Tl; X=Cl, Br, I) suggested that some systems could have bandgaps similar to those of CH3NH3PbX3 lead compounds, particularly for M=Cu, Ag, and Tl. Based on these predictions, (MA)2TlBiBr6, which is isoelectronic with CH3NH3PbBr3, was synthesized and found to have a direct bandgap of 2.16 eV . However, due to the high toxicity of Tl, (MA)2TlBiBr6 is not a viable alternative to lead-based perovskites despite its promising electronic properties. They later synthesized (MA)2AgBiBr6, a hybrid halide double perovskite with a low indirect bandgap of 2.02 eV, which is relatively stable and nontoxic . The material is stable in both air and moisture and has a higher decomposition temperature compared to MAPbBr3. In 2017, the same research group successfully synthesized (MA)2AgSbI6 and (MA)2AgBiI6 , both having an indirect bandgap of around 2 eV and exhibiting high stability in air. Although Sb and Bi belong to the same group, there are notable differences between them. Sb has a smaller atomic mass and

ion radius than Bi, and the smaller radius of Sb causes structural distortion in $(MA)_2AgSbI_6$, whereas $(MA)_2AgBiI_6$ forms an orthogonal structure. Additionally, due to strong relativistic effects in the heavier Bi atom, the influence of spin–orbit coupling on the bandgap of $(MA)_2AgBiI_6$ is more significant. Around the same time, $(MA)_2KGdCl_6$ and $(MA)_2KYCl_6$ were synthesized via a solution evaporation method, adopting a rhombohedral structure with $R\bar{3}m$ symmetry. Both phases undergo a rhombohedral-to-cubic phase transition at around 435 K. Density functional calculations suggest that these materials have large direct bandgaps of approximately 5 eV and mechanical stability. In 2018, (MA)2AgInBr6 single crystals were synthesized by using Pb2+ from $CH_3NH3PbBr_3$ to control the formation of soluble intermediates. In the same year, (MA)2SnI6 powder was synthesized by mixing SnI4 with CH3NH3I at room temperature . The powder was evaporated in a tungsten boat at 120 °C in a vacuum chamber to create $(MA)_2SnI_6$ films, which exhibited a direct bandgap of 1.81 eV and a strong absorption coefficient of around 7 × 10^4 cm^{-1}. The films were found to be n-type with a carrier concentration of ~2 × 10^{15} cm^{-3} and an electron mobility of ~3 $cm^2/V/s$. Additionally, the conductivity increased by a factor of 4 under simulated solar illumination (100 mW cm−2), suggesting that (MA)2SnI6 is a lead-free optical semiconductor suitable for solar cells. These synthesized hybrid halide double perovskites demonstrate much better stability than CH3NH3PbI3. However, there have been no reports on their practical applications to date [59].

I-2.2. Working principle of perovskite solar cells

The complex nature of the medium in perovskite solar cells (PSCs)makes it challenging to fully understand the processes from charge generation to collection. Although the principles of p-n junctions used to describe silicon-based solar cells are still applicable to characterize PSCs, there remains ambiguity in applying existing knowledge to the operational mechanisms of PSCs because of the multiple material layers involved in their fabrication. Some researchers treat PSCs as p-n, p-i-n, or n-i-p junction solar cells, but translating their function remains challenging. Several studies on charge transport dynamics suggest that electron-hole pairs are generated almost immediately after photoexcitation in the perovskite medium and are then dissociated into free charge carriers within less than 2 ps [60], driven by the built-in electric field resulting from the work function difference between

the anode and cathode. The effectiveness of perovskite as a solar absorber is largely due to its long charge diffusion lengths and high carrier mobilities. Electron and hole diffusion lengths in the perovskite medium can reach up to 1 µm, allowing the photo-generated charges to reach the interfacial layers and electrodes without significant geminate or non-geminate recombination, depending on the morphology of the perovskite [61]. Carrier mobilities as high as 25 $cm^2/(V{\cdot}s)$ [62] have been reported, which is three orders of magnitude greater than the mobilities in bulk heterojunction organic solar cells. Two main device architectures are commonly used in PSC fabrication: mesoporous-PSC and planar-PSC structures. As a result, charge transport in PSCs is often discussed in relation to these structures. In the mesoporous structure, the perovskite layers are deposited on a porous metal-oxide semiconductor (typically TiO2), creating an interpenetrating network between the two phases. In this configuration, photogenerated electrons are transported through the titanium oxide phase to the cathode, while holes travel through the perovskite phase to the anode (see Figure I-5).

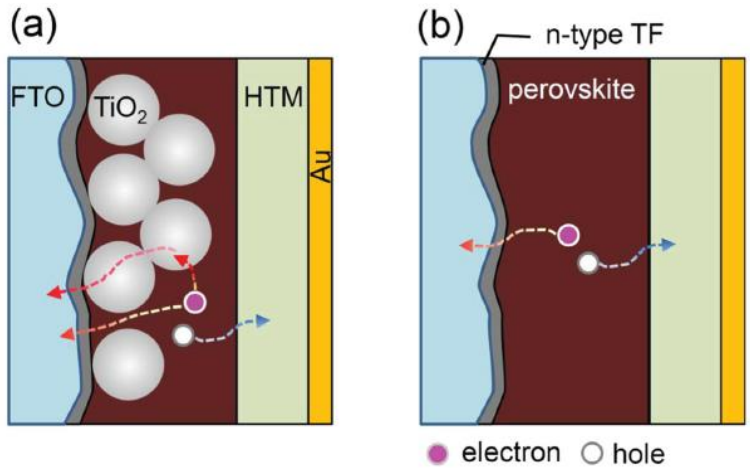

Figure I-6: Charge transport channels in perovskite solar cells (a) using mesoporous medium (b) planar perovskite structure [63].

In planar structure, devices interfacial buffer layers of hole and electron transport material (ETM and HTM) are used to fabricate the devices. These layers help drive the photo-generated charges from the photoactive medium to the electrodes, either through built-in potential or an external applied field. The power conversion efficiency of these devices heavily relies on the quality of the perovskite film morphology. Poor morphology can lead to charge accumulation in the medium, increasing charge recombination and reducing device

performance. Establishing Ohmic contact between the active and ETM/HTM layers is crucial for successful charge collection in these devices. Effective solar energy conversion depends on the optical absorption of the photoactive medium, ideally overlapping with the visible and near-infrared regions of the solar spectrum due to the high intensity of radiation in these areas. If the band gap of a solar absorber is too small (<1 eV), the device can collect extra current from infrared emission but may have a low open-circuit voltage. Conversely, if the band gap is too wide (>2 eV), only a small fraction of solar radiation can be harvested. A semiconductor with a band gap of approximately 1.2–1.6 eV is considered ideal for single-junction solar cell fabrication. Hybrid perovskite films are direct band gap semiconductors with low bulk trap densities, exhibiting significant luminous properties. The band gap of hybrid perovskites can be adjusted through molecular engineering, allowing for tuning of the compound composition.

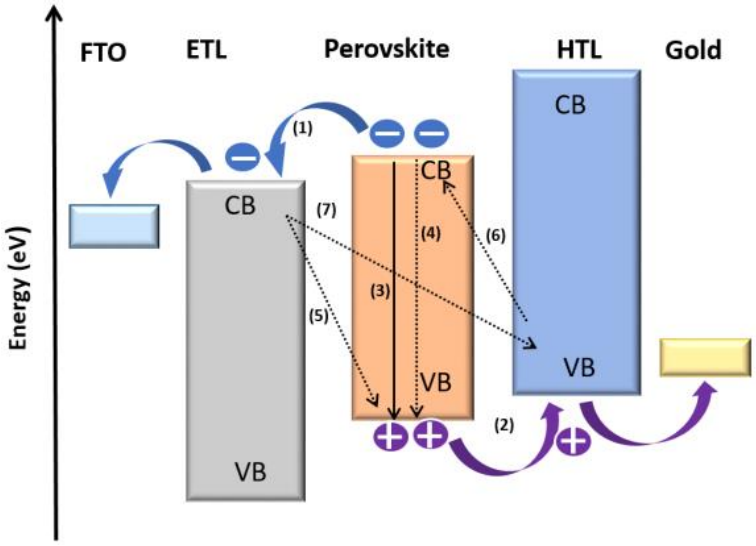

Figure I-7 : A Energy band levels diagram and charge transport processes of electrons and holes in perovskite solar cells. The arrows (1-7) indicate the direction of the charge transfer. The blue circle represents the electrons with a white minus sign, and the holes are the purple circles with a white plus sign. (FTO-Fluorine –doped Tin Oxide coated glass) [64].

I-2.3 Recent Advances in Perovskites Ferroelectric Materials for Photovoltaic Applications

Ferroelectric perovskites have attracted significant interest in photovoltaics due to their distinctive properties and potential to enhance solar cell performance. Perovskite solar cells, like CH3NH3PbI3-xClx mixed-halide perovskite cells, have demonstrated high efficiency and cost-effectiveness in production [65]. The incorporation of ferroelectric polymers, such as polyvinylidene difluoride (PVDF), as additives has been found to improve electron transport, further boosting the efficiency of these solar cells. Recent progress in molecular ferroelectrics with perovskite structures has also advanced the development of high-performance photovoltaic devices. These molecular materials offer benefits like low acoustic impedance, flexible structural design, and ease in achieving functional properties, making them promising for ferroelectric perovskite applications [66]. Additionally, research on the ferroelectric and photovoltaic characteristics of (Ba, Ca)(Ti, Sn, Zr)O3 perovskite ceramics has revealed their potential in solar energy conversion [67]. Efforts to enhance photovoltaic effects, such as reconstructing perovskite structures to achieve quasi-2D ferroelectrics, have shown potential in improving the bulk photovoltaic effect and enabling passive X-ray detection in electronic devices [68].

Moreover, the advancement of fatigue-resistant layered hybrid perovskite ferroelectrics such as BCPB has proven to possess stable spontaneous polarization and a high Curie temperature, indicating their potential for use in photovoltaic non-volatile memories and next-generation electronic devices [69]. Theoretical research has also been conducted to examine the photoelectric characteristics of ferroelectric perovskites like $CsGeBr_3$, emphasizing the significance of strain manipulation in adjusting ferroelectric polarization and enhancing photovoltaic efficiency [70]. Furthermore, the remarkable ferroelectric photovoltaic effect observed in dissimilar double-perovskite thin films further highlights the promise of ferroelectric perovskites in advancing solar cell technology [71]. In summary, the review of literature on ferroelectric perovskites in photovoltaics demonstrates substantial progress in comprehending and utilizing these materials to enhance solar energy conversion. Researchers are continuously exploring innovative methods to enhance the effectiveness and functionality of photovoltaic devices through the use of ferroelectric perovskite

materials,ranging from molecular ferroelectrics to fatigue-resistant layered hybrid perovskites.

I-2.4 Evolution of Perovskite Solar Cells

Despite the remarkable success and high efficiency of Metal Halide Perovskite (MHP) solar cells, their development history is surprisingly short, spanning less than a decade. Although various MHP structures were synthesized and tin-based MHP transistors were developed during the 20th century, it wasn't until 2009 that perovskites were first integrated into a solar cell [72]. Over the past few decades, inorganic perovskite oxides (e.g., CaTiO3, BaTiO3, LaMnO3) and halides (e.g., CsSnI3, CsPbI3) have been extensively researched for their wide range of applications in optics , magnetics , electronics , and superconductors [73]. Recently, organic-inorganic halide perovskite (OIHP) materials have emerged as a groundbreaking class in thin-film photovoltaics. In the 1990s, Mitzi et al. [74] pioneered research on the structural properties of OIHP materials and adapted them for various thin-film devices, including solar cells and transistors [75]. The first application of OIHP in photovoltaics came in 2009, with the use of MAPbBr3 as light absorbers in dye-sensitized solar cells (DSSCs), achieving a solar energy conversion efficiency of 3.8% [72]. These perovskite-sensitized cells used a thin perovskite layer for light absorption, while charge carriers were transported via a mesoporous TiO2 scaffold and a solid or liquid hole transport layer [76]. This architecture led to rapid improvements in the power conversion efficiency (PCE) of perovskite-sensitized DSSCs, reaching a record value of 9.7% [77].

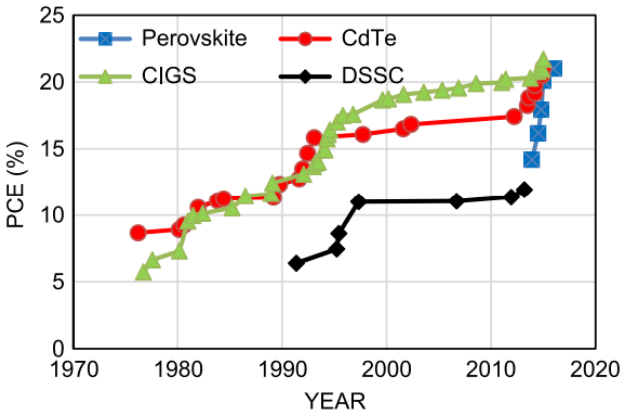

Figure I-8: Graph showing the rise in power conversion efficiency (PCE) of Perovskite Solar cells.

The liquid electrolyte caused degradation of the perovskite material in solar cells, leading to instability. As a result, perovskite solar cells (PSCs) received little attention due to reported degradation and low power conversion efficiency. In 2011, a group achieved a power conversion efficiency (PCE) of 6.5% using $CH_3NH_3PbI_3$-based iodide liquid electrolyte, but the perovskite nanocrystals decomposed quickly, lasting only about 10 minutes [78]. However, in 2012, organic-inorganic hybrid perovskite solar cells reappeared with an improved efficiency of 10.9% [79]. To address degradation and efficiency issues, the liquid electrolyte was replaced with a stable solid-state version [80]. Solar cells were fabricated with a similar architecture to DSSCs, using TiO2 as the n-type electron transporting material and Spiro-OMeTAD as the p-type hole transporting material, with CH3NH3PbI3 as the active layer [79]. Since the introduction of all-solid-state halide perovskite-based solar cells, the PCE has increased significantly from 3.8% [72] to 25.5% [81]for single-junction architectures in 2020. This breakthrough has propelled the PV field forward, generating widespread excitement for this novel material class. Over the past decade, PSCs have gained a reputation for being highly efficient and cost-effective technology. The bandgap of organic-inorganic halide perovskites can be adjusted between 1.55-2.3 eV by altering cation or anion elements, allowing access to different parts of the solar spectrum [82]. Various research groups have reported on methods of device preparation and PSC performance enhancements through material optimizations, architectural designs, interfacial engineering, and improved fabrication conditions, as detailed in Tables 1.

Active material	Deposition Method	ETM	HTM	J_{SC} $mAcm^{-2}$	Voc (V)	FF %	PCE %	Year	Ref
$CH_3NH_3PbBr_3$	Spin coating	TiO2	–	5.57	0.96]	0.59	3.13	2009	[83]
$CH_3NH_3PbI_3$	Spin coating	TiO2	–	11	0.61	0.61	3.81	2009	83]
$CH_3NH_3PbI_3$	Spin coating	m-TiO2	Spiro-OMeTAD	17.6	0.888	0.62	9.7	2012	[84]
$CH_3NH_3PbI_{3-x}Cl_x$	Spin coating	c-TiO2	Spiro OMeTAD	21.5	1.07	0.67	15.4	2013	[85]
$CH_3NH_3PbI_3{}_xClx$	Spin coating	m-TiO2/Al2O3	Spiro OMeTAD	21.5	1.02	0.71	15.9	2014	[86]
$CH_3NH_3PbI_3$	Spin coating	m-TiO2/Al2O3	Spiro OMeTAD	23.83	1.086	76.2	19.71	2015	[87]
$FAPbI_3$	direct intra molecular exchange	m-TiO2	PTAA	24.7	1.06	77.5	20.2	2015	[88]
$CH_3NH_3PbI_3$	Spin coating	m-TiO2	Spiro OMeTAD	23.69	1.113	77.3	20.4	2016	[89]
$CH_3NH_3PbI_3$	simple solution based PbCl2	-	-	23.7	1.05	-	18.1–19	2017	[90]

Table I-1 : Photovoltaic parameters of the PSCs .

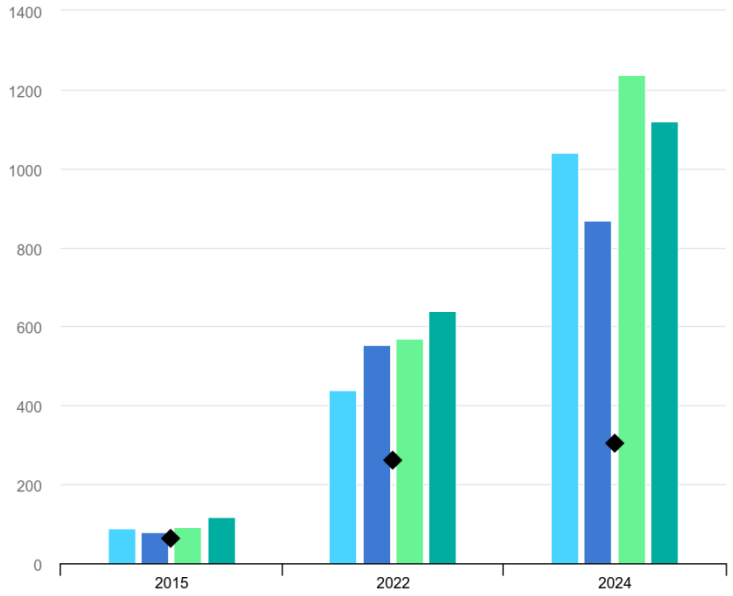

Figure I-9: numbers of publications with the topic on perovskite solar cells (PSCs) from 2015 to 2024. The publication data is adapted from ISI web of science database.

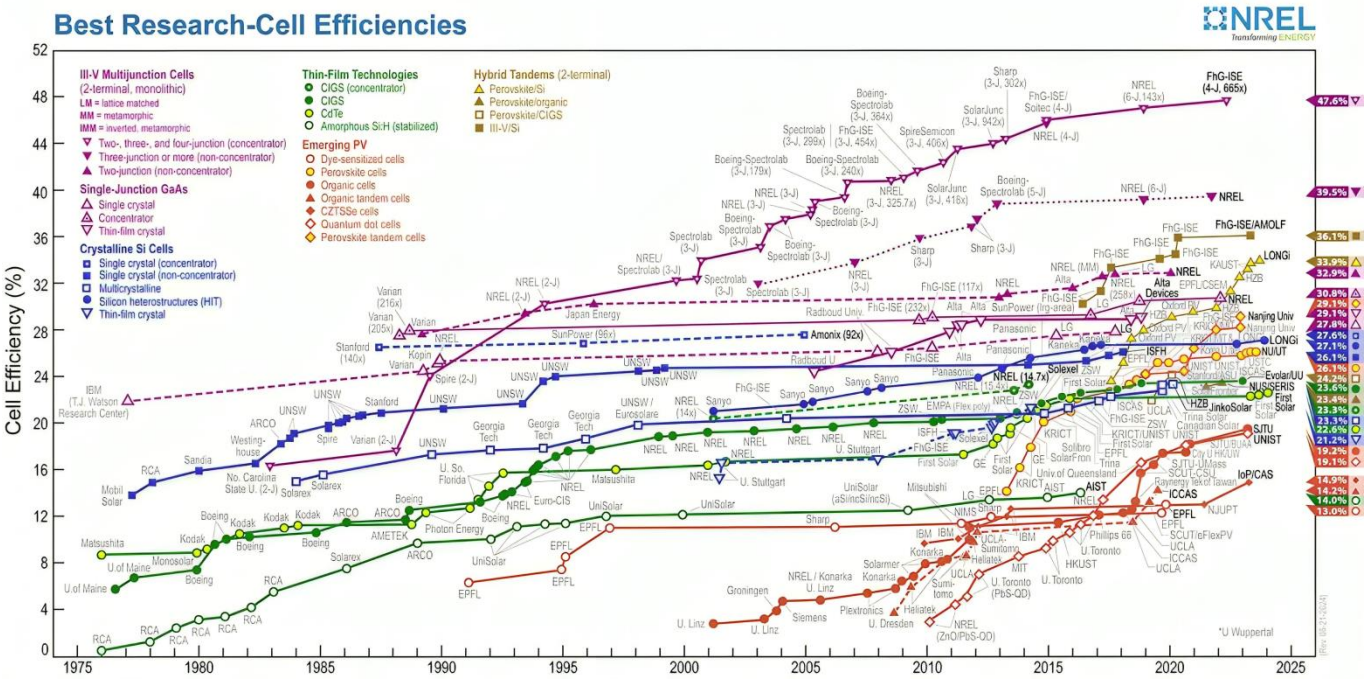

Figure I-10: Chart depicting the record cell efficiencies for multiple materials families, published as of the end of 2024. This plot is courtesy of National Renewable Energy Laboratory (NREL), Golden, CO Available from: https://www.nrel.gov/pv.

I-3 Energy: the case for Renewables and Photovoltaics

The generation of usable energy has been a driving force behind technological and societal advancement throughout history, from the early use of fire and water mills for food processing to the vast international electricity consumption required to power modern devices and industries. As the global population and development continue to grow, our ability to meet the increasing demand for energy must also expand. With the global population expected to surpass 9 billion by 2050, energy consumption is projected by the US and EU to at least double, rising from 13.5 TW in 2001 to 27.6 TW by that time [91].

In the latter half of the 20th century and into the 21st, it has become evident that while the growing energy demand could be met by consuming existing reserves of natural gas, oil, and coal, this approach would exacerbate the harmful effects of human-driven global warming and ocean acidification, impacting ecosystems, food production, and numerous natural and human systems [92]. To avoid these consequences and meet governmental and international emissions targets, a shift away from fossil fuels towards renewable energy sources is essential. Wind and solar energy offer low-carbon solutions without the significant upfront costs and hazardous waste associated with nuclear fission reactors, making them some of the most promising and rapidly expanding alternatives [91].

Solar energy, in particular, holds the greatest potential, as the power the Sun delivers to Earth far exceeds our energy needs. Harnessing just 0.001% of this energy would be enough to power the entire planet. Despite this, renewable energy sources currently account for less than 20% of global energy production, dropping to around 5% when biomass is excluded. Photovoltaic (PV) cells, which convert sunlight directly into electricity, provide a highly practical means of capturing solar energy. With few mechanical parts and long lifespans, PV modules can be installed on individual buildings to supply power where needed.

Historically, the higher cost of PV energy compared to fossil fuels limited its widespread adoption. However, recent improvements in efficiency and reductions in cost have driven significant growth in the PV market. From 2000 to 2015, while global renewable energy capacity increased tenfold, PV capacity grew by a factor of 60, now comprising nearly one-third of the total [93]. As photovoltaics continue to play a crucial role in a decentralized energy generation system, they are increasingly viewed as a direct competitor to traditional energy sources. Achieving electricity costs of $0.03/kWh would enable parity with fossil

fuels, paving the way for future expansion. This goal requires both high thermodynamic efficiency and a reduction in module costs—from around $4/W in 2010 to approximately $0.30/W [94]. Therefore, improving current solar cell designs and developing new, non-toxic, abundant, and highly efficient photovoltaic materials are vital areas of scientific research to meet or even surpass these targets.

I-3.1 The Photovoltaic effect

In 1839, Edmond Becquerel discovered the effects of chemical radiation from sunlight on electric currents. He observed the response of a galvanometer between two platinum electrodes submerged in a solution of chloride salt when exposed to light. This was the first known description of light-generated electric current [95]. In 1877, Adams and Day conducted experiments on bars of selenium which confirmed that the response was solely due to light and not heat. They named this electronic response from light the "photoelectric" effect, now known as the photovoltaic effect [96].

In modern times, we have discovered that the photovoltaic effect occurs when light hits a material, causing photons to excite electrons to a higher energy state and leaving behind a positively charged hole. This process occurs in solid semiconductors like selenium, where the electron moves to the conduction band and leaves a hole in the valence band. If the electron and hole are separated, they can act as free charge carriers, increasing conductivity and creating a photocurrent. This separation also creates a potential difference, resulting in a photovoltage. Like other electronic devices, the combination of current and voltage generates electrical power, allowing the conversion of solar power into electrical power without using chemical resources, supporting the goal of renewable energy technologies.

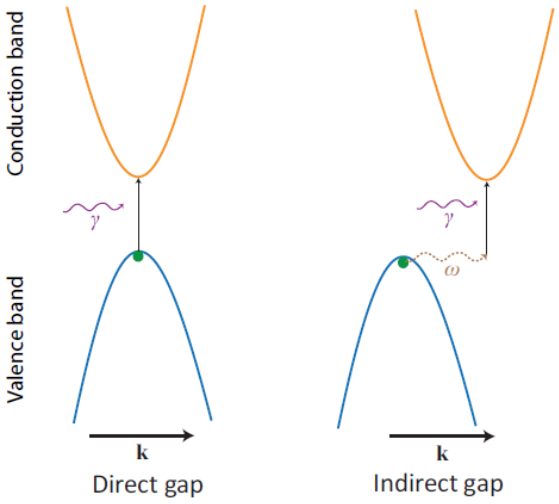

Figure I-11 : Representation of photoexcitation of an electron (green circle) in direct and indirect semiconductors. The electronic transition in each case is represented by the black arrow, while the incident photon is represented by the purple and a phonon, providing the change in momentum for an indirect transition, by the brown arrow respectively [97].

For photo absorption, the first stage of the photovoltaic effect, in semiconductors, there are two arrangements of valence and conduction band that need to be considered: when the minimum of the conduction band (CBM) and maximum of the valence band (VBM) occur in k-space at the same point, forming a direct fundamental band gap; or when they occur at different points in k- space, where the band gap is termed indirect. The excitation of an electron at these two conditions are depicted in Figure I-10: for a direct gap, the energy of the incident photon of the correct energy is absorbed, exciting the electron to the conduction band; in an indirect gap material, the absorption of a photon must be accompanied by an additional particle, such as a phonon (lattice vibration), to facilitate the change in k, as the momentum of the photon is negligible and the overall momentum must be conserved during the transition. The necessity for a three-particle interaction, as opposed to a two-particle interaction in a direct transition, severely reduces the probability of such an excitation occurring. The second stage of the photovoltaic effect charge separation can be performed in multiple ways, but in general requires some gradient, whether electrical/charge-based or thermodynamic, to drive the process.

I-3.2 The Schockley-Queisser limit

Throughout this section, we have contemplated the behaviour of a hitherto qualitative `ideal' solar cell, representing perfect diode behaviour and minimal avoidable losses. In 1961, Shockley and Queisser applied the thermodynamic principle of detailed balance, where all processes, such as absorption and recombination, are in equilibrium, to the behaviour of a solar cell to find the thermodynamic theoretical limit to the efficiency, ηof a single junction solar cell.[98]

In this, they considered the incident power on a cell on the surface of the earth from the Sun, as well as the dependencies of both Jsc and Voc to formulate an expression for η that depends on only a few factors, in their labels: x_g, the ratio between band gap and thermal energy, x_c, the ratio between the temperature of the cell and that of the Sun, m, the impedance matching (essentially the FF), ts, which corresponds to the EQE, and f, a factor considering other deviations from ideality, including fr, the fraction of total recombination that is radiative, as well as the angle of the sun to the cell.

This analysis also includes the assumption that only one electron-hole pair is generated from the excitation of one photon (EQE is limited to 100%), and that the excited carriers with energy in excess of the band gap relax (usually through the intercession of phonons) to the band edges, with the remaining energy lost as heat. They then fix some of these parameters to ideal values to obtain the detailed balance limit, now also known as the Shockley-Queisser (SQ) limit: a 100% FF and EQE above the band gap energy, a cell and ambient temperature of 25 °C, entirely radiative recombination and the position of the (unconcentrated) Sun directly normal to the cell surface lead to the dependence of η on solely the band gap, resulting in the curve depicted in Figure 1.7. This curve reaches a maximum of ~33:7% for the AM 1.5G spectrum at around 1:34 eV, limiting a single junction solar cell to this efficiency. No current solar cell has reached this ideal efficiency, although for some materials, it is being approached. Nevertheless, the SQ limit provides a target for developments in photovoltaic systems, as well as a key first target for the proposal of any new solar absorbers, if the band gap of the absorber layer falls outside a 0.9 eV to 1.6 eV range, then the absolute limit on the efficiency of a cell utilising that material will be limited to <30%, and thus compare unfavorably to other current absorbers which have band gaps within this range [99].

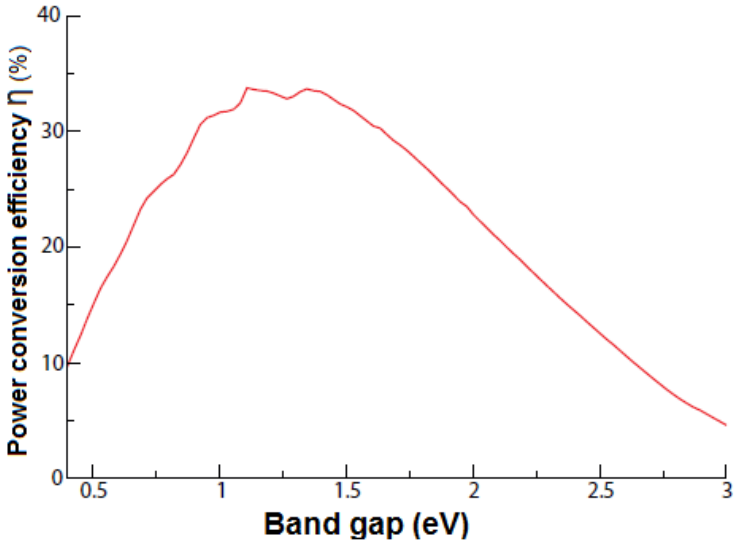

Figure I-12 : The Shockley Queisser limit for a single junction solar cell, given as a function of cell efficiency against band gap of the absorber layer[98].

We note here that some of the assumptions in the SQ limit are not absolute: for example, concentrators to enable a higher intensity of light are commonplace, and methods of multiple exciton generation (producing more than one carrier pair per photon) such as singlet fission are an active topic of research interest for integration with photovoltaics [99].

I-3.3. General Photovoltaic properties: Voc, Jsc, FF and efficiency

The focus now shifts to analyzing the measured outputs and properties of the solar cell, as well as comparing these metrics between different cells. The primary output of interest is the power generated in the form of electricity, which depends on the input power (intensity of incident photons) and the conversion efficiency. The efficiency of the solar cell in converting input power to output power is a critical factor in determining its overall performance. By understanding and optimizing this efficiency, we can enhance the power output of the cell and improve its overall energy conversion. Comparing the performance of different solar cells involves evaluating their power outputs and efficiencies. This comparison allows researchers to identify the most effective cells and technologies for specific applications. By conducting these comparisons, advancements in solar cell technology can be made to increase efficiency and performance. Solar cells rely on light sources for their operation. The standard method for comparing different solar cells in the laboratory involves using the output of an `artificial sun' known as the AM1.5G spectrum. This spectrum

represents the global average of spectral irradiance from the Sun onto the Earth under specific conditions, accounting for atmospheric losses. By using the AM 1.5G spectrum as a reference, researchers can evaluate the power conversion efficiency (PCE) of photovoltaic (PV) devices. PCE, denoted by η, is a crucial factor in maximizing the performance of PV devices. It is calculated as the ratio of maximum output power to incident power. The efficiency of a solar cell is determined by its ability to convert light into electrical power. The maximum output power (Pmax) of a solar cell is the product of the current and potential difference, similar to other electronic devices. In the case of a photovoltaic cell, the calculation also involves a specific current, voltage, and a variable known as the fill factor.

$$\eta = \frac{P_{max}}{P_{in}} = \frac{V_{OC}J_{SC}FF}{P_{in}} \quad (2)$$

Where V_{oc} represents the open-circuit voltage, J_{sc} denotes the short-circuit current (density), and FF stands for the fill factor, all of these parameters are associated with the extrinsic characteristics of a solar cell , They will be further explained in the subsequent discussion.To ensure consistency across measurements for various devices, solar cell efficiency testing is conducted under standard conditions: the AM1.5G spectrum, a temperature of 25°C, and an incident power density P_{in} defined as 1 kW/cm² [100].

The first parameter to discuss is the short-circuit current, which is the current that flows through the cell when it is short-circuited (i.e., the contacts on both sides of the cell are directly connected), resulting in zero output voltage. This represents the maximum current that can be achieved within the cell. As mentioned earlier, photocurrent is generated by charge carriers (electrons or holes) under illumination, making J_{sc} dependent on various internal and external factors. Two of these factors—the cell area and the intensity spectrum of incident light—are standardized for comparing different cells; the latter is standardized for terrestrial cells using the AM 1.5G spectrum, while the former is typically accounted for by expressing the short-circuit current I_{sc} as a current density J_{sc} in units of mA/cm². The remaining factors are directly related to the cell's ability (through the absorber layer) to generate charge carriers, which depend on its optical absorption and reaction. For ideal cell behavior, every photon with energy above the absorber's band gap is absorbed, producing two charge carriers for the external circuit. As a result, J_{sc} is solely dependent on the band gap, and the highest theoretical J_{sc} occurs when the band gap is minimal but still finite.

The open circuit voltage is the maximum potential difference across a cell when there is no net current flowing through it, and is the opposite property to the Jsc. The absolute maximum of the Voc is determined by the band gap of the absorber layer, representing the greatest potential difference between the negatively charged electron and positively charged hole at their respective band edges. However, additional mechanisms such as band alignment in transport or contact layers and electron-hole recombination within the cell can further constrain the Voc. This reduction in Voc is influenced by the dark current, J0, which is the current that flows through the cell naturally in the absence of light, as a result of thermally-generated carriers. The Jsc, on the other hand, reflects the immediate current generated by light-induced carriers. As a solar cell functions as a diode, the Voc can be calculated using the diode equation for a charge q at J = 0[101].

$$V_{OC} = \frac{nk_BT}{q} \ln\left(\frac{J_L}{J_0} + 1\right) \quad (3)$$

The ideality factor, n, is determined by the Boltzmann constant, k_B, the temperature, T, and the light-generated current, JL, which is approximately equal to the short-circuit current, J_{sc}, for most absorbers JL ≈J_{sc} . The reverse saturation current, J_0, is heavily influenced by recombination within the solar cell material, leading to a decrease in the open-circuit voltage, V_{oc}, from the band gap value. However, in an ideal absorber, V_{oc} tends to increase with the band gap until J_{sc} becomes very small. The ideality factor is also influenced by recombination mechanisms. The fill factor, FF, can be observed through the J(V) curve, which shows the current-voltage relationship of the cell under illumination and is used to calculate efficiency. Figure I-12 illustrates an example of a J-V curve and defines FF and P_{max}[101].

$$FF = \frac{P_{max}}{J_{SC}V_{OC}} = \frac{J_{MP}V_{MP}}{J_{SC}V_{OC}} \quad (4)$$

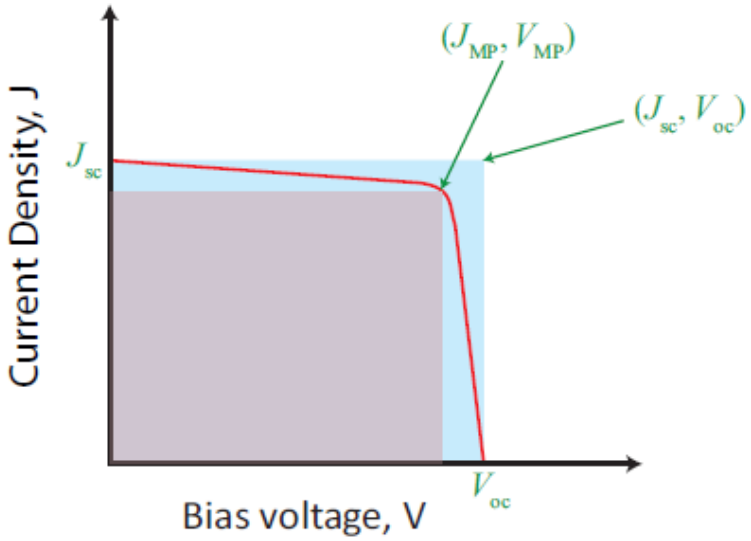

Figure I-13 : J(V) curve for a hypothetical solar cell, marked by a red line, with the positions of J_{sc} and Voc marked. The fill factor, FF, is represented by the ratio of the areas of the blue rectangle (defined by J_{sc} and Voc) and the pink rectangle (defined by the point of maximal power output, at (J_{MP},V_{MP})).[101]

The fill factor (FF) is essentially an indicator of how "square" the JV curve is. The maximum power that can be extracted from the cell occurs at the point where the product of current (J) and voltage (V) is greatest, typically located at the top-right corner of the curve. In an ideal solar cell, there would be no losses, and the curve would perfectly match the area of the blue rectangle in Figure I-12, with maximum power occurring at J_{sc} and V_{oc}. However, in real solar cells, parasitic resistances cause deviations from ideal performance, resulting in a curve that follows a path like the hypothetical red line in Figure I-12, which corresponds to a smaller area (represented by the pink rectangle). The maximum power is then given by J_{MP}-V_{MP}, and the fill factor measures the ratio of the actual area to the ideal area under the JV curve. It quantitatively represents the power loss due to non-ideal behavior as a percentage. With these terms defined, we now understand the key physical properties of a solar cell that can be externally measured and contribute to overall efficiency. However, it's also important to consider how a solar cell deviates from ideality, causing losses in efficiency and performance. Recognizing and understanding these loss mechanisms is essential for identifying efficient absorber materials for photovoltaic (PV) cells.

I-4. SLME

Spectroscopic Limited Maximum Efficiency (SLME) is a metric recently introduced by Yu and Zunger for evaluating photovoltaic absorbers using first-principles calculations [102]. This metric is valuable for comparing the intrinsic properties of the materials analyzed in this thesis. The Shockley-Queisser (SQ) limit, discussed in Section I-9, defines the theoretical thermodynamic efficiency limit of single-junction solar cells based on the absorber's band gap. While SLME largely follows the thermodynamic "detailed balance" approach of the SQ limit, it diverges in two key aspects related to the optical behavior of the absorber.

The first difference lies in the treatment of recombination. In the original SQ method, factors representing both light transmission and non-radiative recombination are combined into a single factor. Although Shockley and Queisser considered various values for this factor, the SQ limit is typically quoted in its highest efficiency form, assuming the factor is 1, meaning the absorber behaves as a perfect blackbody with only radiative recombination. This assumption is reasonable for direct band gap materials like GaAs. However, in materials with an indirect band gap or where the direct gap is forbidden, radiative recombination is much less significant, and other pathways such as Shockley-Read-Hall or Auger recombination account for a greater proportion of losses. Due to higher non-radiative recombination, the efficiency is lower than the SQ limit. SLME accounts for this non-radiative recombination by treating the fraction of total electron-hole recombination that is radiative (*fr*) as:

$$f_r = e^{-\Delta/k_B T} \quad (5)$$

where k_B is the Boltzmann constant, T, the temperature, and Δ is the difference between the lowest direct allowed transition (E_g^{da}) and the fundamental band gap (E_g). For allowed direct-gap materials, Δ =0 and f_r=1, restoring the radiative limit; for Δ>0, f_r is reduced, and non-radiative recombination is increased. As the non-radiative recombination increases, the SLME reduces, representing the increased total recombination (from both radiative and non radiative sources) impacting the overall available charge carrier concentration, and thus the reduction of the short-circuit current.

The second modification in SLME concerns photon absorptivity, α(E), which is similar to external quantum efficiency. In the SQ limit, absorptivity is simplified as a step-wise function, with 0 below the band gap and 1 above, assuming the absorber acts like a perfect blackbody.

However, in SLME, absorptivity is modeled using Beer-Lambert behavior, where it depends on both the calculated absorption coefficient, α(E), and the thickness of the material, L.

$$\alpha(E) = 1 - e^{-2\alpha(E)L} \quad (6)$$

A higher absorption coefficient results in a lower overall exponential factor, bringing the material's behavior closer to that of a blackbody above the band gap (with α(E)still being 0 below the band gap, as there is no sub-gap absorption in the calculations). By incorporating material-specific optical absorption, SLME provides better differentiation between absorbers with the same band gap, highlighting those that may experience optical losses in practical applications.

Overall, SLME is a valuable tool for the theoretical evaluation of potential thin-film solar absorbers, as it incorporates intrinsic properties like band gap type and absorption coefficient to assess their impact on cell efficiency. However, SLME is not a perfect theoretical model of cell efficiency. Like the SQ limit, it does not account for defect properties, which can significantly affect carrier mobilities and recombination in real systems. It also overlooks the effects of interfaces between cell layers and the potential series resistance that may arise. Additionally, recent work by Blank et al. has shown that the omission of the refractive index in SLME oversimplifies the relationship between internal properties like α and the external efficiencies that would be observed in actual devices [103]. Despite these limitations, SLME remains a useful screening metric. It is cost-effective (relying solely on calculable static optical properties), does not depend on empirical models, and is especially beneficial for assessing emerging materials, which may lack prior characterization or study. SLME is particularly relevant to thin-film absorbers, where optical losses, such as those from indirect band gap behavior, can be substantial.

I-5. Ferroelectric photovoltaics

Perovskite materials are of interest for optoelectronic and photovoltaic applications due to their unique semiconductor properties, such as high-absorption coefficient, ambipolar charge transport, low exciton-binding energy, and ferroelectric properties. Materials like BiFeO3, Bi2FeCrO6, and BiMnO3 have been extensively studied for their ferroelectric and photovoltaic effects, as they exhibit spontaneous polarization and switchable polarization, enabling efficient charge carrier separation in photovoltaic cells [104]. Despite the advantages of these metal oxide based perovskite photovoltaic cells, they suffer from low power conversion efficiency (PCE) due to their large bandgap and insulating properties, which are typical characteristics of ferroelectric materials.

I-5.1. Ferroelectric material

Ferroelectrics are versatile materials with spontaneous polarization that occurs without an applied electric field [105]. One of their key features is ferroelectricity, which allows for the switching of polarization using an electric field. Since the discovery of ferroelectricity in Rochelle salt in 1921[106], materials like BiFeO3 (BFO), BaTiO3 (BTO), and PbZr1-xTixO3 (PZT) have been extensively studied. Ferroelectrics have reversible electric polarization that can be controlled by electric fields, temperature, composition, or pressure [107], making them ideal for applications like non-volatile memories [108]. The coupling of electric polarization with strain or magnetization also makes ferroelectrics useful for sensors and actuators [109]. Light-matter interactions in ferroelectrics have revealed novel phenomena like the photovoltaic effect and photostrictive effect [110] , and the photostrictive effect (nonthermal photo-induced deformation) [111]. More recently,. Photo-ferroelectric materials, especially in thin films, are gaining attention for their potential applications [112] and the ability to control material functionalities through electric polarization (tuning photocurrent or photostriction [113]). This offers exciting possibilities for future applications [114].

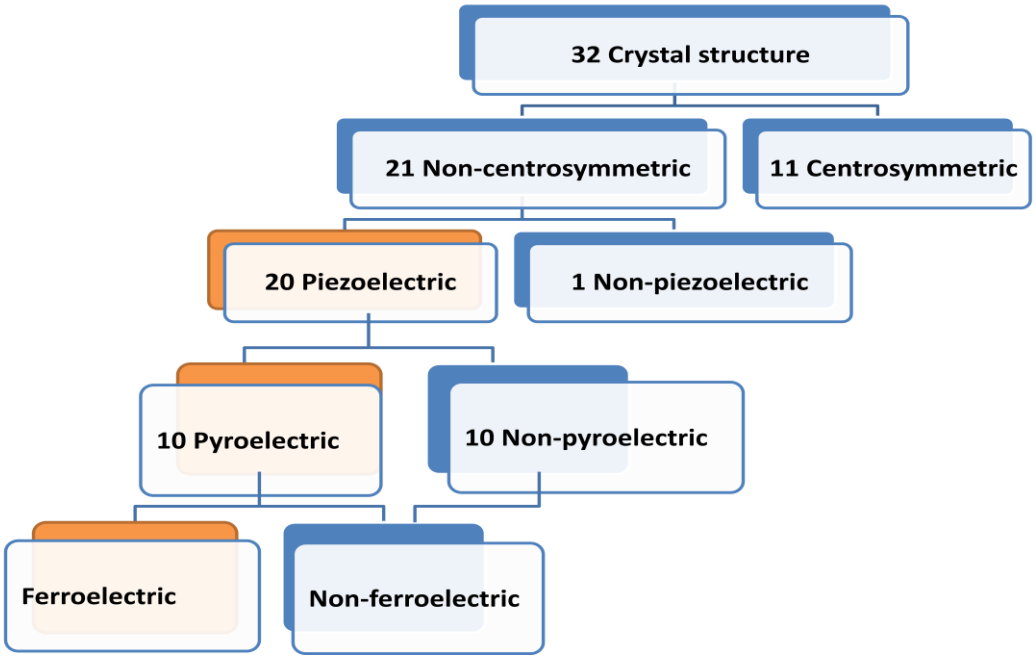

Figure I-14. Flow chart of 32 crystal classes [115].

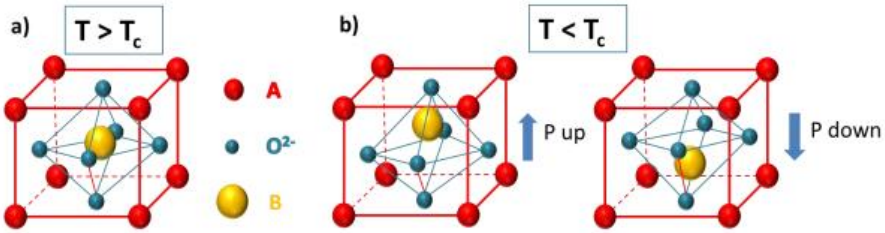

Figure I-15. Ferroelectric ABO3 perovskite structure in a) cubic phase above Tc, b) tetragonal phase below Tc for up and down polarization states[115].

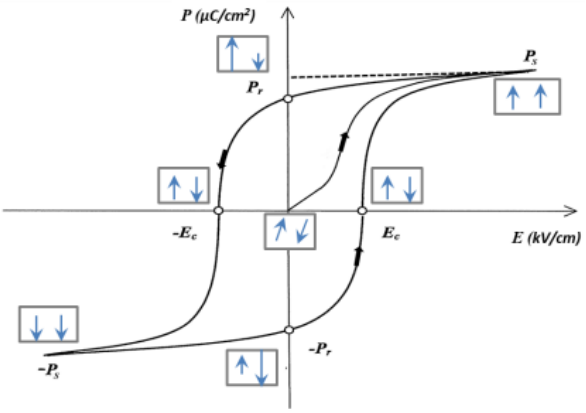

Figure I-16. Typical P-E hysteresis loop of a ferroelectric material below its Curie temperature (Tc). Above Tc, the crystal has no spontaneous polarization.[115]

I-5.2 The perovskite ferroelectric:

Perovskite oxides with ferroelectric properties are well-suited for stable photovoltaic cells that exhibit high open-circuit voltages. In these materials, the photoexcited carriers are separated by an internal electric field created by polarization, rather than the electric field at p-n junctions found in conventional solar cells. These devices can produce an open-circuit voltage that exceeds the band gap of the perovskite material. Ferroelectric perovskite materials like BaTiO3 [116], LiNbO3 [117] and BaFeO3 have been studied for their potential in photovoltaic applications. However, solar cells based on ferroelectric perovskites typically have low power conversion efficiencies (PCEs) due to their large band gaps, which limit absorption to UV light—only 3.5% of the solar spectrum. Among these materials, BaFeO3 has the smallest band gap at 2.2 eV (absorbing 25% of the spectrum), but this is still higher than the ideal band gap of 1.34 eV for optimal photovoltaic performance.

The light-harvesting efficiency of ferroelectric oxide perovskite materials can be improved by reducing their band gap, thereby expanding their absorption range to include more visible light. This band gap reduction can be achieved through careful selection of A- and B-site elements, such as in the case of the Bi,$FeCr0_6$ double perovskite [118], or by combining different perovskite materials, like in $[KNbO3]_{1-x}[BaNi_{1/2}Nb_{1/2}O_{3-\sigma}]_x$(KBNNO) [119], to form perovskite solid solutions. Examples of such solid solutions include Bi_4TiO_{12}-LaCoO3 [120] and $BiMnO_3$-$BiMn_2O_5$, where a low-bandgap ferroelectric perovskite is combined with a non-ferroelectric material, leading to better performance than single perovskite compounds.

Ferroelectric materials with a perovskite structure have low conductivity, which can impact their dielectric properties by allowing charge carriers to leak. This poor conductivity hinders the efficiency of photovoltaic charge transport in bulk perovskites. Increasing the electrical conductivity is crucial for improving the efficiency of these materials, but it can also lead to increased leakage current and affect the ferroelectric behavior of the perovskite. Balancing conductivity and ferroelectric properties is essential for enhancing the efficiency of ferroelectric photovoltaics. Oxide perovskites containing 3d transition metals have low carrier mobilities and high carrier recombination. On the other hand, oxide double perovskites with a A_2MnMv0_6 structure, which do not contain 3d transition metals, have lower bandgaps and smaller carrier effective masses, making them excellent absorbers for

photovoltaics[121].

I-5.3 Photovoltaic effect in the perovskite ferroelectric oxides

Approximately fifty years ago, researchers discovered the ferroelectric photovoltaic effect in noncentrosymmetric ferroelectric materials , which is distinct from traditional p-n junctions. In ferroelectric materials, the inherent ferroelectricity causes a separation of photoexcited charges upon light absorption, leading to the generation of high photovoltage. Additionally, other photovoltaic mechanisms, such as the PV effect resulting from the Schottky barrier at the ferroelectric/electrode interface, may also be present in ferroelectric materials sandwiched between electrodes. The first part of this discussion will explore the charge separation mechanisms in conventional p-n photovoltaic cells with interface-induced photovoltaic effects. Subsequently, various photovoltaic mechanisms that can occur in ferroelectric materials will be examined in depth, along with the latest advancements in different types of ferroelectrics.

I-6 Classical PV effect in p-n junction

Silicon-based solar cells utilize p-n junctions created by doping the semiconductor with impurities to form hole-rich (p-type) and electron-rich (n-type) regions. These regions combine at equilibrium through a narrow depletion junction. When photons with energies higher than the bandgap are absorbed, free charges are generated as shown in Figure I-16a. The photogenerated charges are separated by the internal electric field, Ebi, created by the energy barrier at the depletion interface layer, resulting in short circuit current Isc and open-circuit voltage Voc. The maximum Voc is limited by the difference in quasi-Fermi levels of electrons and holes and cannot exceed the bandgap energy, Eg, of the material. The efficiency of a single p-n junction is capped at 31% of incoming light when the energy gap is Eg = 1.35 eV[122], known as the Shockley-Queisser limit. This efficiency is determined by the interface properties of the p-n junction.

The primary limitation of the PV effect in p-n junctions is that the open-circuit voltage (V_{oc}) cannot exceed the bandgap value, while the short circuit current density (J_{sc}) can reach levels

of mA/cm^2. This principle also applies to metal-semiconductor junctions, and ferroelectrics can be utilized as an alternative to enhance solar cell efficiency as illustrated in Figure I-16b. The lack of center of symmetry in ferroelectrics aids in the separation of photogenerated carriers, leading to higher V_{oc} values exceeding the bandgap, up to kV. Unlike p-n junctions, the PV effect in ferroelectrics is based on a single bulk material, known as the bulk photovoltaic effect in non-centrosymmetric crystals (BPE).

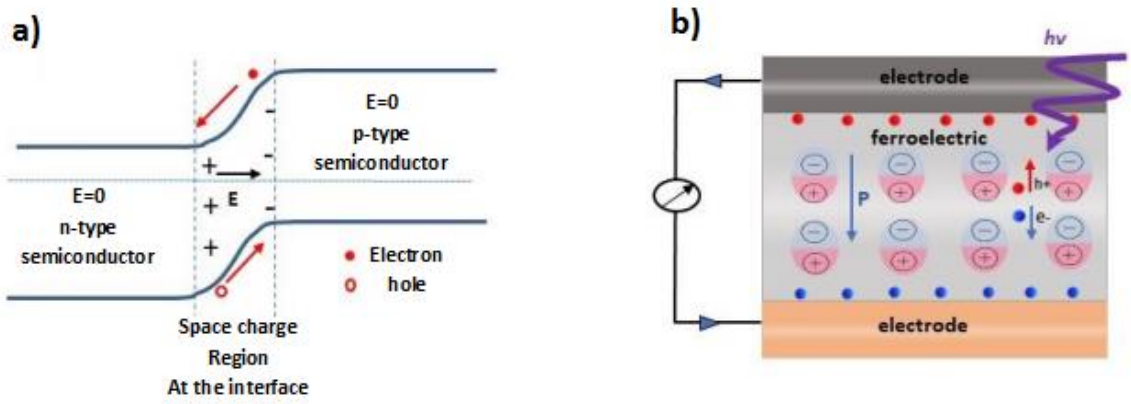

Figure I-17. Photovoltaic effect schematics in a) a semiconductor p-n junction and b) ferroelectric based capacitor device [115].

I-7 Bulk photovoltaic effect (BPVE)

The BPVE is a continuous photocurrent produced within the bulk area of the FE material due to the lack of lattice non-centrosymmetry.

Many Ferroelectrics, like silicon, are wide bandgap semiconductors. The first photovoltaic effect in ferroelectrics was observed in BaTiO3 (BTO) in 1956[123]. Glass et al. developed a theory for this effect in 1974, focusing on LiNbO3 (LNO)[124] crystals without a center of symmetry. They suggested that the photocurrent is proportional to the light intensity, and the steady state photoinduced current can be expressed as:

$$J_{SC} = k\alpha I_l \tag{7}$$

Where k is the Glass constant (A.cm/W) and α is the absorption coefficient (cm^{-1}). The photo-induced currents measured in LNO single crystals are of the order of nano-ampere.

The photo-induced current is related to the film thickness, as shown by the relationship [123]:

$$I_{SC} \sim A\alpha\Phi * exp(-\alpha) \quad (8)$$

Where, ϕ is the photon flux density per second, d the film thickness and A is a constant depending on many parameters such as the internal field, quantum efficiency, the lifetime of charge carriers, their mobility, and energy. Since, the current increases when the thickness decreases, the use of thin-film is preferred to increase the PV efficiency of the device.

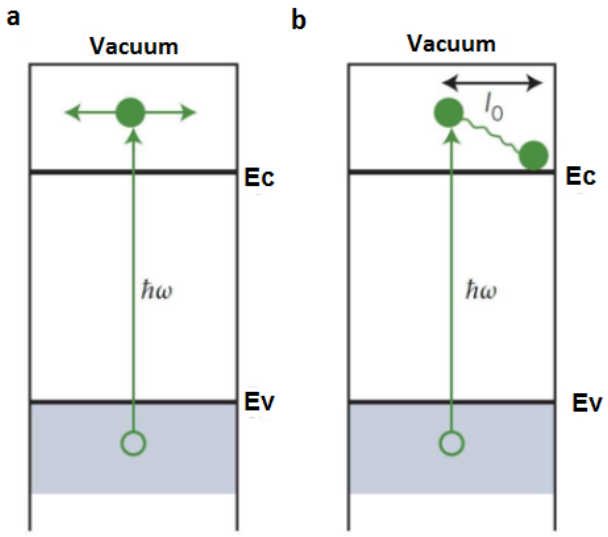

Figure I-18. Schematic illustrating the photoexcitation processes in (a) centrosymmetr ic crystal and (b) non-centrosymmetr ic crystal.[125]

The current in the BPVE is influenced by the alignment of light in relation to the ferroelectric polarization. This phenomenon demonstrates a second-order nonlinear optical behavior and is represented by a third rank tensor when illuminated with linearly polarized light . Therefore, the impact of BPVE on the photocurrent and its reliance on the polarization vector of the light wave can be expressed as

$$J_{SC} = \beta_{ijk}^{L} e_j e_k^* I \quad (9)$$

Where, $\beta ijk\ L$ is BPVE third rank tensor for linearly polarized light, e denotes polarization vector in direction j and k and I is the intensity of light [126]. The light-induced voltage of up to kV is a unique feature of this photovoltaic effect [127]. The open circuit

photovoltage Voc arising from photocurrent depends on the electrode spacing (d) and the conductivity (σ), [123]:

$$V_{OC} = J_{SC}(\frac{d}{\sigma}) \quad (10)$$

Where, σ is the combination of dark conductivity (σ_d) and photoconductivity (σ_{ph}):

$$\sigma = \sigma_d + \sigma_{ph} \quad (11)$$

Internal energy gap levels or, as in other sensitive cases, oxygen deficiency [128] can affect the values of photo-induced voltages.

I-8 Factors affecting PV properties in FE

The photovoltaic characteristics of ferroelectric materials have been demonstrated to rely on various factors including polarization, thickness, domain walls, defects, the bandgap of the ferroelectric material, and the interface between the ferroelectric and electrode. The subsequent chapter will provide a detailed analysis of the factors that influence the photovoltaic properties.

I-8.1 Polarization

Ferroelectric materials have an inherent property known as polarization, which can be altered by an electric field. The orientation of this polarization plays a role in determining the photocurrent direction in thin ferroelectric films . The ability to switch photovoltaic properties in ferroelectrics is important for applications such as photo-ferroelectric memories, but achieving this can be challenging due to factors like the electrode-ferroelectric interface (Schottky barrier), film thickness, and defects.

Choi et al. conducted a study to investigate how polarization affects the photovoltaic properties. They used a BFO single crystal sample with gold electrodes and exposed it to light at a wavelength of 532 nm with an intensity of20 mW/cm^2. The researchers observed a photocurrent density of 7.35 mA/cm^2, indicating that the photovoltaic effect was likely due to changes in the Schottky barrie height at interfaces [129]. Furthermore, the applied electric field can completely alter the diode behavior in BFO ferroelectrics [62]. In 2016, Yang and colleagues demonstrated that polarization can switch the J-V

characteristics of $La_{2/3}Sr_{1/3}MnO_3$/BFO/ITO under standard sunlight [130]. When polarization is upwards, the curve is rectifying, and the photocurrent increases with light intensity. Conversely, when polarization is downward, the curve becomes linear, and the photocurrent flows in the opposite direction to the polarization. This behavior is attributed to polarization-induced changes in Schottky barriers [130]. Another example from Lee et al. showed a photocurrent density of 0.1 mA/cm² in a 400 nm BFO film placed between a platinum top electrode and an $SrRuO_3$ bottom electrode under 10 mW/cm² illumination [131]. The photocurrent direction reversed with polarization, and it reached zero when polarization domains of opposite directions were equal.These findings align with the BPVE, as equal but opposite photocurrents occur for opposite polarization states. Notably, the photocurrent exhibited a hysteresis loop that overlapped with the ferroelectric loop, indicating a strong link between polarization and photocurrent. Additionally, $Pb_{0.97}La_{0.03}(Zr_{0.52}Ti_{0.48})O_3$ doped with WO_3 (PLWZT) [132] demonstrated that reversing the polarization can reverse the photovoltaic current direction or at least adjust its magnitude.

Additionally, previous studies have shown that the photocurrent exhibits a loop pattern, similar to a ferroelectric hysteresis loop, in relation to the poling voltage. This suggests a clear connection between photocurrent and electrically poled polarization in different ferroelectric materials like PbTiO3-based solid solutions [190].

To achieve a similar effect to the switchability of the ferroelectric diode, one could consider changing the direction of polarization to alter the direction of the photocurrent. This concept aligns with the third rank of the BPVE tensor, as reversing the polarization also reverses the BPVE tensor and subsequently the photovoltaic current. Another method of achieving switchability is by adjusting the Schottky barrier height at the ferroelectric-metal interface due to polarization. The switchability feature of the BPVE in ferroelectrics allows for applications beyond electricity generation. The polarization-dependent photo response in PZT was studied for potential use in non-destructive readout ferroelectric memories.

I-8.2 Defects

The impact of defects on photovoltaic (PV) properties is challenging to predict. Like the Schottky barrier effect, defects such as oxygen vacancies can create built-in fields that influence the photovoltaic characteristics of ferroelectric (FE) materials and their ability to switch polarization [134]. Oxygen vacancies are often seen as the cause of leakage in FE materials, leading to a decline in PV effects . Therefore, stringent methods are employed to minimize oxygen vacancies in FE materials to enhance PV device performance. However, oxygen vacancies might also have a positive effect by altering interfacial screening charges, forming trapping centers, and increasing sub-bandgap absorption in PV devices. Moubah et al. demonstrated that PV effects in a single-domain BFO are only noticeable after applying an electric field weaker than the coercive field under illumination . This is explained by the fact that the electric field generates oxygen vacancies, which migrate to the BFO/electrode interface, where they lower the energy barrier, allowing for detectable photocurrent.

Another example shows that BTO/p-Si samples with a high concentration of oxygen vacancies exhibit an enhanced photovoltaic response, which is linked to the formation of p-n junctions at the interface between the oxygen vacancy space charge layer and the p-doped silicon [135]. On the other hand, under certain conditions, oxygen vacancies can significantly reduce leakage in ferroelectric (FE) materials. Shuai et al. [136] report that leakage decreases when more Mn ions are added to BTO films, as this increases the number of oxygen vacancies available for charge compensation, acting as trapping centers within the BTO bandgap [136]. Furthermore, defect centers within the bandgap may induce sub-bandgap levels, which not only expand solar spectrum absorption but also create an asymmetry in k-space between charge generation and recombination, fulfilling the BPVE condition .These findings suggest that controlling defects is crucial for developing efficient ferroelectric-based PV devices.

I-8.3 Bandgap engineering

In photovoltaic devices, it is important for the ferroelectric material to have a bandgap near the maximum of the solar spectrum, which is 1.4 eV. Many ferroelectrics typically have a bandgap in the ultraviolet range of the solar spectrum (refer to Figure I-18.). This wide bandgap is a result of the electronic structure of ferroelectric oxide perovskite, which is determined by the valence band maximum from the oxygen 2p orbital and the conduction band minimum from the transition metal d orbital .

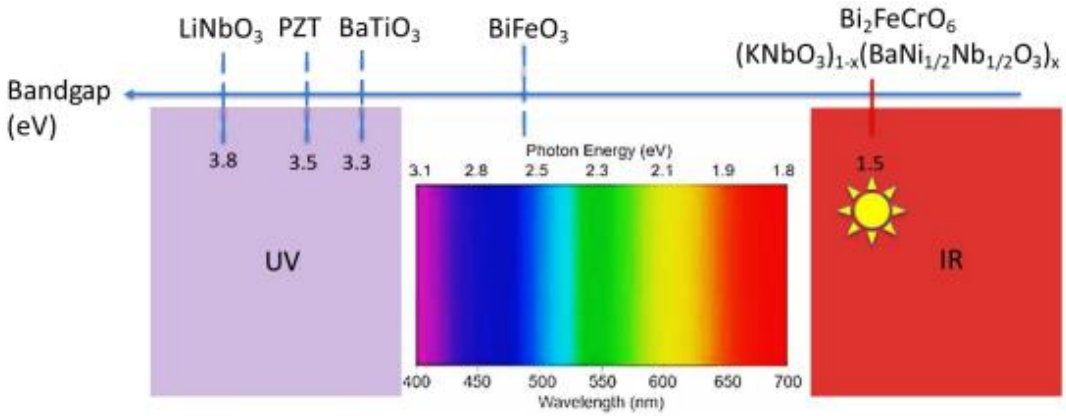

Figure I-19. Various perovskite oxides with their bandgap.

One approach involves adjusting the chemical ordering of materials by using a narrow bandgap material to reduce the overall bandgap. Nechache et al. [137] successfully created a multilayer structure of Bi_2FeCrO_6 (BFCO) with three layers, each absorbing a different part of the solar spectrum due to their varied chemical ordering. This design achieved a record efficiency of 8.1% for traditional ferroelectrics, with typical photovoltaic outputs of Jsc = 11.7 mA/cm² and Voc = 0.79 V under AM1.5 illumination. Previous work on Bi_2FeCrO_6 thin films reported a 6.5% power conversion efficiency (PCE) under red laser illumination, producing one of the highest-ever recorded photovoltaic current densities of 0.99 mA/cm² [138]. Another method to reduce the bandgap is through chemical modifications, such as solid solutions or doping. In 2013, Grinberg et al. [139] demonstrated a bandgap of 1.46 eV in the compound $(KNbO_3)_{(1-x)}(BaNi_{0.5}Nb_{0.5}O_3)_x$ (KBNN), which combines ferroelectric ($KNbO_3$) with an oxygen-deficient perovskite ($BaNi_{1/2}Nb_{1/2}O_3$). Overall, significant efforts have been made to lower the bandgap of ferroelectric materials, which typically have large gaps and poor photovoltaic performance, as outlined in Table I-2.

Compounds	Eg(eV)
$BiMnO_3$	1.2
Bi_2FeCrO_6	1.4-2.0
$LiNbO_3$	3.78
$KNbO_3$	3.3
$(KNO)_x(BNNO)_{(1-x)}$	1.5-3
$KBiFe_2O_5$	1.6

Table I-2 Summary of bandgap of different perovskite oxides [140].

I-9 the ferroelectric switching barrier

The ferroelectric switching barrier refers to the energy required to switch the polarization in ferroelectric materials. In hybrid improper ferroelectrics, this barrier can be reduced by applying biaxial strain, which influences the ferroelectric ground states and adjusts the switching barrier. This reduction is linked to strain-induced phase transitions to nonpolar phases. By understanding and controlling the intrinsic factors affecting the coercive field of hybrid improper ferroelectrics, materials with lower coercive fields and strong polarizations can be engineered. In $A_3B_2O_7$ compounds, biaxial strain can adjust the ferroelectric switching barrier by impacting the ferroelectric ground states. By mapping the strain-tolerance factor phase diagram, the intrinsic switching barrier of hybrid improper ferroelectric Ruddlesden-Popper oxides can be minimized. This is due to strain-induced transitions to nonpolar phases. The research demonstrates that strain is an effective method for reducing the coercive field and creating low-coercive-field ferroelectrics with stable polarization [141].

The switching energies in perovskite ferroelectrics play a crucial role in field-induced phase transformations. Factors such as the energy threshold for 90-degree domain switching, the crystallographic orientation of the applied electric field, and the rotation path between tetragonal variants all influence these transformations. The behavior of these phase transitions is important for accurately assessing and validating Landau coefficients, highlighting the need to understand polarization dynamics and domain switching energies in perovskite ferroelectrics. Consequently, the ferroelectric switching barrier refers to the critical electric field required for a phase transformation from the tetragonal to the orthorhombic phase in ferroelectric materials [142].

The study of ferroelectric switching in $Al_{1-x}Sc_xN$ involves calculating the switching barrier height at both T=0 and finite temperatures using Ginzburg – Landau theory. It has been found that the switching barrier decreases as the Sc concentration increases, indicating the potential for ferroelectric switching. For $Al_{0.8}Sc_{0.2}N$, the estimated switching electric field at room temperature is 26.5 MV/cm, although this value is higher than experimental results due to the assumption of uniform coherent switching. The research also shows that the enhancement of the piezoelectric constant e33 in $Al_{1-x}Sc_xN$ alloys is primarily driven by internal-strain contributions. The addition of Sc to AlN increases e33, with internal-strain effects becoming more significant as scandium concentration rises, leading to a structure closer to a layered hexagonal arrangement. The feasibility of ferroelectric switching is further supported by the decreasing switching barrier with increasing Sc concentration, as well as the temperature dependence of the barrier. Overall, the study highlights the relationship between the switching barrier in Al1−xScxN compounds, the enhancement of piezoelectric properties, and the potential for ferroelectric behavior [143].

External methods can manipulate the effects of spin texture on ferroelectric materials, as demonstrated in ferroelectric α-GeTe and multiferroic $Ge_{1-x}Mn_xTe$. The study shows that operando electrostatic spin manipulation in Rashba semiconductors is possible due to ferroelectric polarization reversal. Additionally, the research reveals the switching of the perpendicular spin component in multiferroic $Ge_{1-x}Mn_xTe$ as a result of electric-field-induced magnetization reversal. This study provides evidence of magnetoelectric coupling, allowing for intertwined spin-switching paths with Rashba-Zeeman splitting in a multiferroic system, enabling mutual control of magnetism and ferroelectricity [144].

I-10 Formal Description of the Berry-Phase Theory

The fundamental property of dielectric materials known as macroscopic polarization can give rise to permittivity, piezoelectric tensors, and various other physical variables. Solids have the ability to polarize either spontaneously, as seen in ferroelectrics, or in response to external factors such as an applied electric field or strain. It was only recently that a comprehensive theory of bulk macroscopic polarization was developed .King-Smith and

Vanderbilt discovered that a change in polarization, typically observed in experiments, is connected to the net adiabatic charge transport [145]. They formulated a clear equation for the change caused by adiabatically altering any Hamiltonian parameter λ[146].

$$\Delta P = -e \int_0^1 d\lambda \int_{\mathrm{BZ}} \frac{\mathrm{d}^3\mathrm{K}}{(2\pi)^3} 2Im \sum_n^{occ} \langle \nabla_K u_{nK} | \partial_\lambda u_K \rangle \quad (12)$$

where u_{nk} is the periodic part of the Bloch state φ_{nk}. The k integral is over the Brillouin zone, and the sum is over occupied bands. The integrand contains a mixed (k, λ) Berry curvature $B_{K\lambda} = 2Im \sum \langle \tilde{\nabla}_K u_{nK} | \partial_\lambda u_K \rangle$[147] which also appears in Thouless charge pumping [148] . The change in polarization in the direction of a lattice vector Rα can be expressed as a Berry phase [146].

$$\Delta P_3 = -\frac{e}{(2\pi)^3} \sum_n^{occ} \int dK_1 dK_2 \int_0^{|G_3|} i \langle u_{nK} | \partial_\lambda u_K \rangle \, dK_3 \Big|_{\lambda=0}^{\lambda=1} \quad (13)$$

Where, $\Delta P_3 = \frac{1}{2\pi} G_3 . \Delta P$ and the (k_1, k_2) integral is taken over the parallelogram spanned by the reciprocal lattice vectors G_1 and G_2. The geometric phase of a Bloch state on a path traversing the Brillouin zone was introduced by Zak and related to Wyckoff positions [149].

Ortiz and Martin [150] extended the King-Smith−Vanderbilt formula to correlated many-body systems by incorporating twisted boundary conditions. This concept has been applied in the analysis of the insulating state of matter [151], the integer quantum Hall effect [152], and topological charge pumping [153]. In the case of one-dimensional systems, the Ortiz−Martin formula can be expressed as:

$$\Delta P = -\frac{e}{2\pi} \lim_{\substack{N,L\to\infty \\ \frac{N}{L}=const}} \int_0^{2\pi/L} i \langle \Phi_0 | \partial_\lambda \Phi_0 \rangle \, dK \Big|_{\lambda=0}^{\lambda=1} \quad (14)$$

where N is the number of electrons in a supercell of length L. The many-body state Φ0 = Φ0(x1, ..., xN) is the ground state of the “twisted” Hamiltonian.

$$\widehat{H}(K,\lambda) = \sum_{i=1}^{N} \frac{(P_i + \bar{h}k)^2}{2m} + \sum_{\langle ij \rangle} \frac{e^2}{|r_i - r_j|} + \widehat{V_{ext}}(\lambda) \quad (15)$$

where $\hat{V}_{ext}(\lambda)$ includes the electron−ion interaction and any other external potentials and the parameter k generates an effective magnetic flux that takes on the role of the twisted boundary conditions. The twisted boundary conditions on the ground state of the original Hamiltonian $\hat{H}$ ' are Φ_0 '(x1, ..., xi + L, ..., xN)=$e^{ikL}\Phi_0$ '(x_1, ..., x_i , ..., x_N) for all i. The ground state of the twisted Hamiltonian $\hat{H}$= $\hat{U}$+ $\hat{H}$ '$\hat{U}$with $\hat{U}$= $e^{ik}(\hat{x}_1 + \hat{x}_2 + \cdots + \hat{x}_N)$ is related to the original ground state by $|\Phi_0\rangle = \hat{U}|\Phi_0'\rangle$.

The key outcome presented here is a geometric phase formula for macroscopic polarization that retains the simplicity and practicality of the King-Smith−Vanderbilt formula, while also incorporating the essential correlations found in the Ortiz−Martin result. The simplified formula is

$$\Delta P_{red} = -e\int_0^1 d\lambda \int_{BZ} \frac{d^3K}{(2\pi)^3} 2Im \sum_{n=1}^{\infty} \langle \nabla_K v_{nK} | \partial_\lambda v_{nK} \rangle \quad (16)$$

Where $v_{nK}(r) = \sqrt{f_{nK}} e^{i\zeta_{nK}} u_{nK}(r)$ is the periodic part of the natural Bloch state $\Psi_{\mathrm{nK}}(\mathrm{r}) = e^{iK.r} v_{nK}(r)$; $v_{nK}(r)$ is analogous to u_{nk}(r) in eq 1. The natural Bloch orbitals $\Phi_{nK}(r) = e^{iK.r} u_{nK}(r)$ and occupation numbers f_{nk} are eigenfunctions and eigenvalues of the one-body reduced density matrix (rdm) ρ1(rσ, r'σ'),31 and ζ_{nk} is a crucial additional phase variable that determines the gauge of ψnk(r). Given any gauge choice for the natural Bloch orbitals φnk(r), the ground state ζnk can be determined from the stationary conditions ∂E/∂ζnk = 0, where E = ⟨Φ'|$\hat{H}$ '|Φ'⟩ and $|\Phi'\rangle = exp[i\sum_{nK} \zeta_{\mathrm{nK}} \hat{f}_{\mathrm{nK}}] \left|\Phi^{Ansatz}\right\rangle$. Here, $\hat{f}_{nk} = b_{nk}$. b_{nk} is the number operator for φ_{nk}(r) and

$$|\Phi^{Ansatz}\rangle = \sum_{n_1K_1,\ldots,n_NK_N} c_{n_1K_1} c_{n_2K_2}, \ldots\ldots\ldots, c_{n_NK_N} \left|\Phi_{n_1K_1} \Phi_{n_NK_N}\right\rangle \quad (17)$$

is an Ansatz for the wave function as a superposition of Slater determinants of natural Bloch orbitals. It follows from this definition that if we make a gauge transformation $\varphi_{nk}(r) \rightarrow e^{i\theta}{}_{nk}$ $\varphi_{nk}(r)$, the ζ_{nk} transform as $\zeta_{nk} \rightarrow \zeta_{nk} - \theta_{nk}$. Hence, the phases of $\psi_{nk}(r)$ and $v_{nk}(r)$ are invariant under such a transformation, and any geometric or topological quantity constructed from them, including ΔP_{red} in eq 16, is gauge invariant .

Equation 16 represents the change in polarization as a sum of single-particle band contributions, similar to the King-Smith−Vanderbilt formula, but it utilizes natural orbitals instead of Kohn−Sham orbitals. Natural orbitals are intrinsic to the many-body wave

function, unlike the eigenstates of a mean-field Hamiltonian. Since the natural Bloch state ψnk includes the factor fnk, where $0 \leq f_{nk} \leq 1$ due to quantum and thermal fluctuations, the valence band contributions are reduced compared to the non-interacting case, and there are non-zero contributions from the conduction bands. Here, "valence" refers to bands with occupation numbers $f_{nk} > 1/2$, while "conduction" refers to those with $f_{nk} < 1/2$ (a more precise definition will follow). Equation 16 is based on the assumption that the sum of the natural orbital geometric phases closely approximates the geometric phase of the fully correlated many-body state.

For band insulators, the Berry phase can be expressed using the Bloch function in momentum space. In more complex situations, such as with interactions or disorder, the many-body ground state as a function of the flux through the system can be used instead. However, the definition of the Bloch function and the description of the flux are not unique, leading to variations in the Berry phase's value depending on its precise definition. This concept was formalized in the "modern theory of polarization" developed in the 1990s. Following important foundational work by Resta [154], King-Smith and Vanderbilt [155] made the principal contributions to the theory, which was later reviewed by Resta [154]. This theory is often referred to as the "Berry-phase theory of polarization" because polarization is described in terms of a quantum phase known as the Berry phase [156]. To address macroscopic systems, whether crystalline or disordered, it is standard in condensed-matter theory to apply periodic (Born–von Karman) boundary conditions [157]. This treats the system as if it were in a finite box that repeats periodically in all three Cartesian directions, effectively creating a ring-like structure. Eventually, the system is considered in the limit of an infinitely large box. For practical purposes, the thermodynamic limit is reached when the box is much larger than atomic scales. This approach ensures the system has no surface, and all properties are considered "bulk" properties. In the case of many-electron systems, periodic boundary conditions mean the wavefunction and Hamiltonian must also be periodic within the box.

I-11 Wannier representation and Berry Phase

The main result of the theory of bulk polarization (TBP) is an expression for the electronic contribution to polarization, PPP, which is formulated as a Berry phase [158] of the valence-

band Bloch wave functions transported across the Brillouin zone (BZ). Alternatively, this expression can be reformulated in real space as the vector sum of the charge centers of the valence-band Wannier functions. Practical methods for calculating both the Berry phase[158] and the Wannier functions [159] have been developed and are now standard in first-principles electronic structure calculations.

Remember that the Wannier function, $w_n(r)$, in unit cell R associated with band n is defined as [160].

$$w_n(r-R) = \frac{\Omega}{(2\pi)^3}\int_{BZ} d^3K e^{-iK.R}\,\Psi_{nK}(r) = \frac{\Omega}{(2\pi)^3}\int_{BZ} d^3K e^{-iK.(r-R)}\,u_{nK}(r) \quad (18)$$

where $\Psi_{nK}(r)$ = $e^{ik.r}u_{nk}(r)$ are the Bloch functions, written as usual in terms of the cell-periodic part, $u_{nk}(r)$. Here Ω is the unit cell volume, and the integral is over the Brillouin zone.

In contrast to Bloch functions, which are spread out in space, Wannier functions are localized. This makes them useful for visualizing chemical bonding and for serving as basis sets in electronic structure calculations, where their minimal overlap leads to favorable scaling with system size. Their relevance here lies in their localized nature, providing an atomic-like description of charge density in a solid. While the actual charge density in a solid is continuous, this localized approach allows dipole moments to be calculated by summing charges multiplied by their positions [161].

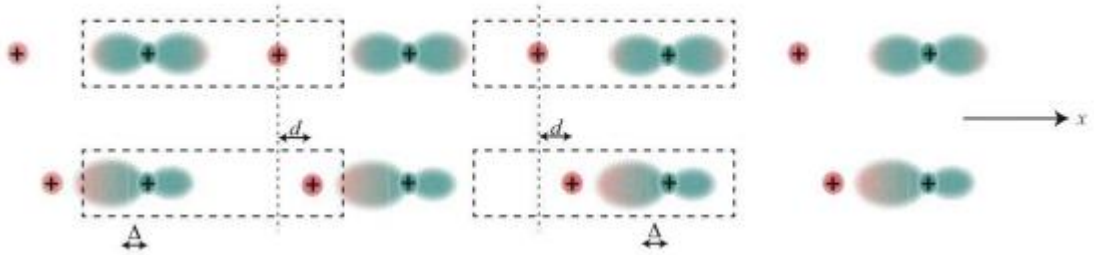

Figure I-20 One-dimensional chain of alternating cations (pink postively charged ion cores) and anions (green positively charged ion cores with their associated negatively charged valence electron cloud) [161].

I-12 Conclusion

Ferroelectric perovskite materials are a class of compounds that exhibit spontaneous electric polarization, which can be reversed by the application of an external electric field. These materials possess unique properties, such as high dielectric constants, strong piezoelectric effects, and the ability to exhibit polarization switching, which make them promising candidates for various electronic and energy applications. In the context of photovoltaics, ferroelectric perovskites have gained significant attention due to their ability to enhance charge separation and improve energy conversion efficiency. The intrinsic polarization in these materials can help to spatially separate photogenerated charge carriers, reducing recombination losses and increasing the overall efficiency of solar cells. Additionally, the ability to tailor their electronic and ferroelectric properties through doping or structural modifications provides a versatile platform for optimizing photovoltaic performance. As a result, ferroelectric perovskites are being actively researched for their potential in next-generation solar cell technologies, where they could offer a combination of high efficiency, low cost, and scalability for large-scale energy harvesting.

Bibliography

[1] De Wolf, S.; Holovsky, J.; Moon, S.-J.; Löper, P.; Niesen, B.; Ledinsky, M.; Haug, F.-J.; Yum, J.-H. and Ballif, C. 'Organometallic halide perovskites: sharp optical absorption edge and its relation to photovoltaic performance'. J. Phys. Chem. Lett. 2014, 5, 1035–1039.

[2] Moreira, M. L., Paris, E. C., Nascimento, G. S., Longo, V. M., Sambrano, J. R., Mastelaro, V. R., Bernardi, M. I. B., Andrs, J., Varela, J. A., & Longo, E. (2009). Structural and optical properties of CaTiO3 perovskite-based materials obtained by microwaveassisted hydrothermal synthesis: An experimental and theoretical insight. Acta Materialia,57(17), 5174-5185.

[3] Chilvery AK, Batra AK, Yang B, Xiao K, Guggilla P, Aggarwal MD, et al. Perovskites transforming photovoltaics, a mini-review. J Photon Energy 2015;5(1), 057402–057402.

[4] Y.-Y. Sun, Chalcogenide perovskites for photovoltaics, Nano Lett. 15 (1) (2015) 581-585.

[5] N.-G. Park, Perovskite solar cells: an emerging photovoltaic technology, Mater. Today. 18 (2) (2015) 65-72.

[6] A. Walsh, D.O. Scanlon, S. Chen, X. Gong, S.H. Wei, Self-regulation mechanism for charged point defects in hybrid halide perovskites, Angew. Chem. 54 (6) (2015) 1791-1794.

[7] Kieslich, G.; Sun, S. and Cheetham, A. K. 'An extended tolerance factor approach for organic–inorganic perovskites'. Chem. Sci. 2015, 6, 3430–3433.

[9] M.A. Green, A. Ho-Baillie, H.J. Snaith, The emergence of perovskite solar cells, Nat. Photonics 8 (7) (2014) 506-514.

[10] F. Hao, C.C. Stoumpos, R.P.H. Chang, M.G. Kanatzidis, Anomalous band gap behavior in mixed Sn and Pb perovskites enables broadening of absorption spectrum in solar cells, J. Am. Chem. Soc. 136 (22) (2014) 8094-8099.

[11] M.T. Weller, O.J. Weber, P.F. Henry, A.M. Di Pumpo, T.C. Hansen, Complete structure and cation orientation in the perovskite photovoltaic methylammonium lead iodide between 100 and 352 K, Chem. Commun. 51 (20) (2015) 4180-4183.

[12] D.A. Egger, A.M. Rappe, L. Kronik, Hybrid organic-inorganic perovskites on the move, Acc. Chem. Res. 3 (2016) 573-581.

[13] C.K. Moller, Crystal structure and photoconductivity of caesium plumbohalides, Nature 182 (4647) (1958) 1436.

[14] D.B. Mitzi, Synthesis, structure, and properties of organic-inorganic perovskites and related materials, Progress in Inorganic Chemistry, John Wiley & Sons, Inc., 2007, pp. 1-121.

[15] A. Kojima, K. Teshima, Y. Shirai, T. Miyasaka, Organometal halide perovskites as visible-light sensitizers for photovoltaic cells, J. Am. Chem. Soc. 131 (17) (2009) 6050-6051.

[16] H.-S. Kim, C.-R. Lee, J.-H. Im, K.-B. Lee, T. Moehl, A. Marchioro, et al., Lead iodide perovskite sensitized all-solid-state submicron thin film mesoscopic solar cell with efficiency exceeding 9%, Sci. Rep. 2 (2012) 591.

[17] H.J. Snaith, Perovskites: the emergence of a new era for low-cost, high-efficiency solar cells, J. Phys. Lett. 4 (21) (2013) 3623-3630.

[18] Laboratory, N. R. E., Best Research-Cell Efficiencies. 2017.

[19] A. Polman, M. Knight, E.C. Garnett, B. Ehrler, W.C. Sinke, Photovoltaic materials: present efficiencies and future challenges, Science 352 (6283) (2016) aad4424-1 - aad4424-10.

[20] Song Z, Watthage SC, Phillips AB, Heben MJ. Pathways toward high-performance perovskite solar cells: review of recent advances in organo-metal halide perovskites for photovoltaic applications. J Photon Energy 2016;6(2). [022001–022001].

[21] W.-J. Yin, T. Shi, Y. Yan, Unusual defect physics in CH3NH3PbI3 perovskite solar cell absorber, Appl. Phys. Lett. 104 (6) (2014) 063903-1-063903-4.

[22] H. Choi, J. Jeong, H.-B. Kim, S. Kim, B. Walker, G.-H. Kim, et al., Cesium-doped methylammonium lead iodide perovskite light absorber for hybrid solar cells, Nano Energy 7 (2014) 80-85.

[23] M. Gra¨tzel, The light and shade of perovskite solar cells, Nat. Mater. 13 (9) (2014) 838-842.

[24] Longo, G. (2017). Hybrid perovskites for light-emitting and photovoltaic devices (Doctoral dissertation, Facultat de Ciències Químiques).

[25]Bidault, O., Maglione, M., Actis, M., Kchikech, M., & Salce, B. (1995). Polaronic relaxation in perovskites. Phys. Rev. B, 52(6), 4191□4197.

[26]Correa, H. P. S., Cavalcante, I. P., Souza, D. O., Santos, E. Z., Orlando, M. T. D., Belich, H., Silva, F. J., Medeiro, E. F., Pires, J. M., Passamai, J. L., Martinez, L. G., & Rossi, J. L. (2010). Synthesis and structural characterization of the Ca2MnReO6 double perovskite. Cermica, 56(338), 193-197.

[27]Ishida, S., Fujii, S., Kashiwagi, S., & Asano S.,(1995). Search for half-metallic compounds in Co2MnZ (Z=IIIb, IVb, Vb Element). J. Phys. Soc. Jpn., 64(7), 2152-2157.

[28] Fert, A. (2008). Nobel lecture: origin, development, and future of spintronics. Rev. Mod. Phys., 80(4), 1517-1530.

[29] Wolf, S. A., Awschalom, D. D., Buhrman, R. A., Daughton, J. M., von Molnar, S., Roukes, M. L., Chtchelkanova, A. Y., & Treger, D. M. (2001). Spintronics: a spin-based electronics vision for the future. Science, 294(5546), 1488-1495.

[30]Tokura, Y. (2006). Critical features of colossal magnetoresistive manganites. Rep. Prog. Phys., 69(3), 797-851.

[31] Shimakawa, Y., Azuma, M., & Ichikawa, N. (2011). Multiferroic compounds with doubleperovskite structures. Materials, 4(1), 153-168.

[32] Rogado, N. S., Li, J., Sleight, A. W., & Subramanian, M. A. (2005). Magneto-capacitance and magneto-resistance near room temperature in a ferromagnetic semiconductor: La2NiMnO6. Adv. Mater., 17(18), 2225-2227.

[33] Ghimire, M. P., & Hu, X. (2016). Compensated half metallicity in osmium double perovskite driven by doping e-ects. Mater. Res. Express, 3(10), 106107-106113.

[34] K.W. Bagnall, J.B. Laidler, M.A.A. Stewart, Americium chloro-complexes. J. Chem. Soc. A **0**, 133–136 (1968). https ://doi.org/10.1039/J1968 00001 33

[35] L.R. Morrs, W.R. Robinson, Crystal structure of Cs2NaBiCl6. Acta Crystallogr. B **28**(2), 653–654 (1972). https ://doi. org/10.1107/S0567 74087 20029 48

[36] I.N. Flerov, M.V. Gorev, K.S. Aleksandrov, A. Tressaud, J. Grannec, M. Couzi, Phase transitions in elpasolites (ordered perovskites). Mater. Sci. Eng. **24**(3), 81–151 (1998). https :// doi.org/10.1016/S0927 -796X(98)00015 -1

[37] E.T. McClure, M.R. Ball, W. Windl, P.M. Woodward, Cs2AgBiX6 (X = Br, Cl): new visible light absorbing, leadfree halide perovskite semiconductors. Chem. Mater. **28**(5), 1348–1354 (2016). https ://doi.org/10.1021/acs.chemm ater.5b042 31

[38] G. Volonakis, M.R. Filip, A.A. Haghighirad, N. Sakai, B. Wenger, H.J. Snaith, F. Giustino, Lead-free halide double perovskites via heterovalent substitution of noble metals. J.

Phys. Chem. Lett. **7**(7), 1254–1259 (2016). https ://doi. org/10.1021/acs.jpcle tt.6b003 76

[39]A.H. Slavney, T. Hu, A.M. Lindenberg, H.I. Karunadasa, A bismuth-halide double perovskite with long carrier recombination lifetime for photovoltaic application. J. Am. Chem. Soc. **138**(7), 2138–2141 (2016). https ://doi.org/10.1021/ jacs.5b132 94

[58] A.H. Slavney, L. Leppert, D. Bartesaghi, A. Gold-Parker, M.F. Toney, T.J. Savenije, J.B. Neaton, H.I. Karunadasa, Defect-induced band-edge reconstruction of a bismuth-halide double perovskite for visible-light absorption. J. Am. Chem. Soc. 139(14), 5015–5018 (2017). https ://doi.org/10.1021/jacs.7b016 29

[40] Y. Bi, E.M. Hutter, Y. Fang, Q. Dong, J. Huang, T.J. Savenije, Charge carrier lifetimes exceeding 15 µs in methylammonium lead iodide single crystals. J. Phys. Chem. Lett. 7(5), 923–928 (2016). https ://doi.org/10.1021/acs.jpcle tt.6b002 69

[41] K.Z. Du, W. Meng, X. Wang, Y. Yan, D.B. Mitzi, Bandgap engineering of lead-free double perovskite Cs2Ag- BiBr 6 through trivalent metal alloying. Angew. Chem. Int. Ed. **56**(28), 8158–8274 (2017). https ://doi.org/10.1002/ anie.20170 3970

[42] T.T. Tran, J.R. Panella, J.R. Chamorro, J.R. Morey, T.M. McQueen, Designing indirect-direct bandgap transitions in double perovskites. Mater. Horiz. **4**(4), 688–693 (2017). https ://doi.org/10.1039/C7MH0 0239D

[43] S.E. Creutz, E.N. Crites, M.C. De Siena, D.R. Gamelin, Colloidal nanocrystals of lead-free double perovskite (elpasolite) semiconductors: synthesis and anion exchange to access new materials. Nano Lett. **18**(2), 1118 (2018). https ://doi. org/10.1021/acs.nanol ett.7b046 59

[44] C. Zhang, L. Gao, S. Teo, Z. Guo, Z. Xu, S. Zhao, T. Ma, Design of a novel and highly stable lead-free Cs2NaBiI6 double perovskite for photovoltaic application. Sustainable Energy Fuels **2**(11), 2419 (2018). https ://doi.org/10.1039/ C8SE0 0154E

[45] X.G. Zhao, J.H. Yang, Y. Fu, D. Yang, Q. Xu, L. Yu, S.H. Wei, L. Zhang, Design of lead-free inorganic halide perovskites for solar cells via cation-transmutation. J. Am. Chem. Soc. **139**(7), 2630–2638 (2017). https ://doi.org/10.1021/ jacs.6b096 45

[46] X.G. Zhao, D. Yang, Y. Sun, T. Li, L. Zhang, L. Yu, A. Zunger, Cu-In halide perovskite solar absorbers. J. Am. Chem. Soc. **139**(19), 6718–6725 (2017). https ://doi. org/10.1021/jacs.7b021 20

[47] Z.W. Xiao, K.Z. Du, W.W. Meng, J.B. Wang, D.B. Mitzi, Y.F. Yan, Intrinsic instability of Cs2In(I)M(III)X6 (M=Bi, Sb; X=Halogen) double perovskites: a combined density functional theory and experimental study. J. Am. Chem. Soc. **139**(17), 6054–6057 (2017). https ://doi.org/10.1021/jacs.7b022 27

[48] A.E. Maughan, A.M. Ganose, A.M. Candia, J.T. Granger, D.O. Scanlon, J.R. Neilson, Anharmonicity and octahedral tilting in hybrid vacancy-ordered double perovskites. Chem. Mater. **30**(2), 472–482 (2018). https ://doi.org/10.1021/acs. chemm ater.7b045 16

[49] B. Lee, C.C. Stoumpos, N. Zhou, F. Hao, C. Malliakas, C.Y. Yeh, T.J. Marks, M.G. Kanatzidis, R.P.H. Chang, Air-stable molecular semiconducting iodosalts for solar cell applications: Cs2SnI6 as a hole conductor. J. Am. Chem. Soc. **136**(43), 15379–15385 (2014). https ://doi.org/10.1021/ja508 464w

[50] A. Wang, X. Yan, M. Zhang, S. Sun, M. Yang, W. Shen, X. Pan, P. Wang, Z. Deng, Controlled synthesis of lead-free and stable perovskite derivative Cs2SnI6 nanocrystals via a facile hot-injection process. Chem. Mater. **28**(22), 8132–8140 (2016). https ://doi.org/10.1021/acs.chemm ater.6b013 29

[51] Z. Tan, J. Li, C. Zhang, Z. Li, Q. Hu et al., Highly efficient blue-emitting Bi-doped Cs2SnCl6 perovskite variant: photoluminescence induced by impurity doping. Adv. Funct. Mater. **28**(29), 1801131 (2018). https ://doi.org/10.1002/ adfm.20180 1131

[52] L. Zhou, J.F. Liao, Z.G. Huang, X.D. Wang, Y.F. Xu, H.Y. Chen, D.B. Kuang, C.Y. Su, All-inorganic lead-free Cs2PdX6 (X=Br, I) perovskite nanocrystals with single unit cell thickness and high stability. ACS Energy Lett. **3**(10), 2613–2619 (2018). https ://doi.org/10.1021/acsen ergyl ett.8b017 70

[53] M.G. Ju, M. Chen, Y. Zhou, H.F. Garces, J. Dai et al., Earthabundant nontoxic titanium (IV)-based vacancy-ordered double perovskite halides with tunable 1.0 to 1.8 eV bandgaps for photovoltaic applications. ACS Energy Lett. **3**(2), 297–304 (2018). https ://doi.org/10.1021/acsen ergyl ett.7b011 67

[54] Filip, M. R., Volonakis, G., & Giustino, F. (2020). Hybrid halide perovskites: fundamental theory and materials design. *Handbook of Materials Modeling: Applications: Current and Emerging Materials*, 295-324.

[55] Volonakis G, Haghighirad AA, Snaith HJ, Giustino F (2017b) Route to stable lead-free double perovskites with the electronic structure of CH3NH3PbI3: a case for mixed-cation [Cs/CH3NH3/CH(NH2)2]2InBiBr6. J Phys Chem Lett 8-3917

[56]Giustino F, Snaith HJ (2016) Toward lead-free perovskite solar cells. ACS Energy Lett 1(6): 1233–1240

[57] Jain A, Ong SP, Hautier G, Chen W, Richards WD, Dacek S, Cholia S, Gunter D, Skinner D, Ceder G, Persson KA (2013) The materials project: a materials genome approach to accelerating materials innovation. APL Mater 1:011002

[58] Xiao Z, Du KZ, Meng W, Wang J, Mitzi DB, Yan Y (2017a) Intrinsic instability of Cs2In*(I)*M*(III)*X6 (M = Bi, Sb; X = halogen) double perovskites: a combined density functional theory and experimental study. J Am Chem Soc 139(17):6054–6057

[59] Chu, L., Ahmad, W., Liu, W., Yang, J., Zhang, R., Sun, Y., ... & Li, X. A. (2019). Lead-free halide double perovskite materials: a new superstar toward green and stable optoelectronic applications. Nano-Micro Letters, 11, 1-18.

[60] Ponseca Jr CS, Savenije TJ, Abdellah M, Zheng K, Yartsev A, Pascher TR, et al. Organometal halide perovskite solar cell materials rationalized ultrafast charge generation, high and microsecond-long balanced mobilities, and slow recombination. J Am Chem Soc 2014;136(14):5189–92.

[61] Snaith HJ, Abate A, Ball JM, Eperon GE, Leijtens T, Noel NK, et al. Anomalous hysteresis in perovskite solar cells. J Phys Chem Lett 2014;5(9):1511–5.

[62] Son D-Y, Lee J-W, Choi YJ, Jang I-H, Lee S, Yoo PJ, et al. Self-formed grain boundary healing layer for highly efficient CH3 NH3 PbI3 perovskite solar cells. Nat Energy 2016;1-16081.

[63] Jung HS, Park NG. Perovskite solar cells from materials to devices. Small 2015;11(1):10–25.

[64] Pan, H., Zhao, X., Gong, X., Li, H., Ladi, N. H., Zhang, X. L., ... & Fu, Y. (2020). Advances in design engineering and merits of electron transporting layers in perovskite solar cells. *Materials Horizons*, *7*(9), 2276-2291.

[65] Hamaneh Zarenezhad; Hamaneh Zarenezhad; Masoud Askari; Mohammad Halali; Navid Solati; Timuçin Balkan; Sarp Kaya; "Enhanced Electron Transport Induced By A Ferroelectric Field in Efficient Halide Perovskite Solar Cells", Solar Energy Materials And Solar Cells, 2020.

[66] Yu'an Xiong; Zijie Feng; Zhengyin Jing; Qiang Pan; Taiting Sha; Shurong Miao; Jie Yao; Guowei Du; Yumeng You; "Recent Progress in Molecular Ferroelectrics with Perovskite Structure", Chinese Science Bulletin, 2020.

[67] Wen-Yuan Pan; Yu-Cheng Tang; Yang Yin; Ai-Zhen Song; Jing-Ru Yu; Sheng Ye; Bo-Ping Zhang; Jing-Feng Li; "Ferroelectric and Photovoltaic Properties of (Ba, Ca)(Ti, Sn, Zr)O3 Perovskite Ceramics", Ceramics International, 2021.

[68] Chengmin Ji; Yezhan Li; Xitao Liu; Yaxing Wang; Tingting Zhu; Qin Chen; Lina Li; Shuao Wang; Junhua Luo; "Monolayer-to-Multilayer Dimensionality Reconstruction in Hybrid Perovskite for Exploring Bulk Photovoltaic Effect Enables Passive X-ray Detection", ANGEWANDTE CHEMIE, 2021. (IF: 3)

[69] Yunpeng Yao; Yu Peng; Lina Li; Xinyuan Zhang; Xitao Liu; Maochun Hong; Junhua Luo; "Exploring A Fatigue-Free Layered Hybrid Perovskite Ferroelectric for Photovoltaic Non-Volatile Memories", angewandte Chemie (International Ed. In English), 2021. (IF: 3)

[70] Junxi Yu; Huan Wang; Fengyuan Zhang; Jiangyu Li; Boyuan Huang; "Polarization Suppresses Local Photocurrent in Triple-cation Mixed-halide Perovskite", Journal Of Applied Physics, 2022.

[71] Xudong Liu; Jie Tu; Yue-Wen Fang; Guoqiang Xi; Hangren Li; Rong Wu; Xiuqiao Liu; Dongfei Lu; Jiushe He; Junwei Zhang; Jianjun Tian; Linxing Zhang; "Colossal Ferroelectric Photovoltaic Effect in Inequivalent Double-Perovskite Bi 2 FeMnO 6 Thin Films", Journal Of The American Chemical Society, 2024.

[72] A. Kojima, K. Teshima, Y. Shirai, T. Miyasaka, J. Am. Chem. Soc. 2009, DOI 10.1021/ja809598r.

[73] J.G. Bednorz, K.A. Mu¨ ller, Perovskite-type oxides—the new approach to high-Tc superconductivity, Rev. Mod. Phys. 60 (1988) 585-600.

[74] Mitzi David B., Progress in Inorganic Chemistry. Volume 48, Wiley, 1999.

[75] D. B. Mitzi, P. Brock, Inorg. Chem. 2001, 40, 2096.

[76] Hagfeldt, A.; Boschloo, G.; Sun, L.; Kloo, L. and Pettersson, H. 'Dye-sensitized solar cells'. Chem. Rev. 2010, 110, 6595 6663.

[77] Kim, H.-S.; Lee, C.-R.; Im, J.-H.; Lee, K.-B.; Moehl, T.; Marchioro, A.; Moon, S.-J.; Humphry-Baker, R.; Yum, J.-H.; Moser, J. E. et al. 'Lead iodide perovskite sensitized all-solid-state submicron thin film mesoscopic solar cell with efficiency exceeding 9%'. Sci. Rep. 2012, 2, 591.

[78] Niu G, Guo X, Wang L. Review of recent progress in chemical stability of perovskite solar cells. J Mater Chem A 2015;3(17):8970–80.

[79] M. M. Lee, J. Teuscher, T. Miyasaka, T. N. Murakami, H. J. Snaith, Science (80-.). 2012, 338, 643.
[80] J. H. Im, C. R. Lee, J. W. Lee, S. W. Park, N. G. Park, Nanoscale 2011, 3, 4088.
[81] NREL, 2019. National Renewable Energy Laboratory (NREL)
[82] S. D. Stranks, G. E. Eperon, G. Grancini, C. Menelaou, M. J. P. Alcocer, T. Leijtens, L. M. Herz, A. Petrozza, H. J. Snaith, Science (80-.). 2013, 342, 341.
[83] Im J-H, Lee C-R, Lee J-W, Park S-W, Park N-G. 6.5% efficient perovskite quantumdot-sensitized solar cell. Nanoscale 2011;3(10):4088–93.
[84] Kim H-S, Lee C-R, Im J-H, Lee K-B, Moehl T, Marchioro A, et al. Lead iodide perovskite sensitized all-solid-state submicron thin film mesoscopic solar cell with efficiency exceeding 9%. Sci Rep 2012:2.
[85] Liu M, Johnston MB, Snaith HJ. Efficient planar heterojunction perovskite solar cells by vapour deposition. Nature 2013;501(7467):395–8.
[86] Sum TC, Mathews N. Advancements in perovskite solar cells photophysics behind the photovoltaics. Energy Environ Sci 2014;7(8):2518–34.
[87] Ahn N, Son D-Y, Jang I-H, Kang SM, Choi M, Park N-G. Highly reproducible perovskite solar cells with average efficiency of 18.3% and best efficiency of 19.7% fabricated via Lewis base adduct of lead (II) iodide. J Am Chem Soc 2015;137(27):8696–9.
[88] Yang WS, Noh JH, Jeon NJ, Kim YC, Ryu S, Seo J, et al. High-performance photovoltaic perovskite layers fabricated through intramolecular exchange. Science 2015;348(6240):1234–7.
[89] Son D-Y, Lee J-W, Choi YJ, Jang I-H, Lee S, Yoo PJ, et al. Self-formed grain boundary healing layer for highly efficient CH3 NH3 PbI3 perovskite solar cells. Nat Energy 2016;1:16081.
[90] Pham ND, Tiong VT, Chen P, Wang L, Wilson GJ, Bell J, et al. Enhanced perovskite electronic properties via a modified lead (ii) chloride Lewis acid-base adduct and their effect in high-efficiency perovskite solar cells. J Mater Chem A 2017;5(10):5195–203.
[91] Lewis, N. S.; Nocera, D. G. Proc. Natl. Acad. Sci. U.S.A. 2006, 103, 15729-15735.
[92] Field, C. B. et al. In Climate Change 2014: Impacts, Adaptation, and Vulner- ability. Part A: Global and Sectoral Aspects. Contribution of Working Group II to the Fifth Assessment Report of the Intergovernmental Panel on Climate Change; Field, C. B. et al. , Eds.; Cambridge University Press: Cambridge, United Kingdom and New York, NY, USA, 2014; pp 35-94.
[93] Haegel, N. M. et al. Science 2017, 356, 141{143.
[94] Woodhouse, M.; Jones-Albertus, R.; Feldman, D.; Fu, R.; Horowitz, K.; Chung, D.; Jordan, D.; Kurtz, S. On the Path to SunShot: The Role of Advancements in Solar Photovoltaic Efficiency, Reliability, and Costs; 2016.
[95] Becquerel, E. C. R. Acad. Sci. 1839, 9, 145{149.
[96] Adams, W. G.; Day, R. E. Phil. Trans. Roy. Soc. London 1877, 167, 313{349.
[97] Savory, C. N. (2018). A Theoretical Exploration of Emerging Solar Absorber Materials (Doctoral dissertation, UCL (University College London)).
[98] Shockley, W.; Queisser, H. J. J. Appl. Phys. 1961, 32, 510{519.
[99] Miyata, K.; Kurashige, Y.; Watanabe, K.; Sugimoto, T.; Takahashi, S.; Tanaka, S.; Takeya, J.; Yanai, T.; Matsumoto, Y. Nat. Chem. 2017, 9, 983{ 989.
[100] Nelson, J. The Physics of Solar Cells; Imperial College Press, 2003.

[101] Savory, C. N. (2018). *A Theoretical Exploration of Emerging Solar Absorber Materials* (Doctoral dissertation, UCL (University College London)).

[102] Yu, L.; Kokenyesi, R. S.; Keszler, D. A.; Zunger, A. Adv. Energy Mater. 2013, 3, 43{48.

[103] Blank, B.; Kirchartz, T.; Lany, S.; Rau, U. Phys. Rev. Appl 2017, 8, 024032.

[104]Paillard, C., Geneste, G., Bellaiche, L., Kreisel, J., Kreisel, J., Alexe, M., & Dkhil, B. (2018). Photovoltaics in Ferroelectric Materials: Origin, Challenges and Opportunities. Emerging Photovoltaic Materials: Silicon & Beyond, 103-140.

[105] Lines M E and Glass A M 2001 Principles and Applications of Ferroelectrics and Related Materials (Oxford University Press)

[106] Valasek J 1921 Piezo-Electric and Allied Phenomena in Rochelle Salt Phys. Rev. 17 475–81

[107] Wadhawan V 2000 Introduction to Ferroic Materials (CRC Press)

[108] Scott J F 2000 Ferroelectric Memories vol.3 (Berlin, Heidelberg: Springer Berlin Heidelberg)

[109] Uchino K 2010 Ferroelectric devices (Boca Raton: CRC Press)

[110] Chynoweth A G 1956 Surface Space-Charge Layers in Barium Titanate Phys. Rev. 102 705–14

[112] Kundys B, Viret M, Colson D and Kundys D O 2010 Light-induced size changes in BiFeO3 crystals Nature Mater 9 803–5

[113] Paillard C, Bai X, Infante I C, Guennou M, Geneste G, Alexe M, Kreisel J and Dkhil B 2016 Photovoltaics with Ferroelectrics: Current Status and Beyond Advanced Materials 28 5153–68

[114] Matzen S, Guillemot L, Maroutian T, Patel S K K, Wen H, DiChiara A D, Agnus G, Shpyrko O G, Fullerton E E, Ravelosona D, Lecoeur P and Kukreja R 2019 Tuning Ultrafast Photoinduced Strain in Ferroelectric-Based Devices Adv. Electron. Mater. 5 1800709

[115] Rani, K. (2022). Switchable photovoltaic properties in ferroelectric PZT thin films (Doctoral dissertation, Université Paris-Saclay).

[116]Dharmadhikari, V. S., & Grannemann, W. W. (1982). Photovoltaic properties of ferroelectric BaTiO3 thin films rf sputter deposited on silicon. Journal of Applied Physics, 53(12), 8988-8992.

[117] Glass A M, von der Linde D and Negran T J 1974 High-voltage bulk photovoltaic effect and the photorefractive process in LiNbO 3 Appl. Phys. Lett. 25 233–5

[118]Nechache, R., Harnagea, C., Li, S., Cardenas, L., Huang, W., Chakrabartty, J., & Rosei, F. (2015). Bandgap tuning of multiferroic oxide solar cells. Nature photonics, 9(1), 61-67.

[119]Grinberg, I., West, D. V., Torres, M., Gou, G., Stein, D. M., Wu, L., ... & Rappe, A. M. (2013). Perovskite oxides for visible-light-absorbing ferroelectric and photovoltaic materials. Nature, 503(7477), 509-512.

[120]Choi, M. J., Torralba, A., & Willsky, A. S. (2012). Context models and out-of-context objects. Pattern Recognition Letters, 33(7), 853-862.

[121] Yin, W. J., Weng, B., Ge, J., Sun, Q., Li, Z., & Yan, Y. (2019). Oxide perovskites, double perovskites and derivatives for electrocatalysis, photocatalysis, and photovoltaics. Energy & Environmental Science, 12(2), 442-462.

[122] Sze S M 1981 Physics of semiconductor devices (New York, N.Y.: Wiley)

[123] Chynoweth A G 1956 Surface Space-Charge Layers in Barium Titanate Phys. Rev. 102 705–14

[124] Glass A M, von der Linde D and Negran T J 1974 High-voltage bulk photovoltaic effect and the photorefractive process in LiNbO 3 Appl. Phys. Lett. 25 233–5

[125] Spanier, J. E. et al. Power conversion efficiency exceeding the Shockley–Queisser limit in a ferroelectric insulator. Nature Photonics 10, 611-616 (2016).

[126] Sturman B I and Fridkin V M 1992 The photovoltaic and photorefractive effects in noncentrosymmetric materials (Philadelphia: Gordon and Breach Science Publishers)

[127] Glass A M, von der Linde D and Negran T J 1974 High-voltage bulk photovoltaic effect and the photorefractive process in LiNbO 3 Appl. Phys. Lett. 25 233–5

[128] Moubah R, Rousseau O, Colson D, Artemenko A, Maglione M and Viret M 2012 Photoelectric Effects in Single Domain BiFeO 3 Crystals Adv. Funct. Mater. 22 4814–8

[129] Choi T, Lee S, Choi Y J, Kiryukhin V and Cheong S-W 2009 Switchable Ferroelectric Diode and Photovoltaic Effect in BiFeO 3 Science 324 63–6

[130] Yang Y, Xu W, Xu X, Wang Y, Yuan G, Wang Y and Liu Z 2016 The enhanced photocurrent of epitaxial BiFeO 3 film at 130 °C Journal of Applied Physics 119 044102

[131] Lee D, Baek S H, Kim T H, Yoon J-G, Folkman C M, Eom C B and Noh T W 2011 Polarity control of carrier injection at ferroelectric/metal interfaces for electrically switchable diode and photovoltaic effects Phys. Rev. B 84 125305

[132] Yao K, Gan B K, Chen M and Shannigrahi S 2005 Large photo-induced voltage in a ferroelectric thin film with in-plane polarization Appl. Phys. Lett. 87 212906

[133] Wu L, Burger A M, Bennett-Jackson A L, Spanier J E and Davies P K 2021 Polarization-Modulated Photovoltaic Effect at the Morphotropic Phase Boundary in Ferroelectric Ceramics Adv. Electron. Mater. 7 2100144.

[134] Moubah R, Rousseau O, Colson D, Artemenko A, Maglione M and Viret M 2012 Photoelectric Effects in Single Domain BiFeO 3 Crystals Adv. Funct. Mater. 22 4814–8

[135] Xing J, Jin K-J, Lu H, He M, Liu G, Qiu J and Yang G 2008 Photovoltaic effects and its oxygen content dependence in BaTiO3−δ⁄Si heterojunctions Appl. Phys. Lett. 92 071113

[136] Shuai Y, Zhou S, Bürger D, Reuther H, Skorupa I, John V, Helm M and Schmidt H 2011 Decisive role of oxygen vacancy in ferroelectric versus ferromagnetic Mn-doped BaTiO 3 thin films Journal of Applied Physics 109 084105.

[137] Nechache R, Harnagea C, Li S, Cardenas L, Huang W, Chakrabartty J and Rosei F 2015 Bandgap tuning of multiferroic oxide solar cells Nature Photon 9 61–7

[138] Nechache R, Harnagea C, Licoccia S, Traversa E, Ruediger A, Pignolet A and Rosei F 2011 Photovoltaic properties of Bi2FeCrO6 epitaxial thin films Appl. Phys. Lett. 98 202902

[139] Grinberg I, West D V, Torres M, Gou G, Stein D M, Wu L, Chen G, Gallo E M, Akbashev A R, Davies P K, Spanier J E and Rappe A M 2013 Perovskite oxides for visible-light-absorbing ferroelectric and photovoltaic materials Nature 503 509–12

[140] Paillard C, Bai X, Infante I C, Guennou M, Geneste G, Alexe M, Kreisel J and Dkhil B 2016 Photovoltaics with Ferroelectrics: Current Status and Beyond Advanced Materials 28 5153–68

[141] Li, S., & Birol, T. (2020). Suppressing the ferroelectric switching barrier in hybrid improper ferroelectrics. npj Computational Materials, 6(1), 168.

[142] Franzbach, D. J., Xu, B. X., Mueller, R., & Webber, K. G. (2011). The effects of polarization dynamics and domain switching energies on field induced phase transformations of perovskite ferroelectrics. Applied Physics Letters, 99(16)

[143] Wang, H., Adamski, N., Mu, S., & Van de Walle, C. G. (2021). Piezoelectric effect and polarization switching in Al1− xScxN. Journal of Applied Physics, 130(10).

[144] Krempaský, J., Muff, S., Minar, J., Pilet, N., Fanciulli, M., Weber, A. P., ... & Dil, J. H. (2018). Operando imaging of all-electric spin texture manipulation in ferroelectric and multiferroic Rashba semiconductors. Physical Review X, 8(2), 021067.

[145] Martin, R. M. Comment on Calculations of Electric Polarization in Crystals. Phys. Rev. B 1974, 9, 1998−1999.

[146] King-Smith, R. D.; Vanderbilt, D. Theory of Polarization of Crystalline Solids. Phys. Rev. B: Condens. Matter Mater. Phys. 1993, 47, 1651−1654.

[147] Berry, M. V. Quantal Phase Factors Accompanying Adiabatic Changes. Proc. R. Soc. London, Ser. A 1984, 392, 45−57.

[148] Thouless, D. J. Quantization of Particle Transport. Phys. Rev. B: Condens. Matter Mater. Phys. 1983, 27, 6083−6087.

[149] Zak, J. Berry's Phase for Energy Bands in Solids. Phys. Rev. Lett. 1989, 62, 2747−2750

[150] Ortiz, G.; Martin, R. M. Macroscopic Polarization as a Geometric Quantum Phase: Many-body Formulation. Phys. Rev. B: Condens. Matter Mater. Phys. 1994, 49, 14202−14210.

[151] Kohn, W. Theory of the Insulating State. Phys. Rev. 1964, 133, A171−181.

[152] Laughlin, R. B. Quantum Hall Conductivity in Two Dimensions. Phys. Rev. B: Condens. Matter Mater. Phys. 1981, 23, 5632−5633.

[153] Niu, Q.; Thouless, D. J. Quantised Adiabatic Charge Transport in the Presence of Substrate Disorder and Many-Body Interaction. J. Phys. A: Math. Gen. 1984, 17, 2453−2462.

[154] R. Resta: Macroscopic polarization in crystalline dielectrics: The geometric phase approach, Rev. Mod. Phys. 66, 899 (1994) 38, 41, 42, 46, 57

[155] R. Resta: Theory of the electric polarization in crystals, Ferroelectrics 136, 51 (1992) 38, 40, 41 [219] R. D. King-Smith, D. Vanderbilt: Theory of polarization of crystalline solids, Phys. Rev. B 47, 1651 (1993) 38, 41, 42, 46, 53, 61

[156] R. Resta: Manifestations of Berry's phase in molecules and condensed matter, J. Phys. Condens. Matter 12, R107 (2000) 42, 43

[157] C. Kittel: Introduction to Solid State Physics, 7th ed. (Wiley, New York 1996) 33, 35, 38, 42

[158]M. V. Berry, Proc. R. Soc. London Ser. A 392, 45 (1984).

[159] N. Marzari and D. Vanderbilt, Phys. Rev. B 56, 12847 (1997).

[160] K. N. Kundin, R. Car, R. Resta, J. Chem. Phys. 126 (2007) 234101.

[161] Spaldin, N. A. (2012). A beginner's guide to the modern theory of polarization. Journal of Solid State Chemistry, 195, 2-10.

Chapter II: Calculation methods and formalisms

II.1 Introduction :

Numerical simulations have acquired an important place in the physical sciences in recent years. The rapid development of information technology has contributed significantly to the prediction of new materials or alloys with important properties. In materials sciences, this type of approximations has been developed to understand and explore the behavior of matter at the atomic scale. First-principles methods known as “ab-initio” are among the most accredited modeling and simulation methods for studying materials at the atomic scale, which makes it possible to obtain a wide range of information on the microscopic origin of materials properties. accurate ‘ab initio’ methods offer valuable insights and predictions that can provide guidance for forthcoming experimental and theoretical endeavors related to these systems. Today, quantum simulation allows the study of systems consisting of hundreds of atoms. The experience acquired shows that quantities as diverse as the atomic structure (distances and bond angles), the width of the forbidden band of semiconductors or even the optical absorption spectra can be calculated with precisions of the order by a few percent compared to the experimental results.a wide variety of properties of materials are commonly calculated in laboratories through a variety of different methods. In addition, these methods are constantly updated to adapt to the speed and memory capacity of the calculator. They are all based on Density Functional Theory « DFT ». The method of full-potential linearized augmented plane waves (FP-LAPW) is one of the most efficient and very precise methods for calculating the electronic structure of condensed matter in a state fundamental, transitional or in an excited state. These calculation methods use approaches from the fundamental laws of quantum mechanics, electromagnetism and statistical physics, to solve the Schrödinger equation, which makes it possible to establish a formal link between structure at the atomic scale and macroscopic properties.

In order to better comprehend the approaches employed in ab-initio procedures, we will discuss the Schrödinger equation, various methods, approximations, and fundamental concepts essential for understanding the work presented in this manuscript.

II.1.1 The Schrödinger Equation :

The Schrödinger equation is the fundamental equation of quantum mechanics, just like Newton's laws in classical physics. It serves as the basic theory for numerous areas of science and technology including solid state physics, atomic physics, particle physics, nuclear physics, chemistry, molecular biology and ….

The Schrödinger equation was proposed inductively by Schrödinger in 1926 and was first developed with the aim of describing small objects (atoms) consisting of a single particle (such as an electron in a hydrogen atom) located in a certain force field.

The central object of Schrödinger theory is a complex valued function psi called the wave function [1], which satisfies:

$$i\bar{h}\,\frac{\partial}{\partial t}psi(\vec{r},t) = \left[\frac{\bar{h}^2}{2m}\overrightarrow{\nabla^2} + V(\vec{r})\right]\psi(\vec{r},t) \qquad (1)$$

Where $\vec{r}$ is the radius -vector identifying the particle in space.

$V(\vec{r})$ is the potential energy of the particle .

$\overrightarrow{\nabla^2}$ is a gradient vector, whose three components are: $(\frac{\partial^2}{\partial x^2}, \frac{\partial^2}{\partial y^2}, \frac{\partial^2}{\partial z^2})$.

i: denotes the fundamental pure imaginary number. m: is the mass of the particle.

In general, the total energy of a system consisting of interacting ions and electrons is calculated by solving the Schrödinger equation [2].

$$H\psi(\{r_j\},\{R_I\}) = E\psi(\{r_j\},\{R_I\}) \qquad (2)$$

With H is the Hamiltonian operator, which is the sum of a kinetic energy operator and the potential energy of the system, $\psi(\{r_j\},\{R_I\})$ a multi-particle wavefunction, which describes the state of the system (r_j represents all electron positions j; $R_I$represents all nucleus positions I) and E is the total energy

$$H = T_e(r) + T_{ions}(R) + V_{int}(r) + V_{ions}(R) + V_{ext}(r,R) \qquad (3)$$

Where T_e and $T_{ions}$the kinetic energy operators of electrons and ions; V_{int} and $V_{ions}$the interaction potentials between electrons and between ions; V_{ext} The external potential

might be the Coulomb electrostatic potential due to the nuclei of the atoms. These quantities can be written:

$$T_e(r) = -\frac{\bar{h}^2}{2m_e}\sum_j \nabla_{rj}^2 \quad (4.a)$$

$$T_{ions}(R) = -\frac{\bar{h}^2}{2M_I}\sum_I \nabla_{RI}^2 \quad (4.b)$$

$$V_{int}(r) = \frac{1}{8\pi\varepsilon_0}\sum_{i,j}\frac{e^2}{|\vec{r_i}-\vec{r_j}|} \quad (4.c)$$

$$V_{ions}(R) = \frac{1}{8\pi\varepsilon_0}\sum_{i,j}\frac{e^2 z_i z_j}{|\vec{R_i}-\vec{R_j}|} \quad (4.d)$$

$$V_{ext}(r,R) = \sum_{j,I}\frac{z_I e^2}{|r_j - R_I|} \quad (4.e)$$

Where:$\bar{h} = \frac{h}{2}$ and h is the planck constant .e electron charge. m_e Electrons mass. M_I nuclei mass.r_i , $r_j$define the positions of the electrons. R_I , R_J Define the positions of the nucleus I. z_i , z_jAtomic numbers of nucleus. ∇ The gradient operator of the particle.

Therefore, the exact Hamiltonian of the crystal is written as follows:

$$\hat{H} = -\frac{\bar{h}^2}{2M_I}\sum_I \nabla_{RI}^2 - \frac{\bar{h}^2}{2m_e}\sum_j \nabla_{rj}^2 - \frac{1}{4\pi\varepsilon_0}\sum_{i,j}\frac{e^2 z_i}{|\vec{R_i}-\vec{r_j}|} + \frac{1}{8\pi\varepsilon_0}\sum_{i,j}\frac{e^2}{|\vec{r_i}-\vec{r_j}|} + \frac{1}{8\pi\varepsilon_0}\sum_{i,j}\frac{e^2 z_i z_j}{|\vec{R_i}-\vec{R_j}|} \quad (5)$$

Resolving the Schrödinger equation for a specific system holds significance in comprehending the system's behavior, obtaining details about its density of states, and understanding a particle's response to an external perturbation [3]. However, the Schrödinger equation offers exact solutions for only a limited set of physical problems, such as the particle in a box, the simple harmonic oscillator, and the hydrogen atom. When dealing with many-body systems containing N electrons and, generally, multiple nuclei, exact solutions for the Schrödinger equation become unattainable due to the electron-electron and nuclear-electron interactions terms in the Hamiltonian (II.5). Consequently, the Schrödinger equation is non-separable. Therefore, approximation methods play a crucial role in solving the Schrödinger equation for many-body systems [4].

II.1.2 the different approximations of the Schrödinger equation

II.1.2.1 The Born-Oppenheimer approximation

The Born-Oppenheimer approximation refers to the division of nuclear and electronic motion into distinct mathematical frameworks. Max Born(1882-1970) and Robert Oppenheimer (1904-1967) proposed that the nuclei move significantly slower than the electrons, allowing us to treat them as effectively stationary[5]. This approximation permits the exclusion of the kinetic energy of the nuclei from the Hamiltonian, with the electrostatic repulsion between nuclei being viewed as a constant in the electronic problem [6]. According to the Born-Oppenheimer approximation, the total wave function for the multi-body system can be expressed as follows:

$$\psi_{total}(\{r_j\},\{R_I\}) = \psi_{electron}(\{r_j\})\psi_{nuclei}(\{R_I\}) \quad (6)$$

Here, The electronic Hamiltonian can now be written as

$$\hat{H} = -\sum_i \frac{\bar{h}^2}{2m_e}\nabla_i^2 - \sum_{i,I}\frac{e^2 z_I}{|\vec{r_j}-\vec{R_I}|} + \frac{1}{2}\sum_j \frac{e^2}{|\vec{r_i}-\vec{r_j}|} \quad (7)$$

The three components in this equation delineate, in order, the kinetic energy of all electrons, the external potential experienced by the electrons, and lastly, the potential interaction among distinct electrons. The current Schrodinger equation is too difficult to solve due to the electron-electron interaction term.

II.1.2.2 The Hartree approximation

One of the first methods making it possible to solve the problem of the real and complex atom on the basis of a single-electronic case was that of Hartree [7] proposed in 1928. It is an approximation which consists of assuming that each electron moves in a manner Independent in the mean field created by the other electrons and nuclei. So the problem goes from a system of electron-electron pair repulsion to a problem of a particle immersed in an average electrostatic field created by the charge distribution of all other electrons and nuclei. This approximation reduces the problem with N interacting bodies to that of a problem of independent electrons. The global wave function N electrons ψ(r1,r2,…rN) becomes like a product of single-electron wave functions ψi(ri).

$$\psi(r_1, r_2 \ldots\ldots r_N) = \psi(r_1).\psi(r_2) \ldots\ldots \psi(r_N) \quad (8)$$

This is an self-consistently equation for a singular particle, which describes the electronic structure of an atom approximately.

Each atom is considered to be moving in an effective potential. The Schrödinger equation in Hartree's approach for an electron [8]:

$$-\frac{\bar{h}^2}{2m}\nabla^2\psi_i(\vec{r}) + V_{eff}(\vec{r})\psi_i(\vec{r}) = E\psi_i(\vec{r}) \quad (9)$$

The electron moves in an average Coulomb interaction potential $V_H(\vec{r})$(the Hartree potential or mean field potential) between a single electron and the rest of the electrons in the system, which form a negative charge distribution $\rho(\overrightarrow{r'})$

$$V_H(\vec{r}) = -e\int d\overrightarrow{r'}\,\rho(\overrightarrow{r'})\frac{1}{\left|\vec{r}-\overrightarrow{r'}\right|} \quad (10)$$

The eigenfunctions resulting from the solution make it possible to calculate a new electron density:

$$\rho\left(\overrightarrow{r'}\right) = \sum_i \psi_i{}^*(\vec{r})\,\psi_i(\vec{r}) \quad (11)$$

The density-potential relationship is obtained by the Poisson equation:

$$\Delta V_H(\vec{r}) = -\frac{\rho(\vec{r})}{\varepsilon_0} \quad (12)$$

The potential that the electron experiences in the field of all the nuclei is (the electron-nuclei interaction) is:

$$V_{ext}(\vec{r}) = -Ze^2\sum_R \frac{1}{|\vec{r}-\vec{R}|} \quad (13)$$

Finally, actual potential is expressed as the sum of these two contributions:

Where:

$$V_{eff}(\vec{r}) = V_H(\vec{r}) + V_{ext}(\vec{r}) \quad (14)$$

This approach gave self-consistently solution to the physical system problem The equation is now simple to solve, but does not give very good results. Due to the neglect of the Pauli Exclusion Principle and the spin of electrons, this requires the call to another approximation to better describe the term responsible for this contribution.

II.1.2.3 The Hartree-Fock Approximation

The Hartree-Fock approximation serves as a fundamental foundation for quantum mechanical computations involving many-body systems. This approach estimates the wave function of such systems by expressing them as products of single-electron wave functions. In this methodology, the total Hamiltonian, H, is represented as the sum of individual single-electron Hamiltonian operators, H_i.

The wave function of many electron systems can be described as a single product of individual electron wave functions.

These individual electron wave functions are referred to as spin orbitals. Each spin orbital consists of a combination of a specific function and a spin state (either "up" or "down"). This representation of Ψ is commonly referred to as a Hartree product [9].

The Hartree product composed of spin orbitals possesses a significant limitation. It fails to adhere to the antisymmetry principle, which is a fundamental requirement for wave functions of many fermions. In quantum mechanics, electrons are classified as fermions, and the antisymmetry principle dictates that if two electrons are exchanged, the wave function must alter its sign accordingly.

$$\psi(\overrightarrow{r_1}, \overrightarrow{r_2} \dots \dots \overrightarrow{r_{N_e}}) = -\psi(\overrightarrow{r_1}, \overrightarrow{r_2} \dots \dots \overrightarrow{r_{N_e}}) \quad (15.a)$$

Writing a many-electron system's wave function in terms of a Slater determinant of single-electron wave functions is the most practical method [9].Incorporating a Slater determinant representation of the many-electron system into the Hartree theory results in the formulation of the Hartree-Fock theory.

For a system comprising N electrons and spin orbitals, the Slater determinant can be expressed as:

$$\psi(r_1, r_2 \dots \dots r_N) = \frac{1}{\sqrt{N!}} \begin{vmatrix} \chi_1(r_1) & \dots & \chi_1(r_N) \\ \chi_N(r_1) & \dots & \chi_N(r_N) \end{vmatrix} \quad (15.b)$$

where, $\frac{1}{\sqrt{N!}}$ is normalization factor

The Slater determinant satisfies the Pauli exclusion principle. Swapping any two rows of the determinant alters the sign of Ψ, thus upholding the antisymmetry principle. When any two rows of the determinant are identical, it results in the determinant becoming zero.

This reflects the impossibility of having two identical electrons occupying the same spin orbitals simultaneously. The Hartree-Fock method provides a precise explanation of electron exchange [9].

The Hartree-Fock approach can be deduced from the Rayleigh-Ritz variational principle. According to this principle, for any non-zero eigenstate |Ψ>, the Hamiltonian expectation value obeys a certain inequality.

$$E_0 = \frac{\langle \Psi | H | \Psi \rangle}{\langle \Psi | \Psi \rangle} \quad (16)$$

The energy eigenvalue E0 represents the ground state energy, achieved by minimizing the Hamiltonian's expectation value with respect to a tentative wave function.

For the processing of extended systems such as solids, Due to the rapid increase in the number of configurations with the number of electrons involved, the correlation of short-distance Coulomb interactions is ignored. This may have a significant impact on the computational accuracy of periodic solids. Therefore, this method cannot find the exact energy of real systems. A more powerful solid theory can bypass these limitations, namely the Density Functional Theory (DFT).

II.2 Density Functional Theory

In Hartree-Fock theory, the N-electron wave function can be estimated by employing a single Slater determinant, formed by the summation of individual electron wave function products. The fundamental concept of density functional theory (DFT) is to utilize electron density as a fundamental parameter, rather than relying on the many-electron wave function. The origins of density functional theory can be attributed to the research conducted by Thomas and Fermi in the 1920s [10, 11] ,which marked the initial endeavors to utilize the observable electron density as a basis, moving away from the more complex, abstract wavefunction. The whole discipline of density functional theory is based on the two fundamental mathematical theorems established by Hohenberg and Kohn in 1964 [12], alongside the development of the Kohn-Sham formulation of density functional theory in 1965 [13].

II.2.1. the Electron density

The electron cannot be located as an individual particle, however its probability of presence in a volume element can be estimated and corresponds to the electron density (ρ). The

electron density allows us to know the regions of space where the electrons reside most often. The electrons are essentially located in the vicinity of the nuclei. The electron density $\rho(r)$. is a positive function depending only on the spatial coordinates (x,y,z) of space. This quantity vanishes to infinity and is worth N when integrated over all space. It is sufficient for the complete determination of the properties of an atomic system.

II.2.2. The Thomas-Fermi approximation

Thomas and Fermi independently demonstrated in the 1920s that one could use electron density $\rho(r)$ as the central variable to solve the Schrödinger equation [14, 15]. Thomas and Fermi theory is a true density functional theory. In their research, Thomas and Fermi utilized the homogeneous or uniform electron gas, commonly referred to as jellium, as the foundational model system. This system consists of an infinite array of electrons enveloped by an evenly distributed positive charge, symbolizing the nuclei. Notably distinct from the orbital-centered approach of Hartree-Fock, the uniform electron gas model closely mirrors the characteristics of solids, especially metals. In the Thomas-Fermi model, both the kinetic and electrostatic energies of the uniform electron gas are expressed in terms of the electron density. This density encompasses the repulsive electron-electron interaction ($E_{e\text{-}e}$) described by the classical Hartree energy, along with the attractive Coulomb interaction between electrons and nuclei ($V_{N\text{-}e}$). Nevertheless, by adding only classical terms and rough approximations in T_{TF}, such an expression is inadequate for characterizing the features of real systems. The energy of the E_{TF} ground state is obtained by minimizing:

$$E_{TF}(\rho) = \underbrace{\frac{3}{10}(3\pi^2)^{2/3}\int \rho(r)^{5/3}dr}_{T_{TE}} - \underbrace{\int \frac{z\rho(r)}{r}dr}_{V_{N-e}} + \underbrace{\frac{1}{2}\iint \frac{\rho(r)\rho(r')}{|r-r'|}drdr'}_{E_{e-e}} \quad (17)$$

II.2.3. The Hohenberg-Kohn Theorems

The starting point of any discussion of DFT is the fundamental theorems proposed by Hornberg and Cohen in 1964 [16], that allows it to solve for physical, electronic systems. The first theorem asserts that in a system of interacting particles within an external potential, the electron density, denoted as $\rho(r)$, completely and uniquely defines the external potential $V_{ext}(r)$. Put differently, there exists a direct and exclusive correspondence between the electron density and the external potential. According to this theorem, the total energy

functional $E(\rho)$ of a system is also required to be a functional expression of the electron density, as follows:

$$E(\rho) = \int V_{ext}(r)\rho(r)dr + F_{HK}[\rho(r)] \quad (18)$$

here,V_{ext} (r) represents an external potential generated by the nuclei. $F_{HK}[\rho(r)]$ is referred to as a Hohenberg-Kohn universal functional since it remains independent of the external potential. It encompasses both the kinetic energy of the electrons and the electron-electron interactions. It is expressed as:

$$F_{HK}[\rho(r)] = T[\rho(r)] + \frac{1}{2}\sum V_H\,[\rho(r)]\rho(r)dr \quad (19)$$

The second Hohenberg-Kohn theorem shows that if $\rho(r)$ is normalized to the number of particles in the system, then the total energy of the system $E(\rho)$ becomes a minimum if and only if $\rho(r)$ is the exact ground state density [17].

II.2.4. The Kohn-Sham Equations

The Hohenberg-Kohn theorems state that the ground state density uniquely determines all ground state observables and it can be determined from the ground state energy functional $E(\rho)$. However, the theorem does not give us a hint about how to solve the full Schrödinger equation. For example, there is no exact expression for the electron exchange-correlation functional which includes all quantum mechanical effects.

Kohn and Sham tackled these challenges in 1965 [18]. In the Kohn-Sham approach, the ground state electron density is represented through a series of equations that exclusively pertain to a non-interacting electron system. This non-interacting system possesses the identical electron density $\rho(r)$ as the original system. The energy functional for this system can be formulated as follows:

$$E(\rho) = T_s[\rho(r)] + \int V_{eff}\,(r)\rho(r)d^3r \quad (20)$$

The equations of Kohn-Sham for electrons navigating within an effective external potential can be expressed as:

$$\left[-\frac{\bar{h}^2}{2m_e}\nabla^2 + V_{KS}(r)\right]\varphi_i(r) = \varepsilon_i\varphi_i(r) \quad (21)$$

The resolution of this Schrödinger equation produces the Kohn-Sham eigenvalues. The kinetic energy of a system comprising non-interacting electrons with density $\rho(r)$ is provided by:

$$T_s[\rho(r)] = \sum_i \left\langle \varphi_i \left| -\frac{\nabla^2}{2} \right| \varphi_i \right\rangle \quad (22)$$

Where, the density of the system under interaction is established by:

$$\rho_s(r) = \sum_i |\varphi_i(r)|^2 \quad (23)$$

The effective external potential is defined as

$$V_{KS}(r) = V_{ext}(r) + V_H(r) + V_{XC}(r) \quad (24)$$

In this context, $V_{ext}(r)$ represents the Coulomb interaction between an electron and the atomic nuclei, $V_H(r)$denotes the classical (Hartree) potential accounting for the Coulomb interaction among the electrons, and $V_{XC}(r)$ characterizes the exchange and correlation potential, encompassing all quantum mechanical influences.

The exchange and correlation potential can be formally expressed as the functional derivative of the exchange-correlation energy concerning the electron density.

$$V_{XC}(r) = \frac{\delta E_{XC}[\rho(r)]}{\delta n(r)} \quad (25)$$

II.2.5 The Exchange-Correlation Functionals

The primary challenge in solving the Kohn-Sham equations arises from the lack of knowledge regarding the exact form of the exchange-correlation functional. To address this, two primary approximation techniques have been developed. The first method, known as the local density approximation (LDA), is employed to approximate the exchange-correlation functional in DFT computations. In this approach, the local exchange-correlation potential at each position r is determined by the exchange-correlation potential for a uniform electron gas corresponding to the electron density observed at that position [9].

$$V_{XC}^{LDA}(r) = V_{XC}^{electron\ gas}[\rho(r)] \quad (26)$$

The LDA approximation is precise for a uniform electron gas, yet actual electron densities tend not to be uniformly distributed throughout the entire system. Another widely recognized category of approximations to the Kohn-Sham exchange-correlation functional is the generalized gradient approximation (GGA). Within the GGA framework, the exchange and correlation energies incorporate both the local electron density and the local gradient in the electron density[9].

$$V_{XC}^{GGA}(r) = V_{XC}^{electron\ gas}[\rho(r)] \quad (27)$$

II.2.6 Solving The Kohn-Sham Equations

After approximating the exchange-correlation energy, we can proceed to solve the Kohn-Sham equations. These equations necessitate an iterative solution and must be solved self-consistently. In order to tackle the Kohn-Sham equations for a many-body system, it is necessary to define both the Hartree potential and the exchange-correlation potential. However, to define these potentials, we require knowledge of the electron density, denoted as n (r). Yet, to determine the electron density accurately, we must first know the single electron wave functions. These wave functions, however, are unknown until we solve the Kohn-Sham equations. A common approach to solving these equations is to initiate the process with an initial trial electron density, as depicted in Figure II.1. Subsequently, the equations are solved using this trial electron density. After solving the Kohn-Sham equations, a series of single electron wave functions is obtained. With these wave functions, the new electron density can be computed. This updated electron density serves as input for the subsequent iteration. Finally, the discrepancy between the computed electron densities for consecutive iterations is assessed. If the difference falls below a predetermined convergence threshold, the solution of the Kohn-Sham equations is deemed self-consistent. At this point, the calculated electron density is regarded as the ground state electron density, enabling the computation of the system's total energy [9].

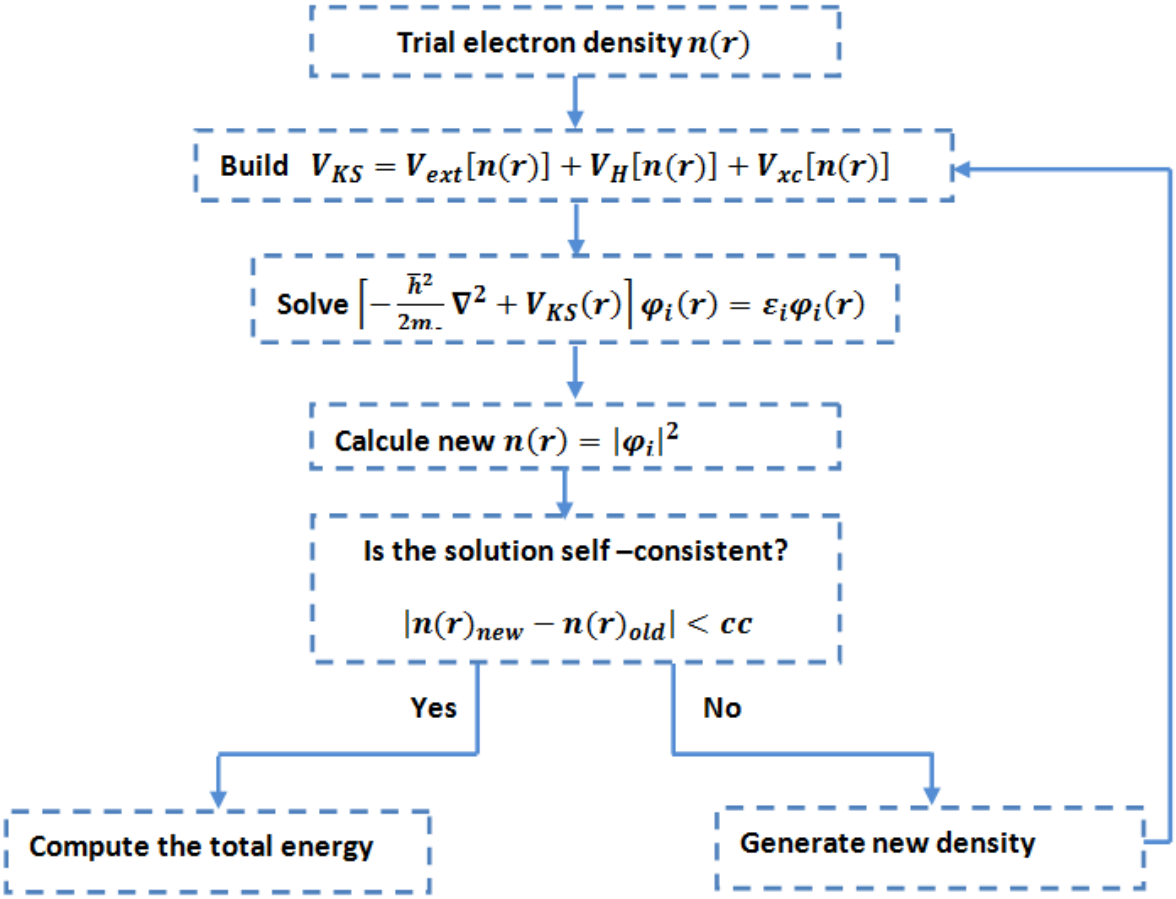

Figure.II.1: Illustration of the self-consistent field (SCF) procedure for solving the Kohn-sham equations where cc represents a suitably selected convergence criterion.

II.3. Approximations used in DFT

II.3.1. The local density approximation LDA

The Local Density Approximation (LDA) is the simplest approximation of the potential, proposed in 1965 by Kohn-Sham [13]. It consists of assuming an inhomogeneous (real) gas similar to a homogeneous gas of the same density $\rho(r)]$, for the calculation of the exchange–correlation energy. This approximation is based on the following two assumptions:

- The exchange-correlation effects are dominated by the density located at point r.
- The electron density $\rho(r)]$ is a function changing slowly with relative to r.

Therefore the contribution of the exchange-correlation energy $\boldsymbol{E_{xc}[\rho(r)]}$ to the total energy of the system can be added cumulatively from each portion of the non-uniform gas as if it were locally uniform, the total exchange and correlation energy $\boldsymbol{E_{xc}}$ can then be given by[19]

$$E_{xc}^{LDA}[\rho(r)] \approx \int \varepsilon_{xc}^{LDA}[\rho(r)]\rho(r)dr \quad (28)$$

$\boldsymbol{\varepsilon_{xc}^{LDA}[\rho(r)]}$:is the exchange-correlation energy per electron in a homogeneous gas. Starting from $\boldsymbol{\varepsilon_{xc}^{LDA}[\rho(r)]}$, the exchange-correlation potential $\mathrm{V}_{\boldsymbol{xc}}^{\boldsymbol{LDA}}[\boldsymbol{\rho(r)}]$: can be obtained in a variational way according to:

$$\mathrm{V}_{\boldsymbol{xc}}^{\boldsymbol{LDA}}[\boldsymbol{\rho(r)}] = \frac{\boldsymbol{\delta(\rho(r)\varepsilon_{xc}^{LDA}[\rho(r)])}}{\boldsymbol{\delta\rho(r)}} \quad (29)$$

The exchange-correlation energy for a uniform electron gas is given by the Dirac formula [20]

$$\varepsilon_{xc}^{LDA}[\rho(r)] = \varepsilon_{x}^{LDA}[\rho(r)] + \varepsilon_{c}^{LDA}[\rho(r)] \quad (30.a)$$

The relative term exchange $\boldsymbol{\varepsilon_{x}^{LDA}[\rho(r)]}$ is:

$$\varepsilon_{x}^{LDA}[\rho(r)] = -\frac{3}{4}\left(\frac{3}{\pi}\right)^{1/3}\int \rho^{4/3}(r)d\vec{r} \quad (30.b)$$

While the term correlation $\boldsymbol{\varepsilon_{c}^{LDA}[\rho(r)]}$ cannot be expressed exactly.

In the case of magnetic materials, the electronic spin provides an additional degree of freedom and the LDA must then be extended to the local spin density approximation (LSDA: local spin density approximation)[21,22].

$$\boldsymbol{\varepsilon_{x}^{LSDA}[\rho(\vec{r})]} = -2^{1/3}C_x[\rho_{\downarrow}{}^{1/3}(\vec{r}) + \rho_{\uparrow}{}^{1/3}(\vec{r})] \quad (30.c)$$

$$\mathrm{E}_{\boldsymbol{x}}^{\boldsymbol{LSDA}}[\boldsymbol{\rho(r)}] = -2^{1/3}C_x\int[\rho_{\downarrow}{}^{4/3}(\vec{r}) + \rho_{\uparrow}{}^{4/3}(\vec{r})]d\vec{r} \quad (30.d)$$

Where $C_x = \boldsymbol{\frac{3}{4}\left(\frac{3}{\pi}\right)^{1/3}}$ The treatment of exchange-correlation energy from LDA works relatively well in the case of metals[23, 24], for which the density is highly uniform but also for unexpected cases such as materials characterized by ionic-covalent bonds or containing transition metals. However, LDA tends to underestimate the exchange energy by around 10% and overestimate the binding energy [25] (relative errors are typically of the order of 20-30% and can reach 50%) and predicts equilibrium bond lengths shorter than those determined experimentally.

II.3.2. Generalized Gradient Approximation GGA

For systems characterized by pronounced electronic delocalization, where local electronic densities are typically non-uniform, it becomes preferable to incorporate a correction into this functional that considers the rate of change of ρ(r). A natural approach to enhance the LDA involves accounting for the electron density's inhomogeneity by integrating exchange energy and correlation terms that depend on the density gradient. The Generalized Gradient Approximation (GGA)[26] represents a methodological advancement in this direction. GGA entails modifying the exchange and correlation terms, expanding them beyond a sole reliance on density to include its local variation. This approach facilitates a blend of local and gradient-dependent terms within the functionals, outlined by the following equation:

$$E_{xc}^{GGA} = \int f_{xc}^{GGA}\,[\rho(r), \nabla_n(r)]d^3r \qquad (31.a)$$

In the case where spin polarization is taken into account, the exchange and correlation energy is described as follows:

$$E_{xc}^{GGA}[\rho_\uparrow(r), \rho_\downarrow(r)] = \int \rho(r)\,\epsilon_{xc}^{GGA}[\rho_\uparrow, \rho_\downarrow, \nabla\rho_\uparrow(r), \nabla\rho_\downarrow(r)]d^3r \qquad (31.b)$$

There exist numerous iterations of function f_{xc}^{GGA} . Such an approximation is inherently more effective for systems characterized by substantial variations in electron density. GGA represents advancement over LDA in addressing exchange-correlation energy by incorporating its dependence not solely on electron density but also on its gradient. Several variants of GGA exist, with the most commonly utilized ones being those pioneered by Perdew and Wang (GGA-PW91)[27], Perdew, Burke, and Ernzerhof (GGA-PBE)[29], Engel and Vosko (EV-GGA)[30], among others.

In many cases, the GGA approximation provides better results than LDA for total energies, cohesive energies, and equilibrium volume and bulk modulus [30].

However, the bandgap of insulators and semiconductors remain far too small. Systems with strong correlations are poorly described. Also due to its local character, GGA does not manage to correctly treat systems characterized by Van-Der-Waals interactions, linked to long-range correlations.

II.3.3. Modified Becke-Johnson potential (mBJ)

For semiconductors and insulators, in order to improve the results obtained concerning the gap energy, where they are underestimated by the previous methods (LDA and GGA). in 2006 Becke and Johnson[31] proposed a version of the exchange potential (BJ), then it was corrected and published by Tran-Blaha in 2009[32]. Known as the modified potential of Becke and Johnson (Modified Becke Johnson potential), it is expressed by:

$$V_{x,\sigma}^{TB-mBJ}(r) = cV_{x,\sigma}^{BR}(r) + (3c-2)\frac{1}{\pi}\sqrt{\frac{5}{6}\sqrt{\frac{t_\sigma(r)}{\rho_\sigma(r)}}} \quad (32.a)$$

Where $\rho_\sigma(r) = \sum_{i=1}^{N_\sigma}\left|\phi_{i,\sigma}(r)\right|^2$ represents the electron density.

$t_\sigma(r) = \frac{1}{2}\sum_{i=1}^{N_\sigma}\nabla\phi_{i,\sigma}^*(r)\nabla\phi_{i,\sigma}(r)$ indicates the density of kinetic energy.

The parameter c is given by the following relation:

$$c = \alpha + \beta\left(\frac{1}{V_{cell}}\int_{cell}\frac{|\nabla\rho(r')|}{\rho(r')}d^3r'\right)^{1/2} \quad (32.b)$$

With: V_{cell} is the volume of the elementary cell, α and β are two independent parameters whose values are obtained by a dependent adjustment to the experimental results:

α = - 0.012 et β =1.023 $Bohr^{1/2}$

$V_{x,\sigma}^{BR}(r)$ represents the Becke-Roussel (BR) potential [33], which was proposed to model the Coulomb potential created by the exchange hole.

$$V_{x,\sigma}^{BR}(r) = -\frac{1}{b_\sigma(r)}\left(1 - e^{-x_\sigma(r)} - \frac{1}{2}x_\sigma(r)e^{-x_\sigma(r)}\right) \quad (32.c)$$

Where: $x_\sigma$is determined from$\rho_\sigma(r)$,$\nabla\rho_\sigma(r)$,$\nabla^2\rho_\sigma(r)$ and $t_\sigma(r)$.

$b_\sigma(r)$is calculated by the following equation :

$$b_\sigma(r) = \left[\frac{x_\sigma^3(r)e^{-x_\sigma(r)}}{8\pi\rho_\sigma(r)}\right]^{1/3} \quad (32.d)$$

By changing the c for a given material, it was found [32] that for several solids, the gap energy increases monotonically with respect to c. Specifically, for solids with small gaps. Tran and Blaha used the principle of hybrid potential to adjust the coefficient c in order to have the “exact” value of the exchange potential.

II.4 Spin-orbit coupling

Spin-orbit coupling (SOC) is a relativistic interaction that connects an electron's inherent spin property to its motional degree of freedom [34]. This coupling occurs because the spin of an electron generates a magnetic dipole moment, which interacts with surrounding magnetic fields. The fundamental spin-orbit coupling at the atomic level originates from the electric field produced by a positively charged nucleus. However, additional forms of spin-orbit coupling can emerge from diverse electric fields, such as those encountered when a sample is positioned on a substrate. In such cases, the resulting irregularity in the periodic crystal potential within the sample induces spin-orbit coupling effects, which can be elucidated by considering the corresponding point group symmetries of these external influences [35].

Two prevalent forms of spin-orbit coupling exist: one arises due to the asymmetry of the confining potential, known as Rashba-type spin-orbit coupling, which results in a distinctive "sombrero" shaped potential in momentum space when the system lacks broken mirror symmetry along a high-symmetry axis [36]. The other type, Dresselhaus-type spin-orbit coupling, originates from the absence of inversion symmetry within the bulk[37].

Therefore SOC in materials can be generally described by:

$$H_{SO} = \frac{\bar{h}}{4m_0^2c^2}\vec{\sigma}.(\vec{p} \times \vec{E}(\vec{r})) \tag{33}$$

Where $\vec{\sigma}$ and $\vec{p}$ are the electron's spin and linear momentum,respectively,and $\vec{E}(\vec{r})$ is the electric field generated by the electric potential from the nucleus.here $\vec{E}(\vec{r})$, is Lorentz transformed to a magnetic field in the rest fram of a moving electron,so it acts on the spin[38].

II.4.1. Intrinsic Spin-orbit Coupling

The process of deriving the intrinsic spin-orbit coupling interaction in matrix form closely resembles that described in references [39]. By solving the angular component of the Schrödinger equation for the hydrogen atom, one can obtain the spherical harmonics, which are utilized here. These harmonics are expressed according to the Condon-Shortley phase convention [40] as follows:

$$Y_l^m(\theta, \phi) = \sqrt{\frac{(2l+1)(l-m)!}{4\pi(l+m)!}} P_{lm}(\cos\theta)e^{im\phi} \tag{34.a}$$

The Laguerre polynomials linked to this context are defined as follows:

$$P_l^m(x) = \frac{(-1)^m}{2^l l!}(1-x^2)^{m/2}\frac{d^{l+m}}{dx^{l+m}}(x^2-1)^l \quad (34.b)$$

The $Y_l^m(\theta,\varphi)$ are eigenfunctions to the $\hat{L}^2$ and $\hat{L}_z$ operators with eigenvalues $\hat{L}_z Y_l^m = \bar{h}m Y_l^m$ and $\hat{L}^2 Y_l^m = \bar{h}^2 l(l+1) Y_l^m$. In this basis, the spin is included via direct product .for an angular momentum operator $\hat{j}$,the matrix elements in the basis $|j,m\rangle$ are derived [41]via:

$$\langle j',m'|\hat{J_x}|j,m\rangle = \left\langle j',m'\left|\frac{\hat{J_+}+\hat{J_-}}{2}\right|j,m\right\rangle = \frac{\bar{h}}{2}\left\{\delta_{jj'}\delta_{m',m} + 1[(j-m)(j+m+1)]^{1/2} + \delta_{jj'}\delta_{m',m} - 1[(j+m)(j-m+1)]^{1/2}\right\} \quad (34.c)$$

And with

$$\langle j',m'|\hat{J_y}|j,m\rangle = \left\langle j',m'\left|\frac{\hat{J_+}-\hat{J_-}}{2i}\right|j,m\right\rangle = \frac{\bar{h}}{2i}\left\{\delta_{jj'}\delta_{m',m} + 1[(j-m)(j+m+1)]^{1/2} + \delta_{jj'}\delta_{m',m} - 1[(j+m)(j-m+1)]^{1/2}\right\} \quad (34.d)$$

Using Eqs.final 34.c and 34.d and the elements of the Hilbert space $|j,m\rangle$ on the space of the l = 1 quantum number, the different parts of the operator $\hat{L}$ are derived as

$$\hat{L}^+ = \begin{pmatrix} 0 & \sqrt{2} & 0 \\ 0 & 0 & \sqrt{2} \\ 0 & 0 & 0 \end{pmatrix} \qquad \hat{L}^- = \begin{pmatrix} 0 & 0 & 0 \\ \sqrt{2} & 0 & 0 \\ 0 & \sqrt{2} & 0 \end{pmatrix} \qquad \hat{L}_z = \begin{pmatrix} 1 & 0 & 0 \\ 0 & 0 & 0 \\ 0 & 0 & -1 \end{pmatrix} \quad (35.a)$$

and for the spin $\hat{\vec{S}}$, they are the Pauli matrices $\hat{s_x}$, $\hat{s_y}$ and $\hat{s_z}$. Using Eqs. 34.c and 34.d, the Hamiltonian for the spin-orbit coupling can be written in terms of the ladder operators

$$\hat{\vec{L}}.\hat{\vec{S}} = \frac{\hat{L}^+\hat{S}^- + \hat{L}^-\hat{S}^+}{2} + \hat{L}_z\hat{S}_z \quad (35.b)$$

In atoms, the cartesian atomic orbitals p_x, p_y and p_z may be expressed via the complex spherical harmonics [42].

They are no eigenfunctions of the angular momentum operator $\hat{L}_z$. If the linear combinations in terms of the spherical harmonics are respected, the representation of the spin-orbit coupling operator in the basis $\{|p_x,\uparrow\rangle, |p_x,\downarrow\rangle, |p_y,\uparrow\rangle, |p_y,\downarrow\rangle, |p_z,\uparrow\rangle, |p_z,\downarrow\rangle\}$ [38].

$$H_{SOC}^{P} = \xi_P \begin{pmatrix} 0 & -i\hat{s}_z & i\hat{s}_y \\ i\hat{s}_z & 0 & -i\hat{s}_x \\ -i\hat{s}_y & i\hat{s}_x & 0 \end{pmatrix} \quad (35.c)$$

and in the same compact notation, in the basis of directed d-orbitals with both spin components and ordered as{d_{xy}, $d_{x^2-y^2}$, d_{xz}, d_{yz}, d_{z^2g}}, the intrinsic spin-orbit coupling operator becomes

$$H_{SOC}^{D} = \xi_d \begin{pmatrix} 0 & 2i\hat{s}_z & -i\hat{s}_x & i\hat{s}_y & 0 \\ -2i\hat{s}_z & 0 & i\hat{s}_y & i\hat{s}_x & 0 \\ i\hat{s}_x & -i\hat{s}_y & 0 & -i\hat{s}_z & i\sqrt{3}\hat{s}_y \\ -i\hat{s}_y & -i\hat{s}_x & i\hat{s}_z & 0 & -i\sqrt{3}\hat{s}_x \\ 0 & 0 & -i\sqrt{3}\hat{s}_y & i\sqrt{3}\hat{s}_x & 0 \end{pmatrix} \quad (35.d)$$

Here the parameters for the spin-orbit coupling strengths are denoted ξ_p and ξ_d, respectively. Due to the term $\delta_{jj'}$ in Eqs. 34.c and 34.d, there is no spin-orbit coupling matrix element between l = 1 and l = 2 states.

In order to discuss the splitting of the π-bands at the Dirac cones, the intrinsic spin-orbit coupling Eq. II-35.d, is reduced to a low-energy form, on the basis $\{|A,\uparrow\rangle, |A,\downarrow\rangle, |B,\uparrow\rangle, |B,\downarrow\rangle\}$ of the p_z-orbitals. In analogy to the Rashba Hamiltonian , it leads to the form [43]

$$H_{SOC} = \xi_d \hat{\Gamma}_z \hat{s}_z \hat{\sigma}_z \quad (35.e)$$

This reduced form of the intrinsic spin-orbit coupling Hamiltonian may be used to compute the gap at the Dirac points and a gap of $2\lambda_I = 9\frac{\tilde{V}_{pd\pi}^2}{E_d^2}\xi_d = 26\mu eV$ is obtained for a parameter of ξd = 0.8meV [39].

II.4.2. Dresselhaus-type Spin-orbit Coupling: Bulk Inversion Asymmetry

Dresselhaus [44] used k .p-theory to determine band splittings of semiconductors with diamond structure due to spin-orbit coupling. First they derived secular equations in the basis of degenerate unperturbed functions that would transform according to various irreducible representations of the double point group T_d of zinc blende [45, 46]. In a following step, the degenerate functions are then subject to spin-orbit coupling, which

incorporates the symmetry of the lattice by symmetries of its matrix elements. Spin splittings occur when along high-symmetry lines the previously degenerate functions reorder according to the irreducible representation of the point groups across the Brillouin zone. The main difference of the zinc blende structure to the diamond structure is the lack of inversion symmetry, as a consequence of the two different types of elements in the crystal. Dresselhaus found that the lower conduction band Γ6 of zinc blende is spin-split by [47].

$$E = C_0k^2 \pm C_1[k^2\left(k_x^2k_y^2 + k_y^2k_z^2 + k_z^2k_x^2\right) - 9k_x^2k_y^2k_z^2]^{1/2} \quad \text{(36.a)}$$

with two material constants C_0 and C_1. This splitting is the central feature of the linear and cubic Dresselhaus-type spin-orbit coupling effect and a result of the absence of inversion symmetry. Using the theory of invariants, one can derive the Hamiltonian for the conduction electrons [47] and one can construct the following invariant Hamiltonian in the$\{|\uparrow\rangle, |\downarrow\rangle\}$ space.

$$\widehat{H}_k^{6c6c} = \gamma_c(\left[k_x\left(k_y^2 - k_z^2\right)\right]\widehat{s_x} + c.p) \quad \text{(36.b)}$$

Here, c.p. stands for cyclic permutation. This Hamiltonian results in the same splitting as in Eq. II-36.a For two dimensions, Eq.36.b is modified by $k_z \to \langle k_z\rangle = 0$ and ${k_z}^2 \to \langle {k_z}^2\rangle \neq 0$ and by using the notation $k_\pm = k_x \pm ik_y$ it becomes

$$\widehat{H}_{6c6c}^{b} = b\begin{pmatrix} 0 & \frac{1}{4}k - (k_+^2 - k_-^2) - k_+\langle k_z^2\rangle \\ \frac{1}{4}k + (k_-^2 - k_+^2) - k_-\langle k_z^2\rangle & 0 \end{pmatrix} \quad \text{(36.c)}$$

where b is a material constant. In a two-dimensional system it can be rewritten into the linear Dresselhaus term [48-50]

$$\widehat{H}_D^{lin} = -\langle k_z^2\rangle(\hat{\mathrm{s}}_\mathrm{x}\mathrm{k}_\mathrm{x} - \hat{\mathrm{s}}_\mathrm{y}\mathrm{k}_\mathrm{y}) \quad \text{(36.d)}$$

And the cubic Dresselhaus term

$$\widehat{H}_D^{cub} = \mathrm{k}_\mathrm{x}\mathrm{k}_\mathrm{y}(\mathrm{k}_\mathrm{y}\hat{\mathrm{s}}_\mathrm{x} - \mathrm{k}_\mathrm{x}\hat{\mathrm{s}}_\mathrm{y}) \quad \text{(36.e)}$$

These two effective forms of the Dresselhaus spin-orbit coupling are encountered in models with explicitly broken inversion symmetry in general. In fact, operators invariant under the D2d point group as in Eqs. II-36.d and II-36.e are referred to as Dresselhaus-type, because of their identical transformation behavior.

II.4.3 Rashba-type Spin-orbit Coupling: Structure Inversion Asymmetry

Rashba and Sheka have computed the energy bands of the wurtzite structure and proceeded in similar fashion to Dresselhaus and employed k .p-theory to the wurtzite structure point group C6v [51]. Only terms ~ k2 in the momentum are retained in the Löwdin perturbative treatment and the spin-splitting of the Γ^6_7 valence band becomes [52]

$$E_{1,2} = ak_{\parallel}^2 + bk_{\perp}^2 + \varepsilon \pm \alpha k_{\parallel} \qquad (38.a)$$

using constants a, b, ε and α, with the in-plane momentum $k_{\parallel}$ and out-of-plane momentum $k_{\perp}$. Then, an extremum of the energy splitting for both solutions is located on a circle with radius $k_{\parallel} \sim \left|\frac{\alpha}{2a}\right|$

This feature of Eq. 38.a occurs in situations, when a crystal exhibits a single high-symmetry axis of at least threefold rotational symmetry [53]. Let such an axis be parallel to the cartesian z-coordinate. In a two-dimensional system perpendicular to said axis, an effective Hamiltonian [54].

$$\widehat{H}_R = \alpha(\hat{s} \times k)_z = \alpha(\hat{s}_x k_y - \hat{s}_y k_x) \qquad (38.b)$$

can be formulated, which has the same qualitative feature of the spin-splitting discussed above [54]. Causes for the Rashba-type spin-orbit coupling can be electric fields [56], which reduce the symmetry of the system, leading to lifted degeneracies [57] as a consequence of the Stark effect [39]. In graphene, spin-flip terms due to Rashba-type spinorbit coupling connect π-bonds, made up of pz-orbitals, which are symmetric along the z-axis, to the s-, px- and py-orbitals from the σ-bonds. DFT calculations have shown, that the spinorbit coupling from the px- and py-orbitals is much weaker than that of the d-orbitals [58]. Other DFT calculations have shown that in-plane deformations may enhance the Rashbatype spin-orbit coupling strongly [59].

Rashba-type spin-orbit coupling originates from breaking the mirror symmetry along an axis perpendicular to the graphene plane, which has at least three-fold symmetry [54]. Such a structure-inversion asymmetry leads to a form of spin-momentum-locking [60], resulting ultimately in a spin-orbit coupling term of the form Eq. II-38.b. This spinorbit coupling causes a so-called trigonal warping, an effect that splits each Dirac cone at the K and K' point into 4 distinct cones. Before this particular effect of the Rashba-type spin-orbit coupling is

discussed in the following sections, an effective term in the low-energy representation is stated. In the basis of directed orbitals in spherical coordinates the Stark effect, due to an electric field perpendicular to the flat graphene plane, introduces matrix elements among states located at identical lattice sites, such that integrals of the type.

$$\langle \varphi_i | \hat{z} | \varphi_j \rangle = \int \varphi_i^*(r) r \cos\theta \varphi_j(r) d^3r \tag{38.c}$$

have to be solved, where e.g. i = p_z and j = s denote the different quantum numbers of the hydrogen orbitals ϕ_i and ϕ_j . The interaction couples either on-site s- and p_z-orbitals, p_y- and d_{yz}-orbitals, p_x- and d_{xz}-orbitals or d_{z2} - and p_z-orbitals, due to the symmetry of the atomic wave functions. In this case the dominant contribution to the π-bands is due to the on-site coupling of s- and p_z-orbitals [61], while the influence of the d-orbital coupling via the Stark effect is small in comparison and can be neglected [54]. The finite overlap of the pz-orbitals with the sp^2-orbitals at each lattice site can lead to a transition from the π-bands to the sp^2-hybridized bands, followed by a hopping to the sp2-orbitals at a neighboring site. There, the intrinsic spin-orbit coupling in the p-orbitals allows an electron to return to the π-bands with a spin flip [62]. This is depicted in Figure.II.2 Such an interaction may be cast into an effective term, describing hopping among pz orbitals, together with a spin-flip. It can be derived via Löwdin partitioning, where the influence of the hopping in the sp^2-orbitals and the intrinsic spin-orbit coupling may be expressed effectively via a a term in the subspace of sublattice and real spin states of only the pz-orbitals. The resulting real-space representation of the effective Rashba-type spin-orbit coupling among the pz-orbitals is given as [43]

$$\hat{H}_R = i\lambda_R \sum_{\langle ij \rangle} \hat{c}_i \left(\hat{s} \times d_{ij} \right) z \hat{c}_j \tag{38.d}$$

In this notation the operators $\hat{?}_?$ represent either $\hat{?}_?$ or $\hat{?}_?$, depending on the sublattice at the sites i or j. The vector d_{ij} is the vector pointing from site i to site j and $\hat{?}$ is the vector containing the Pauli spin matrices. λ_R is the parameter denoting Rashba-type spin-orbit coupling strength. A full expression is discussed by Rakyta et al. [63]. It may first be Fourier decomposed and then expanded around the Dirac points. This leads to an interaction matrix in the basis $\{\psi A \uparrow, \psi B \uparrow, \psi A \downarrow, \psi B \downarrow\}$at the K-point, where the p_z-orbitals

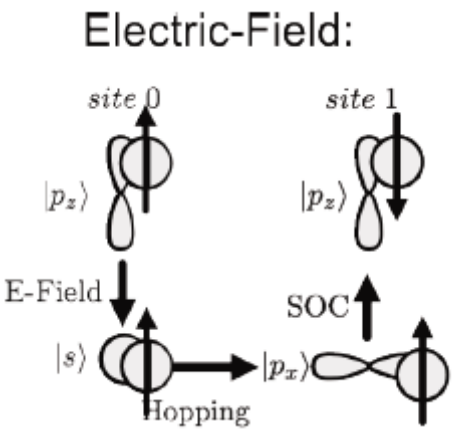

Figure II.2: A schematic overview of the effective term of the Rashba-type spin-orbit coupling originating from an electric field. The z-component of the real spin is indicated by an arrow at each orbital.

located at sublattices A or B with their respective spin indicated, are of the form

$$\widehat{H}_R^k = \begin{pmatrix} 0 & 0 & 0 & -\frac{3\lambda_R a}{2}(k_x + ik_y) \\ 0 & 0 & 3i\lambda_R & 0 \\ 0 & -3i\lambda_R & 0 & 0 \\ -\frac{3\lambda_R a}{2}(k_x + ik_y) & 0 & 0 & 0 \end{pmatrix} \quad (38.d)$$

Only taking the zeroth-order of Eq. II-38.d into account leads to the effective term in Eq. 38.b [64].

II.5. The linearized augmented plane wave method (FP-LAPW)

II.5.1.Introduction

Different calculation methods based on the DFT formalism have been developed to simplify the resolution of the Kohn-Sham equations.

These methods are mainly based on two points:

- Choice of the basis of the wave functions to project the Kohn-Sham mono-electronic states.
- Choice of the form of the effective potential generated by an infinite number of nuclei or ions, that is to say, the external potential.

We present in the following the FP-LAPW method (Full Potential Linearized Augmented Planes waves) and which is the method used in the ab initio calculation, and implemented in the wien2k calculation code [65].

II.4.2. The APW method

Slater in 1937 published an article [66], in which he considered that in the space in the vicinity of an atomic nucleus, the potential and the wave functions are of the form "Muffin-Tin", with a symmetry spherical inside the MT spheres of radius Ra (Figure II.3). Outside the spheres in the interstitial region between the atoms, the potential and the wave functions can be considered to be smooth. This allowed a development of wave functions in different bases depending on the treated region: radial solutions of the Schrödinger equation inside the MT sphere and plane waves in the interstitial region.

If the total potential has spherical symmetry in each sphere $(V(\vec{r}) \rightarrow V(r)$, and the potential of the interstitial region is constant $(V(\vec{r}) \rightarrow V_0$, we call this potential “Muffin-Tin”.

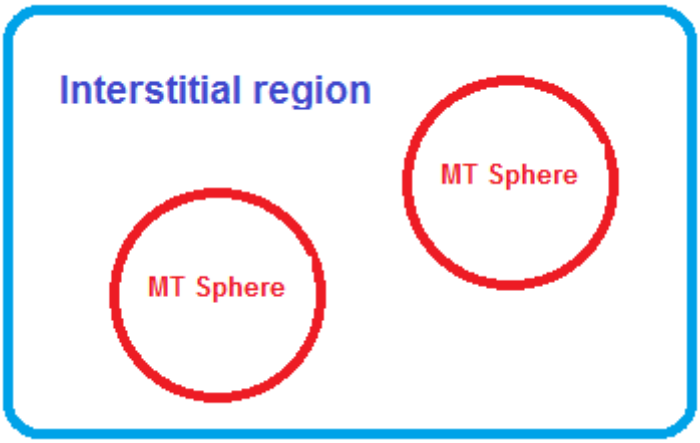

Figure.II.3: Muffin-tin potential

In the APW method, each basis function is represented as a singular plane wave in the interstitial region [67]. In the vicinity of the atomic nucleus, the potential and wave functions are of the form "Muffin-Tin".

$$\varphi(\vec{r}) = \begin{cases} \varphi_I(\vec{r}) = \frac{1}{\Omega^{\frac{1}{2}}} \sum_G C_G e^{i(\vec{K}+\vec{G})\vec{r}} & , r > Ra \\ \varphi_{Ra}(\vec{r}) = \sum_{lm} A_{lm}\, u_l(r, E_l) Y_{lm}(r) & , r > Ra \end{cases} \quad (39.a)$$

$\varphi_I(\vec{r})$: The wave function in the interstitial region.

$\varphi_{Ra}(\vec{r})$:The wave function in the MT sphere of radius Ra.

Ra :Represents the radius of the sphere MT

Ω :The volume of the unit cell

$\vec{G}$:The reciprocal network vecto

$\vec{r}$:The position inside the sphere

$\vec{K}$:The wave vector in the first Brillouin zone (ZIB)

C_G et A_{lm} The coefficients of the development in plane waves and spherical harmonics.

Y_{lm}:The polar coordinate position inside the sphere.

the functions u_l are the numerical solutions of the Schrödinger equation of the radial part ,with energy $E_l$written as:

$$\left\{-\frac{d^2}{dr^2} + \frac{l(l+1)}{r^2} + V(r) - E_l\right\} r u_l(r) = 0 \quad (39.b)$$

Which can be solved numerically with precision.V(r) represents the Muffin-tin potential and $E_l$the linearization energy. The expansion of the coefficients A_{lm} is obtained by equating the solutions inside the Muffin-Tin with the plane waves outside (the continuity condition).

II.4.3. La méthode FP-LAPW

The FP-LAPW (full potential -LAPW) method [68] combines the choice of a LAPW basis set with the full potential and charge density without any shape approximation in the interstitial region and inside the MT spheres:

$$V(\vec{r}) = \begin{cases} \sum_{\vec{K}} V_{\vec{K}} e^{i\vec{K}\vec{r}} & r > R_a \\ \sum_{L} V_{L}(r) Y_{L}(\hat{r}) & r < R_a \end{cases} \quad (40.a)$$

The charge density is developed in the form:

$$\rho(\vec{r}) = \begin{cases} \sum_{lm} \rho_{lm}(\vec{r}) Y_{lm}(\vec{r}) \\ \sum_{\vec{K}} \rho_{\vec{K}} e^{i\vec{K}\vec{r}} \end{cases} \quad (40.b)$$

This method is possible with the development of a technique for obtaining the Coulomb potential for a periodic charge density without shape approximation and with the inclusion of the Hamiltonian matrix elements. The FP-LAPW Hamiltonian is composed of two contributions from the two regions in which the space is deviated (MT and Interstitial). These two contributions must be calculated separately [69].

$$H = H_I + H_{MT} \quad (40.c)$$

II.6. WIEN2K code

WIEN2k is a widely used code for electronic structure calculations of solids based on the LAPW method within density functional theory. It allows for solving the Kohn-Sham equations .The program is written in Fortran and is popular for its full-potential approach to quantum mechanical calculations on periodic solids. WIEN2k offers a web-based graphical user interface (w2web) for ease of use and has a large and growing user community. Researchers can use WIEN2k to study various properties of materials, such as electron density and spectra, making it a valuable tool in materials science research.

The method used in this study is FP-LAPW (Linear Enhanced Plane Wave), implemented using the computational code "Wien2k" developed by Blaha, Schwartz, and colleagues at the Institute of Materials Chemistry, Vienna Institute of Technology (Austria) [69,70]. This code was first released in 1990 and has been continuously revised and updated multiple times to add computational properties or solve some computational problems. This numerical calculation code is based on the programming language "FORTRAN" and runs on the UNIX operating system based on density functional theory (DFT) and methods (FP-LAPW). It contains multiple 'independent program' packages that are linked through C-Shell scripts, allowing for self coherent computation. The calculation process usually includes three steps.

II.6.1. Initialization

In this step we must insert the important parameters, we fill an input file named case.struct with the atomic parameters, After generating this file, We perform the initialization by the init_lapw command to trigger several programs that execute in a successive manner.

II.6.2. Self-Consistent Field (SCF)

In this step, the SCF cycle process "Self Consistent Field" is then launched and iterated until the convergence of the solution.

II.6.3. Calculations and determination of properties

Once the self-consistent calculation is completed, it is possible to access the properties of the ground state (charge density, band structure, thermodynamic properties, thermoelectric

properties, etc.). Each of these properties is calculated separately with a "package" program which is launched with consecutive steps [72].

II.7. Conclusion

First-principles density functional theory (DFT) calculations are a widely used quantum mechanical approach in materials science for predicting and analyzing the electronic and structural properties of materials. By starting from fundamental principles and using the positions of constituent atoms, DFT computes the electronic structure of a material. This method offers valuable insights into properties such as the electronic band structure, density of states, and total energy of a material. The calculations involve solving the Schrödinger equation with approximations for the exchange-correlation energy, which accounts for electron-electron interactions. DFT has diverse applications, including understanding material properties, designing new materials with tailored characteristics, and optimizing existing materials for specific purposes. DFT calculations can provide valuable insights into these effects, which can be used to guide experimental investigations and optimize materials for specific applications.

Bibiography

[1] E. C. C. d. Souza and R. Muccillo, "Properties and applications of perovskite proton conductors," Materials Research, vol. 13, pp. 385-394, 2010.

[2] J. Scott and M. Dawber, "Oxygen-vacancy ordering as a fatigue mechanism in perovskite ferroelectrics," Applied Physics Letters, vol. 76, pp. 3801-3803, 2000.

[3] J. Singh, Smart Electronic Materials: Fundamentals and Applications, Cambridge university press, United Kingdom, (2005).

[4] Leach, A. R. Molecular Modelling: Principles and Applications, 2nd ed.; Prentice Hall: Upper Saddle River, New Jersey, (2001)

[5] S. A. Khan, F. Akram, R. A. Malik, J. C. Kim, R. A. Pasha, S. Lee, et al., "Piezoelectric and ferroelectric properties of lead-free Ga-modified 0.65 BiFeO3–0.35 BaTiO3 ceramics by water quenching process," Ferroelectrics, vol. 541, pp. 54-60, 2019.

[6] D.S. Sholl, J.A. Steckel, Density functional theory: a practical introduction, John Wiley & Sons, Inc, Hoboken, New Jersey, (2009).

[7] B. Garbarz-Glos, W. Bąk, A. Kalvane, M. Antonova, and G. Klimkowski, "Effects of CuO doping on structure, microstructure and dielectric properties of BaTiO3–PbTiO3 solid solution," Integrated Ferroelectrics, vol. 196, pp. 70-77, 2019.

[8] R. Gotardo, E. Silva, R. Alonso, J. Rosso, D. Silva, G. Santos, et al., "Dielectric, magnetic and structural characterizations in Mn doped 0.9 BiFeO3-0.1 BaTiO3 compositions," Ferroelectrics, vol. 534, pp. 95-102, 2018.

[9] D.S. Sholl, J.A. Steckel, Density functional theory: a practical introduction, John Wiley & Sons, Inc, Hoboken, New Jersey, (2009).

[10] W. Kohn, A.D. Becke, and R.G. Parr, Density Functional Theory of electronic structure, J. Phys. Chem.100 (31), (1996)

[11] E.K.U Gross and Reiner M. Dreizler, Density Functional Theory, Plenum Press, New York, (1995).

[12] P. Hohenberg and W. Kohn, Inhomogeneous electronic gas, Phys. Rev. 136, B864, Nov (1964).

[13] W. Kohn and L. J. Sham, Phys. Rev. 140 (4A), A1133–A1138, Nov (1965).

[14] M. Kulbak, D. Cahen, and G. Hodes, "How important is the organic part of lead halide perovskite photovoltaic cells? Efficient CsPbBr3 cells," The journal of physical chemistry letters, vol. 6, pp. 2452-2456, 2015.

[15] C. C. Stoumpos, C. D. Malliakas, J. A. Peters, Z. Liu, M. Sebastian, J. Im, et al., "Crystal growth of the perovskite semiconductor CsPbBr3: a new material for high-energy radiation detection," Crystal growth & design, vol. 13, pp. 2722-2727, 2013.

[16] F. Igbari, Z. K. Wang, and L. S. Liao, "Progress of Lead-Free Halide Double Perovskites," Advanced Energy Materials, vol. 9, p. 1803150, 2019.

[17] H. Zhu, Y. Fu, F. Meng, X. Wu, Z. Gong, Q. Ding, et al., "Lead halide perovskite nanowire lasers with low lasing thresholds and high quality factors," Nature materials, vol. 14, p. 636, 2015.

[18] M. A. Green, Y. Hishikawa, E. D. Dunlop, D. H. Levi, J. Hohl-Ebinger, and A. W. Ho-Baillie, "Solar cell efficiency tables (version 52)," Progress in Photovoltaics: Research and Applications, vol. 26, pp. 427-436, 2018.

[19]L. Chu, R. Hu, W. Liu, Y. Ma, R. Zhang, and J. Yang, "Screen printing large-area organometal halide perovskite thin films for efficient photodetectors," Materials Research Bulletin, vol. 98, pp. 322-327, 2018.

[20]P. Becker, J. A. M|rquez, J. Just, A. Al-Ashouri, C. Hages, H. Hempel, et al., "Low Temperature Synthesis of Stable γ-CsPbI3 Perovskite Layers for Solar Cells Obtained by High Throughput Experimentation," Advanced Energy Materials, vol. 9, p. 1900555, 2019.

[21] F. Zhang, B. Yang, K. Zheng, S. Yang, Y. Li, W. Deng, et al., "Formamidinium Lead Bromide Perovskite Microcrystals for Sensitive and Fast Photodetectors."

[22] Y. Wang, X. Zhang, D. Wang, X. Li, J. Meng, J. You, et al., "Compositional Engineering of Mixed-Cation Lead Mixed-Halide Perovskites for High-Performance Photodetectors," ACS applied materials & interfaces, 2019.

[23] A. Babayigit, A. Ethirajan, M. Muller, and B. Conings, "Toxicity of organometal halide perovskite solar cells," Nature materials, vol. 15, p. 247, 2016.

[24] A. Babayigit, D. D. Thanh, A. Ethirajan, J. Manca, M. Muller, H.-G. Boyen, et al., "Assessing the toxicity of Pb-and Sn-based perovskite solar cells in model organism Danio rerio," Scientific reports, vol. 6, p. 18721, 2016.

[25] H. Zhu, Y. Fu, F. Meng, X. Wu, Z. Gong, Q. Ding, et al., "Lead halide perovskite nanowire lasers with low lasing thresholds and high quality factors," Nature materials, vol. 14, p. 636, 2015.

[26] J. Longo and R. Ward, "Magnetic compounds of hexavalent rhenium with the perovskite-type structure," Journal of the American Chemical Society, vol. 83, pp. 2816-2818, 1961.

[27] M. Welch, "RH Mitchell Perovskites Modern and Ancient. Thunder Bay, Ontario (Almaz Press, www. almaz-press. com) 2002. 316 pp. Price US $70.00 (+ shipping and handling). ISBN 0 9689411 0 9," Mineralogical Magazine, vol. 67, pp. 419-420, 2003.

[28] T. Negas and R. Roth, "Phase equilibria and structural relations in the system BaMnO3−x," Journal of Solid State Chemistry, vol. 3, pp. 323-339, 1971.

[29] B. Chamberland, A. Sleight, and J. Weiher, "Preparation and characterization of BaMnO3 and SrMnO3 polytypes," Journal of Solid State Chemistry, vol. 1, pp. 506-511, 1970.

[30] C. C. Stoumpos, C. D. Malliakas, J. A. Peters, Z. Liu, M. Sebastian, J. Im, et al., "Crystal growth of the perovskite semiconductor CsPbBr3: a new material for high-energy radiation detection," Crystal growth & design, vol. 13, pp. 2722-2727, 2013.

[31] T. He, Q. Huang, A. Ramirez, Y. Wang, K. Regan, N. Rogado, et al., "Superconductivity in the non-oxide perovskite MgCNi 3," Nature, vol. 411, p. 54, 2001.

[32] G. Volonakis, N. Sakai, H. J. Snaith, and F. Giustino, "Oxide Analogs of Halide Perovskites and the New Semiconductor Ba2AgIO6," The journal of physical chemistry letters, vol. 10, pp. 1722-1728, 2019.

[33] N. Reyren, S. Thiel, A. Caviglia, L. F. Kourkoutis, G. Hammerl, C. Richter, et al., "Superconducting interfaces between insulating oxides," Science, vol. 317, pp. 1196-1199, 2007.

[34]. Czycholl, G. Theoretische Festkörperphysik Band 1 (Springer Spektrum, 2016).

[35]. Premasiri, K. & Gao, X. P. A. Tuning Spin–Orbit Coupling in 2D Materials for Spintronics: A Topical Review. Journal of Physics: Condensed Matter 31, 193001 (2019).

[36]. Rashba, E. I. & Sheka, V. I. Symmetry of Energy Bands in Crystals of Wurtzite Type II. Symmetry of Bands with Spin-Orbit Interaction Included. New Journal of Physics 17, 050202 (2015).

[37]. Dresselhaus, G. Spin-Orbit Coupling Effects in Zinc Blende Structures. Physical Review 100, 580–586 (1955).

[38]Edelstein, V.M.Spin polarization of conduction electrons induced by electric current in two-dimensional asymmetric electron systems.solid state commun.73,233-235(1990).

[39] Konschuh, S., Gmitra, M. & Fabian, J. Tight-Binding Theory of the Spin-Orbit Coupling in Graphene. Physical Review B 82, 245412 (2010).

[40] Edmonds, A. R. Angular Momentum in Quantum Mechanics (Princeton University Press, 1957).

[41]. Shankar, R. Principles of Quantum Mechanics (Springer, 2011).

[42] Chisholm, C. D. H. Group Theoretical Techniques in Quantum Chemistry (London New York Academic Press, 1976).

[43] Kane, C. L. & Mele, E. J. Z2 Topological Order and the Quantum Spin Hall Effect. Physical Review Letters 95, 146802 (2005).

[44] Dresselhaus, G. Spin-Orbit Coupling Effects in Zinc Blende Structures. Physical Review 100, 580–586 (1955).

[45]Elliott, R. J. Theory of the Effect of Spin-Orbit Coupling on Magnetic Resonance in Some Semiconductors. Physical Review 96, 266–279 (1954).

[46] Elliott, R. J. Spin-Orbit Coupling in Band Theory—Character Tables for Some ”Double” Space Groups. Physical Review 96, 280–287 (1954).

[47] Vaughan, M. P. & Rorison, J. M. Modeling Spin Relaxation in Semiconductor Quantum Wells: Modifying the Elliot Process. Semiconductor Science and Technology 33, 094003 (2018).

[48] Ganichev, S. D. & Golub, L. E. Interplay of Rashba/ Dresselhaus Spin Splittings Probed by Photogalvanic Spectroscopy – A Review. Phys. Status Solidi B 251, 1801– 1823 (2014).

[49] Gmitra, M., Kochan, D., Högl, P. & Fabian, J. Trivial and Inverted Dirac Bands and the Emergence of Quantum Spin Hall States in Graphene on Transition-Metal Dichalcogenides. Physical Review B 93, 155104 (2016).

[50] Hao, Y. F. Rashba and Dresselhaus Spin-Orbit Interaction in Semiconductor Quantum Wells. The European Physical Journal B 85, 84 (2012).

[51] Bihlmayer, G., Rader, O. & Winkler, R. Focus on the Rashba Effect. New Journal of Physics 17, 050202 (2015).

[52] Rashba, E. I. & Sheka, V. I. Symmetry of Energy Bands in Crystals of Wurtzite Type II. Symmetry of Bands with Spin-Orbit Interaction Included. New Journal of Physics 17, 050202 (2015).

[53] Bychkov, Y. A. & Rashba, E. I. Properties of a 2D Electron Gas with Lifted Spectral Degeneracy. JETP Letters 39, 78 (1984).

[54] Rashba, E. I. Graphene with Structure-Induced Spin-Orbit Coupling: Spin-Polarized States, Spin Zero Modes, and Quantum Hall Effect. Physical Review B 79, 161409 (2009).

[55] Bihlmayer, G. & Blügel, S. Electronic Structure of Matter in Lecture Notes f the 47th IFF Spring School 2016 ”Memristive Phenomena - From Fundamental Physics to Neuromorphic Computing” (eds Waser, R. & Wuttig, M.) 113 (2016).

[56] Shanavas, K. V. & Satpathy, S. Electric Field Tuning of the Rashba Effect in the Polar Perovskite Structures. Physical Review Letters 112, 086802 (2014).

[57] Ast, C. R. & Gierz, I. Sp-Band Tight-Binding Model for the Bychkov-Rashba Effect in a Two-Dimensional Electron System Including Nearest-Neighbor Contributions from an Electric Field. Physical Review B 86, 085105 (2012).

[58] Lado, J., García-Martínez, N. & Fernández-Rossier, J. Edge States in Graphene-like Systems. Synthetic Metals 210, 56–67 (2015).

[59] Berche, B., Mireles, F. & Medina, E. Rashba Spin-Orbit Interaction Enhanced by Graphene in-Plane Deformations. Condensed Matter Physics 20, 13702 (2017).

[60] Shanavas, K. V. Theoretical Study of the Cubic Rashba Effect at the SrTiO3 (001) Surfaces. Physical Review B 93, 045108 (2016).

[61] Shanavas, K. V., Popovićć, Z. S. & Satpathy, S. Theoretical Model for Rashba Spin- Orbit Interaction in d-Electrons. Physical Review B 90, 165108 (2014).

[62] Huertas-Hernando, D., Guinea, F. & Brataas, A. Spin-Orbit Coupling in CurvedGraphene, Fullerenes, Nanotubes, and Nanotube Caps. Physical Review B 74, 155426 (2006).

[63] Rakyta, P., Kormányos, A. & Cserti, J. Trigonal Warping and Anisotropic Band Splitting in Monolayer Graphene Due to Rashba Spin-Orbit Coupling. Physical Review B 82, 113405 (2010).

[64] van Gelderen, R. & Morais-Smith, C. Rashba and Intrinsic Spin-Orbit Interactions in Biased Bilayer Graphene. Physical Review B 81, 125435 (2010).

[65] M. Kim, J. Im, A. J. Freeman, J. Ihm, and H. Jin, "Switchable S= 1/2 and J= 1/2 Rashba bands in ferroelectric halide perovskites," Proceedings of the National Academy of Sciences, vol. 111, pp. 6900-6904, 2014.

[66] G. Murtaza, R. Khenata, M. Khalid, and S. Naeem, "Elastic and optoelectronic properties of RbMF3 (M= Zn, Cd, Hg): A mBJ density functional calculation," Physica B: Condensed Matter, vol. 410, pp. 131-136, 2013.

[67] J. W. Fergus, "Perovskite oxides for semiconductor-based gas sensors," Sensors and Actuators B: Chemical, vol. 123, pp. 1169-1179, 2007.

[68] C. Kittel, M. Poumellec, R. Mégy, and C. Dupas, Physique de l'état solide vol. 7: Dunod France, 1983.
[69] L. Smart, "Introduction à la chimie du solide," 1997.
[70] A. WIEN, "Improving the efficiency of FP-LAPW calculations. M. Petersen, F. Wagner, L. Hufnagel, M. Scheffler, P. Blaha, K. Schwarz."
[71] P. Blaha, "WIEN97, Technical University of Vienna, 1997; P. Blaha, K. Schwarz, P. Sorantin, and SB Trickey," Comput. Phys. Commun, vol. 59, p. 399, 1990.
[72] P. Blaha, K. Schwarz, G. Madsen, D. Kvasnicka, and J. Luitz, "WIEN2k: An Augmented Plane Wave Plus Local Orbitals Program for Calculating Crystal Properties User's Guide, WIEN2k 14.2," ed: Institute of Physical and Theoretical Chemistry, Vienna University of …, 2014.

Chapter III:

Switchable photovoltaic properties in ferroelectric Lead Free Bismuth Halide Double Perovskites

III.1 Introduction:

In the face of current energy crises, global research efforts are focusing on transitioning from dependence on fossil fuels, such as petroleum and natural gas, to renewable energy sources [1]. Solar energy has emerged as a promising candidate to meet future energy demands due to its ease of use, inexhaustible supply,and environmentally friendly nature [2]. Consequently, the development of photovoltaic (PV) technology has significantly advanced in response to the increasing global energy consumption. Several criteria are used to evaluate the performance of photovoltaic materials, including thermodynamic stability, positive decomposition enthalpy, high dielectric constants, high optical absorption coefficients, suitable direct band-gaps ranging from 0.8-2.0 eV (corresponding to the visible and near-infrared regions of electromagnetic radiation), advantageous ambipolar carrier conduction and efficient carrier extraction, both electron and hole effective masses less than 1.0 m_0, defect tolerance, high charge carrier mobility, extended photogenerated carrier diffusion lengths and lifetimes, and small exciton binding energy (< 100 meV) [3,4].

The fulfillment of these criteria has led to a remarkable increase in power conversion efficiency (PCE) for PV materials. In light of these criteria, the exploration and development of new PV materials is crucial for the ongoing advancement of solar energy technology. By identifying materials that exhibit these desirable properties, researchers can contribute to the improvement of photovoltaic devices and the widespread adoption of solar energy as a sustainable and clean energy source. Perovskite-structured compounds represent a vast class of materials that are being explored for more efficient photovoltaics. Owing to their remarkable efficiency in converting solar energy into electricity, perovskite materials have emerged as a promising PV technology [5]. Specifically, halide perovskites with the chemical formula $AM^{IV}X^{VII}$ have garnered significant attention in the photovoltaic industry. In this formula, A represents a monovalent organic molecule such as methylammonium, formamidinium or inorganic cations (Cs^+, Rb^+); MIV denotes a divalent Group IVA cation (MIV = Pb^{+2}, Sn^{+2}, Ge^{+2}); and XVII refers to a halogen anion (I^-, Cl^-, Br^-).

Halide perovskites have demonstrated rapid advancements in photovoltaic conversion efficiency (PCE) since their introduction in 2009. The initial PCE of a $CH_3NH_3PbI_3$-based solar

cell was 3.8% [6], but recent laboratory-scale research has pushed the record high-efficiency to an impressive 25% [7]. This substantial increase in efficiency underscores the potential of halide perovskites for revolutionizing the solar cell industry and further driving the adoption of solar energy as a sustainable and clean energy source. As research into perovskite materials and their photovoltaic properties continues, we can expect to see further advancements in the efficiency and stability of perovskite-based solar cells. The exceptional performance of halide perovskites in photovoltaics is attributed to their inherent optical and photophysical properties. These unique intrinsic characteristics, combined with low-cost solution-based fabrication techniques, make halide perovskites excellent candidates for next-generation PV absorbers [8]. Their efficiencies surpass those of conventional solar cells, such as Cu(In,Ga)Se_2 (CIGS) at 22.6%, poly-Si at 22.3%, and CdTe at 22.1% [9].

Recently, halide perovskites have not only been explored for PV applications but have also attracted considerable interest for other optoelectronic applications. These include optoelectronic detectors , light-emitting diodes (LEDs) , lasers , X-ray detectors [10], as well as magnetoelectronic and thermoelectronic applications [11]. The versatility and promising performance of halide perovskites across a wide range of applications highlight their potential to revolutionize the fields of renewable energy and optoelectronics, paving the way for more sustainable and efficient technologies. In recent years, extensive efforts have been made to understand the underlying origins of the unique and exceptional photovoltaic capabilities of Pb-halide perovskites. It has been discovered that the high symmetry of the perovskite structure and the ns2 lone pair electrons of lead may be key factors influencing the optoelectronic properties of Pb-halide perovskites [12]. Among these factors, a plausible explanation for the excellent photoelectric characteristics of $MAPbI_3$ is its association with ferroelectric polarization [13]. This has motivated researchers to explore hybrid lead perovskites with ferroelectric polarization, such as (cyclohexylammonium) Pb_2Br_4, (benzylammonium)Pb_2Cl_4, and (n-butylammonium)$(MA)_2Pb_3Br_{10}$ [14].

The potential connection between the ferroelectric properties and the photovoltaic performance of Pb-halide perovskites provides a promising avenue for further research and development. By elucidating the mechanisms underlying the exceptional optoelectronic properties of these materials, researchers can contribute to the design and synthesis of new

perovskite materials with enhanced photovoltaic performance and stability. Ultimately, this understanding can lead to the development of more efficient and sustainable solar cell technologies. Theoretical research has shown that ferroelectricity in halide perovskites is associated with order-disorder transitions of the cations and/or anions displacements in the MX_6 octahedron of their structures. This ferroelectricity is activated by the ns^2 lone-pair electrons of the cation center [15]. Similar mechanisms have been observed in complex oxides such as multiferroic $BiFeO_3$, $BiMnO_3$, and ferroelectric $PbTiO_3$, where structural distortions caused by lone-pair electrons are responsible for the emergence of ferroelectricity [16]. Furthermore, Zhao et al. demonstrated that the ferroelectricity in the [H2dmdap][SbCl5] (dmdap=N ,N-dimethyl-1,3-diaminopropane) compound arises from the relative displacements of the Sb and Cl ions in the crystal lattice. These displacements are driven by the $5s^2$ lone-pair electrons of the Sb^{III} center [17]. Understanding the role of lone-pair electrons and their influence on the ferroelectric properties of halide perovskites provides valuable insights for the design and development of new materials with enhanced photovoltaic performance. By exploiting the connection between ferroelectricity and photovoltaic characteristics, one can potentially create materials with improved efficiency, stability, and suitability for various optoelectronic applications.

Ferroelectric materials, which are characterized by switchable spontaneous polarizations, have attracted significant interest as potential alternatives to traditional photonic and photovoltaic systems [18]. In these non-centrosymmetric materials, the conversion of solar energy into electric current is known as the bulk photovoltaic effect (BPVE) [19]. BPVE leads to a shift current, a nonlinear optical process resulting from second-order interaction with monochromatic light. This phenomenon is technologically significant because it can generate photovoltages greater than the material's band gap [20]. Furthermore, unlike conventional p-n junction solar cells, the photoconversion efficiency of ferroelectric materials exhibiting BPVE is not limited by the Shockley-Queisser limit [21]. To achieve strong shift current enhancements, electronic states with delocalized, covalent bonding that is highly asymmetric along the current direction are required, as reported by Young et al. [22]. The unique properties of ferroelectric materials, particularly their ability to generate photovoltages exceeding their band gap and circumvent the Shockley-Queisser limit, make

them promising candidates for the development of advanced photovoltaic systems. By harnessing the potential of BPVE and understanding the underlying mechanisms, researchers can explore innovative materials and device designs to improve the efficiency and performance of solar energy conversion technologies.

To overcome the obstacles associated with Pb-based perovskites, researchers have looked into substituting Pb^{+2} by combining monovalent (M^{+}) and trivalent lone-pair cations (M^{+3}) to synthesize a new structure of lead-free double-perovskite halides ($A_2M^{+}M^{+3}X_6$) . Double halide perovskites $A_2M^{+}M^{+3}X_6$ (M^{+} = Cu, Ag; M^{+3} = In, Sb, Bi) have been extensively investigated for PV applications. These materials offer a promising alternative to silicon solar cells due to their lower manufacturing costs, absence of toxicity, and high light absorption rates [23]. Within this family of double-perovskite halides, $Cs_2AgCrCl_6$ has been experimentally synthesized with a hexagonal structure [24]. In similar experimental research, devices based on $Cs_2AgBiBr_6$ exhibit high stability and long carrier lifetimes [25]. The efficiency of perovskite solar cells using Cs2AgBiBr6 film was reported to be 2.43% [26]. Additionally, the mixed-halide Cs2AgBiX6 (X = Br, Cl, I) compound, with band gaps ranging from 1.5 to 2.8 eV, has been studied both theoretically and experimentally [27,28].

Further analysis reveals that $Cs_2AgBiBr_6$ is more thermally stable than other metal halide perovskites, although this material exhibits an indirect band gap [28]. The development of lead-free double-perovskite halides has the potential to address the environmental and stability concerns associated with lead-based perovskites, paving the way for more sustainable and efficient solar cell technologies.

In this chapter, we aim to investigate the ground-state crystal structures, electronic and optical properties of cesium halide double perovskites Cs_2InBiX_6 (X = Cl, Br). To the best of our knowledge, a comprehensive study of these compounds has not yet been undertaken. We briefly discuss the ferroelectric mechanism and report on the role of lone pair cations in ferroelectric Cs_2InBiX_6 using first principles calculations [29]. Additionally, to evaluate the photovoltaic performance of the optimal materials, we calculate the maximum solar cell efficiency, known as the "spectroscopic limited maximum efficiency (SLME)" [30]. Through this investigation, we hope to shed light on the potential of Cs_2InBiX_6 as an alternative to

lead-based perovskites in photovoltaic applications and provide insights into the role of ferroelectricity and lone pair cations in these materials.

Our comprehensive study will contribute to the understanding of cesium halide double perovskites and their potential for use in sustainable and efficient solar cell technologies. By identifying the most promising compounds and their key properties, we aim to guide further research and development efforts in the field of photovoltaics.

III-2 Lead-Free Halide Double Perovskite Materials Toward Green and Stable Optoelectronic Applications

Lead-based halide perovskites have proven to be highly effective semiconductors for various optoelectronic applications, such as solar cells, lighting, lasers, and photon detection. However, concerns over lead toxicity and their instability pose major challenges. Fortunately, halide double perovskites with the formulas $A_2M(I)M(III)X_6$ or $A_2M(IV)X_6$ have been identified as potential stable and eco-friendly alternatives for these applications. In these materials, the toxic divalent lead ions are replaced by a combination of one monovalent and one trivalent ion, or by a single tetravalent ion. Recently, these halide double perovskites have been explored as green alternatives to lead halide perovskites, maintaining charge balance by substituting the lead ions with one monovalent and one trivalent ion, or a tetravalent ion and a vacancy site (denoted as "□"), as illustrated in Fig. 1a [38]. The $A_2M(IV)X_6$ compounds, known as vacancy-ordered halide double perovskites, are analogous to $A_2M(I)$ systems with three-dimensional structures featuring corner-sharing metal halide octahedra, and have garnered significant attention as promising candidates for optoelectronic applications.

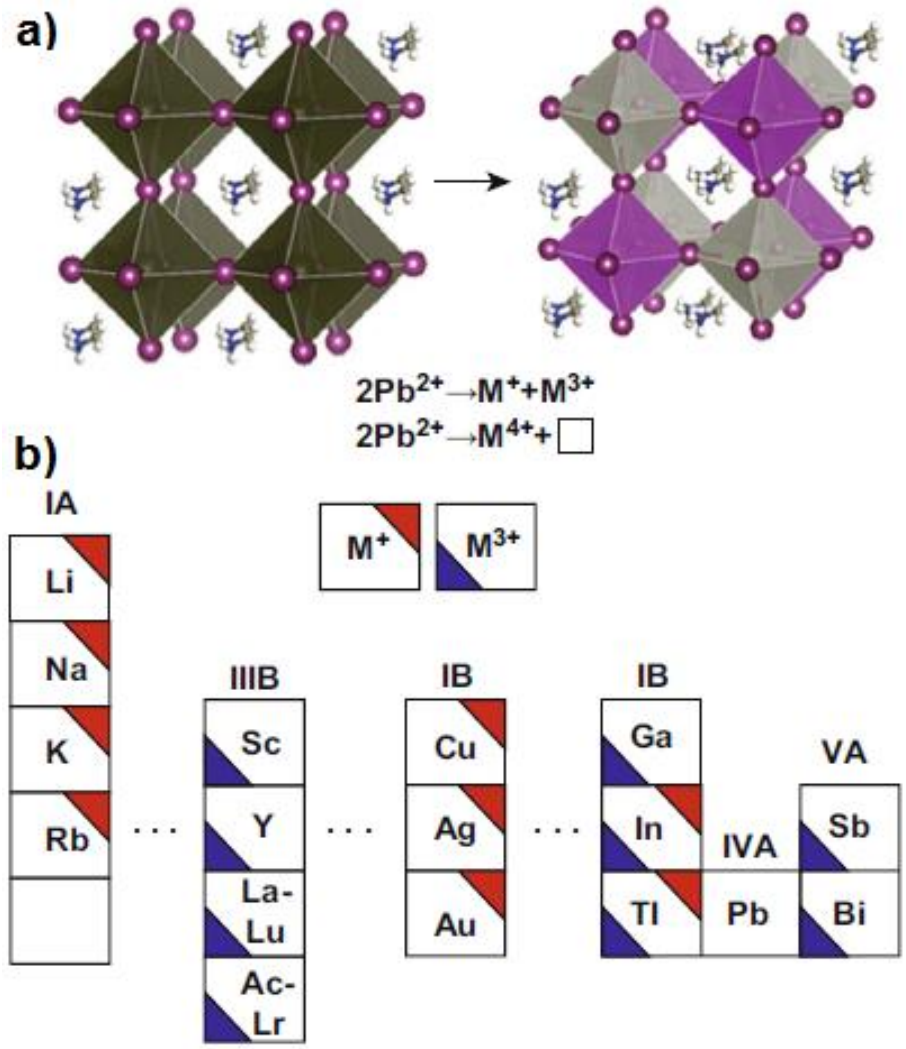

Figure . III-1 a) Schematic illustration of the transformation from APbX3 to A2M(I)M(III)X6 or A2M(IV)X6, where two toxic Pb2+ ions are substituted by combining M+ and M3+ ions (or M4+ ion). "□" denotes M-site vacancy. **BB** Elements of M-location cations with M+ and M3+ in the periodic table for halide double perovskites. When any M-site elements are localized at IA or IIIA groups of the periodic table, the materials have direct bandgaps.

III-3 Computational methods

In this study, we perform computations by solving the Kohn-Sham equation. We have applied the self-consistent full potential linear augmented plane wave (FP-LAPW) method, as employed in the Wien2k simulation code. This implementation is based on density functional theory (DFT) with several approximations for the exchange-correlation (XC) potential. In the full-potential method, the unit cell is divided into an interstitial region and atomic spheres that surround the nucleus. Inside the atomic spheres, the wavefunctions are expanded using

spherical harmonic basis functions, while plane waves are used as basis functions for the interstitial region [31]. The wavefunctions in the interstitial region are expanded in the form of plane waves with a cutoff of $R_{MT} \times k_{max}$ equal to 7.0, where R_{MT} represents the minimum radius of the muffin-tin (MT) spheres, and k_{max} stands for the maximum modulus for reciprocal k vectors. The maximum value of the angular expansion for valence wavefunctions inside the spheres is expanded up to lmax = 10. A dense mesh of 1000 k-points in the first Brillouin zone is used for the self-consistent field (SCF) calculations to obtain the densities of states (DOS). The atomic sphere radii (R_{MT}) are selected to ensure that no core charge leaks out of the MT spheres and the spheres do not overlap. The muffin-tin radii for Cs_2InBiX_6 are chosen to be 2.5, 2.08, 1.98, 1.70, and 2.42 a. u for Cs, In, Bi, Cl, and Br, respectively.

III-4 Main calculated results:

III-4.1 Structural properties and stability structural parameters:

As a first step of our study, we determined the Crystal structure information of Cs_2InBiX_6 materials in the rhombohedral phase (space groups R3m), By calculating the total energy at different volumes and fitting the resulting E(V) curve to the empirical Birch -Murnaghan equation of state [32]then relaxing simultaneously the cell shape and atomic positions.

The results of our structural parameters such as the equilibrium volume, lattice constants, bulk modulus B, its first pressure derivative B' were obtained and the relaxed atomics fractional coordinates. Are summarized in table 1.The obtained values are used to investigate the electronic properties.

Table III.1: The lattice parameters (a and c), volume V ,bulk modulus B and its first pressure derivative B' of the Cs_2InBiX_6 (space group R3m) :

Compounds	a(Å)	c(Å)	V(Å^3)	B'	B(GPa)
$Cs_2InBiCl_6$	8.115	10.518	379.409	4.588	21.521
$Cs_2InBiBr_6$	8.514	20.856	438.137	4.6931	18.182

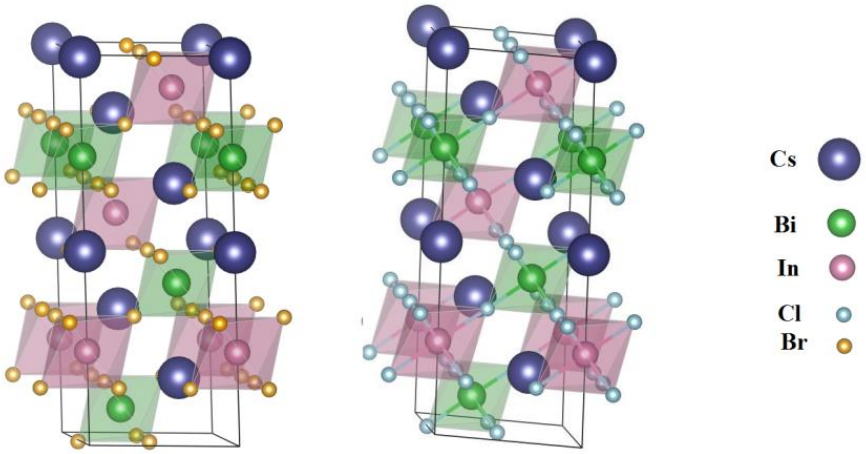

Figure III.2. Crystal structure of Rhombehedral of double perovskites (a) Cs2InBiBr6 and (b) Cs2InBiCl6.

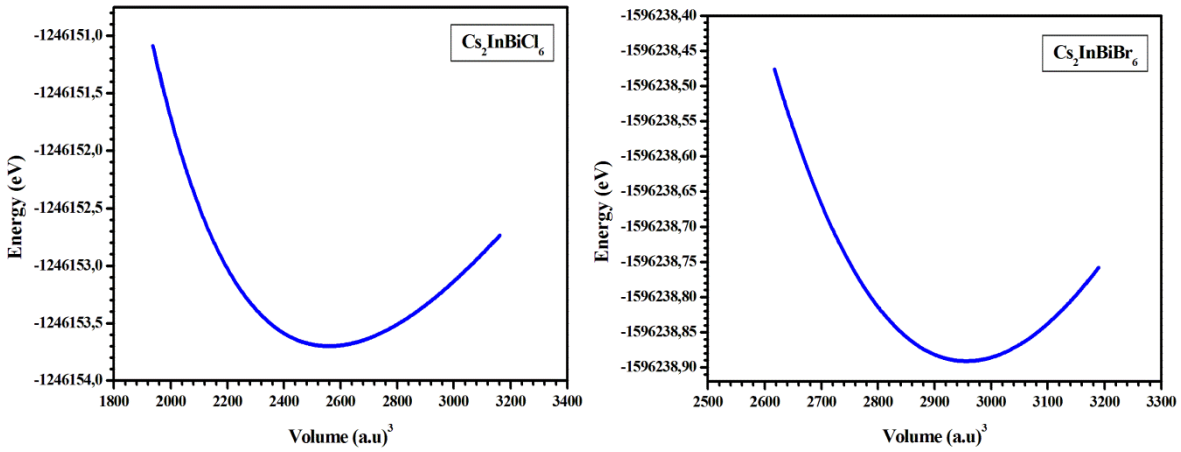

Figure III.3. Total energy versus volume.

Total energy versus volume curves for calculated Using equation of state provided by Birch-Murnaghan equation is plotted in Figure. 2. Furthermore, the thermodynamic stability of these materials are determined by calculated The formation energies of Cs2InBiX6 (X = Cl, Br) [33]:

We have computed formation energies per atom of various ordered configurations of Cs2InBiX6 with respect to the elemental standard states and it is defined as

$$\Delta E = \frac{E_{total} - \sum nE_a}{N} \quad (1)$$

where E_{total} represent the DFT compute total energies of an ordered bulk perovskite phase of the three compounds . "*Ea*" is the ground-state energy of a pure element in its stable

structure, "*n*" is the number of atoms of that species, and "*N*" represents total number of atoms in the unit cell.

The calculated value of formation energies for $Cs_2InBiCl_6$, and $Cs_2InBiBr_6$ are -0.210, and -0.133 eV/atom, respectively. According to The negative formation energies of these compounds, indicat the criterion thermodynamic stability.

III-3.2 Band structure and density of states :

The study of band structure for the photovoltaic material and particularly for the crystal presents very important task. It allow to evaluate the spectral distribution of the absorption, charge density distribution, their mobility. The evaluated electronic features may serve as a basis for the further optimization of the optical properties in the desired direction. The calculated band structures of Cs_2InBiX_6 in high-symmetry axis of the crystal using GGA-PBE functional ,TB-mBJ and mBJ + SOC method are presented in Figure III-4 and figure III-5 . the Brillouin zone (BZ) is set as Γ (000), F (0.5 -0.5 0), L (0.5 0 0) and Z (0.5 -0.5 0.5). All Cs_2InBiX_6 exhibit both dispersive CBM and VBM, providing a facile pathway for charges carries transport. .Here, we notice that these three methodes present a similar behavior; the only noticeable difference is the values of the band gap.

to investigate the effects of different functional on the electronic features, The total density of states (TDOS) of all compounds were also calculated to identify the type of band alignment more clearly, as shown in Figure III-6

Following Figure.3, As the top of the valence band (VB) and the bottom of the conduction band (CB) of $Cs_2InBiCl_6$ and $Cs_2InBiBr_6$ are both located at Γ (0, 0, 0) point in Brillouin zone, which show the direct band-gap nature.

A comparison of calculated band-gap values with the three methods are presented in **Table III-2.**

Table III-2 : Calculated electronic band gaps (eV).

Compound	GGA-PBE	TB-mBJ	TB-mBJ+SO
$Cs_2InBiCl_6$	1.358	1.706	0.543
$Cs_2InBiBr_6$	1.132	1.458	0.403

It can be seen that the band-gap values decrease with increasing radius atomic from Cl to Br, **Table III-2** also reveals that mBJ form gives energy band gap larger then GGA-PBE ,Whereas the mbj+SOC effect underestimates the bandgaps.

Because the completely occupied lone-pair s2 states are present for both the In (I)) and Bi(III) cations. These halide double perovskites have Pb(II)-like shells, and their band structures resemble those of the lead halide perovskites (MAPbI3, CsPbI3) [34]. and The predicted band-gaps of Cs2InBiCl6 and Cs2InBiBr6 made using mBJ are in the same range as those previously reported for cesium lead halides (CsPbX3) [35].

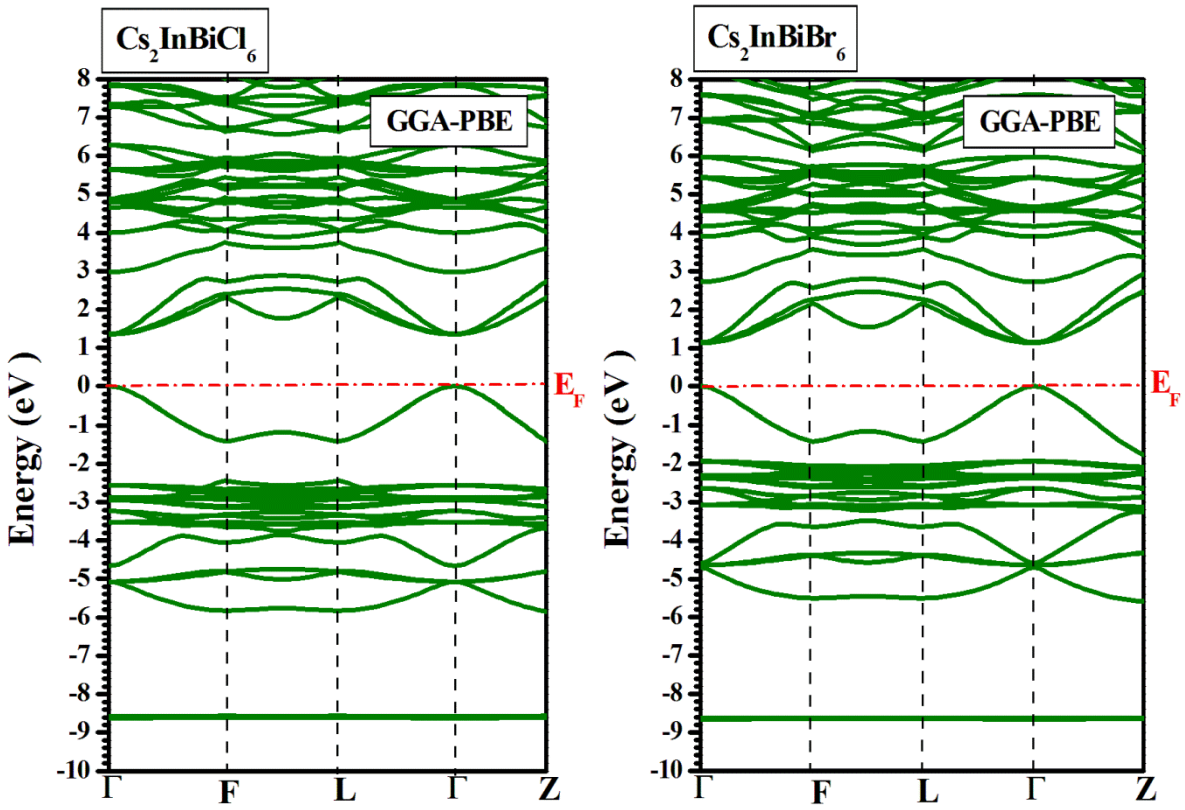

Figure III-4. The calculated band structures of Cs2InBiCl6, and Cs2InBiBr6 using GGA-PBE.

In principle the spin-orbit coupling causes the energy band splitting at Γ point. The momentum dependent splitting of energy bands that occurs in these structures (Figure5) is the Rashba-type splitting. The effect of spin-orbit coupling on the momentum dependent splitting of energy band is reported in table 3. Hence, the value of Rashba coefficient $\alpha = \frac{2\delta E}{\delta K}$ where, δE Rashba spin-splitting energy, and offset momentum δK[36]. The study reveals a strong dependence of Rashba interaction coefficient of $Cs_2InBiBr_6$ compared with

$Cs_2InBiCl_6$.The multi energy band gaps structure allows more photons with different wavelengths are absorbed. Therefore, the new energy band structure has features of good solar absorber.

Table III-3: Rashba parameters for band-splitting at Γ point for Cs2InBiCl6and Cs2InBiBr6 compounds.

Compounds	Valence band			conduction band		
	δE (meV)	$\delta K_{L-\Gamma}$ (Å^{-1})	α_v (eVÅ)	δE (meV)	$\delta K_{L-\Gamma}$ (Å^{-1})	α_c (eVÅ)
$Cs_2InBiCl_6$	1.351	0.0064	0.427	2.690	0.0053	1.02
$Cs_2InBiBr_6$	5.576	0.0108	1.032	7.074	0.00887	1.595

We have analyzed the contribution of the anion and cations states to each set of bands by decomposing the DOS into s, p, and d-orbital contributions. The result is the site-projected partial density of states shown in Figure III-5. This figure shows that SOC not only splits the peaks, but also pushes the bands toward the Fermi level in the CB, which reduces band-gaps.the presence of Bi-$6s^2$ states at the bottom of the VB,as well as the In-5s2 states are shown in the energy region from −6 to −5eV .

the Bi^{3+} lone pair $6s^2$ states and the In^{1+} lone pair $5s^2$ states interact strongly with p states of anion (Cl 3p and Br 4p), giving rise to (Bi 6s – Xp) bonding states and (In-5s – Xp) bonding states at the low-energy set of valence bands for all perovskites .as well as antibonding (Bi 6s – Xp)* states appear at energy of -4 to -2 Ev hybridized with unoccupied In-5p states and antibonding (In-5s – Xp)* states further hybridized with unoccupied Bi-6p states at the top of the upper valence band.

Because of the higher energy of In- 5s orbital than that of antibanding Bi-6 s orbital. , resulting in asymmetric occupied bonding states, which tends to promote the $6s^2$ lone electron pair in Bi^{3+} and $5s^2$ lone electron pair in In^{+1} stereochemical activity.[37]

Where, sp hybridized orbitals generated in these materials that have stereochemical active lone pairs explaining the distorted structures (ferroelectric) of these non centrosymetric sites. we note that there a significant hybridization betwen the Bi-6p orbitals states and the

p states of halogens (Cl-3p, and Br- 4p states) located between-5eV and -3.9eV . The bottom of the CBM is dominated by the unoccupied 5p-In and 6p-Bi states, with a small contribution from the unoccupied p states of the halogens (Cl 3p, and Br 4pstates). Meanwhile, The top of the CB is mostly derived from The 4d states of Cs atom hybridized with In-5p orbital making a contribution to the formation of the frontier bands. Additionally, cross-gap mixing of cation (p) and anion (p) states is evident, which has been associated polar instability in halides doubles perovskites [38]. It is also clear from the PDOS that Substitution with a halogen causes a red shift of the X-p states in the CBM also the unoccupied In- 5p and unoccupied Bi- 6p states are shifted toward the Fermi level on going from Cl to Br is the main cause of band-gap reduction. Our results concerning the DOS and the contributions of different orbitals are consistent with previously reported work It has been established that in $A_2 M^{+} M^{3+} X$ VII6 doubles perovskites the VBM is composed of anti-bonding states between M^{+}/M^{3+} s orbitals and X VII - p orbitals, and the CBM is mainly dominated by M^{+}/M^{3+} p characters [39]. From the viewpoint of electronic and optoelectronic properties, the Cs2InBiX6, type (s2+s2) halide double perovskites with suitable bandgaps resembling those of MAPbI3 are promising for photovoltaic applications with high solar cell conversion efficiencies.

Both the VBM and the CBM have large band dispersion. This corresponds to quite small carrier effective masses and strongly delocalized band-edge wave-functions, which are good for carrier extraction.

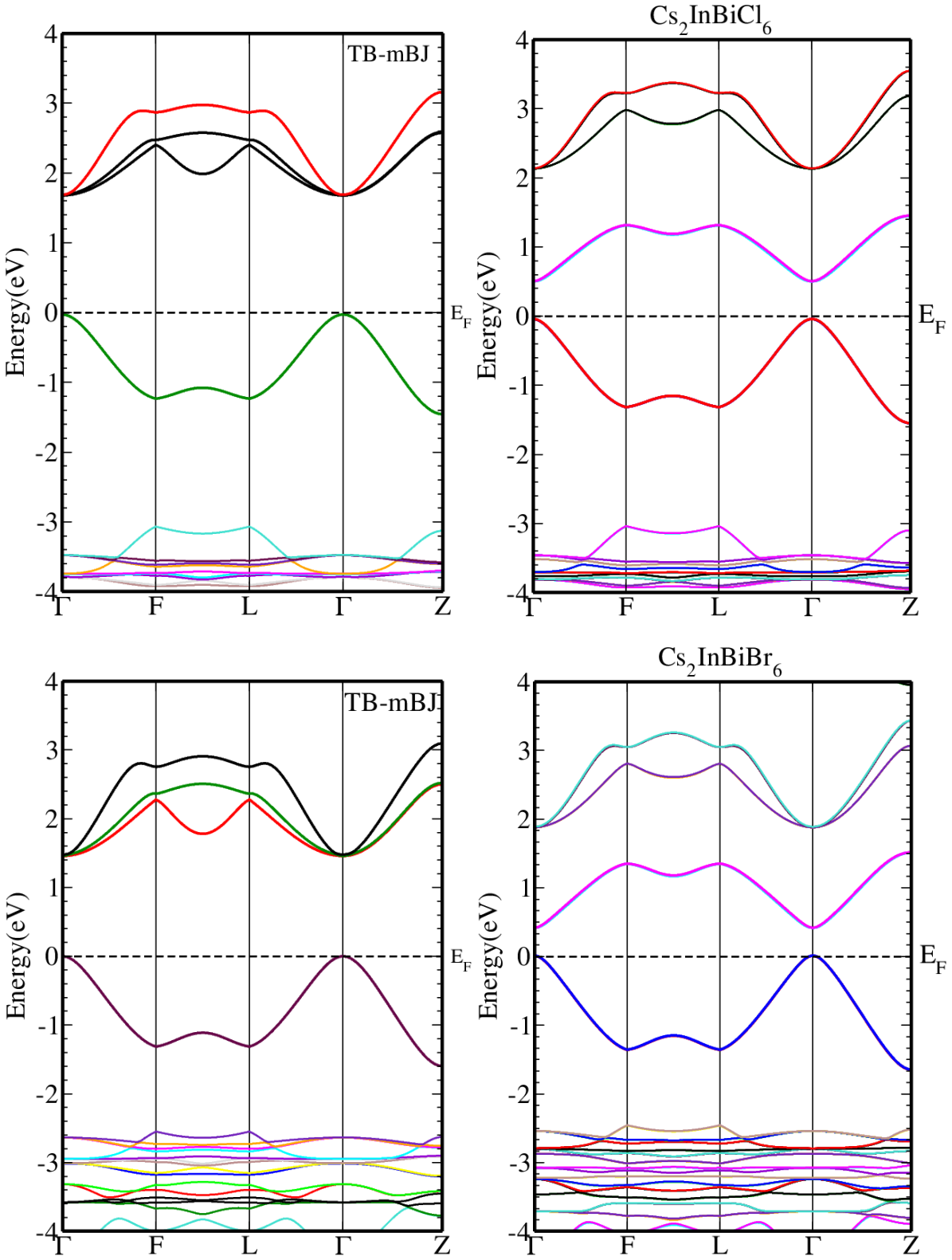

Figure III-5. The calculated band structures of Cs2InBiCl6, and Cs2InBiBr6 using TB-mBJ with and without SOC.

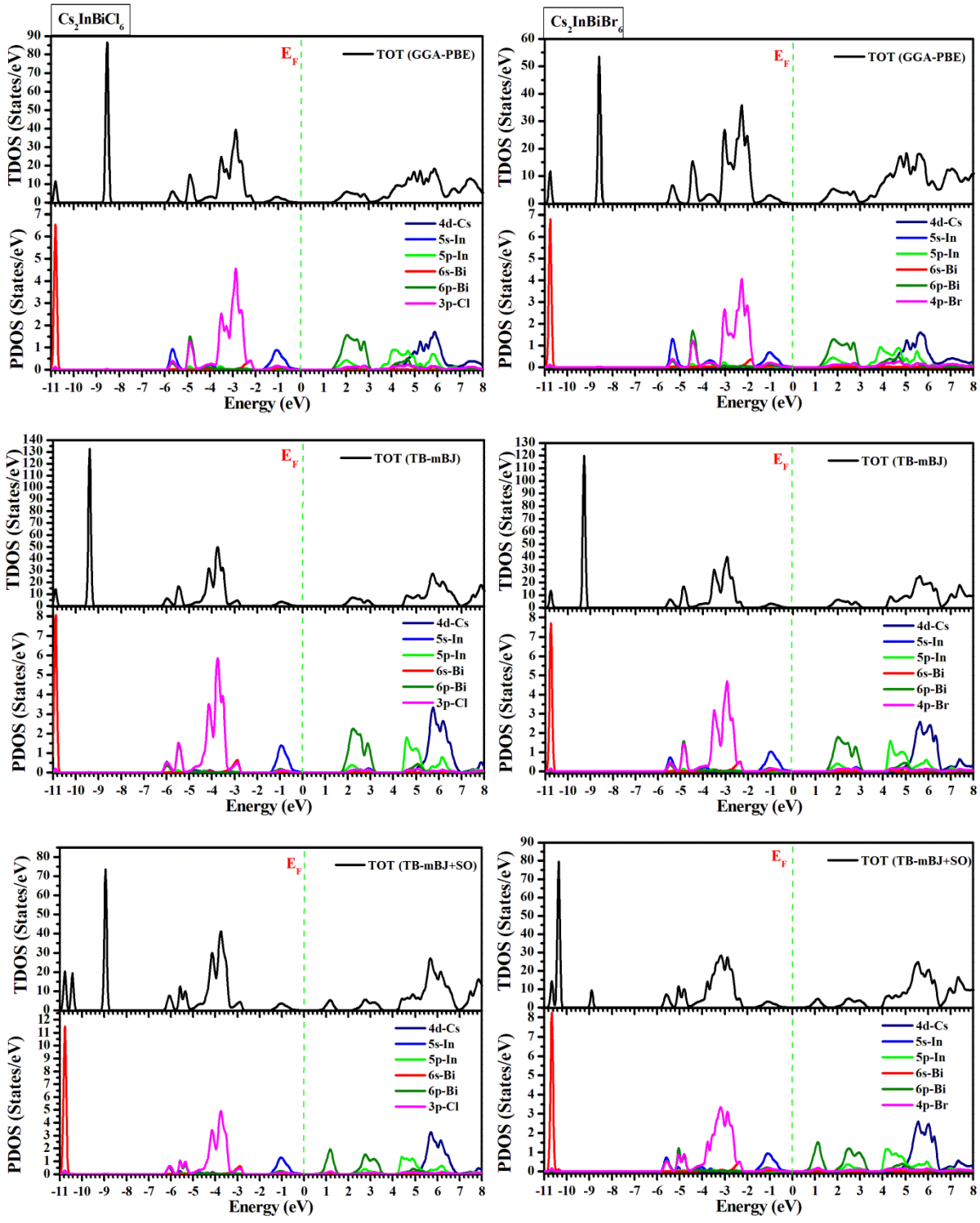

Figure III-6. Calculated total densities of states TDOS for *R*3*m* Cs2InBiX6, and partial densities of states PDOS within Tb-mBj with and without spin orbit coupling SOC.

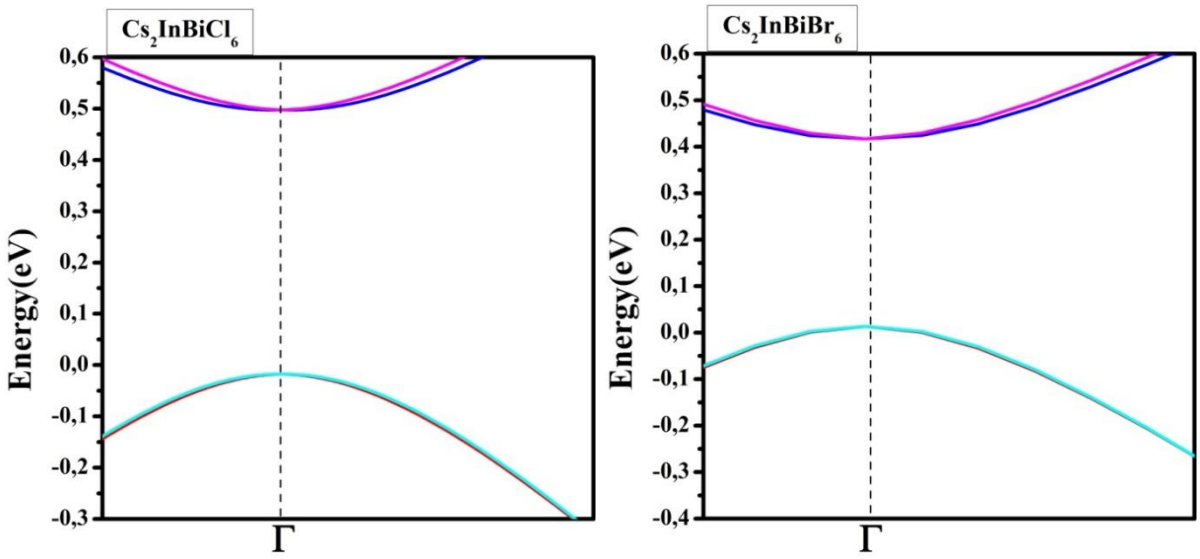

Figure III-7. Rashba spin splitting (with SOC) on the energy bands in $Cs_2InBiCl_6$ and $Cs_2InBiBr_6$.

III.3.3 Effective mass tensor :

On the basis of the computation and visualization of the curvature of the electronic bands of these compounds, effective masses tensors of charge carriers, m*, for the Cs2InBiX6 were determined. The effective masses of the electron (m*e) and the hole (m*h), calculated at the T-points wich correspond to the highest valence band and the lowest conduction band, respectively [30]. For all materials, Table 3 provides a summary of the calculated values for the diagonal components (non-diagonal are zero) of the effective mass tensor of electrons and holes as well as their average value, i.e., m* = (m*xx + m*yy + m*zz)/3.

According to the results in Table 3, we can see that the flow of charge-carriers is anisotropic. Also, as compared to the Cs2InBiBr6 structure, the Cs2InBiCl6 has much higher m* e(ii) and m* h(ii) values. Due to the clearly lower *m**(*zz*) in comparison to the *m** (*xx*) and *m** (*yy*) This is also the direction of the ferroelectric polarization of All Cs2InBiX6 (rhombohedral c-axis). the shift current flow is much stronger along the z-direction in all the compounds .It is known through investigations of the effective masses of charge carriers in commercial conventional semiconductor photovoltaics such as Si, CdTe, and GaAs that a good charge-carrier mobility is attained if the material shows m* = 0.5 m0, at least along one of the crystallographic orientations [40]. Therefore, the Cs_2InBiX_6 are closer to satisfy this

requirement. Thus, a smaller *m** would result in a larger mobility of electrons and holes.as well as longest diffusion lengths.

Table III-4. Calculated hole (m^*_h) and electron (m^*_e) effective masses (in units of electron mass rest, m_0) of the compound at **Γ** points of the Brillouin zone. $|m^*_h(ii)|$ and $m^*_e(ii)$ are the average values of the diagonal components of hole and electron effective mass tensor, i.e., $m^*ii = (m^*_{xx} + m^*_{yy} + m^*_{zz})/3$.

Compounds	m*e			m* e(ii)	m^*_h			|m*h(ii)|	Methods
	xx	yy	zz		xx	yy	zz		
Cs2InBiCl6	0.556	0.556	0.379	0.497	1.288	1.288	0.890	1.155	GGA-PBE
	0.670	0.670	0.463	0.601	0.200	0.200	0.199	0.199	TB-mBJ
	0.067	0.067	0.021	0.052	0.160	0.160	0.159	0.159	mBJ+SOC
Cs2InBiBr6	0.457	0.457	0.302	0.405	0.123	0.123	0.120	0.122	GGA-PBE
	0.572	0.572	0.378	0.507	0.154	0.154	0.153	0.102	TB-mBJ
	0.077	0.077	0.075	0.076	0.045	0.045	0.043	0.044	mBJ+SOC

III-3.4 Electron localization function ELF and Chemical bonding:

To investigate the chemical bonding character and the transfer of charge between atoms for Cs2InBiCl6 and Cs2InBiBr6 structures, we calculated Electron Localization Function (ELF) along the body diagonal plane using ELK code [41]. As illustrated in Fig. 1(b), the ELF takes the values in the range of 0 to $1e^{-}A^{\circ -3}$. It is evident from Figure. 5(b) that The ELF maps are the same for both these compounds .In fact, the ELF distribution shows a maximum value at the anion sites and minimum value at the In and Bi sites indicating the charge-transfer interaction from Bi/In to Cl/Br sites.

On the other hand, as The Cs atom has a completely spherical charge distribution, with no charge contours overlapping those of the Cl/Br atoms which lead to an ionic bond between the Cs atom and the Cl/Br atoms. as well as,The overlapping contours between In and X atoms reveal strong covalent bonds and correspond to InX6 octahedra. Also, the contours of Bi and X overlap with one another, again confirming covalent bonds and the formation of BiX6 octahedra.

Moreover, the ELF clearly depicts the lobes distribution around In/Bi cations in both materials which indicated of lone-pair s2 electrons. In fact, the conclusions arrived at on the basis of the ELF studies corroborates with those obtained from the DOS studies. Using the optimized crystal structure of all compounds, the short and long bond lengths among various ions along with bond angles have been calculated and are given in Table.3. It can be seen from the table that X-In-X and X-Bi-X angles are different while indicating that both materials having polar behavior along with the exhibition of ferroelectricity. It can also be seen from the table that Bi/In-X bond lengths are higher for Cs2InBiBr6 and are lesser for Cs2InBiCl6.

Table III-5. The bond length (Å) and bond angles (degree) of doubles perovskites.

Compounds	bond length(Å)	bond angles (degree)
$Cs_2InBiCl_6$	Cs1-Cl2(3)=3.968 Cs2-Cl1(3)=3.920 In1-Cl1(3)=2.982 In1-Cl2(3)=3.021 Bi1-Cl2(3)=2.728 Bi1-Cl1(3)=2.744	Cl-In-Cl=178.785 Cl-Bi-Cl=179.354
$Cs_2InBiBr_6$	Cs1-Br2(3)=4.167 Cs2-Br1(3)=4.114 In1-Br1(3)=3.129 In1-Br2(3)=3.181 Bi1-Br2(3)=2.855 Bi1-Br1(3)=2.874	Br1-In-Br1=179.044 Br-Bi-Br=179.613

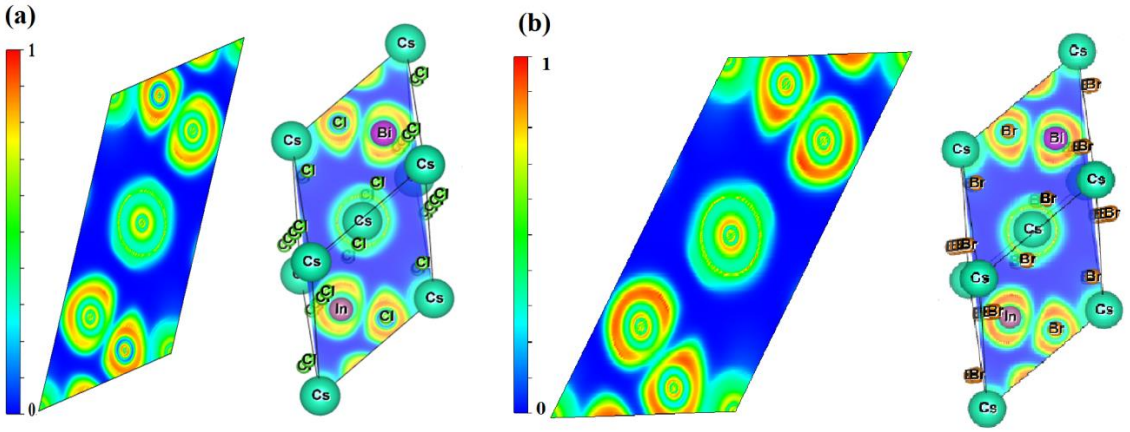

Figure III-8 : Electron localization function ELF for (a)$Cs_2InBiCl_6$ and (b) $Cs_2InBiBr_6$.

The Bader charge refers to the number of electrons that an atom gets or loses. The Bader charge value of each atom is the difference between the calculated number of electrons and the number of neutral electrons. Table III.6 lists the Bader charge values of the Cs2InBiCl6 and Cs2InBiBr6 compounds. It displays that the Bader charge of all atoms becomes smaller from Cl to Br. However, We find that the Bader charges of all atoms sum to zero in $Cs_2InBiCl_6$ and $Cs_2InBiBr_6$. In general, the Bader charge of Cs is close to the theoretical value of +1 in both materials, suggesting that Cs doesn't involve much in the covalent bonds. However, the Bader charge of In and Bi are smaller than the corresponding theoretical values of +1 and +3, respectively, indicating that the binding between theme and X exists covalent bonding. Which illustrates that In and Bi network are an electron donor.

Table III-6 The Bader charge distribution of the Cs_2InBiX_6 compounds.

Compounds	Cs	In	Bi	X
Cs2InBiCl6	+0.9078	+0.8164	+1.6067	Cl -0.7057
Cs2InBiBr6	+0.8984	+0.7271	+1.3778	Br -0.6493

III-3.5 Binding energies of the excitons :

The exciton binding energy (Eb) in semiconductor materials assesses the capacity of the electron-hole pair to dissociate when photon absorption raises electrons from the VB to the CB. Higher (Eb) levels, on the other hand, result in the material's Jsc and PCE. In order to calculate the exciton binding energies of Cs2InBiX6 (X = Cl, Br), we used the Wannier-Mott model[42]. employing the formula :

$$E_b \approx 13.56 \frac{1}{m_e} \frac{\mu}{\varepsilon_1(0)^2} \quad (2)$$

where μ = ($m^*e \times m^*h$) /(m^*e+m^*h) is the exciton effective mass, m^*e and m^*h are the average effective masses of the electron and hole, me is electron mass in rest, and $\varepsilon 1(0)$ is the average values $\varepsilon 1(0) = (\varepsilon xx(0) + \varepsilon yy(0) + \varepsilon zz(0))/3$ of static dielectric constant. Using the obtained effective mass values and the static dielectric function, the predicted exciton binding energies for Cs2InBiCl6 are 142.69 meV (246.05meV, 71.44meV) with GGA-PBE(TB-mBJ, mBJ+SOC) respectively, then are76.44meV(156.32meV,34.05meV)for Cs2InBiBr6, Compared to MAPbI3 (25 meV) and CsPbBr3(33 meV), the exciton binding energies of Cs2InBiX6 (X = Cl, Br) are significantly higher[43].

III-3.6 The spin texture

As many physical properties are strongly determined by the band structures, manipulation of the band structures by spin rotation is expected to significantly change the physical properties, leading to many novel magneto-phenomena. To demonstrate the properties of the spin splitting, we investigate the k-space spin textures in Γ point. In this case, the spin textures were calculated at the valence band maximum (VBM) and at the conduction band minimum (CBM) .The Yellow ,purple, and blue lines show the bands with different spin polarizations due to SOC. (b) Spin-texture (forin-plane spin components).Thus, the carrier spin polarization at the VBM can be effectively controlled by the FE polarization, which can in turn be controlled by external electric fields. This would be useful for spintronic applications. Cs2InBiX6 has two heaviest non-metallic elements (In, Bi), hence it has pronounced spin-orbit coupling (SOC) strength, which would be important for the electronic properties, especially when the centrosymmetry is broken. It is particularly interesting to observe that upon the FE

phase, there is large spin splitting between the highest valence bands VBM1 and VBM2 (CBM1 and CBM2). Based on symmetry analysis, there are two inequivalent valleys for the hole(electrons) carriers, as indicated in Figure III- and Figure III- . The states near the VBM (CBM) are spin-polarized, and they show interesting spintextures due to the strong SOC effect. The spin-textures are also valley-dependent.

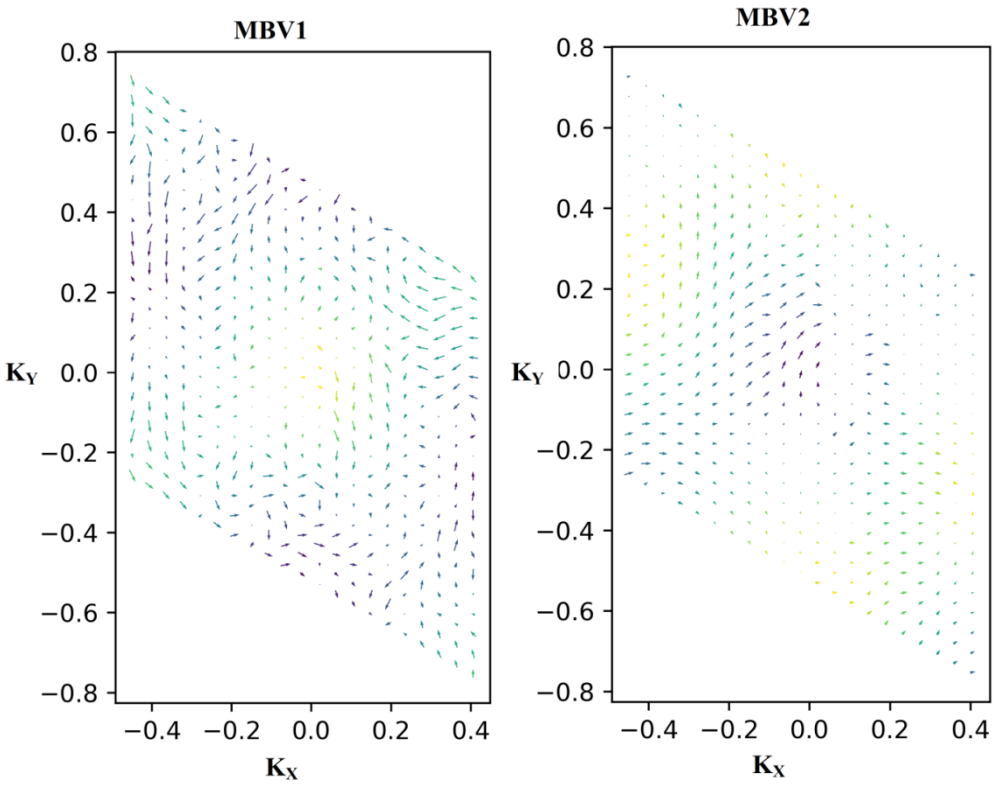

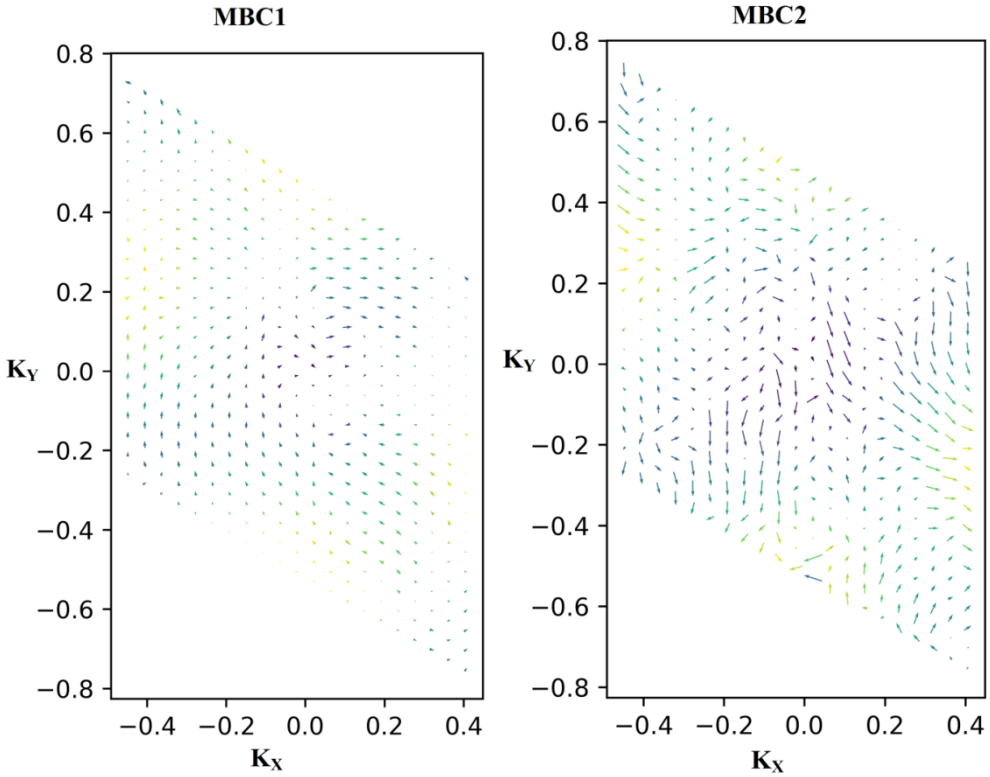

Figure III-9. 2D plot of the spin texture of $Cs_2InBiBr_6$

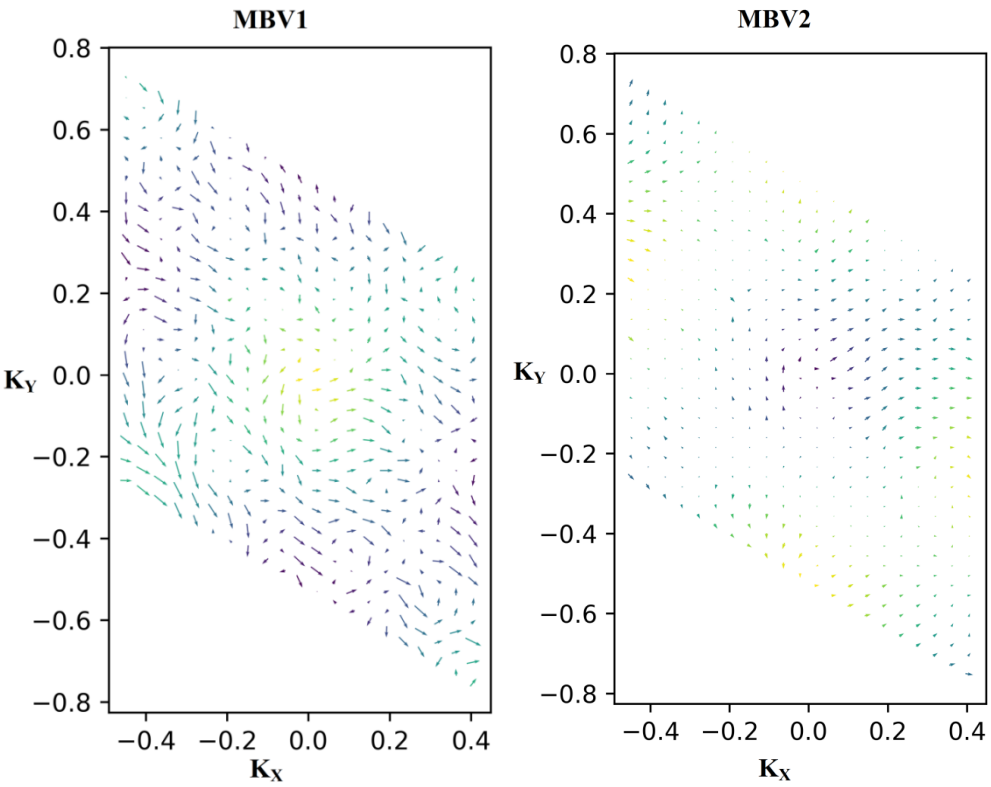

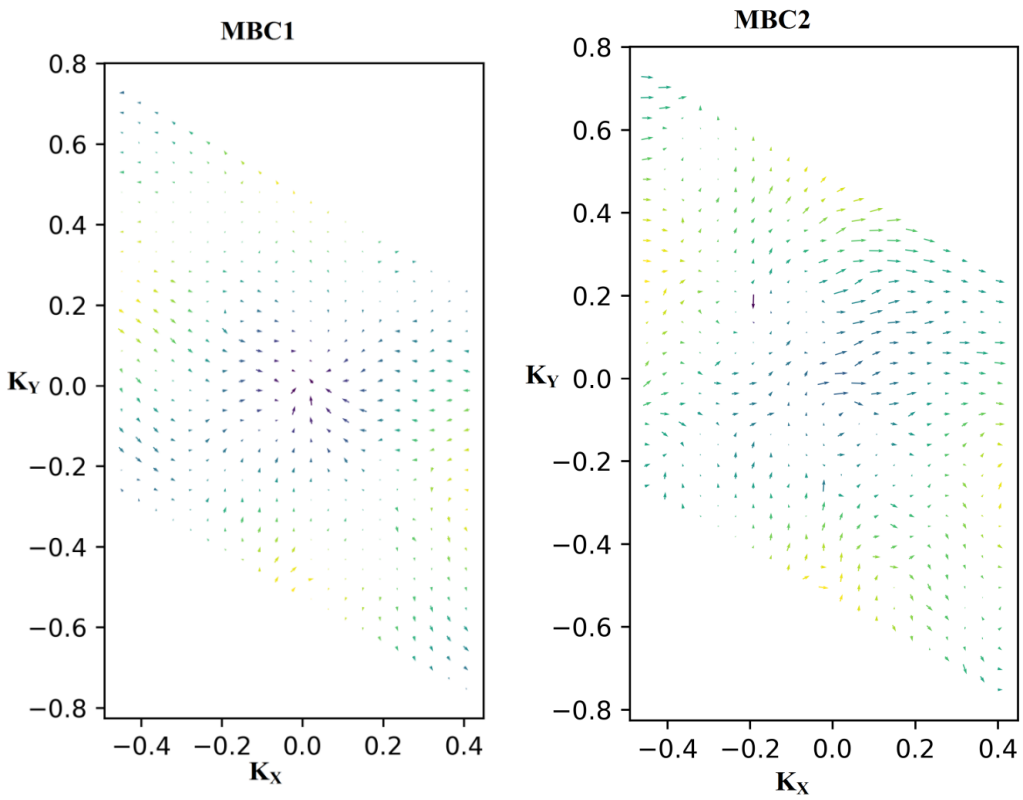

Figure III-10. 2D plot of the spin texture of $Cs_2InBiCl_6$

III-3.7 Optical properties

The internal structure and ability to produce polarization of a material is indicated by its optical properties. The compounds under investigation have potential for many technological applications and to provide more evidence for them as potential candidates for photovoltaic materials, because their band-gaps are less than lie in the infrared and visible regions of the optical spectrum. The frequency-dependent optical coefficients, such as the real part of dielectric functionε1(ω), the imaginary part of dielectric function ε2(ω), the reflectivity R(ω), the energy electron loss function (EELS) L(ω), the refractive index n(ω) and the optical conductivity $\boldsymbol{\sigma}(\omega)$, of these lead-free double-perovskites halides have been calculated. In general, the complex dielectric function described by $\varepsilon(w)=\varepsilon_1(w)+i\varepsilon_2(w)$, Where The real $\varepsilon_1(w)$ and imaginary parts $\varepsilon_2(w)$ of the dielectric function are related to each other by following the Kramers–Kronig relationships[44]:

$$\mathrm{Re}(\omega) = 1 + \frac{2}{\pi} \mathrm{p} \int \frac{\omega' \mathrm{Im}(\varepsilon(\omega))}{\omega' 2 - \omega^2} \mathrm{d}\omega \quad (3)$$

From these two components of dielectric function, various optical properties such as the refractive index n(ω) , extinction coefficient k(ω) ,and reflectivity R(ω) can be measured respectively by the equations given below [45]:

$$n(\omega) = \left[\frac{\varepsilon_1(\omega)}{2} + \frac{\sqrt{\varepsilon_1^2(\omega) + \varepsilon_2^2(\omega)}}{2} \right]^{1/2} \quad (4)$$

$$k(\omega) = \left[\frac{-\varepsilon_1(\omega)}{2} + \frac{\sqrt{\varepsilon_1^2(\omega) + \varepsilon_2^2(\omega)}}{2} \right]^{1/2} \quad (5)$$

$$R(\omega) = \frac{[n-1]^2 + k^2}{[n+1]^2 + k^2} \quad (6)$$

The absorption coefficient α(ω), the energy electron loss function (EELS) L(ω), and the optical conductivity $\boldsymbol{\sigma}(\omega)$ are given by the equations below, respectively.

$$\alpha(\omega) = \frac{2\omega}{c} k(\omega) \quad (7)$$

$$L(\omega) = Im\left[\frac{-1}{\varepsilon(\omega)} \right] \quad (8)$$

$$\sigma(\omega) = -i \frac{\omega}{4\pi} [\varepsilon(\omega) - 1] \quad (9)$$

Herein, We have calculated all the optical properties of these compounds versus incident photon energy (eV) by using GGA, and TB-mBJ with and without SOC (mbj+so), the results obtained are presented comparatively. The difference in the calculated results from the three methods is justified by the small shift between the band gap's values. The optical responses are measured along the two polarization directions xx = yy and (in plane and transverse), due to optically anisotropic nature of these compounds. since they are very close , we calculated an average for all optical parameters.

Table III-7. The average of zero-frequency values of the real part of dielectric function, refractive index, and first onset of the imaginary part of dielectric function.

Compounds	ε_1-ave (*0*)	$\varepsilon_2(\omega)$ onset	*n-ave* (*0*)	Maximum n-ave(ω)	R-ave (0) [%]	Maximum R-ave (ω) [%]	Methods
$Cs_2InBiCl_6$	3.38	1.35	1.85	2.35	(9.20)	(63.20)	GGA-PBE
	2.71	1.70	1.65	2.23	(5.80)	(36.20)	TB-mBJ
	1.97	0.54	1.39	1.67	(3.10)	(13.20	TB-mBJ +SO
$Cs_2InBiBr_6$	4.09	1.13	2.02	2.55	(11.4)	(71.60)	GGA-PBE
	3.20	1.46	1.78	2.38	(8.00)	(48.70)	TB-mBJ
	3.92	0.40	1.98	2.19	(10.30)	(72.40)	TB-mBJ +SO

The real part $\varepsilon 1(\omega)$ expresses the polarizability of a material and are plotted in Figure III-11. The calculated average zero-frequency limits (static dielectric constants) ε1-ave (0) for $Cs_2InBiCl_6$, and $Cs_2InBiBr_6$ are given in Table III-7. It can be seen that ε_1-ave(*0*) increases as the band-gap decreases on going from Cl to Br. Thus, there is inverse relation between the static dielectric constants $\varepsilon_1(0)$ and the band-gap energy (Eg) according to Penn's model [46].

$$\varepsilon_1(0) \approx 1 + (\bar{h}_{\omega_p}/E_g)^2 \quad (10)$$

Obviously, the maximum values of these compounds gradually increase as the anion changes from Cl to Br. Beyond these maxima, $\varepsilon_1(\omega)$ decreases with some variations, which attributed to the interband transitions of electrons. The negative values of $\varepsilon_{1\text{-ave}}(\omega)$ that appear in the real dielectric function $\varepsilon_{1\text{-ave}}(\omega)$ spectra for the Cs_2InBiX_6 compounds, show that incident photons are completely reflected from the materials, making them metallic [47]. Interestingly, The dielectric constant value is closer to that of a compound having an active

lone pair (TlBr: $\varepsilon_1(0)$= 5.64) than those with inactive 6s electrons like MgO ($\varepsilon_1(0)$ = 2.95).[48]

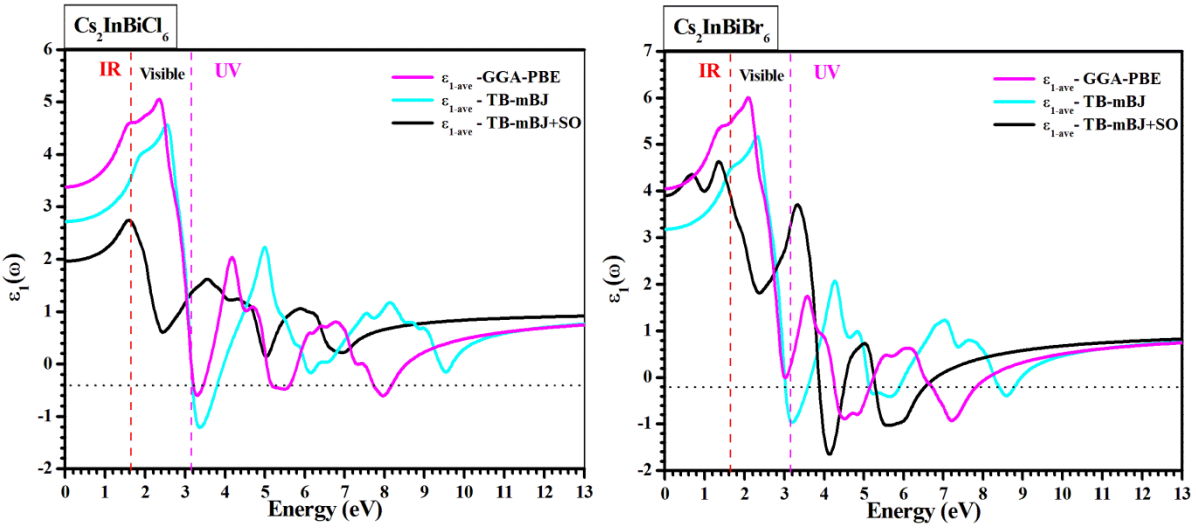

Figure III-11. The dependence of the The average real part $\varepsilon_1(\omega)$ of dielectric function of double perovskites on energy of incident photons.

The imaginary part $\varepsilon_2(\omega)$ is a seed parameter and can be directly calculated from Fermi's golden rule [49]. It is related to their behavior of light absorption and gives the optical band-gap. The *average* $\varepsilon_2(\omega)$ spectra of the all Cs_2InBiX_6 compounds versus incident photon energy are plotted in Figure III-12. We have analyzed of the interband transitions corresponding to the main peaks of $\varepsilon_2(\omega)$ for all the structures at all the energy region. It can be seen from the figure 3 that the nature of $\varepsilon_2(\omega)$ differ much from each to other due to the different halogens contained for all Cs_2InBiX_6 structures. The thresholds of light absorption shift to lower photon energy with decrease in bandgap values of the studied compounds. Projected density of states will predict states responsible for transitions corresponding to a particular peak in the spectra of $\varepsilon_2(\omega)$. Three remaining major spectral peaks are observed. The first peak in the visible-light range appear due to the electronic transition from 5s-In state of the valence band (VB) to the unoccupied a mixed states of 6p-Bi ,6p-In and p-(I,Br,Cl) in the conduction band (CB). However, The interband transitions between the p-states of the halogens (I ,Br,Cl) atoms of the valence band (VB) to the unoccupied 6p states of the Bi atoms in the conduction band (CB) and p-(I,Br,Cl) states to a mixed states of 5p-In and 6p-Bi states lead to a second and a third absorption peaks in the ultraviolet (UV) light range

respectively. The optical gaps were calculated from the first onset points of $\varepsilon_2(\omega)$ are the same in energy than the electronic direct band-gaps for these materials, suggesting that strong excitonic effects will be operative due to the interaction of electron–hole pairs upon absorption/excitation . The onset points $\varepsilon_2(0)$ of $Cs_2InBiCl_6$, and $Cs_2InBiBr_6$ are listed in Table III.7. Also, the optical band gaps behavior of these compounds is near the optical band gap MApbI3 (1.52 eV) and MAPbBr3 (1.9 and 2.4 eV) [50]. From the dielectric constants ($\varepsilon_1(\omega)$ and $\varepsilon_2(\omega)$), it is clear that our studied materials Cs_2InBiX_6 have a strong absorption edge in the infrared regions, the visible and the ultraviolet region of the solar spectrum .

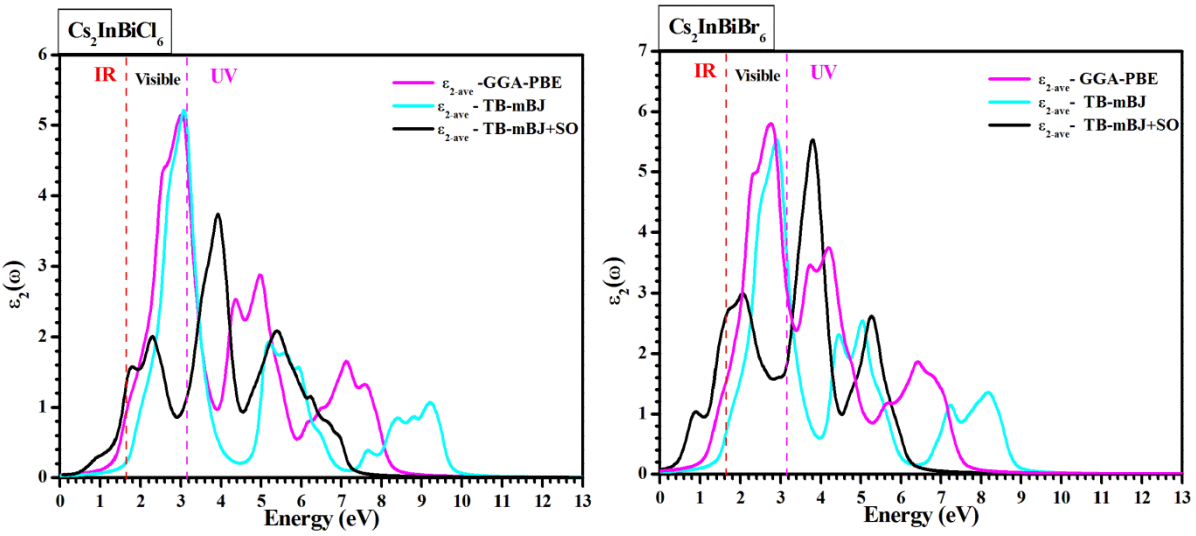

Figure III-12. The dependence of the average imaginary part $\varepsilon 2(\omega)$ of dielectric function of double perovskites on energy of incident photons.

Knowledge of refractive index $\mathrm{n}(\omega)$ and extinction coefficient $\mathrm{k}(\omega)$ are necessary to use materials in photonic and optical devices because they used to measure the phase velocity and attenuation level of electromagnetic waves passing through the given materials, respectively [51]. The calculated average refractive indices and average extinction coefficient $n(\omega)$ for Cs_2InBiX_6 are displayed in Figure III-13.

Also, It can be seen that the refractive index at zero frequency $n(0)$ for Cs_2InBiX_6 increases on going from Cl to Br due to the decreasing band-gap energy, which confirmed that refractive index has an inverse relationship with band-gap. The average static values of refractive index $n(0)$ are listed in Table III.7 , which can also be obtained according to the equation :

$$n(0) = \sqrt{\varepsilon_1(0)} \quad (11)$$

Beyond $n(0)$, the plots closely follow $\varepsilon_1(\omega)$. As the photon energy increases, the n(ω) of the corresponding compound Cs_2InBiX_6 gradually reach their first peaks with the highest values. Since photons are delayed when they penetrate a substance due to interactions with electrons, the refractive index is greater than one and exhibits decreasing tendency for higher photon energy values. The refractive index of Cs_2InBiX_6 are slightly different to that of CsPbI3 (3.7) [52], and much higher than that of diamond [53]. However, these materials become opaque when the refractive indices drop below unity.

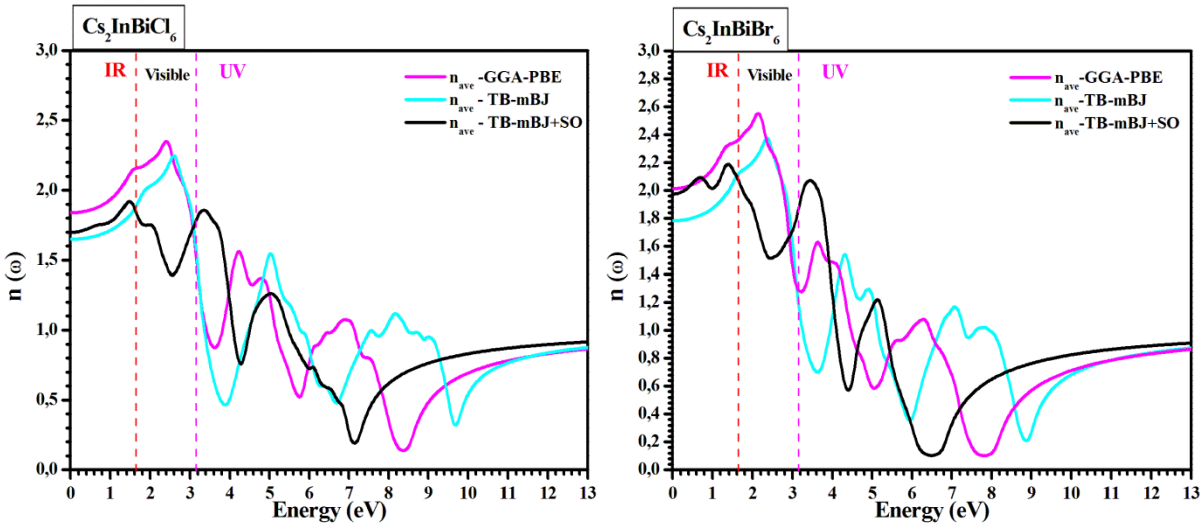

Figure III-13. The dependence of the average refractive index n(ω) of double perovskites on energy of incident photons.

The extinction coefficient $k(\omega)$ shows similar behavior as optical conductivity σ (ω) and imaginary part of dielectric function $\varepsilon_2(\omega)$. The maximum values for extinction coefficient k(ω) of $Cs_2InBiCl_6$ are 1.518 (1.608, 1.263) and The maximum k(ω) of $Cs_2InBiBr_6$ are 1.522 (1.605, 1.702) with GGA (mBj, mBj+SO) respectively(see Table III.7).

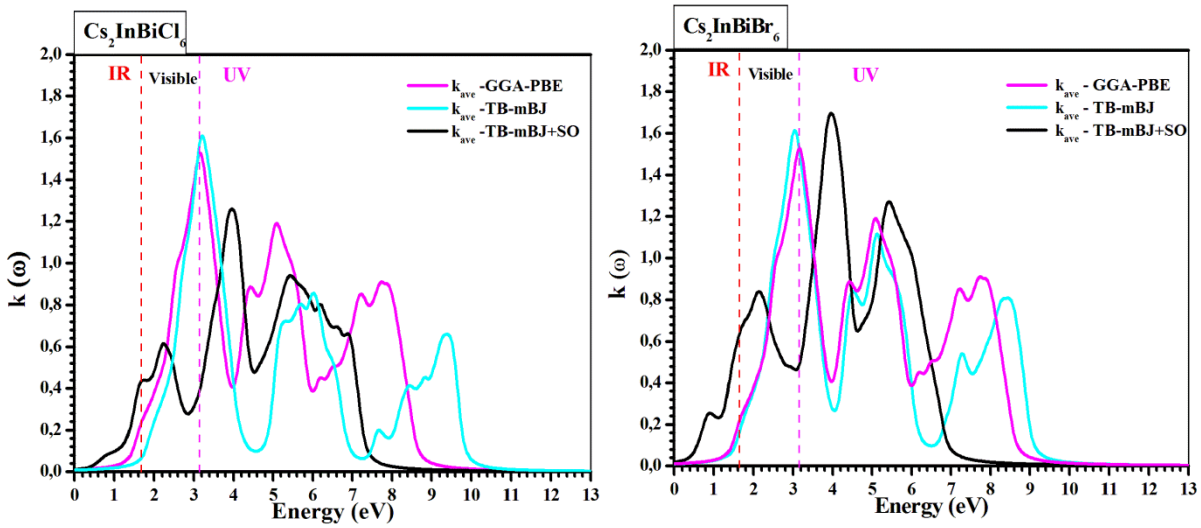

Figure III-14. The dependence of the average extinction coefficient *k*(ω) of double perovskites on energy of incident photons.

Energy loss function *L*(*ω*) is another useful tool in the realm of optical properties, which correlates the numerical value of the observed band-gap with the Plasmon loss value [54]. It provides insight into the interactions of the incident photons and explains various features of a semiconductor like values of the band-gap as well as static dielectric function can be measured using *L*(*ω*) [55]. The calculated average L(*ω*) for Cs_2InBiX_6 are plotted in Figure III.15 , in which no scattering is evident when photon energy is less than the band-gap energy. The peaks appearing in the L_{ave} (*ω*) curves show Plasmon losses, which correspond to a collective oscillation of the valence electrons, and their frequency, are referred to as the plasma frequency.

Concerning the optical reflectivity R(ω) as shown in Figure III.16 , The average static values of reflectivity R(0) for all compounds studies are listed in table III-7. It is observed that the R-ave(0) of these compounds increase with increasing atomic numbers of X-site anions. However, $Cs_2InBiBr_6$ maintains a higher values of reflectivity R_{ave}(ω) than $Cs_2InBiCl_6$, occur in the ultraviolet spectrum.

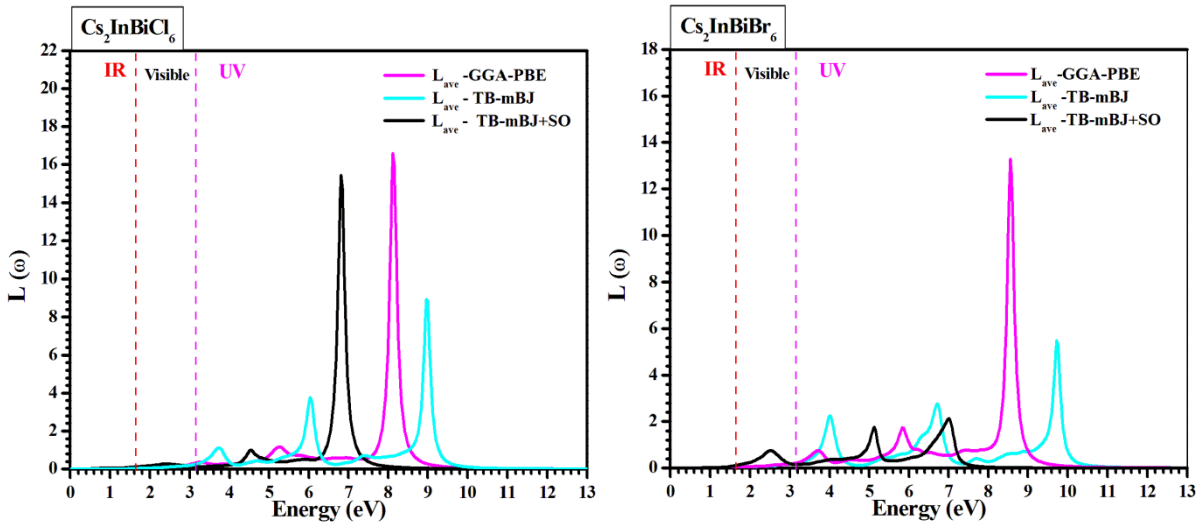

Figure III-15. The dependence of the Energy loss function *L* (*ω*) of double perovskites on energy of incident photons.

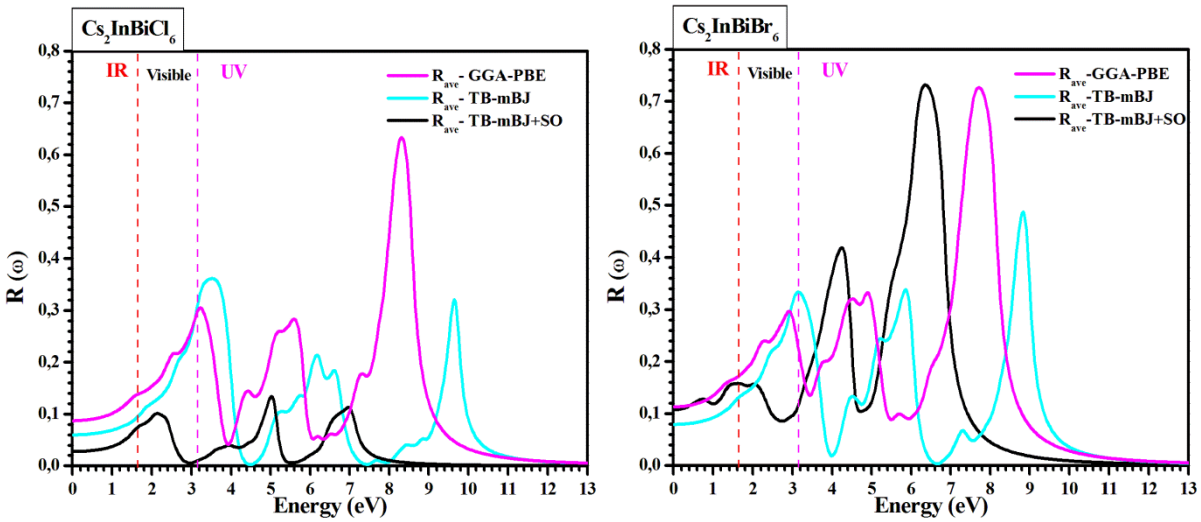

Figure III-16. The dependence of the reflectivity *R*(*ω*) of double perovskites on energy of incident photons.

To assess the optical performance, we have calculated the absorption coefficients for the all crystals. Since the absorption coefficient and imaginary part of dielectric constant are intimately connected we can observe similar features. As illustrated in, the Cs_2InBiX_6 crystals shows exceptional light harvesting ability and can cover a wide solar spectrum, which is consistent with the s^2 lone pair feature. By combining optical absorption spectra results, for two existing candidate perovskites, It can be deduced, that the absorption coefficient of $Cs_2InBiCl_6$ is slightly greater than that of $Cs_2InBiBr_6$ in visible range, indicating strong excitonic effects in many wavelengths, which enhances the absorption coefficients.

Moreover, by taking into account of the spin-orbit coupling (SOC) effect, with the TB-mBj functional, we found that a red shift of the absorption coefficients is attained, thus leading to the expansion of the absorption range from the near-infrared (NIR) spectrum frequency to the ultraviolet (UV) frequency ,owing to the overall corresponding to narrowing of of band gaps .

Table III-8. Calculated optical constants for Cs2InBiCl6 and Cs2InBiBr6: absorption coefficient α(ω); extinction coefficient $k(\omega)$; optical conductivity σ(ω).

Compounds	Maximum α-$_{ave}$ (ω) ($10^4 cm^{-1}$)	Maximum k-$_{ave}$(ω)	Maximum σ-$_{ave}$(ω) (Ω-1cm-1)	Methods
Cs2InBiCl6	71.926	1.499	2141.510	GGA-PBE
	63.402	1.589	2169.135	TB-mBJ
	51.779	1.255	1938.979	mBj+SO
Cs2InBiBr6	77.810	1.515	2161.699	GGA-PBE
	70.138	1.598	2184.715	TB-mBJ
	69.755	1.688	2817.645	mBj+SO

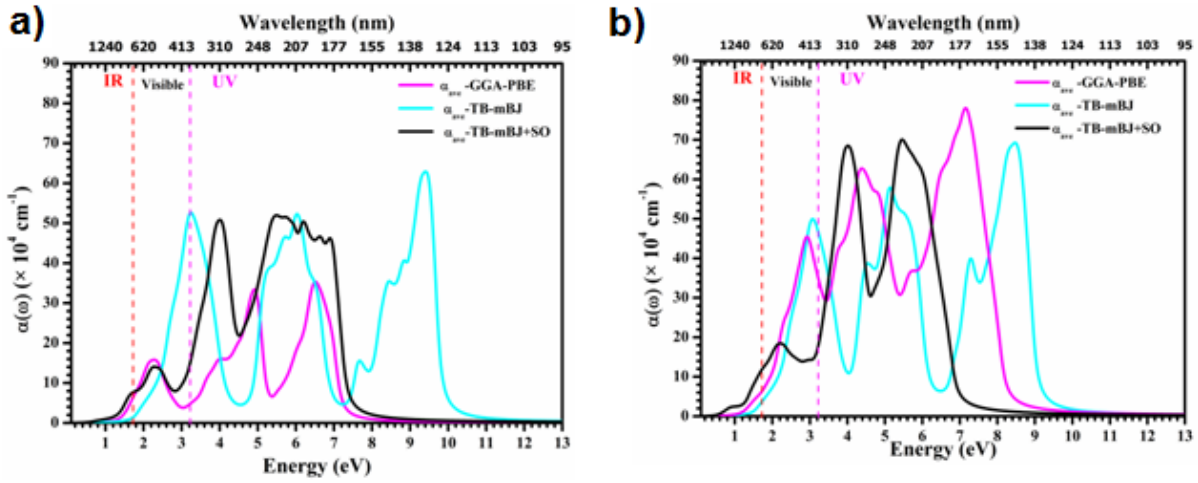

Figure III-17. The dependence of the absorption α (*ω*) of (a) Cs2InBiCl6 and (b) Cs2InBiBr6 on energy of incident photons.

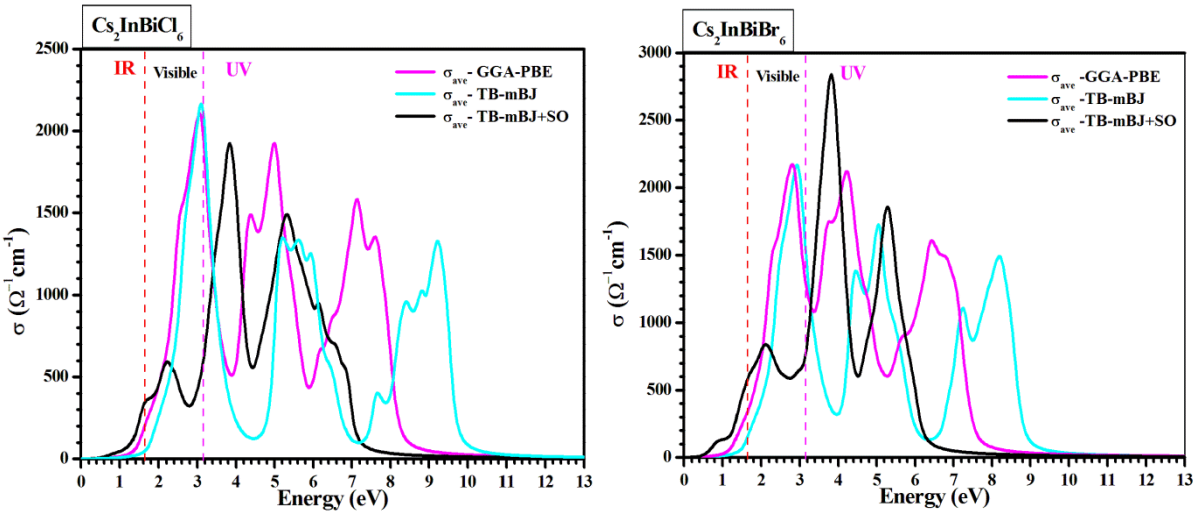

Figure III-18. The dependence of the optical conductivity σ(*ω*) of double perovskites on energy of incident photons.

The curves of average optical conductivity σ(w) of the Cs2InBiX6 compounds are plotted in Figure-III.18. to investigate their optical response, which corresponds to the conduction of electrons in the compounds [56]. Where one can see as the absorption coefficient, the optical conductivity also starts with energy equal to the band gaps. It can be found that $Cs_2InBiCl_6$ shows the largest $\sigma\text{-}_{ave}(\omega)$ value among the studied compounds in visible light. Therefore, This outstanding optical performance affirms that these halides perovskites are especially promising materials for realizing high efficient photovoltaic solar cells.

III-3.8 Photovoltaic (PV) Characteristics:

To analyze the photovoltaic efficiency of a material employed as an absorber layer in a solar cell, the "spectroscopic limited maximum efficiency (SLME)" approach can be employed as reported Liping Yu and Alex Zungere al. [57]. SLME simulation model evaluates solar cell power conversion efficiency based on the extended Shockley-Queisser model.

$$SLME, \eta = \frac{maximum\ output\ power\ density\ (P_{max})}{total\ incident\ solar\ density\ (P_{in})} \quad (12)$$

The value of *Pmax* is computed with the help of voltage – current (V – I) characteristics of solar cell in SLME analysis.

$$P_{max} = max\left\{J - J_0 exp\left[\frac{eV}{KT} - 1\right]\right\} \quad (13)$$

where *JSC*,J0*, e, V, k, T* represents short circuit current density, reverse saturation current, the electronic charge, potential over the absorber layer, Boltzmann's constant, and device temperature, respectively. where *JSC*, *J*0*, e, V, k, T* represents short circuit current density, reverse saturation current, the electronic charge, potential over the absorber layer, Boltzmann's constant, and device temperature, respectively. *ISC* and *I*0 can be calculated using the absorptivity of the material [61]. The input parameters for evaluating the SLME analysis are the computed absorption spectra using DFT, global solar spectra (AM-1.5G), fundamental, and direct allowable band gap (Eg) of the photovoltaic material.[58].

hence, we have carried out the Photovoltaic Characteristics for both the materials as a function of different thicknesses up to 100 µm at fixed temperature (293.15 K), using GGA-PBE ,TB-mBJ , and TB-mBJ+SO approximations. It can be noticed that The thickness of each layer and the band gap have significant effect on PV performance. A comparison of the obtained photovoltaic parameters is shown in **Table III-9** .

Table III-9 : A comparative table listing on Solar cell parameters of Cs2InBiCl6 and Cs2InBiBr6 at *T* = 293.15 K. Here *J-V* and *P–V* parameters of perovskites are calculated at *L* = 50 µm thickness. by different exchange correlation potentials.

Compounds	Approximation	PCE η (%)	JSC (mA/cm2)	V_{OC}(V)	FF
Cs2InBiCl6	GGA-PBE	29.09	40.43	1.10	0.87
	TB-mBJ	26.24	27.44	1.42	0,91
	TB-mB+SOC	14.74	53.30	0.48	0,77
Cs2InBiBr6	GGA-PBE	28.12	49.29	0.88	0,86
	TB-mBJ	28.33	35.95	1.18	0,89
	TB-mBJ+SOC	10.08	81.58	0.24	0,67

Here, current-voltage (I–V) performance were measured To understand the current sensitivity of Cs2InBiX6, we have examined the I-V characteristics, The I-V characteristic of both compounds are depicted in Figure.III-19. It is seen that, the current I is constant from (0 v) voltage to a specific voltages. Then, it starts to decline significantly with increasing the applied voltages until it becomes zero.

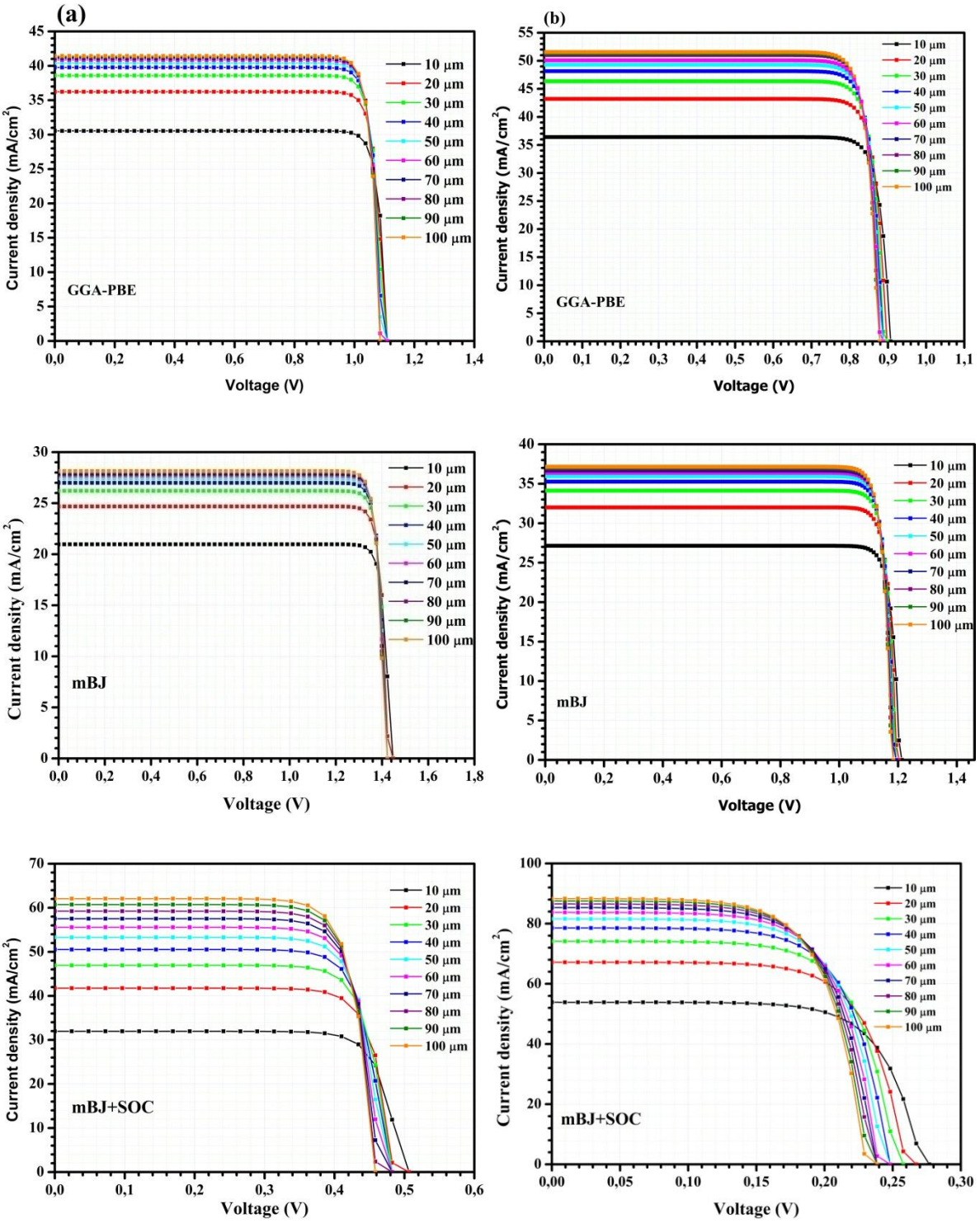

Figure III-19. Photocurrent density as a function of the forward bias voltage for (a) Cs2InBiCl6 and (b) Cs2InBiBr6.

On the other hand, Figure 4 shows that, the open-circuit voltage (VOC) and Fill factor (FF) are not strongly dependent on film thickness. However, short circuit photocurrent density (J_{SC}) is

more significantly influenced by changing the film thickness. The JSC of the absorber materials increases as the film thickness increases and further tends to saturate after a specific thickness.

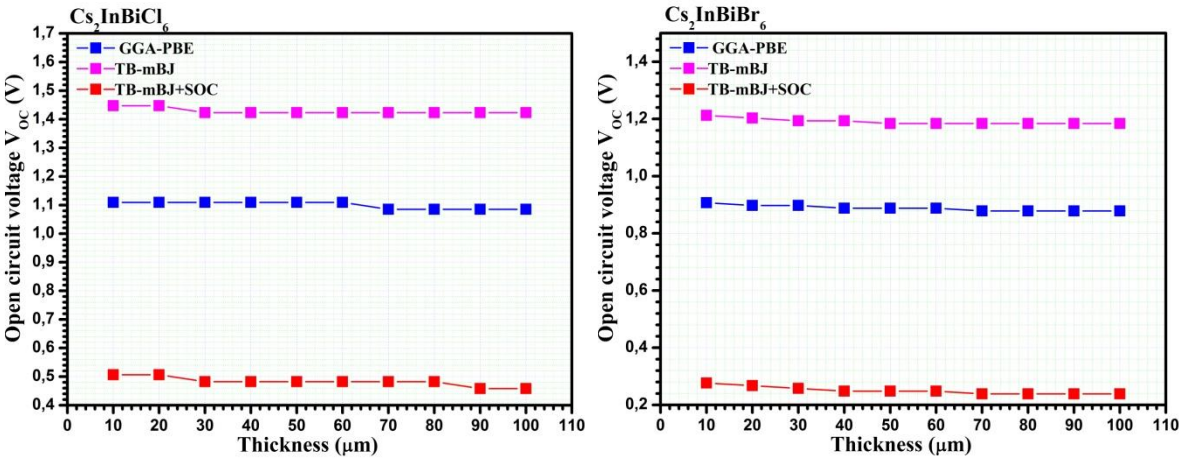

Figure III-20. The Open circuit voltage V_{oc} as function of thickness for $Cs_2InBiCl_6$ and $Cs_2InBiBr_6$.

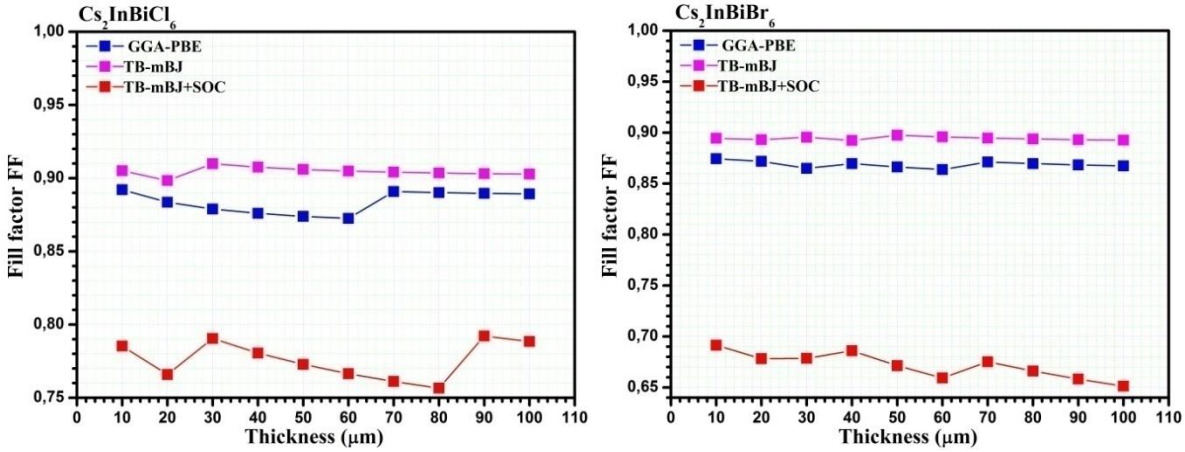

Figure III-21. The Fill factor FF as function of thickness for Cs2InBiCl6 and Cs2InBiBr6.

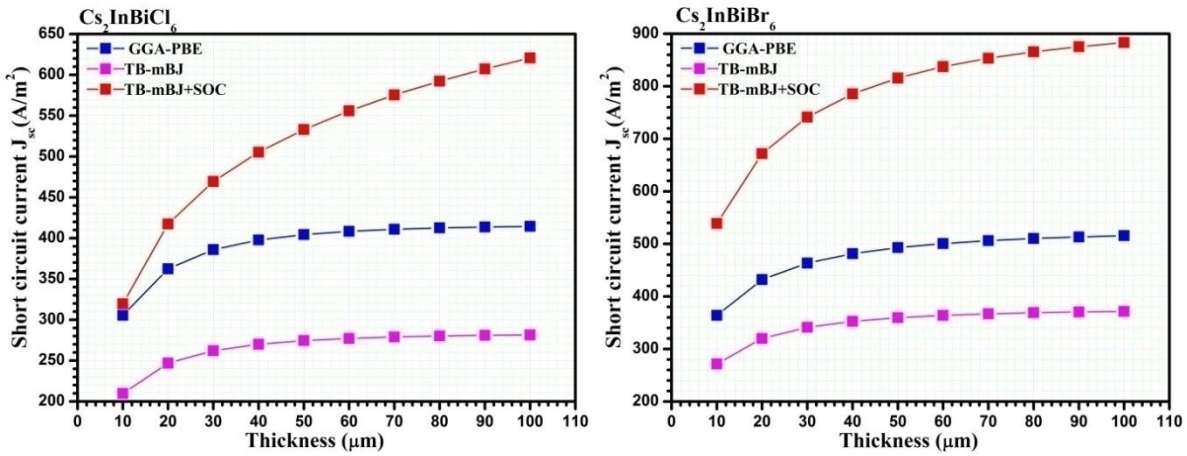

figure III-22. The short circuit photo-current density as function of thickness for Cs2InBiCl6 and Cs2InBiBr6.

After inserting these obtained values, we have computed SLME efficiency of double perovskite Cs_2InBiX_6 at various thickness ranges, as shown in Figure.III.23 .It can be observed that SLME of a compound mainly depends on the energy gap as well as thickness of the material. SLME progressively increases with the thickness of the material for the examined Cs2InBiX6 and becomes slightly constant after 50 µm for all compounds. as the evaluation of their photovoltaic performance. One clearly sees that the SLMEs of Cs2InBiCl6 and Cs2InBiBr6 are comparable to that of $CH_3NH_3PbI_3$ (29%) [59] and of CsPbI3 (30.41%) and even higher than $CsPbBr_3$ (24.53%) [60]. which indicates that incident photons are strongly absorbed by Cs_2InBiX_6 photoactive materials. It can be noticed from Table.III.10 that *Voc* and *FF* calculated using TB-mBJ are higher compared to that calculated using GGA-PBE and mBJ+SO methods for both $Cs_2InBiCl_6$ and $Cs_2InBiBr_6$. Also, SLME efficiency predicted of $Cs_2InBiCl_6$ and $Cs_2InBiBr_6$ at energy gap between 1.1ev and 1.4 ev are the highest.

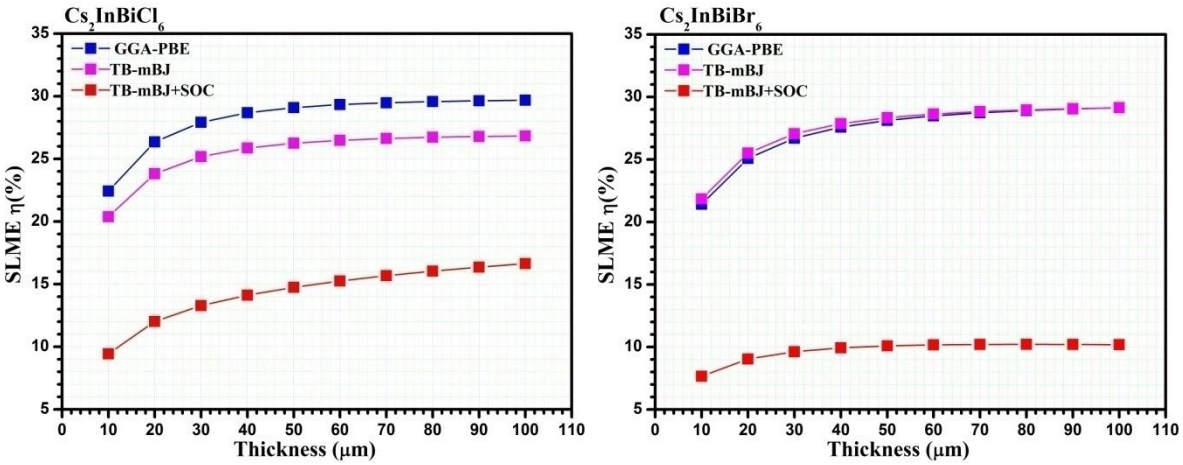

Figure III-23. Calculated efficiency through SLME versus thickness.

III-3.9. Spontaneous polarization

The spontaneous polarization is important for understanding the ferroelectric behavior in materials since they describe its polar ground state and lattice dynamical.

In this study, the calculation of the spontaneous polarizations is carried out by using the modern theory of polarization using Berrypy code . In ferroelectric materials, the total polarization P is the sum of the ionic polarization P_{ion} and the electronic polarization P_{ele}. First, we give the spontaneous polarization of Cs_2InBiX_6 along the x, y and z axes. Because the values of Px and Py are nearly zero, the spontaneous polarization is mainly along the z-axis. The result provides clear evidence of the ferroelectric switching phase of stadies materials belongs to the polar R3m space group by reason of a robust spontaneous polarization of 0.398c/m^2 and –0.404c/m^2 for $Cs_2InBiCl_6$ and $Cs_2InBiBr_6$, respectively. These values are comparable to those of reported devices such as ferroelectric oxide BaTiO3(0.28 C/m^2) [61] , Nevertheless slightly smaller than $LiNbO^3$ (0.75C/m2) [62], Rochelle's salt (20C/m^2), and ammonium sulfate (25C/m^2) [63],$(CH_3)_3NH]_3(MnBr_3)(MnBr_4)$ (45C/m^2)[64], and those of recently reported 2D halide double perovskite ferroelectric (n-propylammonium)$_2$$CsAgBiBr_7$ (150 C/m^2) [65].

III-3.10. Linear bulk photovoltaic effect

The linear photogalvanic effect or called the shift current mechanisms is the dominant DC-current response in the bulk photovoltaic effect (BPVE), which is allows incident photons to induce a photocurrent density term DC independent of time in the materials with lack of inversion symmetry [66]. In contrast to a conventional drift photocurrent under an electric field, the shift current originates from the charge center shifts in real space due to difference in the Berry connection between the valence and conduction bands involved in the optical excitation process [67]. We used the perturbation theory[68]: The shift current tensor is given as

$$\sigma_{\alpha\beta}^{\gamma} = \frac{|e|^3}{8\pi^2\omega^2} Re\left\{\emptyset_{\alpha\beta} \sum_{\Omega=\pm\omega} \sum_{l,m,n} \int_{BZ} dK(f_l - f_n) \times \frac{\langle Kn|\widehat{\vartheta_\alpha}|Kl\rangle\langle Kl|\widehat{\vartheta_\beta}|Km\rangle\langle Km|\widehat{\vartheta_{\gamma\alpha}}|Kn\rangle}{(E_{Kn}-E_{Km}-i\delta)(E_{Kn}-E_{Kl}+\bar{h}\Omega-i\delta)}\right\} \quad (14)$$

the shift current response $\sigma_{\alpha\beta}^{\gamma}$ ($\alpha;\beta;\gamma$ = x; y; z) is a third rank tensor representing the photocurrent J_γ generated by an electrical field via :

$$J_\gamma = \sigma_{\alpha\beta}^{\gamma} \varepsilon_\alpha^* \varepsilon_\beta \quad (15)$$

in which $\emptyset_{\alpha\beta}$ is the phase difference between the driving field ε_α and ε_β [69].

To see the spectral distribution of the shift current tensor elements, the Wannier interpolation method was used within the Wannier90 code[70] ,a tight binding model was obtained by maximally projected Wannier functions (WFs) ,for the Cs-4d ; Bi-6s,6p ;In-5s,5p ;Cl-3p and Br-4p orbitals in the energy range of -5.0 eV to 5.0 eV. using the Perdew-Burke-Ernzerhof (PBE) implementation of the GGA functional, an empirical Tran-Blaha modified Becke-Johnson (TB-mBJ)potential methods with and without SOC using a k-mesh with 100_100_100 subdivisions. Both materials belong to the 3m point group in the ferroelectric phase. Therefore, the shift current tensor is represented in two-dimensional matrix form as

$$\sigma = \begin{bmatrix} 0 & 0 & 0 & 0 & \sigma_{xxZ} & \sigma_{xxY} \\ \sigma_{yxX} & \sigma_{yyY} & 0 & \sigma_{yyZ} & 0 & 0 \\ \sigma_{zxX} & \sigma_{zyY} & \sigma_{zzZ} & 0 & 0 & 0 \end{bmatrix} \quad (16)$$

Such that, there are four nonzero elements: *xxY* = *yxX*=-*yyY*, *xxZ* = *yyZ* , and *zxX* = *zyY* components [71], where, the double small letters represent light polarization and the capital letter indicates the direction of the shift current response. Because The shift current response *σzzZ* for both materials is the dominant current to incident light polarization parallel to the direction zz of ferroelectric distortion among all the tensor components. Therefore, we have plotted just *σzzZ* curves using PBE, TB-mbj with and without SOC.

Figure III-23 presents the shift current spectra of $Cs_2InBiCl_6$ and $Cs_2InBiBr_6$. Both the two materials show broadly similar behavior, the zero-bias photocurrent starts from an photon energy slightly equal to the bandgaps. While, above the bandgaps, the spectra gradually increases across a wide photon energy excitation range from the near-infrared to ultraviolet region. Perhaps because the dissociation of the charge-transfer excitons is accelerated.

Moreover, they have a large shift current response in the visible spectrum range due to the large real space charge center shift between the upper valance band electrons, which contributes mainly from 5s-In states to the unoccupied a mixed states of 6p-Bi ,6p-In and p-(Br,Cl) in the lower conduction band. By extension, this peak of shift current response is highly desired for efficient solar conversion.

Furthermore, our calculations demonstrate that the spin-orbit coupling (SOC) can strongly influences their shift current responses. Being, when SOC is included an angular momentum dependent term is added to the Hamiltonian as well as each Bloch state has spinor form and the current response becomes a sum over spinor components. Interestingly, the Cs2InBiCl6 structure provides a larger shift current response than the $Cs_2InBiBr_6$ structure. Because the orbital character contribution 3p of Cl atom at the CBM is more delocalized than the orbital character contribution 4p of Br atom along the shift current direction.

Although the $Cs_2InBiBr_6$ has a higher magnitude of polarization than $Cs_2InBiCl_6$. Thus, the strength of polarization is not directly correlated to the shift current in any obvious ways.

Additionally, the shift current in these materials are quite larger than that in the prototypical ferroelectrics perovskite oxides such as BaTiO3 (30 $\mu A/V^2$)), PbTiO3 (50 $\mu A/V^2$) in bulk

[72],and the famous multi-ferroelectric compound BiFeO3 (0.5 μA/V ^{2})[73] And are much smaller than the single-layer GeS (∼100 μA⁄V2) [74].

Table III-10. shift current $\sigma_{zzZ}(\mu A/V^2)$ of Cs2InBiCl6 and Cs2InBiBr6.

Compounds	Approximations	shift current $\sigma_{zzZ}(\mu A/V^2)$
Cs2InBiCl6	GGA-PBE	58.70
	TB-mBJ	97.06
	TB-mBJ+SO	431.29
Cs2InBiBr6	GGA-PBE	49.11
	TB-mBJ	69.24
	TB-mBJ+SO	313.71

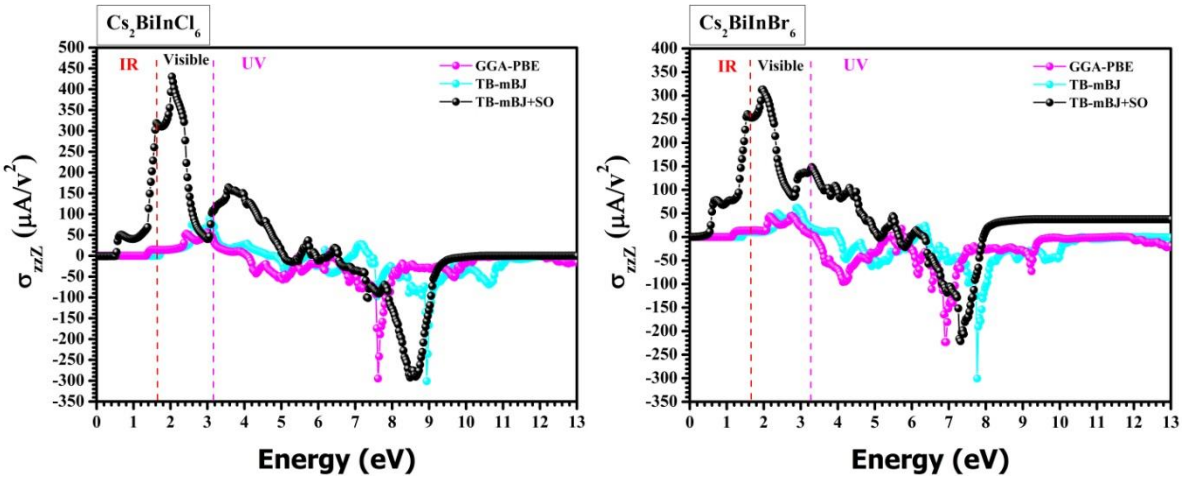

Figure III-24. Shift current response σ_{zzZ} vs incident photon energy for Cs2InBiCl6 and Cs2InBiBr6 structures with the three methods.

III-4. CONCLUSION AND OUTLOOK

In conclusion, we investigated the bulk photovoltaic effect (BPVE) in non-centrosymmetric halides doubles perovskites semiconductor Cs_2InBiX_6 based on first principles calculations. The results of the Structural properties and formation energy prove the structural and thermodynamic stability for both compounds.

Based on a detailed analysis of the electronic properties, although various methods rely, the description of the electronic bands within all these methods is remarkably similar. More importantly, the presence of band edges at the same symmetry points proclaimed their direct bandgap nature and the bandgap value decreases upon replacement of Cl with Br.

These materials With band gaps below 2 eV, have absorption coefficient strength wich it is comparable to other classic semiconductor. The estimated optical properties of this compound indicate that it could be used in the infrared, visible, and ultraviolet regions of the electromagnetic spectrum. We have also reviewed that The stronger cation anion covalent interaction, considerable hybridization s, p orbitals at Bi/In site and p orbitals at Cl/Br site , eventually facilitate the stereochemical activity of the lone pair.In this case The stereochemically active lone pair brings a large structural distortion within the unit cell and creates a polar geometry. the modern theory of polarization based BerryPI code is employed to determine spontaneous polarization.Here, strong spontanous polarization of about 0.39c/m2 for $Cs_2InBiCl_6$ and -0.40 for $Cs_2InBiBr_6$ gets confirmed.

Furthermore, the maximum shift current response for both materials in visible light has been reported along the direction of polarization. While we correlate the high shift current response with the existence of *p* states at both the valence and conduction band edges, as well as the dispersion of these bands. However, the measured low shift current response for $Cs_2InBiBr_6$ compared to $Cs_2InBiCl_6$ indicates that stronger magnitude of polarization does not necessarily imply greater response shift current. Consequently, the present study was an instrumental in understanding the shift current BPVE and was pave the path for designing cost-effective and energy-efficient photovoltaic devices based on Cs_2InBiX_6 and similar halides perovskites. We have also calculated Photovoltaic Characteristics of Cs2InBiCl6 and $Cs_2InBiBr_6$ by using SLME framework .we have shown changes in behavior of *Jsc*, *Voc,FF* and η depending on increasing thickness of absorber layer perovskites. Later on, the efficiencies of $Cs_2InBiCl_6$ and $Cs_2InBiBr_6$ absorber layers calculated using TB-mBJ method at absorber thickness of 50 µm is comes out to be 26.24 % and 28.33%, respectively.

Bibliography

[1] M.A. Ali, T. Alshahrani, G. Murtaza, Mater. Sci. Semicond. Process. 127 (2021) 105728.
[2] Jan-ChristophHebig, I. Kühn, J. Flohre, T. Kirchartz, ACS Energy Lett. 1 (2016) 309–314.
[3] A. Kojima, K. Teshima, Y. Shirai, T. Miyasaka, J. Am. Chem. Soc. 2009,131, 6050.
[4] X. Zhao, J.Yang, Y. Fu, D.Yang, Q. Xu, L.Yu, S. Wei, L. Zhang . Am. Chem. Soc. 2017, 139, 7, 2630–2638,
[5] M.A. Green, A. Ho-Baillie, J.H. Snaith, Nat. Photonics 8 (2014) 506–514.
[6] Kojima, A., Teshima, K., Shirai, Y., and Miyasaka, T. (2009).. J. Am. Chem. Soc. 131, 6050–6051.
[7] https://www.nrel.gov/pv/cell-efficiency.html (accessed: September 2020).
[8] Xingang Zhao, Jihui Yang, Yuhao Fu, Dongwen Yang, Qiaoling Xu, Liping Yu, Su-Huai Wei, and Lijun Zhang . Am. Chem. Soc. 2017, 139, 7, 2630–2638,
[9] W. Ji , K. Yao , Y. C. Liang , Adv. Mater. 2010 , 22 , 1763 .
[10] Zhou, J., and Huang, J. (2018). Photodetectors based on organic-inorganic hybrid lead halide perovskites. Adv. Sci. (Weinh). 5, 1700256.
[11] E. Haque, M.A. Hossain, Comput. Conden. Matter 19 (2019).
[12] Xiao, Z., and Yan, Y. (2017). Progress in theoretical study of metal halide perovskite solar cell materials. Adv. Energy Mater. 7, 1701136.
[13] LI, Weiwei. Investigations of the structural, dielectric, and piezoelectric properties of MAPbI3 hybrid perovskites single crystals. 2021. Thèse de doctorat. Le Mans.
[14] Yuchen Hou, Congcong Wu,Dong Yang, Tao Ye, Vasant G. Honavar, Adri C. T. van Duin, Kai Wang,and Shashank Priya J. Appl. Phys. 128, 060906 (2020); doi: 10.1063/5.0016010
[15] Bi, W.; Leblanc, N.; Mercier, N.; Auban-Senzier, P.; Pasquier, C.. Chem. Mater. 2009, 21, 4099.
[16] Cohen, R. E. Origin of ferroelectricity in perovskite oxides.Nature 1992, 358, 136
[17] Wen-Ping Zhao, Chao Shi, Alessandro Stroppa, Domenico Di Sante, Fanica Cimpoesu, and Wen Zhang, Inorg. Chem. 2016, 55, 20, 10337–10342
[18] Scott, J. F. Applications of Modern Ferroelectrics. Science 2007, 315, 954.
[19]. V. M. Fridkin, Crystallogr. Rep. 46, 654 (2001).
[20] S. Y. Yang, J. Seidel, S. J. Byrnes, P. Shafer, C. H. Yang,M. D. Rossell, P. Yu, Y. H. Chu, J. F. Scott, J. W. Ager, L. W. Martin, and R. Ramesh, Nat. Nanotechnol. 5, 143 (2010).
[21] A.M. Cook, B. M. Fregoso, F. De Juan, S. Coh, and J. E.Moore, Nat. Commun. 8, 14176 (2017).
[22] Young, S. M., & Rappe, A. M. (2012). Physical review letters, 109(11), 116601.
[23] Zhao et al., Rational Design of Halide Double Perovskites for Optoelectronic Applications, Joule (2018), https:// doi.org/10.1016/j.joule.2018.06.017
[24] Y. Zhou, A.M. Askar, J.H. P¨ohls, A.K. Iyer, A.O. Oliynyk, K. Shankar, A. Mar, Z. Anorg. Allg. Chem. 645 (2019) 323–328

[25] Bartesaghi, D., A. H. Slavney, M. C. Gélvez-Rueda, B. A. Connor, F. C. Grozema, H. I. Karunadasa, and T. J. Savenije. 2018. The Journal of Physical Chemistry C. 122 (9):4809–16.

[26] Greul, E., M. Petrus, A. Binek, P. Docampo, T. Bein, et al. 2017. Journal of Materials Chemistry A. 5 (37):19972–81.

[27] Bekenstein, Y., J. C. Dahl, J. Huang, W. T. Osowiecki, J. K. Swabeck, E. M. Chan, P. Yang, and A. P. Alivisatos. 2018. Nano Letters. 18 (6):3502–08.

[28] Su, J., T. Mou, J. Wen, and B. Wang. 2020. The Journal of Physical Chemistry C. 124 (9):5371–77.

[29] P. Blaha, K. Schwarz, G.K.H. Madsen, D. Kvasnicka, J. Luitz, , Ed. K. Schwarz, Vienna Technological University, Vienna, Austria 2001.

[30] Yu, L.; Kokenyesi, R. S.; Keszler, D. A.; Zunger, A. Adv. Energy Mater. 2013, 3 (1), 43–48.

[31] P. Blaha, K. Schwarz, F. Tran, R. Laskowski, G.K.H. Madsen, L.D. Marks, J. Chem. Phys. 152 (2020), 074101, 2020

[32] F. Birch, Finite elastic strain of cubic crystals, Phys. Rev. 71 (11) (1947) 809..

[33] S. Nair, M. Deshpande, V. Shah, S. Ghaisas, S. Jadkar, J. Phys. Condens. Matter 31 (2019) 445902.

[34] Zhao et al., Rational Design of Halide Double Perovskites for Optoelectronic Applications, Joule (2018), https://doi.org/10.1016/j.joule.2018.06.017.

[35] M. Ahmad, G. Rehman, L. Ali, M. Shafiq, R. Iqbal, R. Ahmad, T. Khan, S. J. Asadabadi, M. Maqbool, I. Ahmad, J. Alloys Compd. 705 (2017) 828–839.

[36] Bhumla, P., Gill, D., Sheoran, S., & Bhattacharya, S. (2021). Origin of Rashba Spin Splitting and Strain Tunability in Ferroelectric Bulk CsPbF3. The Journal of Physical Chemistry Letters, 12(39), 9539-9546.

[37] Walsh, A.; Payne, D. J.; Egdell, R. G.; Watson, G. W. Chem. Soc.Rev. 2011, 40, 4455−4463..

[38] Cohen, R. E. Nature 1992, 358, 136−138.n, R. E. Nature 1992, 358, 136−138.

[39] Zhao, X. G., Yang, D., Ren, J. C., Sun, Y., Xiao, Z., & Zhang, L. (2018). Rational design of halide double perovskites for optoelectronic applications. Joule, 2(9), 1662-1673.

[40] T.L. Bahers, M. Rerat, P. Sautet, J. Phys. Chem. C 118 (2014) 5997, https://doi.org/10.1021/jp409724c.

[41] Dewhurst, K., & Sharma, S. (2011). Development of the elk lapw code. Max Planck Institute of Microstructure Physics. Available online: https://elk. sourceforge. io (accessed on 16 September 2021).

[42] U. Jong, C. Yu, Y. Kim, Y. Kye, C. Kim, Phys. Rev. B 98 (2018) 125116.

[43] M. Baranowski, P. Plochocka, R. Su, L. Legrand, T. Barisien, F. Bernardot, Q. Xiong, C. Testelin, M. Chamarro, Photon. Res. 8 (2020) A50–A55.

[44] Riefer, A., F. Fuchs, C. Rödl, A. Schleife, F. Bechstedt, and R. Goldhahn. 2011. Interplay of excitonic effects and van Hove singularities in optical spectra: CaO and AlN polymorphs. Physical Review B. 84 (7):075218. doi:10.1103/ PhysRevB.84.075218

[45] Y. Hu, L. Li, C. Xu, P. Yang, Study of high metal doped SnO2 for photovoltaic devices, Mater. Today Commun. 27 (2021) 102148, https://doi.org/10.1016/j.mtcomm.2021.102148.

[46] D.R. Penn, Wave-number-dependent dielectric function of semiconductors, Phys. Rev. 128 (1962) 2093–2097, https://doi.org/10.1103/PhysRev.128.2093.

[47] B. Xu, X. Li, J. Sun, L. Yi, Eur. Phys. J. B 66 (2008) 483.

[48] Srinivasan, K.; Raghavan, S. L. Strain Derivatives of Dielectric Constants of MgO and Thallous Halides. Phys. Status Solidi B 1986, 137, 33–38.

[49] R.P. Varadwaj, Nanomaterials 10 (2020) 973.

[50] Faghihnasiri, Mahdi, Morteza Izadifard, and Mohammad Ebrahim Ghazi. "DFT study of electronic structure and optical properties of layered two-dimensional CH3NH3PbX3 (X= Cl, Br, I)." Energy Sources, Part A: Recovery, Utilization, and Environmental Effects 41.22 (2019): 2734-2745.

[51] T. Atsue, I.B. Ogunniranye, O.E. Oyewande, Investigation of material properties of halide mixed lead-free double perovskite for optoelectronic applications using firstprinciples study, Mater. Sci. Semicond. Process. 133 (2021) 105963, https:// doi.org/10.1016/j.mssp.2021.105963.

[52] M. Ahmad, G. Rehman, L. Ali, M. Shafiq, R. Iqbal, R. Ahmad, T. Khan, S. J. Asadabadi, M. Maqbool, I. Ahmad, J. Alloys Compd. 705 (2017) 828–839.

[53] T. Ruf, M. Cardona, C.S.J. Pickles, R. Sussmann, Phys. Rev. B 62 (2000) 16578–16581.

[54] I. Khan, I. Ahmad, H.A.R. Aliabad, M. Maqbool, J. Appl. Phys. 112 (2012), 073104.

[55] [76] V.K. Srivasta, Phys. Status Solidi B 114 (1982) 667

[56] M. Bass, Handbook of Optics, McGraw-Hill, New York, 1995.

[57] L. Yu, A. Zunger, Identification of potential photovoltaic absorbers based on first-principles spectroscopic screening of materials, Phys. Rev. Lett. 108 (2012) 68701.

[58] Abraham, J. A., Behera, D., Kumari, K., Srivastava, A., Sharma, R., & Mukherjee, S. K. (2022). A comprehensive DFT analysis on structural, electronic, optical, thermoelectric, SLME properties of new Double Perovskite Oxide Pb2ScBiO6. Chemical Physics Letters, 806, 139987.

[59] Zhao, X. G., Yang, D., Sun, Y., Li, T., Zhang, L., Yu, L., & Zunger, A. (2017). Cu–In halide perovskite solar absorbers. Journal of the American Chemical Society, 139(19), 6718-6725.

[60] Patel, M. J., Gupta, S. K., & Gajjar, P. N. (2023). Investigation of thickness dependent efficiency of CsPbX3 (X= I, Br) absorber layer for perovskite solar cells. Journal of Physics and Chemistry of Solids, 176, 111264.]

[61] Cudney R S, Fousek J, Zgonik M and Günter P: Appl Phys Lett. 1993; 63: 3399.

[62] Kim S and Gopalan V: Appl Phys Lett. 2002; 80:2740.

[63] Z. Wei, W.-Q. Liao, Y.-Y. Tang, P.-F. Li, P.-P. Shi, H. Cai, R.-G. Xiong, J. Am. Chem. Soc. 2018, 140, 8110 – 8113.

[64] F. Jona, G. Shirane, Ferroelectric Crystals, Pergamon, Oxford, 1962.

[65] Zhang, W., Hong, M., & Luo, J. (2020). Halide double perovskite ferroelectrics. Angewandte Chemie, 132(24), 9391-9394.

[66] T. Morimoto and N. Nagaosa, Topological nature of nonlinear optical e_ects in solids, Science Advances 2, 10.1126/sciadv.1501524 (2016).

[67] T. Morimoto and N. Nagaosa, Topological aspects of nonlinear excitonic processes in noncentrosymmetric crystals, Phys. Rev. B 94, 035117 (2016).

[68] R. von Baltz and W. Kraut, Theory of the bulk photovoltaic effect in pure crystals, Phys. Rev. B 23, 5590 (1981).

[69] S. M. Young and A. M. Rappe, First principles calculation of the shift current photovoltaic e_ect in ferroelectrics,Phys. Rev. Lett. 109, 116601 (2012).

[70] G. Pizzi, V. Vitale, R. Arita, S. Blügel, F. Freimuth, G. Géranton, M. Gibertini, D. Gresch, C. Johnson, T. Koretsune,J. Ibañez-Azpiroz, H. Lee, J. M. Lihm, D. Marchand, A.Marrazzo, Y. Mokrousov, J. I. Mustafa, Y. Nohara, Y. Nomura,L. Paulatto et al., J. Phys.: Condens. Matter 32, 165902 (2020).

[71] M. I. Aroyo, J. M. Perez-Mato, D. Orobengoa, E. Tasci, G. de la Flor, A. Kirov "Crystallography online: Bilbao Crystallographic Server" Bulg. Chem. Commun. 43(2) 183-197 (2011)

[72] S. M. Young and A. M. Rappe, Phys. Rev. Lett. 109, 116601 (2012).

[73] S. M. Young, F. Zheng, and A. M. Rappe, First-principles calculation of the bulk photovoltaic e_ect in bismuth ferrite,Phys. Rev. Lett. 109, 236601 (2012).

[74] T. Rangel, B. M. Fregoso, B. S. Mendoza, T. Morimoto, J. E. Moore, and J. B. Neaton, Phys. Rev. Lett. 119, 067402 (2017).

Chapter IV:

Assessing the performance of SF_3PbI_3 from DFT and SLME calculations for photovoltaic applications

IV-1 Introduction

The coupling of ferroelectricity and spin-orbit coupling (SOC) in materials is a fascinating and emerging topic that explores the interplay between electric and magnetic properties in novel quantum materials. Ferroelectricity is a phenomenon that occurs in some materials that have a spontaneous electric polarization that can be reversed by an external electric field. SOC is a quantum effect that describes the interaction of the spin and orbital motion of electrons, which can give rise to exotic electronic and magnetic states. By combining these two effects, one can achieve a tunable and non-volatile control of the spin degree of freedom and the spin-dependent transport properties, which are essential for the development of spintronics and valleytronics [1, 2]

There are different types of materials that exhibit the coupling of ferroelectricity and SOC, such as hybrid organic-inorganic perovskites, transition metal oxides, and two-dimensional materials. Each category of materials exhibits unique mechanisms and characteristics that influence the strength and tunability of the coupling.

In hybrid organic-inorganic perovskites, the ferroelectric polarization is typically induced by the organic cation, while the SOC originates from the metal halide component. A notable example is the methylammonium lead iodide ($MAPbI_3$) perovskite, where the organic methylammonium (MA) cation contributes to ferroelectricity, and the lead iodide framework provides the heavy atoms necessary for SOC. The Rashba effect, which is a type of SOC leading to spin splitting of electronic bands, is particularly significant in these materials. This effect can be modulated by altering the composition, structure, and thickness of the perovskite layer, thereby tuning the electronic properties for potential applications in spintronics and optoelectronics [1, 2]

Transition metal oxides, such as bismuth ferrite ($BiFeO_3$) and bismuth manganite ($BiMnO_3$), exhibit strong coupling between ferroelectricity and SOC due to the presence of heavy transition metal atoms with significant SOC and the inherent ferroelectric properties of the material. In these oxides, the coupling mechanisms are often related to the distortion of the crystal lattice, which enhances both ferroelectric polarization and SOC. These materials are

of great interest for multiferroic applications, where the control of magnetization through electric fields (and vice versa) can lead to advanced functionalities in electronic devices [3,4]

Two-dimensional (2D) materials, such as transition metal dichalcogenides (TMDCs) and layered perovskites, also exhibit a notable coupling of ferroelectricity and SOC. In 2D TMDCs, such as MoS_2 and WSe_2, the lack of inversion symmetry and strong SOC from the transition metal atoms result in significant spin splitting and ferroelectric-like behavior. The tunability of these properties through external stimuli, such as electric fields and mechanical strain, makes them promising candidates for next-generation nanoelectronic and spintronic devices [5, 6]

The compound SF_3PbI_3, also known as sulfur-functionalized lead iodide, shares similarities with $MAPbI_3$, both belonging to a family characterized by heavy elements like lead and iodine, which induce significant spin-orbit coupling (SOC) in their electronic structure. The addition of sulfur (S) further modifies their electronic and optical properties [7] The specific arrangement of sulfur, lead, and iodine likely contributes to the polar nature of SF_3PbI_3, a characteristic attributed to symmetry breaking within its crystal structure.

In materials lacking inversion symmetry, such as non-centrosymmetric crystals or interfaces, SOC induces the Rashba effect, leading to the splitting of valence and conduction band edges and the removal of electron spin degeneracy [8] Recent studies suggest that a bulk Rashba effect, extending beyond surface or interface effects, may influence the observed long carrier lifetimes and diffusion lengths in SF_3PbI_3 [9] While SF_3PbI_3 phases have been experimentally assigned centrosymmetric space groups, there is increasing interest in the potential role of a bulk Rashba effect. In SF_3PbI_3, inversion symmetry can be disrupted either by statically distorting the PbI framework or dynamically rotating the SF_3 group. Static distortion leads to a non-centrosymmetric phase and a persistent bulk Rashba effect, while dynamic disruption arises from rotations of the SF_3 group without distorting the PbI framework. These dynamic fluctuations, influenced by phonon modes or interactions within the SF_3PbI_3 structure, can induce a fluctuating bulk Rashba effect on shorter timescales compared to ion rotations or framework vibrations [7, 8, 9]

In this chapter, we perform density functional theory (DFT) calculations to investigate the electronic band structure, optical properties, ferroelectric behavior, and photovoltaic characteristics of SF_3PbI_3. Our analysis focuses on understanding the strong spin-orbit coupling induced by the heavy elements in its structure, particularly examining the Rashba splitting near the electron band extrema. Additionally, we explore the phenomenon of distortion-induced polarization switching in SF_3PbI_3, revealing its potential for rapid and controllable transition between low and high ferroelectric polarization states.

IV-2 The bulk Rashba effect

The bulk Rashba effect is a phenomenon that occurs in certain materials in which the interaction between the spin of electrons and their orbital motion is modified by an electric field or a broken crystal symmetry. This result in a momentum-dependent splitting of spin bands in bulk crystals and low-dimensional condensed matter systems, depending on the spin orientation. The bulk Rashba effect can be described by a series of formulas that involve the Hamiltonian, the spin-orbit coupling, and the Rashba coupling constant. However, if one considers the relativistic Rashba Hamiltonian [10]

$$H_R = \alpha(k \times E).\sigma \quad , \alpha = \frac{e\hbar^2}{2m^2c^2} \tag{1}$$

where the electric field originates from the non-zero polarization E, α is the Rashba coupling constant, σ is the Pauli matrix vector, k is the momentum operator, e is the absolute value of the electron charge, $\hbar$ is the reduced Planck constant, m is the electron mass, and c is the speed of light. These formulas show that the bulk Rashba effect depends on the strength of the Rashba coupling constant, which is proportional to the electric field gradient in the direction perpendicular to the plane, the direction of the momentum, and the orientation of the spin. The bulk Rashba effect can have important implications for the optoelectronic properties and applications of materials, such as solar cells, light-emitting diodes, and spintronic devices.

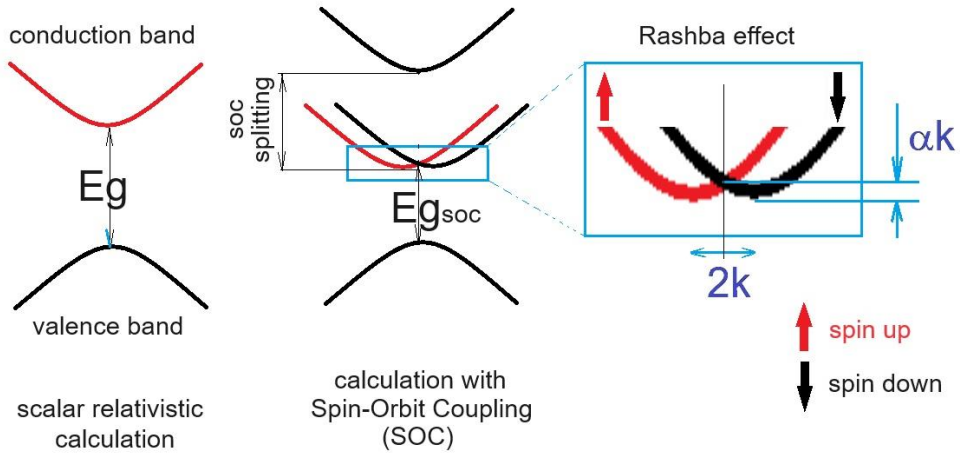

Figure IV-1. The energy bands and spin orientations in a semiconductor material affected by Spin-Orbit Coupling (SOC) and Rashba SOC [11]

IV-3 Methodology

This study employs density functional theory (DFT), a standard in materials science for its accuracy in predicting optoelectronic and structural properties. We analyzed the physical characteristics of SF_3PbI_3 using the all-electron full-potential linearized augmented plane wave (FP-LAPW) method within the WIEN2K code[12] SF_3PbI_3 was examined in its rhombohedral form, which is crucial for highlighting atomic displacements and deducing corresponding ferroelectric polarization. The rhombohedral structure allows for a detailed representation of how atoms shift, providing insights into polarization behavior. We maintained the same atomic arrangement and coordination as observed in the pseudo-cubic structure. The lattice parameters are transformed from the cubic cell, with the rhombohedral lattice parameter a_r calculated as $a_c\sqrt{3}$, where a_c is the cubic lattice constant. The angle α in the rhombohedral system is set to 60°. Atomic positions are converted from the cubic to the rhombohedral system using the appropriate transformation matrix, ensuring that the PbI_6 octahedra and the orientation of the SF_3 groups remained consistent with the original pseudo-cubic structure. This approach preserves the relative distances and angles between atoms, providing an accurate description of SF_3PbI_3 in the rhombohedral framework. Structural optimization was conducted using the Perdew, Burke, and Ernzerhof generalized gradient approximation (GGA-PBE)[13] To enhance the accuracy of the

electronic structure calculations, the modified Becke-Johnson (mBJ) potential was employed [14] The mBJ correction is vital for refining band gap predictions. A plane wave cutoff of kinetic energy R_{MT} K_{max} = 7.0 was used, with muffin-tin radii of 2.5 for S, F, I, and 2.15 for Pb. The charge density's maximum Fourier expansion was set at G_{max} = 20 $a.u.^{-1}$, ensuring precise calculations. Convergence was achieved when total energy differences were less than 10^{-5} Ry. For electronic structure and optical properties, a dense K-mesh of 1000 k-points in the first Brillouin zone was utilized. Spin-orbit coupling (SOC) was incorporated to explore its impact on electronic structure, particularly the Rashba effect [15] This phenomenon, where spin-orbit interaction leads to momentum-dependent spin band splitting, is influenced by electric field gradients and crystal symmetry. Key parameters of the Rashba effect include the Rashba coupling constant (α) and momentum offset (2k), which determine the strength and direction of the effect [16] The rhombohedral symmetry of SF_3PbI_3 is essential for understanding ferroelectric polarization, as it allows for detailed examination of atomic shifts and their contributions to polarization. By assessing these shifts, we can derive the spontaneous polarization and evaluate energy barriers for polarization switching. Additionally, the photovoltaic properties were evaluated using the Spectroscopic Limited Maximum Efficiency (SLME) model [17] to estimate the potential efficiency of SF_3PbI_3-based solar cells.

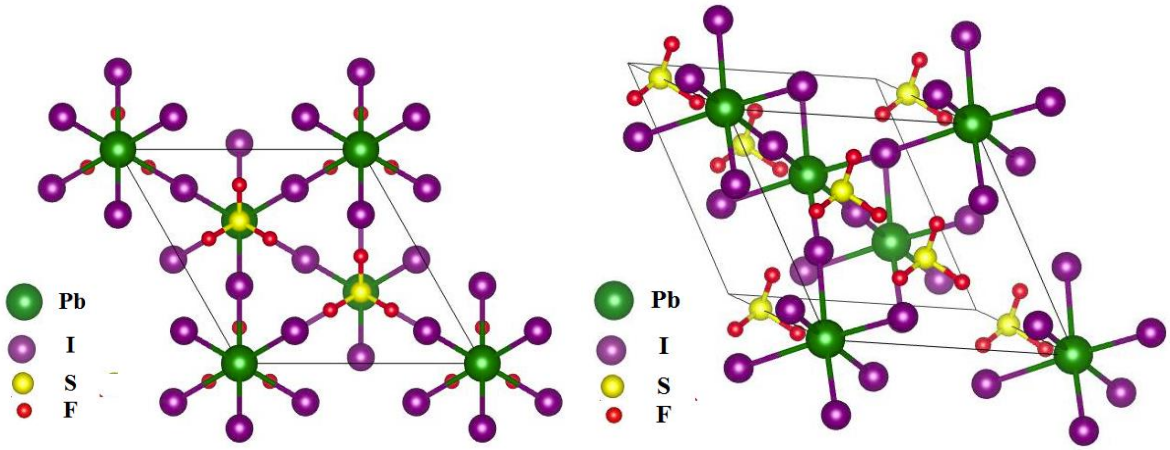

Figure IV-2. Ball-and-stick model illustrating the rhombohedral crystal structure of SF_3PbI_3.

IV-4 Results and Discussion

IV-4.1 Stability and Structural Properties

The first crucial stage before calculating the material properties is to determine its structural properties. The generalized gradient approximation (GGA) is employed to compute the structural properties of SF_3PbI_3 in the rhombohedral R3m phase. Furthermore, the crystal structures are relaxed, allowing the atoms in a crystal lattice to adjust their positions to minimize the system's total energy, a process known as crystal relaxation. This is well depicted by the optimization curves.

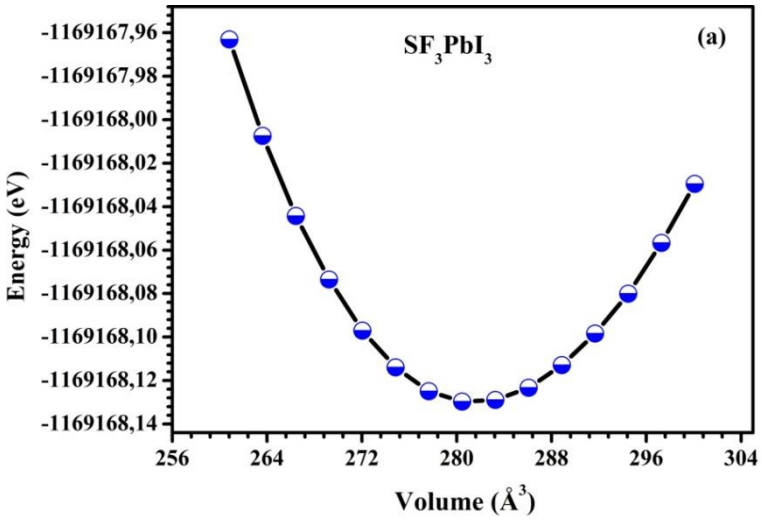

Figure IV-3. The total-energy versus volume optimization for the SF_3PbI_3 compound.

The Murnaghan equation of state is used to evaluate the lattice parameters “a” and “c”, the compressibility modulus “B”, and its primitive derivative “B’” after optimizing the total energy E_0 of the fundamental state [18]:

$$E(V) = E_0 + \frac{BV}{B'(B'-1)}\left(\left(\frac{V_0}{V}\right)^{B'} - 1\right) + \frac{BV}{B'-1} \quad (2)$$

The thermodynamic stability of this compound has been evaluated by calculating the formation energies per atom (E_f) using the following equation [19]:

$$E_f = E_0 - E_S - 3E_F - E_{Pb} - 3E_I \quad (3)$$

Where E_0 is the total ground state energy of the SF_3PbI_3 compound, and E_{Pb}, E_S , E_F, and E_I are the energies of Pb, S, F, and I atoms, respectively, in their bulk forms. This value is given in **Table IV-1**. The table shows that the E_f per atom for the studied compound is negative. According to the computed formation energies, SF_3PbI_3 is stable with respect to its constituent atoms. The energy stability of SF_3PbI_3 in its phase-stable state is confirmed by the negative formation energy value.

Table IV-1. Calculated lattice parameters *a*(Å) and c(Å) , volume of the unit cell V (Å^3), Bulk modulus B (GPa) and its first pressure derivative B', and the formation energy E_f(eV) of SF_3PbI_3 system. The hexagonal lattice parameters *a* and *c* were derived from the rhombohedral lattice parameter a_r and angle α.

Compound	lattice parameters		B(GPA)	B'	V (Å^3)	E_f(eV)
	a (Å)	*c* (Å)				
SF_3PbI_3	9.257	11.337	30.037	4.721	286,066	-0.893

IV-4.2. Electronic Structure

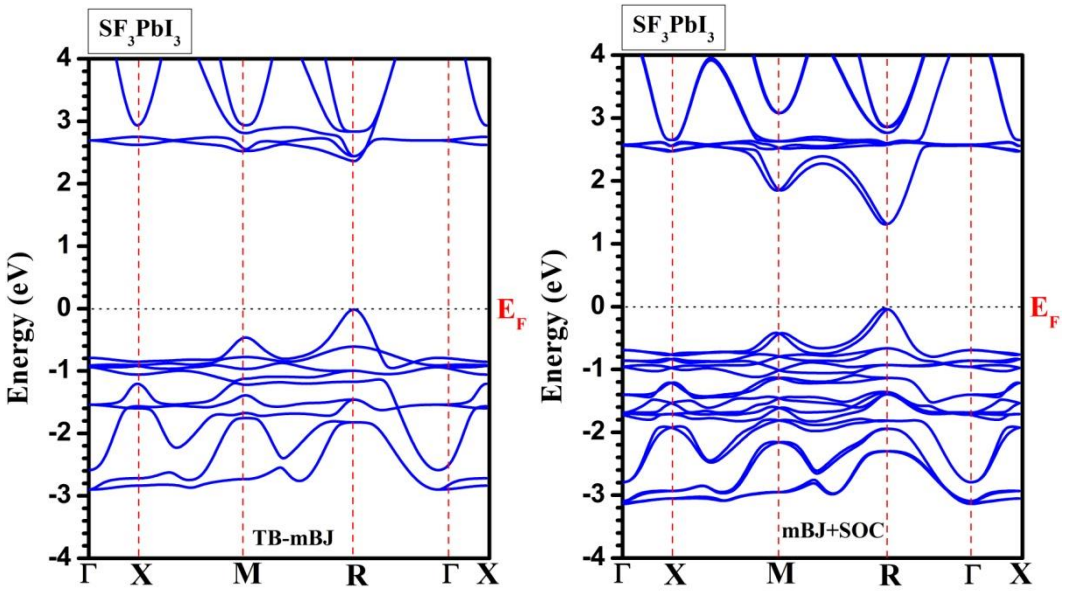

Figure IV-4. Electronic band structures of SF_3PbI_3 in high symmetry directions

Figure IV-4 depicts the electronic band structures estimated for SF_3PbI_3 according to the high-symmetry directions of the first Brillouin zone. The maxima of the valence band and minima of the conduction band are located at the same point of symmetry (R), indicating a direct gap transition in the R–R direction. This confirms the semiconductor behavior of SF_3PbI_3, enhancing its effectiveness and functionality in solar cells. Additionally, the band structure of SF_3PbI_3 displays a notable Rashba spin splitting in both the valence and conduction bands, primarily attributed to the strong spin-orbit coupling (SOC) of lead (Pb) and the structural asymmetry introduced by the SF_3 cation. The spin-polarized states resulting from Rashba spin splitting can further aid in reducing recombination by creating spin-dependent pathways for charge carriers.

Table IV-2. Calculated band gaps compared with other theoretical values (eV) for SF3PbI3.

Compounds	Band gap (eV)		Approximation
	This work	Other work	
SF3PbI3	1.900	2.050 [20]	GGA-PBE
	2.375		TB-mBJ
	1.357		mBJ + SOC

The calculated band gap values for SF_3PbI_3 presented in **Table IV-2** demonstrate significant variations depending on the approximations used: the Generalized Gradient Approximation (GGA), GGA with the modified Becke-Johnson potential (mBJ), and mBJ combined with spin-orbit coupling (SOC). The band gap obtained with GGA is 1.9 eV, confirming the semiconductor nature of the material, although this method is known to underestimate values due to its inherent limitations. Adding the mBJ potential increases the band gap to 2.375 eV, indicating a significant correction. However, including SOC in the mBJ calculations reduces the band gap to 1.357 eV, highlighting the importance of SOC for materials containing heavy elements like lead (Pb). This SOC induces additional effects such as the Rashba phenomenon, which enhances charge separation and reduces recombination losses. Despite this reduction, the band gap remains within a range suitable for photovoltaic

applications, showing that SF_3PbI_3 has promising potential for solar cells with electronic properties significantly influenced by SOC.

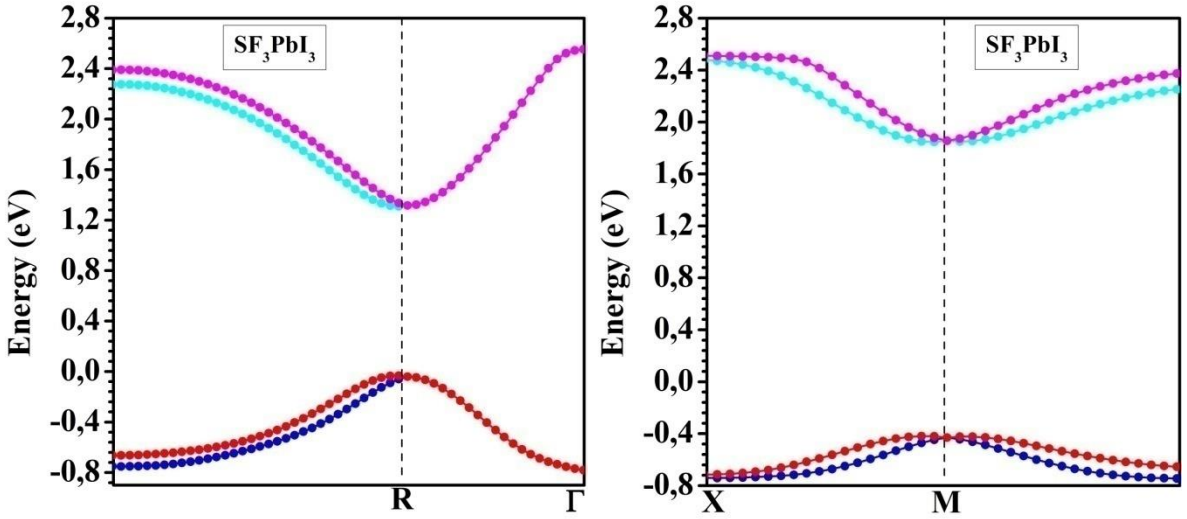

Figure IV-5. Electronic band structure of SF_3PbI_3 showing Rashba spin splitting.

Table IV-3. Rashba parameters α (eVÅ) for band-splitting at R and M point in R3m phase of SF_3PbI_3.

	K_v	α_{Rv}	K_c	α_{Rc}	K_v	α_{Mv}	K_c	α_{Mc}
This work	R	0.439	R	0.714	M	1.561	M	0.675
Other work				0.850[21]				1.611[21]

Figure IV-5 shows the electronic band structure of SF_3PbI_3, highlighting the energy dispersion along specific high-symmetry paths in the Brillouin zone (R to Γ and X to M). The Rashba effect is evident in the splitting of the conduction and valence bands around the high-symmetry points, indicating strong spin-orbit coupling (SOC) in the material. The conduction band minimum (CBM) and valence band maximum (VBM) exhibit clear splitting around the Γ point. This Rashba splitting can be quantified by the energy difference between the split bands at the CBM and VBM, suggesting the presence of a strong SOC, which contributes to the Rashba effect and leads to spin-polarized states. Similar splitting is observed around the M point, with distinct separation of the CBM and VBM. The consistent band splitting along this path further supports the presence of the Rashba effect in different directions within the Brillouin zone. Key parameters that quantify the Rashba effect include α_R (Rashba

parameter), which represents the strength of the Rashba effect; higher values indicate stronger SOC and greater splitting. E_R (Rashba energy) is the energy associated with the Rashba splitting at the band extrema. k_R (Rashba wave vector) is the momentum shift of the band extrema due to the Rashba effect [22]

Table IV-3 presents the Rashba parameters (α) for band-splitting at the R and M points in the R3m phase of SF_3PbI_3, highlighting the strength of the Rashba effect, which is a result of strong spin-orbit coupling (SOC) in the material. At the R point, the Rashba parameter for the valence band (α_{Rv}) is 0.439 eVÅ, and for the conduction band (α_{Rc}) it is 0.714 eVÅ. At the M point, the Rashba parameter for the valence band (α_{Mv}) is significantly higher at 1.561 eVÅ, and for the conduction band (α_{Mc}) it is 0.675 eVÅ. When compared to other works, our results for the M point show higher variability, with a reported Rashba parameter of 0.850 eVÅ for the valence band and 1.611 eVÅ for the conduction band in other studies. The high Rashba parameters, particularly at the M point, suggest strong SOC, which is beneficial for spintronic applications that require precise control over spin states. Furthermore, the Rashba effect enhances charge separation, reducing recombination losses and improving photovoltaic efficiency.

Further analysis of the band structure provides valuable insights into the nature of electronic states, revealing that electronic states in the conduction band (CB) exhibit greater dispersion, while those in the valence band (VB) are less dispersive. This observation suggests that the effective mass of free charge carriers in the VB (holes) is slightly greater than that of carriers in the CB (electrons). To quantify this, we calculated the effective mass of these carriers by fitting the conduction and valence bands to the parabolic equation. The effective mass tensor is defined as [23]:

$$m^* = h^2 \left[\left(\frac{\partial^2 \varepsilon(\mathrm{k})}{\partial \mathrm{k}^2} \right) \right]^{-1} \quad (4)$$

where k represents the wave vector, and ϵ(k) represents the eigenvalue corresponding to the band edge. The subsequent effective mass values at the R high-symmetry point, in the transverse *xx* and longitudinal *zz* directions, are documented in **Table IV-3**. As can be seen, the effective masses for polar SF_3PbI_3 are distinctly anisotropic. Importantly, the effective

mass of carriers for the material under study is significantly below 0.20 with the mBJ + SOC potential. This lower effective mass is advantageous for achieving enhanced carrier mobility, a highly desirable feature for the development of efficient electronic and optoelectronic devices. The electron mass at R is quite small but highly anisotropic, while the hole effective masses are larger.

Table IV-4. Effective masses of electrons and holes along high-symmetry directions (longitudinal and transverse) for SF_3PbI_3, under the GGA + mBJ and mBJ + SOC computational methods.

Method	**Carrier**	**Effective Mass (m_0)**	
GGA + mBJ	Light Electrons (m^*_{le})	0.5583	-
	Heavy Electrons (m^*_{he})	0.4115	-
	Light Holes (m^*_{lh})	0.8368	-
	Heavy Holes (m^*_{hh})	0.7391	-
Method	**Carrier**	**Longitudinal Mass (m_0)**	**Transverse Mass (m_0)**
mBJ + SOC	Light Electrons (m^*_{le})	0.1998	0.2366
	Heavy Electrons (m^*_{he})	0.0755	0.0934
	Light Holes (m^*_{lh})	0.1050	0.1194
	Heavy Holes (m^*_{hh})	0.5110	0.4900

This table compares the effective masses of electrons and holes in SF_3PbI_3 along longitudinal and transverse directions using two computational methods: mBJ+SOC and GGA+mBJ. Under mBJ+SOC, light electrons exhibit a lower effective mass of 0.1998 m_0 longitudinally, indicating higher mobility, while heavy electrons are even lighter at 0.0755 m_0. Light holes have effective masses of 0.1050 m_0 (longitudinal) and 0.1194 m_0 (transverse), suggesting enhanced mobility compared to heavy holes with masses of 0.5110 m_0 (longitudinal) and 0.4900 m_0 (transverse). In contrast, GGA+mBJ yields slightly heavier effective masses for electrons (0.5583 m_0 for light electrons and 0.4115 m_0 for heavy electrons) and lighter masses for holes (0.8368 m_0 for light holes and 0.7391 m_0 for heavy holes).

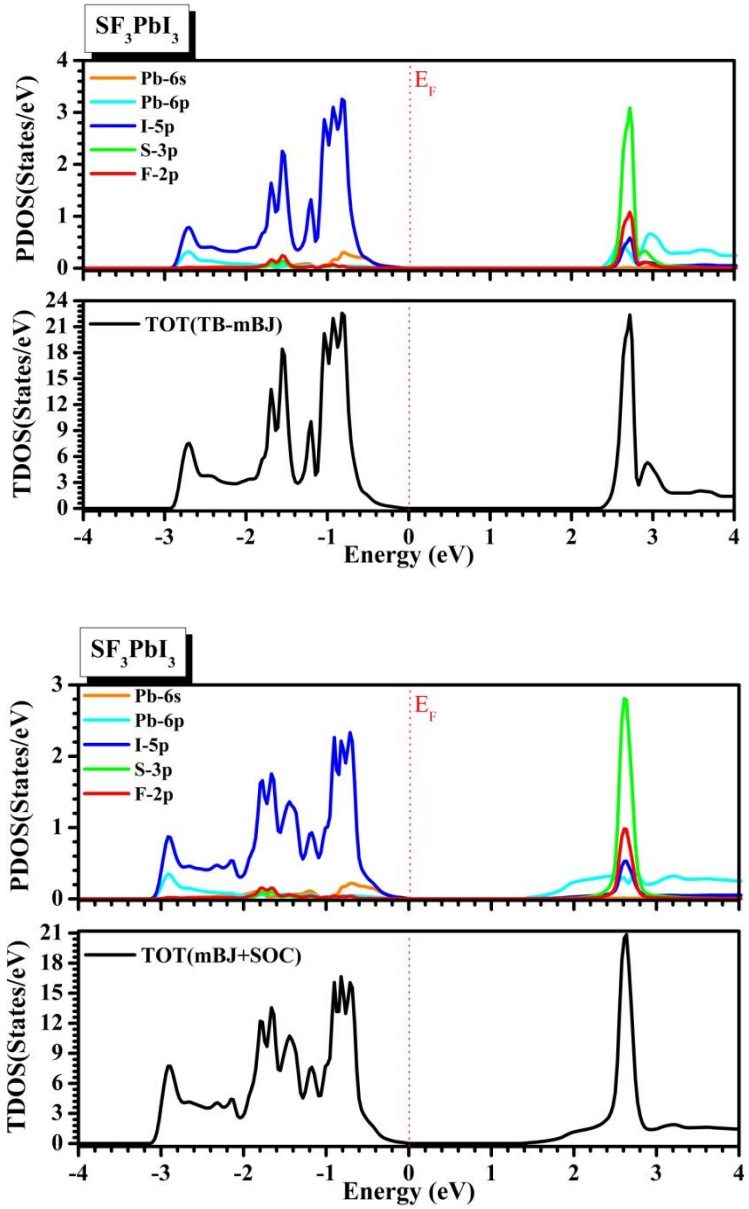

Figure IV-6. Partial Density of States (PDOS) and Total Density of States (TDOS) for SF_3PbI_3 calculated using the modified Becke-Johnson (mBJ) potential with spin-orbit coupling (SOC).

Figure IV-6. shows the partial density of states (PDOS) and total density of states (TDOS) for SF_3PbI_3, calculated using the modified Becke-Johnson (mBJ) potential with spin-orbit coupling (SOC), which provide valuable insights into its electronic properties. The PDOS shows that the valence band is primarily composed of iodine (I-5p) states, with minor contributions from lead (Pb-6s) and sulfur (S-3p) states. The conduction band is largely influenced by lead (Pb-6p), sulfur (S-3p), and fluorine (F-2p) states. The TDOS plot highlights a significant band gap around the Fermi level, confirming the material's semiconductor

nature with an estimated band gap of approximately 1.357 eV. These values are closer to the experimental values of the parent halide perovskite CH3NH3PbI3(Cl,Br) [24].

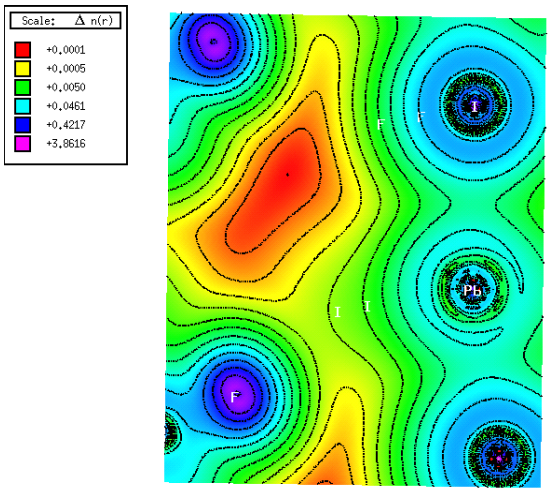

Figure IV-7. Charge density distribution map of SF_3PbI_3.

Figure IV-7 illustrates the electron charge density distribution in SF_3PbI_3. The charge density analysis of SF3PbI3 reveals significant insights into its chemical bonding and structural properties. The electron charge density data, as depicted in **Figure IV-7** , indicates several key characteristics: Firstly, the bonds between Pb and I atoms exhibit covalent character, suggesting a sharing of electron density between these atoms. This covalent nature is typically indicated by a balanced distribution of electron density around the bonded atoms. Secondly, there is a notably high electron density observed at the I (iodine) sites, indicating a concentration of electrons around these atoms. This is consistent with iodine's high electronegativity and its tendency to attract electron density in chemical bonds. Conversely, the electron density is minimal at the Pb (lead) sites, suggesting a lower concentration of electrons around these atoms compared to iodine. This asymmetry in electron density distribution around Pb indicates the presence of a stereochemically active lone pair associated with the Pb atom. Stereochemically active lone pairs are known to contribute to the polar behavior of compounds, suggesting that SF_3PbI_3in its rhombohedral phase may exhibit polar characteristics due to this lone pair. Furthermore, the minimal electron density observed at the F (fluorine) and S (sulfur) sites indicates their lesser involvement in the

electron density distribution within SF_3PbI_3, which is consistent with their roles as electronegative atoms in this compound.

IV-4.3 Optical properties

Driven by the impressive electronic properties of SF_3PbI_3 an exploration into their optical properties has been examined. In terms of optical parameters, the dielectric function is formulated as: $\varepsilon(\omega) = \varepsilon_1(\omega) + i\varepsilon_2(\omega)$, representing the material's optical behavior through the absorption and dispersion of incident rays. The real dielectric functions $\varepsilon_1(\omega)$ and the imaginary dielectric functions $\varepsilon_2(\omega)$ are computed using the Kramer-Kronig expressions provided by equations (3) and (4) [25]

$$\varepsilon_1(\omega) = 1 + \frac{2}{\pi} P \int_0^{\infty} \frac{\omega' \varepsilon_2(\omega')}{\omega'^2 - \omega^2} d\omega' \quad (5)$$

$$\frac{e^2 h'}{\pi m^2 \omega^2} \sum_{V,C} \int_{BZ} |M_{CV}(k)|^2 \delta\left[\omega_{CV}(k) - \omega\right] d^3k \quad (6)$$

Here, P, m, ω and Mcv are polarization, the mass of the electron, angular frequency, and Average Mass.

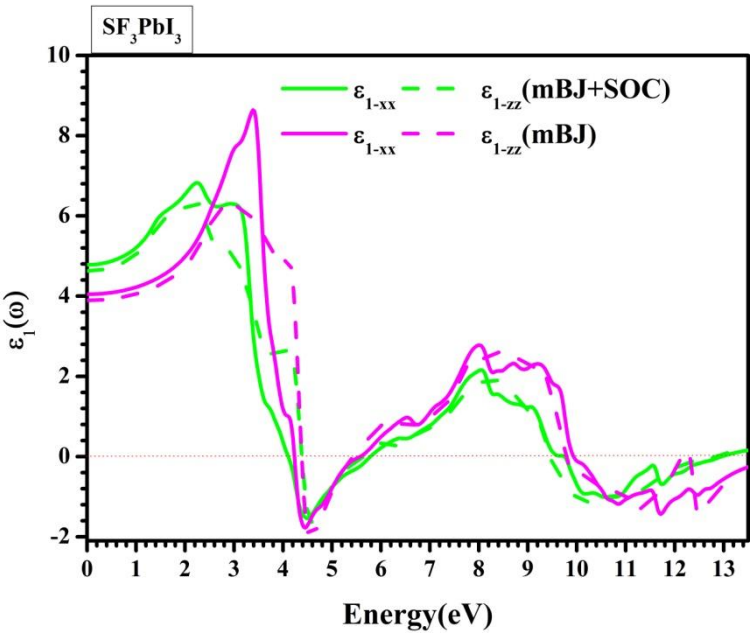

Figure IV-8. The real dielectric functions $\varepsilon_1(\omega)$ of SF_3PbI_3 as a function of energy, displaying anisotropic optical properties with distinct absorption coefficients (α_{xx} and α_{zz}) in the *xx* and *zz* directions.

All of the parameters were calculated using the TB-mBJ functional and TB-mBJ+SO approximation. **Figure IV-8** displays the details $\varepsilon_1(\omega)$ of studied compound. In this context, the static dielectric function $\varepsilon_1(0)$ delineates the material's polarization and dispersion characteristics. The evaluated $\varepsilon_{1\text{-}xx}(0)$ and $\varepsilon_{1\text{-}zz}(0)$ values for SF_3PbI_3 are 4.04,3.86 and 4.83,4.60 for TB-mBJ and TB-mBJ+SO respectively. A higher $\varepsilon_1(0)$ value suggests a reduced probability of charge carrier recombination, signifying enhanced performance in optoelectronic applications.

Subsequently, as the energy levels increase, $\varepsilon_1(\omega)$ demonstrates an upward trend, reaching maximum peaks of 8.73,6.45 and 6.87,6.41 for TB-mBJ and TB-mBJ+SO respectively. Following this, $\varepsilon_1(\omega)$ begins to decrease and eventually becomes negative, indicating a pronounced metallic character.

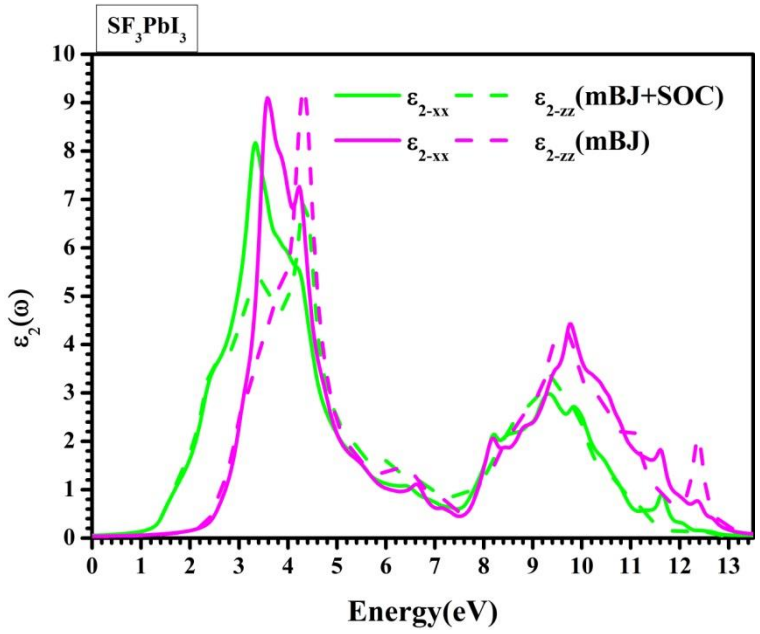

Figure IV-9. The real dielectric functions $\varepsilon_2(\omega)$ of SF_3PbI_3 as a function of energy, displaying anisotropic optical properties with distinct absorption coefficients (α_{xx} and α_{zz}) in the *xx* and *zz* directions.

Figure IV-9 illustrates the graph of the imaginary part $\varepsilon_2(\omega)$ plotted against photon energy, which demonstrates the interband transition from occupied to unoccupied energy states. The energy threshold for these electronic transitions is termed the optical band gap, equivalent to the electronic band gaps. The presence of multiple peaks within the graphs of the imaginary dielectric function, particularly within the visible and ultraviolet regions, signifies that electronic excitations are intricately linked to the calculated electronic properties. To shed light on the source of these peaks, we utilized the partial density of states.

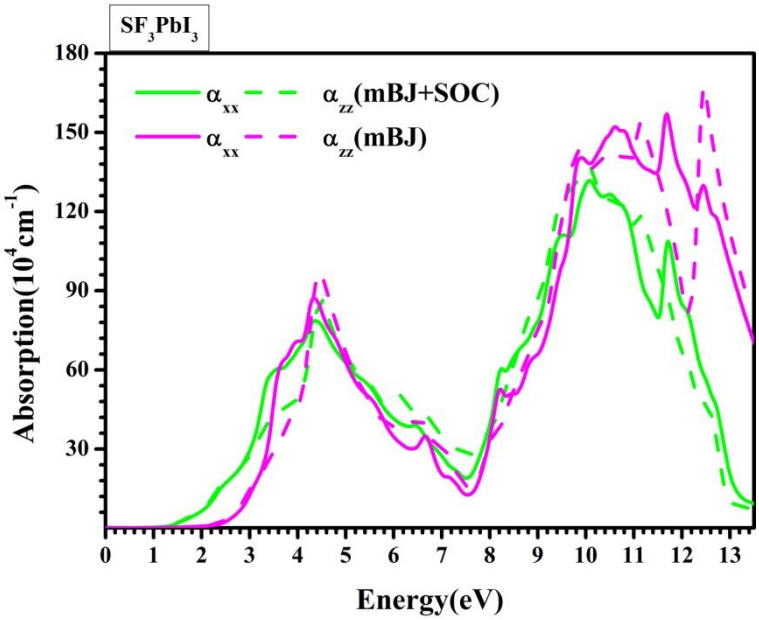

Figure IV-10. Absorption spectra of SF_3PbI_3 as a function of energy, displaying anisotropic optical properties with distinct absorption coefficients (α_{xx} and α_{zz}) in the *xx* and *zz* directions.

Figure IV-10 illustrates the absorption spectra of SF_3PbI_3 as a function of energy, revealing significant anisotropy in the material's optical properties, with different absorption coefficients (α_{xx} and α_{zz}) in the xx and zz directions. Two sets of calculations are presented: one using the modified Becke-Johnson potential with spin-orbit coupling (mBJ+SOC) and the other without SOC (mBJ). The inclusion of SOC (green lines) results in lower absorption in the higher energy range compared to the mBJ calculation (magenta lines), indicating that SOC

affects the optical transitions and reduces absorption strength in certain regions. Both sets of spectra exhibit multiple peaks corresponding to electronic transitions from the valence band to the conduction band, with the initial absorption onset around the band gap energy, consistent with the semiconductor nature of SF_3PbI_3. The comparison shows higher absorption coefficients in the higher energy range for the mBJ calculation, highlighting the impact of SOC on the optical behavior of a material.

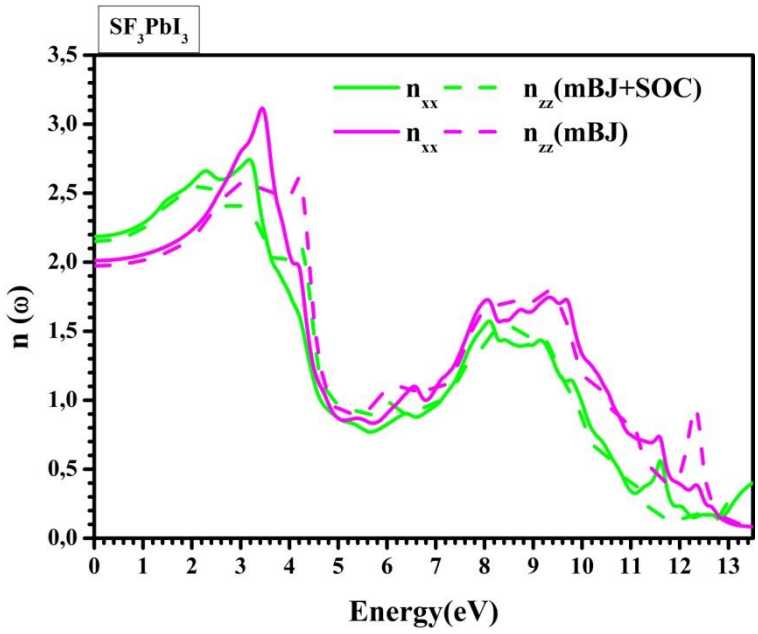

Figure IV-11. Refractive index n(ω) of SF_3PbI_3 as a function of energy, displaying anisotropic optical properties with distinct absorption coefficients (α_{xx} and α_{zz}) in the *xx* and *zz* directions.

Another crucial optical property that offers insights into light-material interactions is the refractive index n(ω). It is also frequency dependent function. As electromagnetic waves traverses a material, its velocity undergoes alterations, resulting in variations in the refractive index of the material. In Fig.3, we present the computed spectra of n(ω) for the given compound. From Figure IV-11, the static refractive index $n_{-xx}(\omega)$ and $n_{-zz}(\omega)$ values are measured as 2.01,1.97 and 2.18,2.14 for TB-mBJ and TB-mBJ+SO, respectively, indicating excellent optical performance for these material.

IV-4.4 Ferroelectric Properties:

Ferroelectric material SF_3PbI_3 exhibits significant spontaneous polarization, creating internal electric fields that enhance the separation of electron-hole pairs and minimize recombination losses. With substantial polarization and manageable energy barriers for switching states, SF_3PbI_3 allows precise control over ferroelectric domains, facilitating dynamic adjustments to its electronic and spin properties for versatile device functionalities suitable for diverse operational conditions [26] The calculated polarization of SF_3PbI_3 is 0.5333 C/m^2, indicative of moderate ferroelectric behavior.

First-principles calculations for SF_3PbI_3 show very low energy barriers for Pb (0.192 meV) and I (0.186 meV) atom displacements, while the barrier for S displacement is higher at 3.297 meV. This suggests that SF_3PbI_3 can achieve polarization switching with minimal energy for Pb and I displacements, although S displacement requires more energy, indicating a mixed ease of switching depending on the atomic movement involved. Figure 6 illustrates how off-center displacements of Pb, I, and S atoms affect total energy and spontaneous polarization, confirming that these displacements result in stable configurations and discrete changes in polarization. The energy curve shows a minimum point, indicating stability, and the polarization curve exhibits discrete jumps corresponding to changes in the polarization state.

In comparison, other ferroelectric materials exhibit varying energy barriers. AlN shows an energy barrier of 0.510 eV per formula unit, derived from first-principles calculations [27], indicating a more stable polarization state that requires more energy for switching. SnS monolayers, with an energy barrier of 0.106 eV [28], are highly efficient for rapid switching, making them ideal for high-speed memory and logic devices. Similarly, the $MAPbI_3$ crystal, with a 0.100 eV [29] barrier obtained from molecular dynamics simulations, balances stability and switching efficiency, making it versatile for various ferroelectric applications.

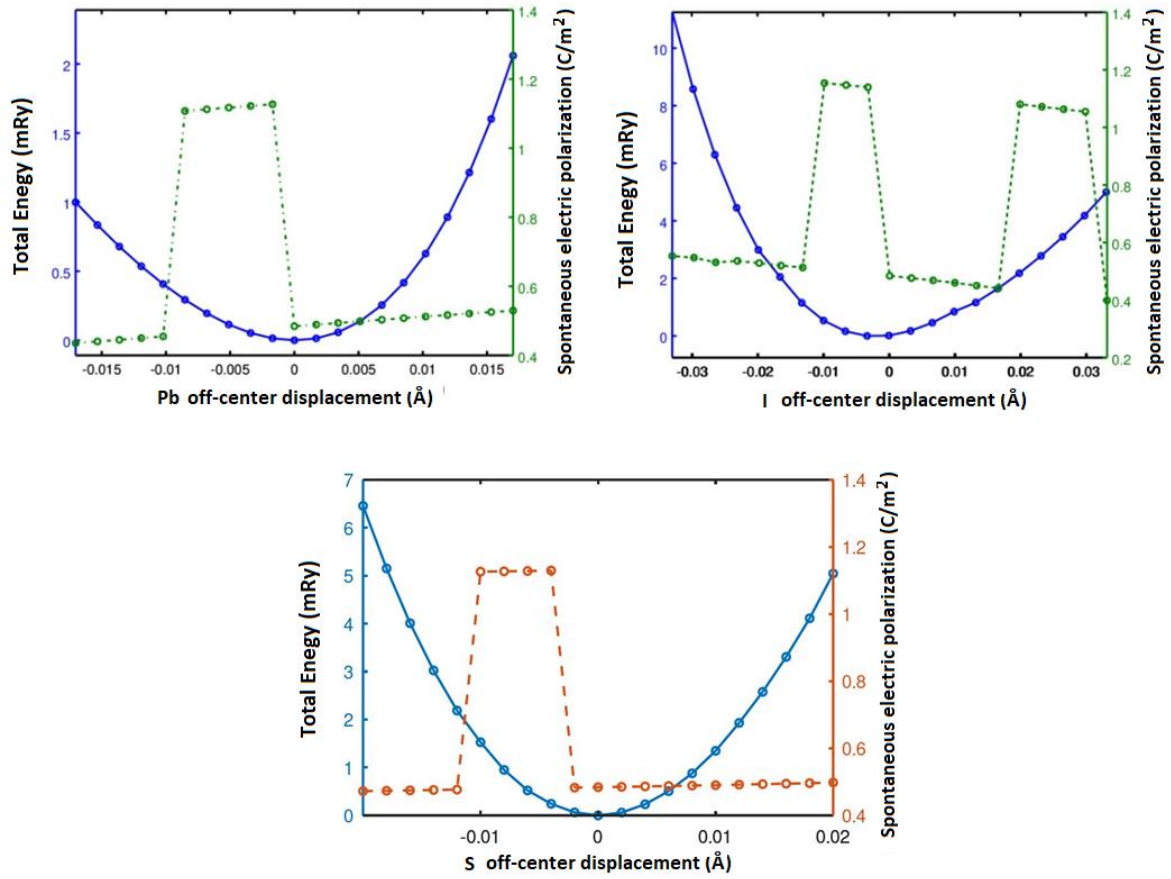

Figure IV-12. The effect of off-center displacements of Pb, I, and S atoms on the total energy and spontaneous polarization in SF_3PbI_3.

Figure IV-12 provides a detailed analysis of the off-center displacements of Pb, I, and S atoms in SF_3PbI_3 and their effects on total energy and spontaneous polarization. The data confirm that these displacements result in stable configurations and discrete changes in polarization, essential for efficient domain manipulation. The energy curves indicate a minimum point, suggesting stability, while the polarization curves exhibit discrete jumps corresponding to changes in the polarization state, further validating the potentiality of the material for efficient ferroelectric switching.

IV-4.5. Photovoltaic Properties:

The concurrent ferroelectric and Rashba effects can synergistically enhance the overall photovoltaic performance [30]

Ferroelectric domains can be controlled to optimize light absorption and charge transport, while Rashba spin splitting can provide additional channels for efficient charge extraction [31]

Using the SLME model, the estimated maximum efficiency of SF_3PbI_3-based solar cells is calculated. The SLME takes into account the absorption spectrum of a material, bandgap, and recombination losses. Our results indicate that SF_3PbI_3 has a high theoretical efficiency, making it a strong contender for efficient solar energy conversion.

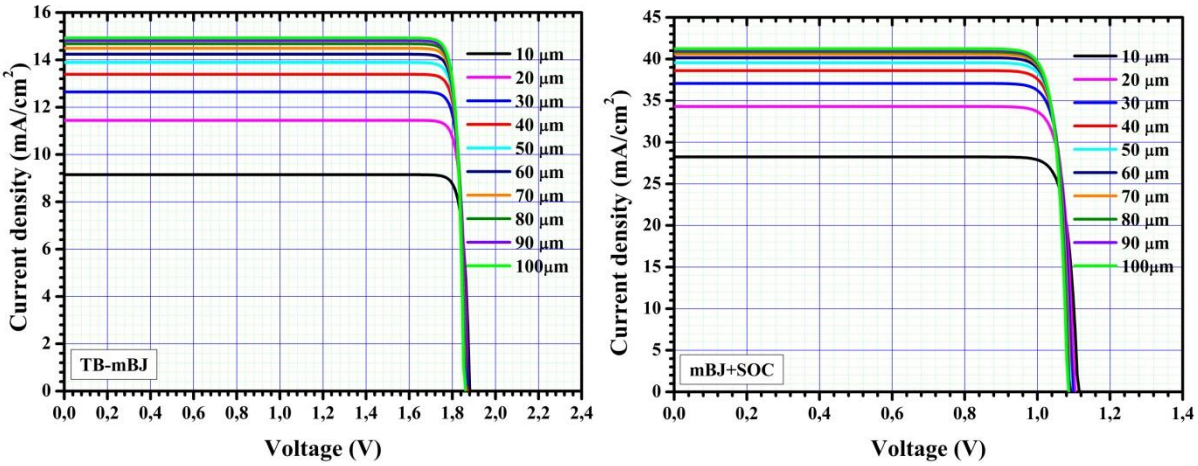

Figure IV-13. Current density-voltage (J-V) characteristics of SF_3PbI_3 solar cells for various thicknesses (10 µm to 100 µm).

Figure IV-13 displays current density-voltage (J-V) characteristics for SF_3PbI_3 solar cells with varying thicknesses, comparing two different calculation methods: TB-mBJ (top graph) and mBJ + SOC (bottom graph). The top graph shows that the current density remains relatively stable across different thicknesses up to a voltage of approximately 1.6 V, after which it drops sharply. The maximum current density achieved is around 16 A/cm². In contrast, the bottom graph (mBJ + SOC) indicates a higher overall current density, reaching up to 45 A/cm². This increase highlights the significant impact of spin-orbit coupling (SOC) on enhancing the current density in SF_3PbI_3 solar cells. Both graphs demonstrate that as the thickness of the material increases from 10 µm to 100 µm, the current density remains largely unchanged up to the critical voltage point, indicating consistent performance across different thicknesses. However, the mBJ + SOC method results in a lower voltage threshold

(approximately 1.2 V) for the sharp decline in current density, compared to TB-mBJ, suggesting that SOC influences the operational voltage range of the material.

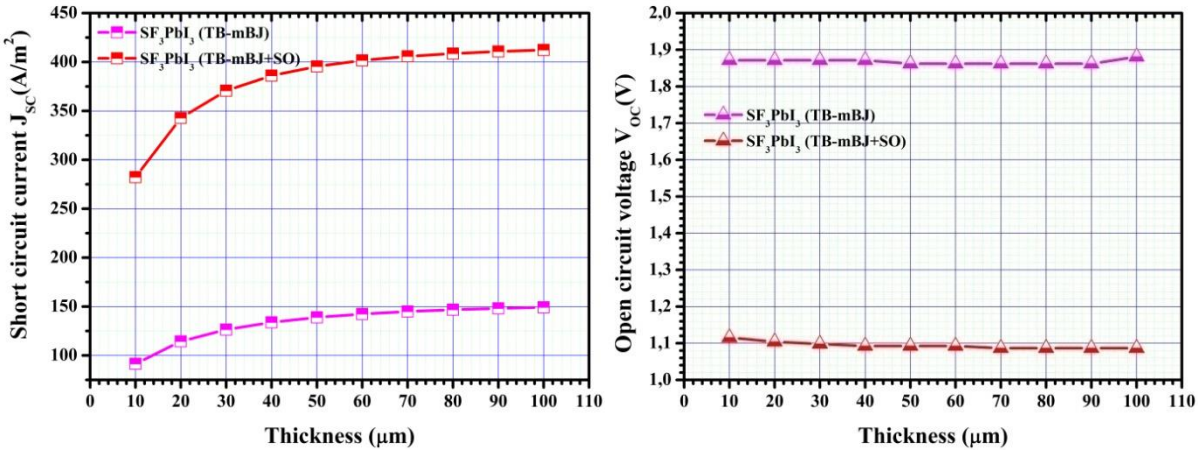

Figure IV-14. Variation of short circuit current density (J_{SC}) and open circuit voltage (VOC) with the thickness of SF_3PbI_3-based photovoltaic devices.

Figure IV-14 presents the variation of short circuit current density (J_{SC}) and open circuit voltage (V_{OC}) with SF_3PbI_3 thickness in photovoltaic devices, comparing outcomes with and without spin-orbit coupling (SOC). J_{SC} increases with thickness up to approximately 60-70 µm, indicating enhanced light absorption and subsequent charge carrier generation. The curve with SOC consistently exhibits higher JSC values compared to the curve without SOC across all thicknesses, highlighting the role of SOC in improving charge separation and transport efficiency. Conversely, V_{OC} remains relatively stable across different thicknesses for both cases, with SOC showing a slight reduction in V_{OC} compared to without SOC, likely influenced by spin-polarized states affecting recombination dynamics.

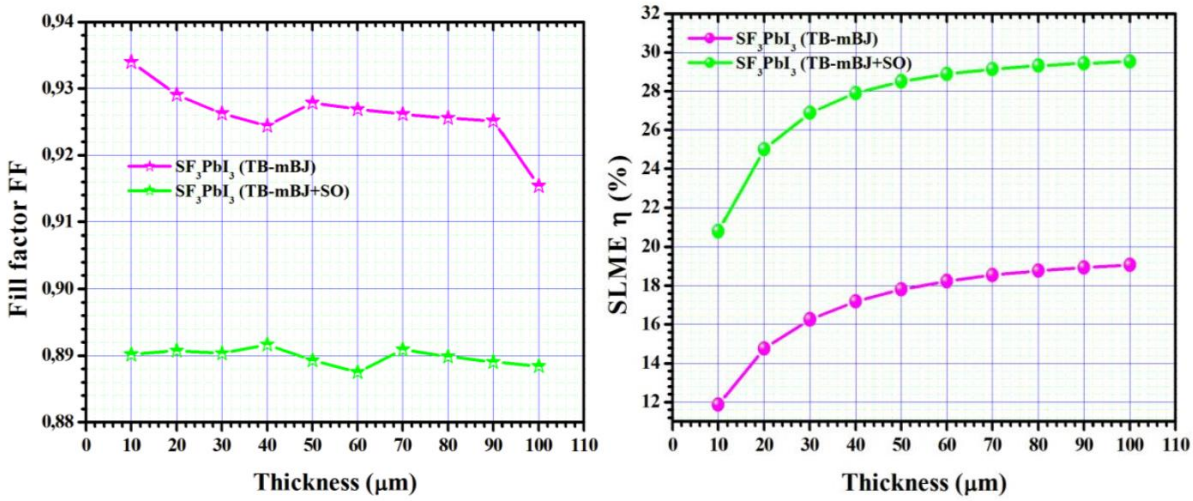

Figure IV-15. Variation of Fill Factor (FF) and Spectroscopic Limited Maximum Efficiency (SLME) with thickness of SF_3PbI_3-based photovoltaic devices.

Figure IV-15 illustrates the fill factor (FF) and spectroscopic limited maximum efficiency (SLME) as functions of SF_3PbI_3 thickness in photovoltaic devices, comparing outcomes with and without spin-orbit coupling (SOC). The FF shows a relatively stable trend with minor fluctuations for both cases, starting slightly higher and maintaining consistency in devices without SOC compared to those with SOC, where FF is consistently lower across all thicknesses. This suggests that SOC, while enhancing J_{SC}, may compromise FF due to increased recombination losses or other complex effects on charge transport. The SLME increases with thickness, reaching peak efficiency at thicker layers, indicating enhanced light absorption. The curve with SOC consistently exhibits higher SLME values compared to the curve without SOC, reflecting the positive impact of SOC on current generation and overall efficiency. Despite SOC leading to a slight reduction in V_{OC} and FF, its significant enhancement of J_{SC} underscores its potential in optimizing SF_3PbI_3-based photovoltaic performance, emphasizing a balance between current density and voltage output for maximum efficiency in solar cell applications.

Table IV-5. Solar cell parameters of SF_3PbI_3 at T = 300 K. Here P–V characteristics of perovskite are calculated at L = 70 µm thickness in case of SLME approach.

Methods	Jsc (A/ m2)	Voc (eV)	η (%)	FF
TB-mBJ	144,909	1,861	18,537	0,926
TB-mBJ +SO	405,760	1,086	29,135	0,890

IV-5 Implications for Photovoltaic and Spintronic Applications

The coexistence of ferroelectricity and Rashba spin splitting in SF_3PbI_3 holds significant promise for enhancing the performance of photovoltaic devices. By leveraging these two properties, improved charge separation and reduced recombination losses can be achieved, leading to higher overall efficiency. The ability to control polarization states provides an additional mechanism to dynamically optimize device performance, making SF_3PbI_3 a versatile material for next-generation solar cells. This potential is illustrated in **Table IV-6**, which examines the effects of off-center displacements of Pb, I, and S atoms in SF_3PbI_3 on spontaneous polarization, Rashba parameters, and SLME.

Table IV-6. Effects of Off-Center Displacements of Pb, I, and S Atoms in SF_3PbI_3 on Spontaneous Polarization, Rashba Parameters, and SLME. The results correspond to changes in the polarization state.

Structures	Polarization (C/m^2)	Rashba parameters α (eVÅ) at R		SLME η (%) at *L* = 70 µm
		α_{Rv}	α_{Rc}	
0 (at equilibrium positions)	0.53334	0.4392	0.7143	29,135
1 (with Pb-distortion)	1.11904	0.8441	2.8138	29.434
2 (with S-distortion)	1.13452	0.8253	1.7307	28.723
3 (with I-distortion)	1.14979	0.7290	2.0522	28.097

At equilibrium positions, the compound exhibits a polarization of 0.5333 C/m^2, with Rashba parameters α_{Rv} and α_{Rc} at 0.4392 eVÅ and 0.7143 eVÅ, respectively, and an SLME of

29.135%. With Pb-distortion, polarization increases to 1.1190 C/m², α_{Rv} and α_{Rc} rise significantly to 0.8441 eVÅ and 2.8138 eVÅ, respectively, and SLME improves to 29.434%. S-distortion results in a polarization of 1.13452 C/m², α_{Rv} and α_{Rc} values of 0.8253 eVÅ and 1.7307 eVÅ, respectively, and an SLME of 28.723%. I-distortion shows the highest polarization at 1.1497 C/m², with α_{Rv} and α_{Rc} at 0.7290 eVÅ and 2.0522 eVÅ, respectively, but a slightly lower SLME of 28.097%. These results indicate that structural distortions in SF_3PbI_3 can significantly enhance its ferroelectric properties and Rashba effect, albeit with varying impacts on photovoltaic efficiency. The increased polarization and Rashba parameters, particularly with Pb and I distortions, suggest improved charge separation and spintronic potential, underscoring the suitability of the material for applications in memory storage, sensors, and advanced photovoltaic devices. Additionally, the presence of strong Rashba spin splitting opens up new avenues for spintronic applications, where the manipulation of spin states through electric fields can lead to the development of efficient spin-based transistors, memory devices, and quantum computing elements.

IV-5.1. Electronic properties

To examines the effects of off-center displacements of Pb, I, and S atoms in SF_3PbI_3 on the electronic properties , we calculated band structures using mBJ potential with and without spin–orbit coupling (SOC). The band structure, displayed in Figure IV-16, presents a distinct large linear spin-splitting around the R symmetry point, resembling the well known Rashba-effect. The characteristic splitting happens both around the M and R symmetry points. We used mBJ + SOC potentials to investigate the band gaps values of Pb-distortion (Eg = 1.408 eV), S-distortion (E_g = 1.391 eV) and I-distortion (Eg = 1.547 eV). Our calculated values of band gaps indicate that these halides can be operated in optoelectronic device, because their values lie in the visible of electromagnetic spectrum. Also, the off-center displacements of Pb, I, and S atoms in SF_3PbI_3 doesn't effects the nature of band gap.

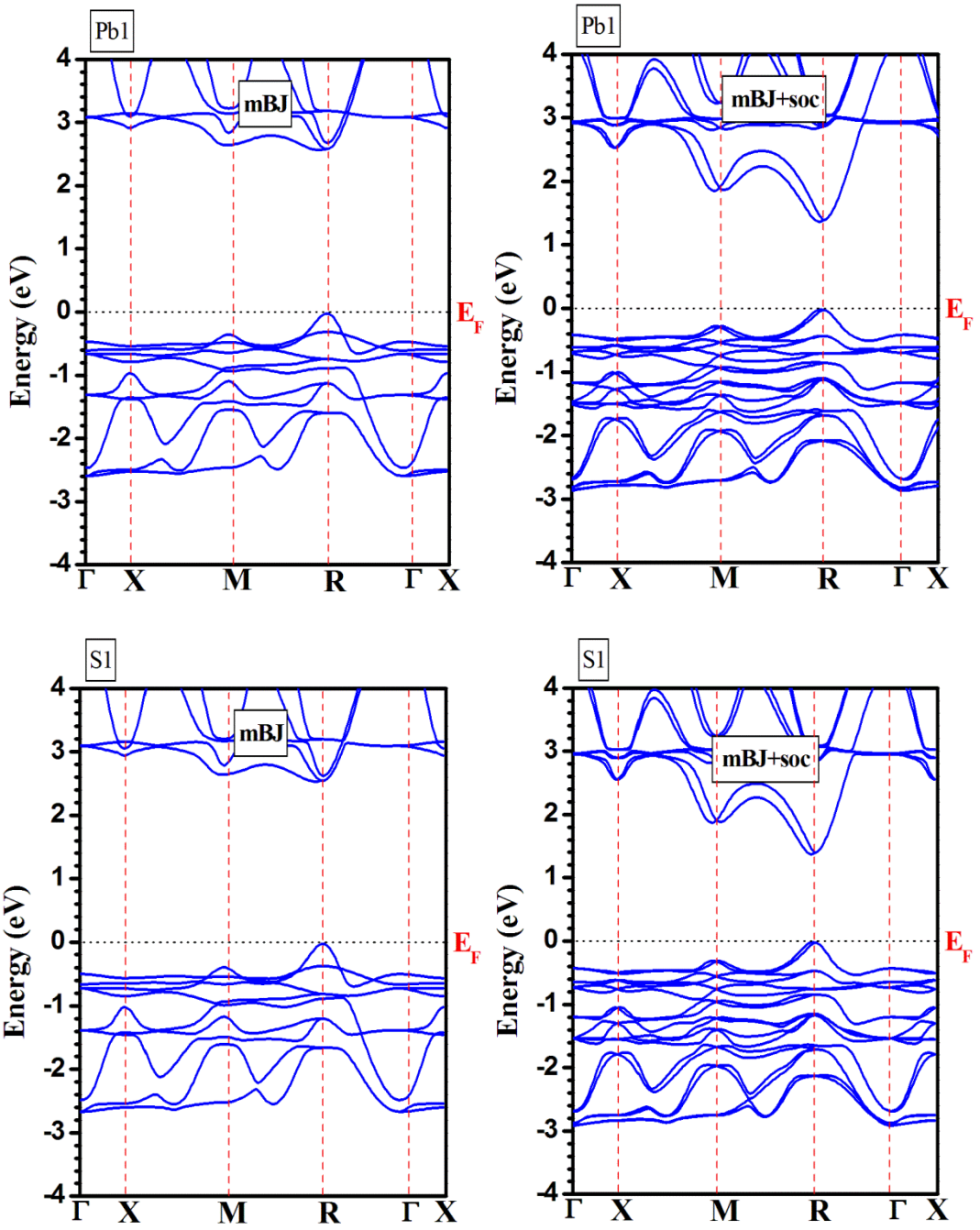
Pb1
mBJ
Energy (eV)
E_F
Γ X M R Γ X
Pb1
mBJ+soc
Energy (eV)
E_F
Γ X M R Γ X
S1
mBJ
Energy (eV)
E_F
Γ X M R Γ X
S1
mBJ+soc
Energy (eV)
E_F
Γ X M R Γ X

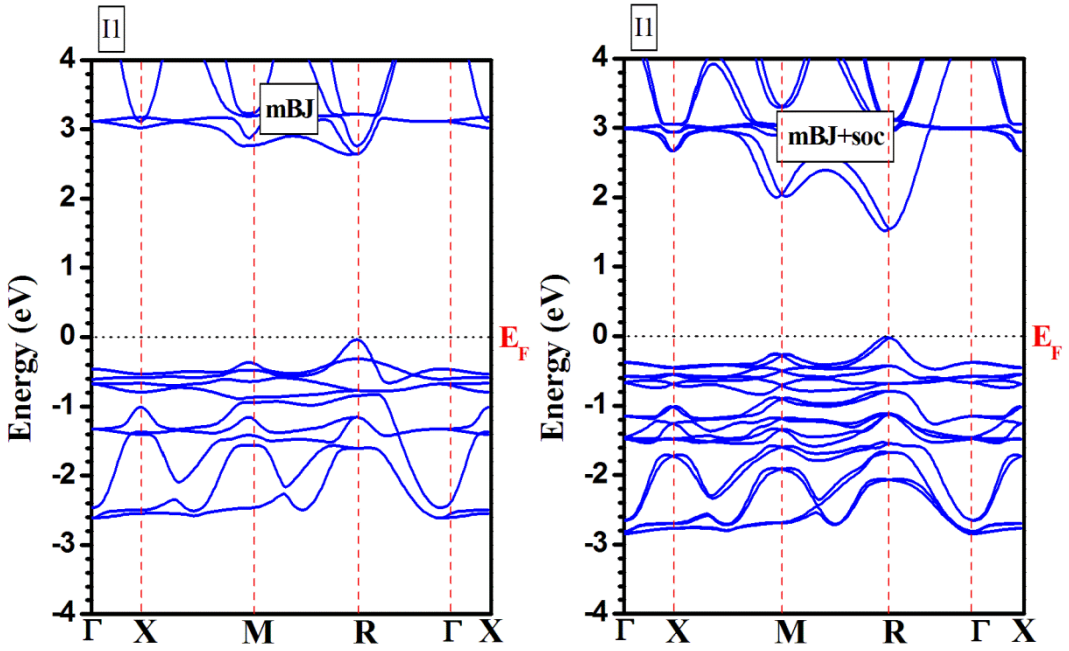

Figure IV-16. The calculated band structures using mBJ without and with SOC for studies compounds

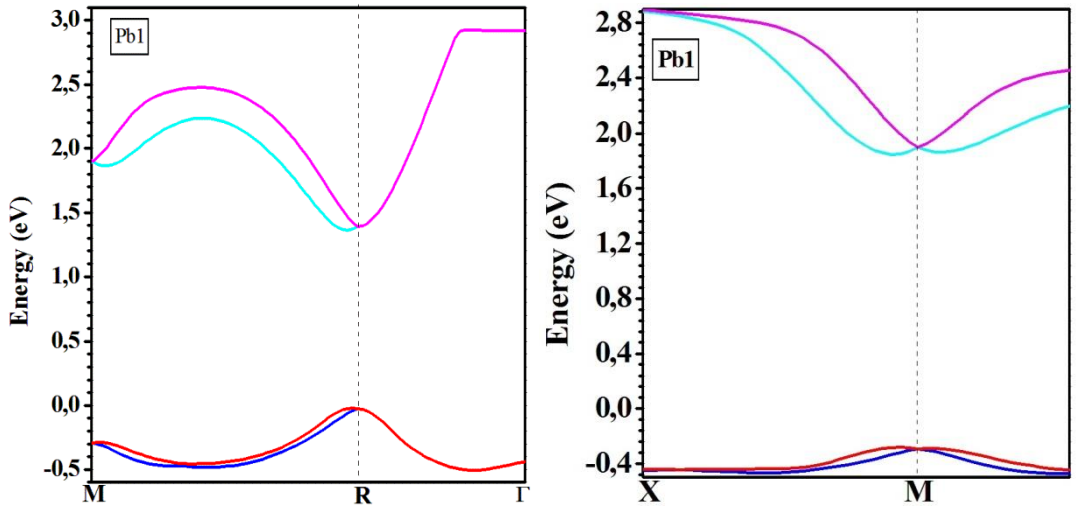

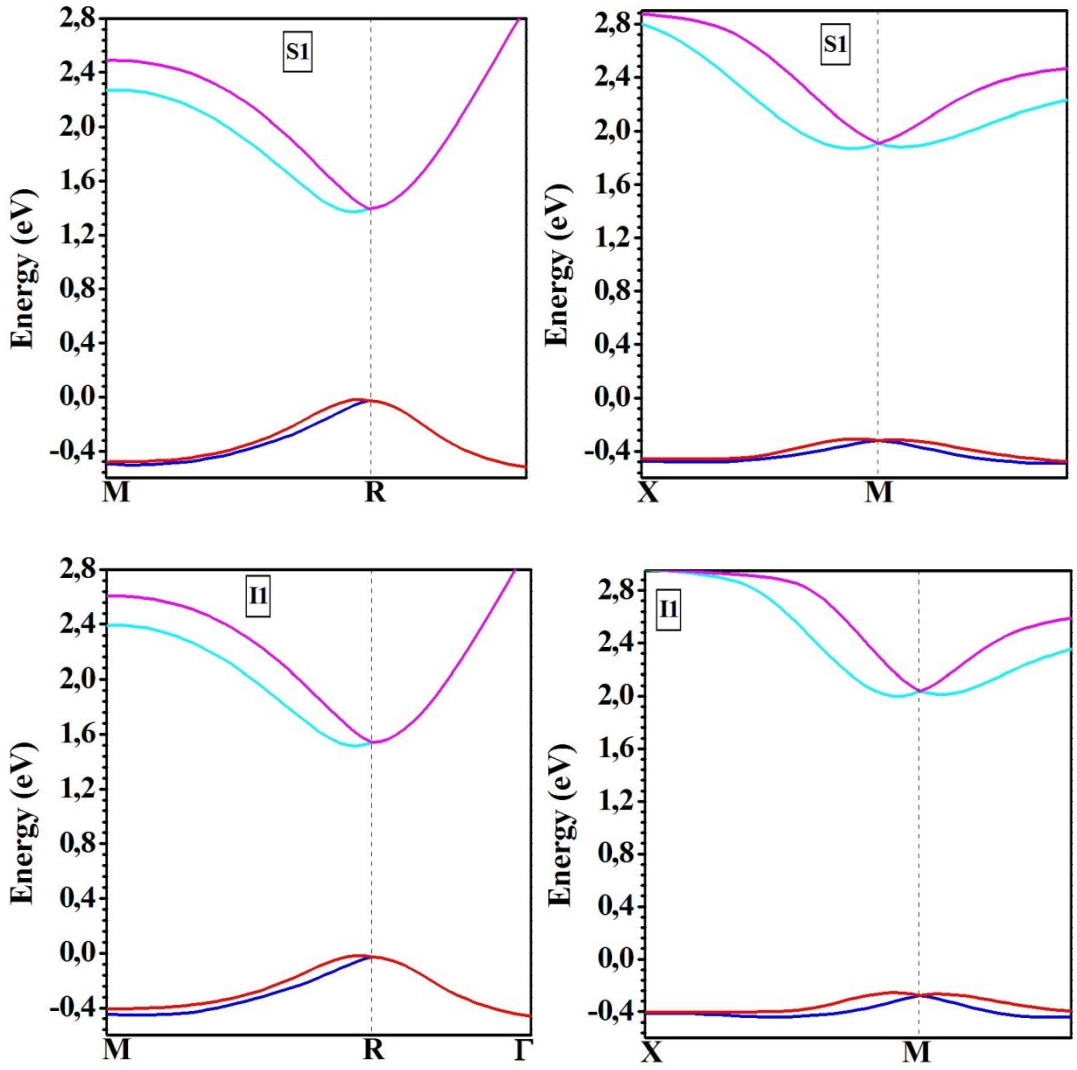

Figure IV-17. Electronic band structure of studies compounds showing Rashba spin splitting

IV-5.2. Optical properties

The absorption coefficient α(ω) can be calculated by [32]

$$\alpha(\omega) = \frac{4\pi k(\omega)}{\vartheta} \quad (7)$$

Figure 7 illustrates the spectrum of the absorption coefficient α(ω) of titled compounds It is evident from Figure 7 that these systems exhibit remarkable capability for optical absorption. This strong absorption characteristic can be attributed to their well-suited electronic properties. The absorption edges for Pb-distortion, S-distortion, and I-distortion are determined as 1.407 eV, S-distortion 1.381 eV and I-distortion 1.621 eV with TB-mBJ+SO respectively, which align with the calculated band gaps. Notably, dominant

absorption and a red shift in absorption edge is obvious resulting from a reduction in the energy band gap when we use spin orbit coupling approximation. Furthermore, The first maxima $\alpha_{xx}(\omega)$ and $\alpha_{zz}(\omega)$ for analyzed compounds are in visible region . On the other hand, in this compound, the first absorption peaks result from electron transitions between I-5p and Pb-6p orbitals. The higher values of $\alpha(\omega)$ demonstrated the greatest amount of electromagnetic radiation in visible and UV region. The excellent optical absorption beyond the optical band gap, demonstrated that these systems are suitable for commercial photovoltaic purposes.

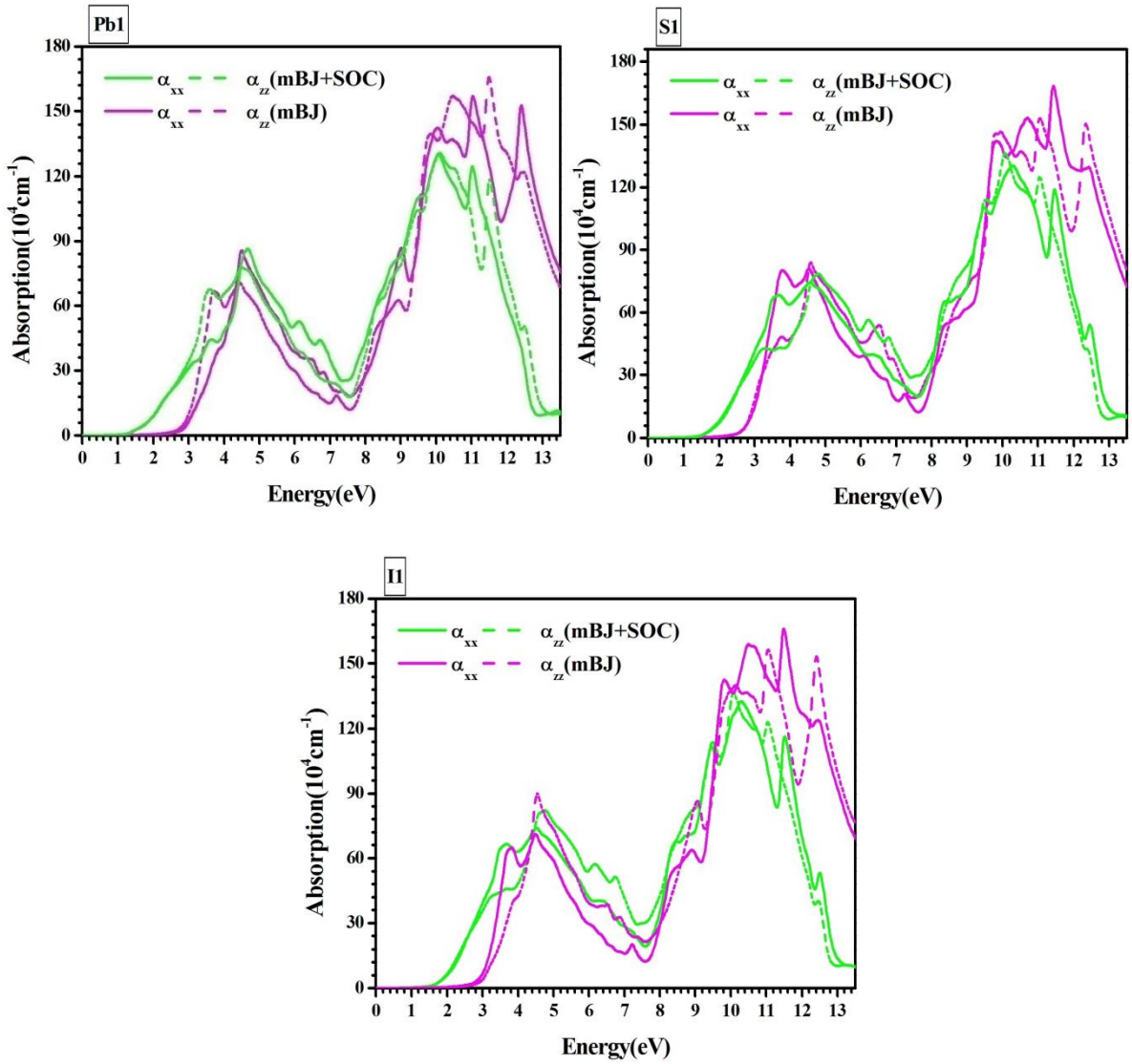

Figure IV-18. Absorption spectra of studies compounds as a function of energy, displaying anisotropic optical properties with distinct absorption coefficients (α_{xx} and α_{zz}) in the *xx* and *zz* directions.

IV-5.3. Solar cell parameters

An effective measure for evaluating the efficiency of a solar absorber in photovoltaics is the spectroscopic-limited maximum efficiency (SLME) criteria [33] . As a result, we employed the SLME metric to forecast solar cell characteristics of the studies perovskite absorber layer as a function to their varying thickness, because the stability and efficiency of perovskite solar cells (PSCs) are affected by the thickness of the absorber layer they contain. The J_{sc} for the compound have been calculated using following equation [32]

$$J_{SC} = \int_0^{\infty} eA(E)I_{sun}(E)dE \tag{8}$$

Here, the absorptivity is denoted by A(E), the elementary charge is represented by e, and the photon flux density is represented by I_{sun}(E), which is derived from the AM1.5G spectrum [34] The equation provided below [35] is employed to derive the values of A(E)

$$A(E) = 1 - e^{-2\alpha(E)L} \tag{9}$$

Where L denotes the thickness of an absorber layer with a reflecting back surface. The formula to calculate J_o is as follows [36]

$$J_0 = \int_0^{\infty} e\pi A(E)I_{bb}(E,T)dE \quad = \int_0^{\infty} e\pi A(E)\frac{2E^2}{h^3c^2}\frac{dE}{e^{\frac{E}{KT}}-1} \tag{10}$$

In eqn (9), T is the temperature of the solar cell, and k is the Boltzmann constant. The expression I_{bb}(E, T) in equation (8) symbolizes the black body spectrum, which is further elaborated in equation (9). When employing the SLME approach, the calculation of Jo disregards the proportion of radiative recombination, as its value equals 1 for a direct bandgap semiconductor. Ultimately, the value of 'J' is determined using the equation provided below [35]

$$J = J_{SC} - J_0(e^{\frac{eV}{KT}} - 1) \tag{11}$$

Where, V signifies the potential across the absorber layer. Utilizing equation iv-11 , a plot illustrating the J-V characteristics can be generated for this compounds ,The power density (P = JV) curve enables the prediction of Pm, which in turn allows for the calculation of the maximum efficiency (η) [36]

$$\eta = \frac{P_m}{P_{in}} \quad (12)$$

In equation iv-12, P_{in} denotes the cumulative incident power density, which is set at 1000 W/m2 for the AM1.5G spectrum. Subsequently, the fill factor (FF) for all materials was computed using the equation below [37]

$$FF = \frac{\vartheta_{OC} - In(\vartheta_{OC} + 0.75)}{\vartheta_{OC} + 1}; \quad (13)$$

$$\vartheta_{OC} = \frac{qxV_{OC}}{KT} \quad (14)$$

In this context, we have computed the short circuit current density (J_{sc}) for varying material thickness, as illustrated in **Figure IV-19**. It is evident from **Figure IV-19** that the Jsc of the absorber material reaches a saturation point beyond a certain thickness. By incorporating these determined Jsc values into equation (IV-11) and applying equation (IV-12) , we derived the SLME efficiency for this material across different thicknesses. The calculated SLME values for our compounds are presented in **Figure IV-20**. According to **Figure IV-20 ,**the SLME efficiency of this materials show a smoothly gradual increasing as the thickness increases .Indeed, the efficiency of these materials are notably responsive to the precise values of their band gaps. Meanwhile, to further investigate open circuit voltage (V_{OC}) we describe the results in **Figure IV-20** which demonstrated that the (V_{OC}) is independent from the absorber thickness. Additionally, the fill factor (FF) was determined as a function of thickness, as illustrated in **Figure IV-20.** Consequently, our thorough analysis of Photovoltaic Performances indicates that this compounds offer optimal Performances as visible-light absorbing materials for PV applications.

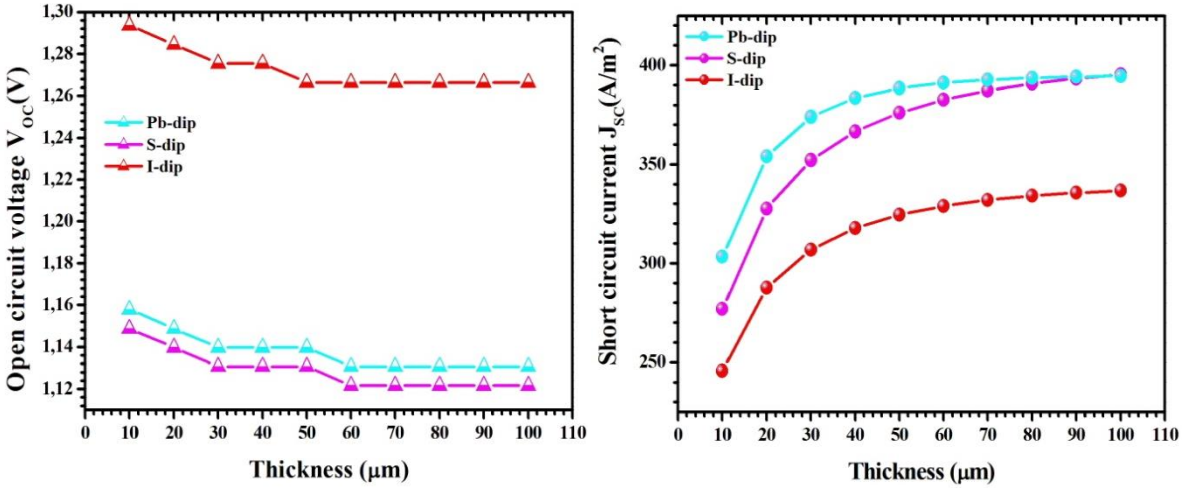

Figure IV-19. open circuit voltage (V_{OC}) and short circuit current density (J_{sc}) with thickness of studies compounds.

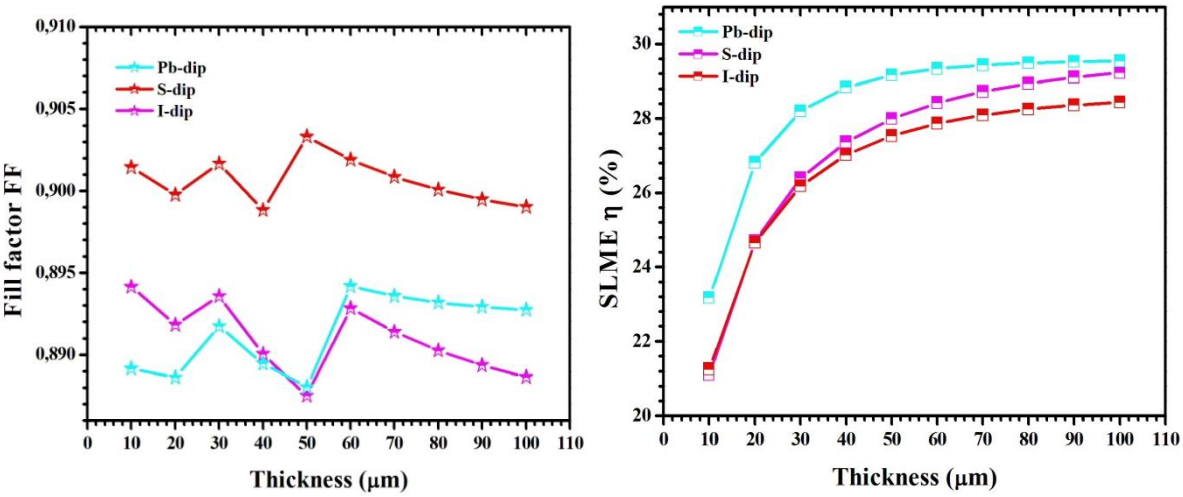

Figure IV-20. Variation of Fill Factor (FF) and Spectroscopic Limited Maximum Efficiency (SLME) with thickness of studies compounds .

IV-5 Conclusion

We present a comprehensive computational study on the compound SF_3PbI_3, a member of the polar halide perovskite family, underscoring its potential for photovoltaic and spintronic applications due to its unique ferroelectric and Rashba spin splitting properties. Utilizing density functional theory (DFT) calculations, this study investigates the electronic band

structure, optical properties, and ferroelectric behavior of SF_3PbI_3. The compound exhibits strong spin-orbit coupling, attributed to the presence of heavy elements like lead and iodine, leading to Rashba splitting near the electron band extrema. This effect enhances charge separation and reduces recombination losses, which is beneficial for photovoltaic applications.

Additionally, the study explores the phenomenon of distortion-induced polarization switching within SF_3PbI_3. At its equilibrium state, the compound shows low ferroelectric polarization due to a pseudo-symmetric atomic arrangement. However, controlled distortions—potentially arising from temperature changes, external pressure, or lattice imperfections—can induce a transition to a high polarization state with a strengthened dipole moment. This transition occurs with a low energy barrier, making SF_3PbI_3 a promising candidate for next-generation devices in memory storage, sensors, and energy harvesting. The tunability of its Rashba parameters via structural distortions provides a versatile platform for designing spintronic devices with optimized performance, integrating ferroelectric control with spintronic functionality. Thus, SF_3PbI_3 stands out as a multifaceted material with significant potential for advancements in both photovoltaic efficiency and spintronic technology.

Bibliography

[1] Kutes, Y., et al. "Direct observation of ferroelectric domains in solution-processed CH3NH3PbI3 perovskite thin films." Journal of Physical Chemistry Letters, vol. 5, no. 19, 2014, pp. 3335-3339.

[2] Niesner, D., et al. "Giant Rashba splitting in CH3NH3PbBr3 organic-inorganic perovskite." Physical Review Letters, vol. 117, no. 12, 2016, p. 126401.

[3] Catalan, G., et al. "Domain wall nanoelectronics." Nature Reviews Materials, vol. 1, no. 2, 2016, p. 16035.

[4] Bibes, M., and A. Barthélémy. "Multiferroics: Towards a magnetoelectric memory." Nature Materials, vol. 7, no. 6, 2008, pp. 425-426.

[5] Cao, T., et al. "Valley-selective circular dichroism of monolayer molybdenum disulphide." Nature Communications, vol. 3, 2012, p. 887.

[6] Yu, P., et al. "Interface control of bulk ferroelectric polarization." Proceedings of the National Academy of Sciences, vol. 109, no. 24, 2012, pp. 9710-9715.

[7] Zhang, Q., et al. "Sulfur Incorporation in Perovskite Materials: A Review on Methods and Impacts." Advanced Energy Materials 8 (2018): 1702102.

[8] Jiang, L., et al. "Giant Rashba Splitting in Two-Dimensional Organic-Inorganic Halide Perovskites." Physical Review B 96, no. 20 (2017): 205305.

[9] Motta, C., et al. "Enhanced Charge Carrier Mobility in Two-Dimensional Perovskites: The Role of Rashba Spin-Orbit Coupling." Journal of the American Chemical Society 139, no. 27 (2017): 9413-9419.

[10] E.Rashba and V.Sheka,Fiz. Tverd.Tela:Collected Paper,162(1959).

[11] Pazoki, M., Imani, R., Röckert, A., & Edvinsson, T. (2022). Electronic structure of 2D hybrid perovskites: Rashba spin–orbit coupling and impact of interlayer spacing. Journal of Materials Chemistry A, 10(39), 20896-20904.

[12] Blaha, et al. (2019). WIEN2k: An Augmented Plane Wave Plus Local Orbitals Program for Calculating Crystal Properties. Techn. Universitat.

[13] Perdew, J. P., Burke, K., & Ernzerhof, M. (1996). Generalized gradient approximation made simple. Physical Review Letters, 77(18), 3865.

[14] Koller, D., Tran, F., & Blaha, P. (2012). Improving the modified Becke-Johnson exchange potential. Physical Review B, 85(15), 155109.

[15] Gmitra, M., Konschuh, S., Ertler, C., Ambrosch-Draxl, C., & Fabian, J. (2009). Band-structure topologies of graphene: Spin-orbit coupling effects from first principles. Physical Review B—Condensed Matter and Materials Physics, 80(23), 235431.

[16] Patel, S., Dey, U., Adhikari, N. P., & Taraphder, A. (2022). Electric field and strain-induced band-gap engineering and manipulation of the Rashba spin splitting in Janus van der Waals heterostructures. Physical Review B, 106(3), 035125.

[17] Fabini, D. H., Koerner, M., & Seshadri, R. (2019). Candidate inorganic photovoltaic materials from electronic structure-based optical absorption and charge transport proxies. Chemistry of Materials, 31(5), 1561-1574.

[18] Murnaghan, F. D. (1944). The compressibility of media under extreme pressures. Proceedings of the National Academy of Sciences, 30, 244–247.

[19] Murtaza, H., et al. (2024). Scrutinize the physical attributes of thermodynamically and elastically stable double perovskite oxides Ba2CdXO6 (X= Mo, U) for optoelectronics, photocatalytic and green technology, 232, 112674.

[20] Tenuta, E., Zheng, C., & Rubel, O. (2016). Thermodynamic origin of instability in hybrid halide perovskites. Scientific Reports, 6(1), 37654.

[21] Andri, M. K., & Absor, M. A. U. (2019, April). K-space Orientation Dependent of the Spin Texture in SF3PbI3 Perovskite Compounds. IOP Conference Series: Materials Science and Engineering, 515(1), 012060.

[22] Bhumla, P., Gill, D., Sheoran, S., & Bhattacharya, S. (2021). Origin of Rashba spin splitting and strain tunability in ferroelectric bulk CsPbF3. The Journal of Physical Chemistry Letters, 12(39), 9539-9546.

[23] He, Y., & Galli, G. (2014). Perovskites for solar thermoelectric applications: A first principles study of CH3NH3AI3 (A = Pb and Sn). Chemistry of Materials, 26, 5394–5400.

[24] Sedighi, R., Tajabadi, F., Shahbazi, S., Gholipour, S., & Taghavinia, N. (2016). Mixed-halide CH3NH3PbI3−xXx (X=Cl, Br, I) perovskites: Vapor-assisted solution deposition and application as solar cell absorber. ChemPhysChem, 17(1), 2382–2388.

[25] M. Fox, G.F. Bertsch, Optical properties of solids, Am. J. Phys. 70 (12) (2002) 1269–1270.https://www.mdpi.com/2079-4991/13/7/1245

[26] Paillard, C., Bai, X., Infante, I. C., Guennou, M., Geneste, G., Alexe, M., ... & Dkhil, B. (2016). Photovoltaics with ferroelectrics: current status and beyond. Advanced Materials, 28(26), 5153-5168.

[27] Wang, H., Adamski, N., Mu, S., & Van de Walle, C. G. (2021). Piezoelectric effect and polarization switching in Al1− xScxN. Journal of Applied Physics, 130(10).

[28] Li, Y. Q., Wang, X. Y., Zhu, S. Y., Tang, D. S., He, Q. W., & Wang, X. C. (2022). Enhanced vertical polarization and ultra-low polarization switching barriers of two-dimensional SnS/SnSSe ferroelectric heterostructures. Journal of Materials Chemistry C, 10(33), 12132-12140.

[29] Li, C., Guerrero, A., Zhong, Y., & Huettner, S. (2017). Origins and mechanisms of hysteresis in organometal halide perovskites. Journal of Physics: Condensed Matter, 29(19), 193001.

[30] Guo, L., Hu, S., Gu, X., Zhang, R., Wang, K., Yan, W., & Sun, X. (2023). Emerging spintronic materials and functionalities. Advanced Materials, 2301854.

[31] Krempaský, J., Muff, S., Minar, J., Pilet, N., Fanciulli, M., Weber, A. P., ... & Dil, J. H. (2018). Operando imaging of all-electric spin texture manipulation in ferroelectric and multiferroic Rashba semiconductors. Physical Review X, 8(2), 021067.

[32] M. Bercx, N. Sarmadian, R. Saniz, B. Partoens, D. Lamoen, First-principles analysis of the spectroscopic limited maximum efficiency of photovoltaic absorber layers for CuAu-like chalcogenides and silicon, Phys. Chem. Chem. Phys. 18 (2016), 20542, https://doi.org/10.1039/C6CP03468C. –20549.

[33] Yu, L., & Zunger, A. (2012). Identification of Potential Photovoltaic Absorbers Based on First-Principles Spectroscopic Screening of Materials. Physical review letters, 108(6), 068701.

[34] Reference air mass 1.5, Spectra | Grid Modernization | NREL, (n.d.) (2021). https://www.nrel.gov/grid/solar-resource/spectra-am1.5.html.

[35] N.N. Som, V. Sharma, V. Mankad, M.L.C. Attygalle, P.K. Jha, Role of CuAlO2 as an absorber layer for solar energy converter, Sol. Energy 193 (2019) 799–805, https://doi.org/10.1016/J.SOLENER.2019.09.098.

[36] M. Bercx, R. Saniz, B. Partoens, D. Lamoen, Exceeding the shockley-queisser limit within the detailed balance framework, many-body approaches at different scales: a tribute to

norman H, March on the Occasion of His 90th Birthday (2018) 177–184, https://doi.org/10.1007/978-3-319-72374-7_15/COVER

[37] M. Leilaeioun, Z.C. Holman, Accuracy of expressions for the fill factor of a solar cell in terms of open-circuit voltage and ideality factor, J. Appl. Phys. 120 (2016), 123111, https://doi.org/10.1063/1.4962511.

Chapter V:

Photoconversion efficiency of polar double Iodide perovskite (CsRb)(GeSn)I_6

Chapter V Photoconversion efficiency of polar double Iodide perovskite $(CsRb)(GeSn)I_6$

V-1. Introduction

Ferroelectric materials have garnered significant attention in recent years due to their promising potential in photovoltaic (PV) applications. This interest stems primarily from their intrinsic bulk polarization, which can enhance effective charge carrier separation and transport—advantages that traditional PV materials do not inherently possess [1-3]. Unlike conventional p-n junction photovoltaics, where the open-circuit voltage is directly related to the bandgap, ferroelectric materials can achieve open-circuit voltages independent of their bandgap, potentially resulting in significantly higher voltages [4-5]. This unique property opens up new avenues for improving the efficiency of solar cells.For example, bismuth ferrite ($BiFeO_3$) has been extensively studied and shown to exhibit photovoltaic effects due to its ferroelectric properties, making it a strong candidate for novel PV applications [2, 3]. Another promising material is Bi_2FeCrO_6, which has demonstrated power conversion efficiencies (PCEs) of 8.1%, highlighting the practical potential of ferroelectric materials in real-world applications [6]. Additionally, theoretical models have predicted that ferroelectric hexagonal terbium manganite ($TbMnO_3$) could achieve efficiencies as high as 33%, showcasing the immense potential these materials hold for future PV technologies [7].

Despite these promising attributes, ferroelectric materials face significant challenges that impede their efficiency in photovoltaic applications. One major issue is their large bandgaps. The ideal photovoltaic material should have a bandgap close to the optimal solar range, around 1.1 eV, to maximize the absorption of solar radiation and enhance the generation of electron-hole pairs. However, most ferroelectric materials, particularly oxides and fluorides, exhibit wide bandgaps that exceed 3 eV. This large bandgap limits their ability to absorb visible light, thereby reducing the overall number of photo-generated carriers and subsequently lowering the efficiency of solar energy conversion [8].Another challenge is the robust exciton binding energies observed in ferroelectric materials. Excitons, which are bound states of electrons and holes, require a certain amount of energy to dissociate into free charge carriers that can contribute to the electric current. In ferroelectrics, the high exciton binding energies make it difficult for these excitons to separate, thus hindering effective charge carrier generation and transport [9].Limited charge carrier mobility is also a significant obstacle. For a photovoltaic material to be efficient, it must facilitate the rapid

movement of charge carriers to the electrodes to minimize recombination losses. However, many ferroelectric materials have low charge carrier mobilities due to their complex crystal structures and the presence of defects, which act as traps for charge carriers. This limited mobility results in increased recombination rates, further reducing the efficiency of the photovoltaic device [10].These challenges highlight the need for continued research and development to enhance the photovoltaic performance of ferroelectric materials. Potential strategies include bandgap engineering to reduce the bandgap, doping to improve charge carrier mobility, and the development of composite materials that combine the beneficial properties of ferroelectrics with those of other photovoltaic materials. By addressing these issues, the full potential of ferroelectric materials in solar energy applications can be more effectively realized [11].

To address these challenges, there is a growing interest in exploring alternative ferroelectric materials, specifically halide perovskites. Halide perovskites are known for their narrow bandgaps and high absorption coefficients [12], making them attractive candidates for solar cells. These materials have demonstrated exceptional performance in photovoltaic applications due to their favorable electronic properties, such as high carrier mobilities, long carrier lifetimes, and tunable bandgaps. Furthermore, halide perovskites can be processed using low-cost solution-based methods, making them economically viable for large-scale production [13]. In this context, we turn our focus to the polar double iodide perovskite (CsRb)(SnGe)I_6. This material has previously been studied for its ferroelectric properties by Young et al. [14], who demonstrated the induction of spontaneous electric polarizations through a hybrid improper ferroelectric mechanism. This mechanism involves the coupling of multiple lattice instabilities, leading to a robust polarization that can be manipulated by external electric fields. The presence of such a mechanism in (CsRb)(SnGe)I_6 indicates strong potential for efficient charge separation and transport, key factors for enhancing photovoltaic performance. Despite the promising ferroelectric properties, the photovoltaic properties of (CsRb)(SnGe)I_6 have not yet been explored. Investigating these properties could provide new insights into its potential for solar energy conversion. The material's narrow bandgap suggests it could absorb a significant portion of the solar spectrum, while its ferroelectric nature could facilitate efficient charge separation and reduce recombination losses [15]. Additionally, the use of mixed cations (Cs and Rb) and mixed metal ions (Sn and

Ge) in the perovskite structure may offer further tunability of the electronic and optical properties, potentially optimizing the material for solar cell applications [16].

This study aims to conduct a thorough investigation of the structural, electronic, and optical properties of $(CsRb)(SnGe)I_6$ using first-principles density functional theory (DFT). Our primary focus is to elucidate how its unique characteristics enhance absorption in the visible spectrum and assess its overall suitability for photovoltaic applications. Specifically, we analyze the band structure and absorption coefficient of $(CsRb)(SnGe)I_6$ to understand its potential for efficient solar energy conversion. Additionally, we evaluate the photovoltaic performance of $(CsRb)(SnGe)I_6$ using the Spectroscopic Limited Maximum Efficiency (SLME) model, which offers a more accurate prediction of solar cell efficiency compared to the traditional Shockley-Queisser limit. The SLME model incorporates critical factors such as absorption coefficient, recombination losses, and the detailed balance of carrier generation and recombination, thus providing a comprehensive and realistic assessment of the material's potential efficiency [17,18].

V-2. Computational Method

For the computation of the physical properties of $(CsRb)(SnGe)I_6$, we employed the Full Potential Linear Augmented Plane Wave (FP-LAPW) method within the framework of Density Functional Theory (DFT), utilizing the WIEN2k code [19]. The Perdew-Burke-Ernzerhof (PBE) generalized gradient approximation (GGA) was used to describe the exchange-correlation energy. To enhance accuracy, particularly in the optical and electronic property calculations, we adopted the modified Becke-Johnson (mBJ) approximation [20]. This modification addresses the common underestimation of bandgaps by standard DFT functionals (GGA).

The crystal structure was relaxed until the force acting on the atoms was less than $0.001 eVÅ^{-1}$, ensuring a stable configuration for subsequent calculations. Ferroelectric materials are characterized by their spontaneous polarization, which occurs when a crystal transitions from a centrosymmetric to a non-centrosymmetric structure. We determined the polarization using the Berry phase method with the BerryPI program, providing a precise measure of the ferroelectric properties [21].

To evaluate the photovoltaic performance of $(CsRb)(SnGe)I_6$, we utilized the Spectroscopic Limited Maximum Efficiency (SLME) model, based on first-principles calculations[17]. This model allows for an initial screening of the material's theoretical efficiency by incorporating the detailed balance of carrier generation and recombination, as well as the material's absorption spectrum. The SLME model enhances the theoretical efficiency prediction by providing a more accurate representation of the J–V characteristics in conjunction with the absorption properties of the material.

V-3. Results and Discussion

V-3.1. Structural properties

In this study, we investigated the ferroelectric double perovskite $(CsRb)(SnGe)I_6$ by introducing simultaneous cation ordering at the Cs and Rb sites in a supercell configuration derived from the centrosymmetric $CsSnI_3$, a non-ferroelectric material in its bulk form. The double perovskite $(CsRb)(SnGe)I_6$ features a layered A-site with layered B-sites ordering (which we give the notation A[001]/B[001]), where the A-sites are occupied by Cs and Rb cations, and the B-sites by Sn and Ge cations. This specific cation arrangement, combined with an $a^0a^0c^+$octahedral rotation pattern, produces a chiral vortex-like A-site displacement pattern [14]. The $a^0a^0c^+$rotation pattern refers to the tilting of the octahedra in the perovskite structure. This structural distortion breaks the centrosymmetry of the parent $CsSnI_3$phase, thereby inducing a non-centrosymmetric phase. The ordering of Cs and Rb cations at the A-sites, along with Sn and Ge at the B-sites, creates a unique environment where polarization can emerge spontaneously due to the asymmetry in the crystal structure. The calculated space group for $(CsRb)(SnGe)I_6$ is P4bm, reflecting a tetragonal structure.

The structural optimization resulted in lattice parameters of a=b=8.36 Å and c=12.28 Å, ensuring a stable crystal structure, as illustrated in Figure 1(a). The energy-volume relationship, shown in Figure 1(b), indicates that the compound achieves its lowest total energy in its optimized configuration, confirming its structural stability.Furthermore, the calculated formation energies of $CsSnI_3$, $CsGeI_3$, and $(CsRb)(SnGe)I_6$ are -1.5232 eV/atom, -0.5376 eV/atom, and -1.6832 eV/atom, respectively, demonstrating the enhanced thermodynamic stability of the double perovskite.This double perovskite configuration

presents significant advantages over its single-cation counterparts, $CsSnI_3$ and $CsGeI_3$. The inclusion of Rb improves structural stability by reducing lattice strain, while the Sn/Ge combination allows for bandgap tuning. Additionally, single-cation perovskites like $CsSnI_3$ often suffer from instability due to Sn^{2+} oxidation, while $CsGeI_3$ faces structural instability. In contrast, the mixed cation system of (CsRb)(SnGe)I_6 offers superior stability, particularly in the presence of environmental factors such as moisture, oxygen, and heat, making it a promising candidate for practical applications.

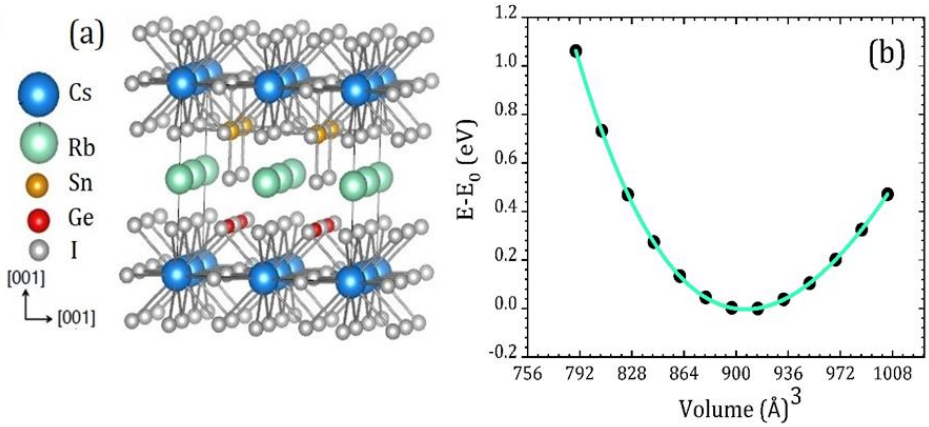

Figure V-1 : (a) Atomic arrangement of the double perovskite (CsRb)(SnGe)I_6. (b) Energy-volume relationship demonstrating the stability of (CsRb)(SnGe)I_6 in its optimized configuration.

V-3.2. Electronic Structure and Optical Properties

The electronic structure analysis of (CsRb)(SnGe)I_6 revealed it to be a semiconductor with a direct bandgap of 0.89 eV along the Γ-Γ direction, as depicted in **Figure V-2**. This value exceeds previously reported theoretical estimations [14], suggesting the potential for efficient absorption of the solar spectrum.The partial density of states (PDOS), shown in **Figure V-2(b)**, further makes clear that both the valence band maximum (VBM) and the conduction band minimum (CBM) are primarily dominated by anti-bonding molecular orbitals involving iodine and Ge (Sn) orbitals.The VBM is largely influenced by the p-orbitals of iodide ions (I^-), with significant contributions from the 5p orbitals of iodine. The presence of Sn^{2+} and Ge^{2+} introduces additional hybridization through their respective s-orbitals (Sn 5s and Ge 4s), resulting in slight modifications to the VBM position. In contrast, the CBM is

mainly derived from the p-orbitals of Sn^{2+} and Ge^{2+}, with hybridization with the iodide ions creating favorable conditions for efficient electron transport.

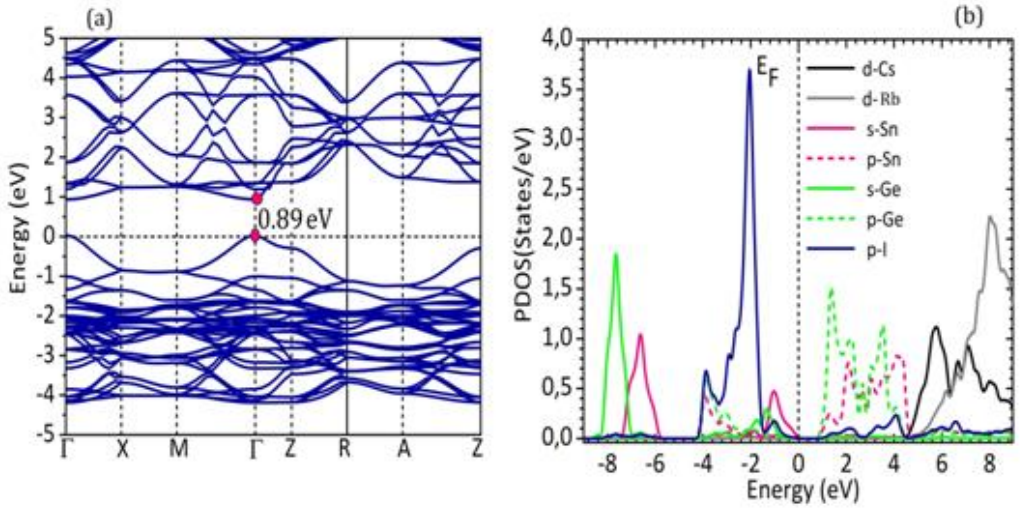

Figure V-2 : (a) Band structure of $(CsRb)(SnGe)I_6$ along high-symmetry directions in the Brillouin zone. (b) Partial densities of states (PDOS) illustrating electronic transitions near the Fermi level.

To validate the accuracy of our results obtained by the mBJ method, we have compared our calculated bandgaps of $CsPbI_3$ and $CsSnI_3$ with available experimental and theoretical values. For $CsPbI_3$, experimental studies report bandgaps in the range of 1.73–1.75 eV for the black cubic phase, which is relevant for photovoltaic applications [22, 23]. Our mBJ-GGA calculation gives a bandgap of 1.71 eV, which closely aligns with these experimental results. Additionally, GGA calculations yield a bandgap of 1.56 eV, further supporting the accuracy of our predictions [24].For $CsSnI_3$, while reliable experimental data are limited due to the compound's instability, theoretical studies provide a reference for comparison. Our mBJ-GGA calculation produces a bandgap of 1.18 eV at the Z symmetry point, which is consistent with other theoretical methods: GGA (0.942 eV), SCAN (1.108 eV), HSE06 (1.230 eV), and machine learning (0.876 eV) [25]. These comparisons show that the mBJ method provides reliable estimations of bandgaps for both $CsPbI_3$ and $CsSnI_3$, reinforcing the credibility of our approach for predicting the electronic structure of $(CsRb)(SnGe)I_6$.

To calculate the effective masses, it is necessary to fit the bands around the VBM (valence band maximum) and CBM (conduction band minimum) to a quadratic function. This is done

by identifying the k-points around the VBM and CBM from the band structure, exporting the corresponding eigenvalues, and then fitting the band dispersion using a parabolic approximation:

$$E(k) = E_0 + \frac{\hbar^2 k^2}{2m^*} \quad (1)$$

where E_0 is the energy at the VBM or CBM, and m^* is the effective mass. The effective mass is calculated from the second derivative of the energy with respect to:

$$\frac{1}{m^*} = \frac{1}{\hbar^2}\frac{d^2E}{dk^2} \quad (2)$$

Carrier mobility in a solid refers to the ability of charge carriers, such as electrons or holes, to move through the material under the influence of an electric field. This mobility is fundamentally influenced by the interactions between the carriers and the lattice structure of the solid, which consists of atoms arranged in a vibrating pattern. As carriers navigate this lattice, they experience collisions with lattice atoms and ionized impurities, leading to scattering events.

The scattering process alters the carriers' trajectories, effectively limiting their speed and overall mobility. Various mechanisms contribute to these scattering events, including interactions with acoustic phonons (vibrational energy quanta associated with sound) and optical phonons (vibrational modes associated with higher energy states). At lower temperatures, the scattering primarily from longitudinal acoustic (LA) phonons plays a significant role in determining carrier mobility.

LA phonons create disturbances in the electronic band structure, causing variations in potential energy that can impede the free movement of carriers. As a result, understanding the mechanisms of scattering, particularly from LA phonons, is crucial for optimizing the electrical properties of materials, especially in the context of semiconductor devices. The mobility of carriers due to LA phonon scattering can be quantitatively expressed through mathematical models that incorporate factors such as effective mass, deformation potential, and phonon velocity, providing insight into the material's performance in electronic applications.

The mobility due to LA phonon scattering can be expressed as:

$$\mu_\alpha = \frac{2\sqrt{2\pi}e\hbar^4 C_\alpha}{3(k_B T)^{3/2} m_\alpha^{5/2} E_\alpha^2} \quad (3)$$

Where $e, \hbar$ and k_B are the elementary charge, the reduced Planck constant, and the Boltzmann constant, respectively. T is the temperature, C_α is the elastic constant, m_α is the effective mass, and E_α is the volume deformation potential. To incorporate the average phonon velocity, v_{avg} , the elastic constant C_α can be expressed as :

$$C_\alpha \propto \rho v_{\text{avg}}^2 \quad (4)$$

Substituting this into the mobility formula yields:

$$\mu_\alpha = \frac{2\sqrt{2\pi}e\hbar^4 \rho v_{\text{avg}}^2}{3(k_B T)^{3/2} m_\alpha^{5/2} E_\alpha^2} \quad (5)$$

The density ρ for $CsRbSnGeI_6$ was determined using:

$$\rho = \frac{M \times Z}{N_A \times V} \quad (6)$$

where the molar mass M is 1020.52 g/mol, and the unit cell volume: V=a×b×c, with a=b=8.36 Å and c=12.28 Å, resulting in a density of ρ=4.53 g/cm^3.

For the double perovskite tetragonal structure (CsRb)(SnGe)I_6, the calculated carrier mobilities are as follows: electron mobility = 115 cm^2/V·s and hole mobility = 31.6 cm^2/V·s. These values are competitive compared to other halide perovskites, making (CsRb)(SnGe)I_6 a strong candidate for optoelectronic applications, particularly in perovskite-based solar cells.

Table V-1. The calculated effective mass, volume deformation potentials, and carrier mobilities for (CsRb)(SnGe)I_6 compared with some other materials.

Compounds	**Carriers**	$\mathbf{m}^*_{xx}/m_0$	$\mathbf{m}^*_{yy}/m_0$	$\mathbf{m}^*_{zz}/m_0$	$\mathbf{m}^*_{a}/m_0$	E_{Da} (eV)	μ_a (cm^2 V^{-1} s^{-1})
(CsRb)(SnGe)I_6	Electrons	1.408	1.408	0.087	0.217	-7.0812	115
	Holes	0.2618	0.2618	0.244	0.256	-10.861	31.6
Si [26, 27]	Electrons	-	-	-	0.97	-	1450
	Holes	-	-	-	0.5	-	450
GaAs [28, 29, 30]	Electrons	-	-	-	0.08	-7	8500
	Holes	-	-	-	0.5	-9.5	400
$MAPbI_3$ [31, 32]	Electrons	-	-	-	0.23	-7.30	2–66
	Holes	-	-	-	0.29	-9.31	2–40
$CsSnI_3$ [33, 34]	Electrons	-	-	-	0.06	-	311
	Holes	-	-	-	0.03	-	400-450

Next, we investigated the optical properties, particularly the absorption coefficient (α), which was calculated from the dielectric function $\epsilon(E)$ using Equation 1:

$$\alpha(E) = \frac{4\pi E}{hc}\sqrt{\left(\frac{|\epsilon(E)|-\epsilon_1(E)}{2}\right)} \quad (7)$$

where *h*is the Planck constant, c is the speed of light, $\epsilon_1(E)$ and $\epsilon_2(E)$ are the real and imaginary parts of the dielectric function, respectively.To further elucidate, the dielectric function $\epsilon(E)$ is a complex quantity expressed as:

$$\epsilon(E) = \epsilon_1(E) + i\epsilon_2(E) \quad (8)$$

Here, $\epsilon_1(E)$ represents the real part of the dielectric function, which is associated with the dispersion of the material. It describes how the phase velocity of light is affected as it propagates through the material.On the other hand, $\epsilon_2(E)$ is the imaginary part of the dielectric function, which is related to the absorption of light within the material. It quantifies the loss of energy from the electromagnetic wave due to absorption as it travels through the material.

The absorption coefficient $\alpha(E)$ provides insight into how much light of a particular energy E is absorbed per unit distance as it passes through the material. It is derived from both $\epsilon_1(E)$ and $\epsilon_2(E)$, indicating that both the dispersive and absorptive properties of the material contribute to its optical behavior.In Equation 1, $|\epsilon(E)|$ represents the magnitude of the complex dielectric function and is given by:

$$|\epsilon(E)| = \sqrt{\epsilon_1(E)^2 + \epsilon_2(E)^2} \quad (9)$$

By incorporating $\epsilon_1(E)$ and $\epsilon_2(E)$ into the calculation of $\alpha(E)$, we can accurately determine the absorption characteristics of the material over a range of energies. These functions were obtained from first-principles calculations. The peaks in $\alpha(E)$ correspond to energies where significant light absorption occurs, which are directly related to the electronic transitions within the material.

Figure V-3 illustrates the absorption coefficient for (CsRb)(SnGe)I_6, showing significant absorption peaks at lower energies and a gradual decrease at higher energies, particularly around 8 eV. This broad absorption spectrum indicates the material's capability to efficiently absorb light across a wide range of wavelengths, essential for high-performance photovoltaic devices.

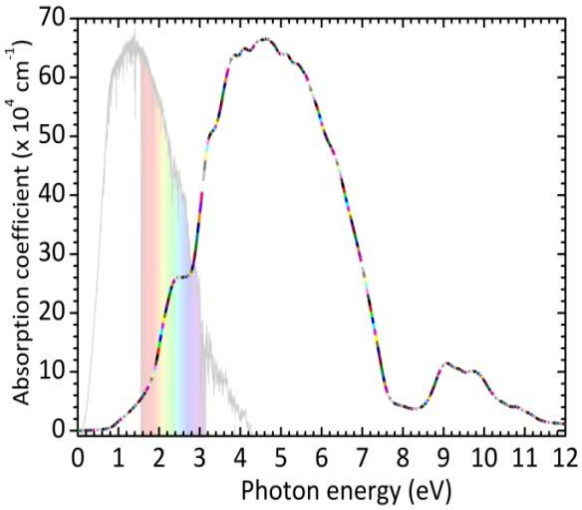

Figure V-3 : Absorption coefficient (α) for (CsRb)(SnGe)I_6, demonstrating its efficient light absorption capability across a broad spectrum.

Studying the exciton binding energy provides valuable insight into the efficiency of charge separation and the overall photovoltaic performance of (CsRb)(SnGe)I_6. The exciton binding energy can be calculated using the Bethe-Salpeter Equation (BSE), which offers a highly accurate description of electron-hole interactions. However, given the computational intensity of the BSE approach, we can also use the Wannier-Mott exciton model [35] as a more practical alternative for estimating the binding energy. The exciton binding energy E_b in the Wannier-Mott model is given by the equation:

$$E_{\mathrm{b}} = \frac{m_{\mathrm{e}}^{*} m_{\mathrm{h}}^{*} R_y}{m_0 (m_{\mathrm{e}}^{*} + m_{\mathrm{h}}^{*}) \varepsilon_{\mathrm{s}}^2} = 13.6 \frac{\mu}{\varepsilon_{\mathrm{s}}^2} \quad (10)$$

Where, ε_s is the static dielectric constant (estimated to 4.5812), m_{e}^{*} and m_{h}^{*} are the average effective masses in all directions, and Ry = 13.6057 eV is the Rydberg energy constant, μ is reduced effective mass derived by the formula $1/\mu = 1/m_{\mathrm{e}}^{*} + 1/m_{\mathrm{h}}^{*}$.

For (CsRb)(SnGe)I_6, the estimated exciton binding energy is 76.30meV, indicating that excitons are relatively easy to separate, which enhances charge carrier generation. This low binding energy is advantageous for photovoltaic applications, as it promotes efficient electron-hole separation and improves device performance.

V-3.3. Photovoltaic Performance

To assess the photovoltaic performance of (CsRb)(SnGe)I_6, we employed the Spectroscopic Limited Maximum Efficiency (SLME) model. This model is more realistic compared to the Shockley-Queisser limit because it incorporates the actual absorption spectrum and considers recombination losses and carrier dynamics.

The SLME model starts by considering the detailed balance of absorption and emission processes. The absorption spectrum is derived from the calculated α(E), and the emission is modeled using the Planck black-body radiation formula, adjusted for the semiconductor bandgap.

The SLME model calculates the maximum efficiency (η_{SLME}) by integrating the absorption coefficient over the solar spectrum and considering the recombination processes:

The absorption spectrum $A(E)$ is given by [36]:

$$A(E) = 1 - \exp(-\alpha(E)L) \quad (11)$$

where L is the absorber layer thickness.

The photogenerated current density J_{gen} is calculated by integrating the product of the absorption spectrum and the incident solar spectrum $I_{AM1.5}(E)$[37]:

$$J_{gen} = q \int_{E_{gap}}^{\infty} A(E) \frac{I_{AM1.5}(E)}{E} dE \quad (12)$$

where E_{gap} is the bandgap energy, and q is the elementary charge.

The radiative recombination current density J_{rad} is given by [38]:

$$J_{rad} = q \int_{E_{gap}}^{\infty} \frac{A(E)}{\exp\left(\frac{E-qV}{kT}\right)-1} dE \quad (13)$$

where V is the voltage, k is Boltzmann's constant, and T is the temperature.

Non-radiative recombination is often modeled using an empirical parameter τ_{nr}, the nonradiative lifetime [39] :

$$J_{nr} = \frac{q \cdot n_1^2 \cdot V}{\tau_{nr}} \quad (14)$$

where n_i is the intrinsic carrier concentration.

The total recombination current density J_{rec} is the sum of radiative and non-radiative components:

$$J_{\text{rec}} = J_{rad} + J_{nr} \quad (15)$$

The current density J as a function of voltage V is:

$$J(V) = J_{gen} - J_{rec} \quad (16)$$

From the current-voltage $(\mathrm{J-V})$ characteristics, several key photovoltaic parameters can be derived:

The short-circuit current density is the current density when the voltage is zero $(V = 0)$:

$$J_{sc} = J(V = 0) \quad (17)$$

The open-circuit voltage is the voltage when the current density is zero $(J = 0)$:

$$V_{oc} = \frac{kT}{q} \ln\left(\frac{J_{gen}}{J_0} + 1\right) \quad (18)$$

where J_0 is the reverse saturation current density.

The fill factor is a measure of the *squareness* of the J-Vcurve and is given by:

$$\mathrm{FF} = \frac{J_{mp} V_{mp}}{J_{sc} V_{oc}} \quad (19)$$

where J_{mp} and V_{mp} are the current density and voltage at the maximum power point, respectively.

The power conversion efficiency (PCE) is the ratio of the maximum power output to the incident power input [40]:

$$\eta_{SLME} = \frac{P_{max}}{P_{in}} = \frac{J_{sc} \cdot V_{oc} \cdot \mathrm{FF}}{P_{in}} \quad \text{VI-20}$$

Where J_{sc} is the short-circuit current density, V_{oc} is the open-circuit voltage, FF is the fill factor,P_{max} is the maximum power output, P_{in} is the incident power density.

Figure V-4 displays the simulated current-voltage (J-V) characteristics as a function of absorber layer thickness at room temperature (T=300 K). The J-V curve indicates that the short-circuit current density (J_{sc}) rises with absorber thickness up to 50 µm, indicating enhanced light absorption. Beyond this point, the rate of increase slows, suggesting diminishing returns in J_{sc} improvement with thicker films. This observation underlines the importance of optimizing the absorber thickness to maximize J_{sc} in (CsRb)(SnGe)I_6-based solar cells.

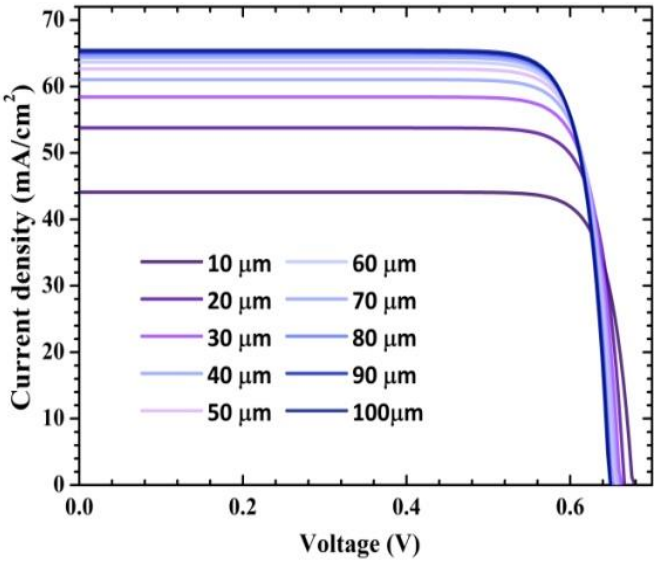

Figure V-4 : Simulated J-V characteristics for $(CsRb)(SnGe)I_6$ as a function of absorber layer thickness (L = 50 µm), highlighting the optimal thickness for maximizing short-circuit current density (J_{sc}).

To validate the accuracy of the SLME model, we compared the photovoltaic performance of $(CsRb)(SnGe)I_6$ with that of $CsPbI_3$, a widely studied material in perovskite solar cells. Our calculations indicate that despite the lower bandgap of $(CsRb)(SnGe)I_6$, its extended absorption range and efficient charge separation contribute substantially to its competitive photovoltaic efficiency.

Table V-1 summarizes the photovoltaic parameters extracted from our simulations, including power conversion efficiency (PCE), open-circuit voltage (V_{oc}), short-circuit current density (J_{sc}), and fill factor (FF) for $(CsRb)(SnGe)I_6$ compared with other materials from the literature. At a thickness of 50 µm, $(CsRb)(SnGe)I_6$ achieves a PCE of 25.55%, with a V_{oc} of 0.656 V, J_{sc} of 62.64 mA/cm², and FF of 0.838. These parameters highlight the competitive potential of $(CsRb)(SnGe)I_6$ in photovoltaic applications, comparable to or exceeding efficiencies of other reported materials.

Table V-2 : Photovoltaic parameters for (CsRb)(SnGe)I_6 at L = 50 µm compared with other materials from literature references.

Compounds	PCE (%)	V_{oc} (V)	J_{sc} (mA/cm²)	FF	Eg (eV)
(CsRb)(SnGe)I_6	25.55	0.656	62.64	0.838	0.89
$CsPbI_3$	25.91	1.424	26.90	0.911	1.71
$Cu_{10}Zn_2Sb_4Se_{13}$ (Ref. [41])	21.00	-	-	-	1.40
$Cs_2AgBi_{0.2}In_{0.8}Br_6$ (Ref. [42])	18.00	1.91	10.14	0.93	2.23
HHP (Ref. [43])	25.69	-	-	-	1.30
$Rb_2AgGaCl_6$ (Ref. [44])	12.00	-	-	-	2.53

V-3.4. Ferroelectric Properties

Incorporating ferroelectric materials into photovoltaic systems has shown potential for significantly enhancing charge separation and collection efficiency. Our study focuses on a [001]-oriented layered configuration of (CsRb)(SnGe)I_6, where alternating layers of RbI and CsI induce structural distortions, primarily caused by off-center displacements of cations such as Sn^{2+} and Ge^{2+}. These displacements, driven by the stereochemical activity of lone pair electrons, break inversion symmetry and generate spontaneous polarization. The material crystallizes in a polar phase, with persistent dipoles formed within the (001) plane, resulting in significant ferroelectric polarization along the z-axis. To evaluate the polarization switching barrier - i.e., the energy required to switch polarization from upward to downward - we employed first-principles methods, such as density functional theory (DFT). This analysis allowed us to calculate the energy difference between the polar state (characterized by ion displacements) and the non-polar state (a higher symmetry phase without a net dipole). The energy difference between the polar state and the highest energy transition state determines the energy required to reverse the polarization under an external electric field. A high switching barrier suggests robust and stable polarization, which is desirable for non-volatile ferroelectric memories, whereas a lower barrier facilitates easier polarization reversal, making it suitable for fast-switching applications like sensors.

The switching barrier, ΔE, is computed as the difference in total energy between the non-centrosymmetric and centrosymmetric states:

$$\Delta E = E_{tot}(\text{non-centrosymmetry}) - E_{tot}(\text{centrosymmetry}) \quad (20)$$

For (CsRb)(SnGe)I_6, the switching barrier energy is calculated to be -9.0484meV/atom.

It is important to note that external factors, such as temperature, strain, and applied electric fields, can influence the switching barrier. For instance, thermal fluctuations may reduce the barrier at elevated temperatures, while mechanical stress can alter the lattice structure and affect polarization stability.

We used the Berry phase method to compute the spontaneous polarization. This method is a sophisticated technique for determining macroscopic polarization in crystalline materials, particularly well-suited for systems with periodic boundary conditions. It is commonly implemented in first-principles calculations using the linearized augmented plane wave (LAPW) method. The macroscopic polarization**P** in a crystal is given by:

$$\mathbf{P} = \frac{e}{(2\pi)^3}\sum_n \int_{\mathrm{BZ}} d\mathbf{k}\langle u_{n\mathbf{k}}|\nabla_{\mathbf{k}}|u_{n\mathbf{k}}\rangle \quad (21)$$

where e is the elementary charge, **k**is the wave vector within the Brillouin zone (BZ), and $u_{n\mathbf{k}}$ represents the periodic part of the Bloch wave function for the n-th band [45, 46]. The Berry phase γ, which is the geometric phase accumulated over a closed loop in**k**-space, is calculated by:

$$\gamma = \mathrm{Im}\ln\prod_{m=1}^{M}\det\left[\langle u_{n\mathbf{k}_m} \mid u_{n\mathbf{k}_{m+1}}\rangle\right] \quad (22)$$

Where k_m are points along a discretized path in k-space [47].

In our LAPW calculations, the Berry phase method was applied through the following steps: (1) Performing a self-consistent field (SCF) calculation to determine the ground-state electron density and Kohn-Sham potential; (2) Computing the Bloch wave functions $\psi_{n\mathbf{k}}$ on a dense $\mathbf{k}$-point mesh to accurately represent the electronic structure; (3) Calculating the overlap matrices $\langle u_{n\mathbf{k}_m} \mid u_{n\mathbf{k}_{m+1}}\rangle$ along discretized paths in**k**-space; and (4) Integrating the Berry phase over the Brillouin zone to obtain the macroscopic polarization [48].

For (CsRb)(SnGe)I_6, the [001] crystal orientation and the alternating RbI and CsI layers facilitated the computation of a net polarization ofP_z = 0.76 μC/cm^2. This magnitude of polarization is notable and comparable to or exceeds the polarization observed in some spin-

driven multiferroic materials [14,49], highlighting the potential of (CsRb)(SnGe)I_6 for advanced photovoltaic applications.

V-4. Conclusions

Our theoretical investigation of (CsRb)(SnGe)I_6 indicates that it holds significant promise as a material for advanced photovoltaic applications. Through comprehensive calculations, we have shown that its intrinsic ferroelectric properties arise from cation ordering, which enhances charge separation, a critical factor for reliable photovoltaic performance. The electronic structure of (CsRb)(SnGe)I_6 features a direct band gap of 0.89 eV and exhibits strong light absorption in both the visible and UV spectrum, making it a strong candidate for efficient light harvesting. According to the SLME model, we estimate that (CsRb)(SnGe)I_6 could achieve an efficiency of up to 25%, making it competitive with other materials. Further experimental work is needed to validate these theoretical predictions and explore practical applications in solar cells, thereby advancing sustainable energy solutions.

Bibliography

[1] Glass, A. M., Von der Linde, D., &Negran, T. J. (1974). High-voltage bulk photovoltaic effect and the photorefractive process in LiNbO3. Applied Physics Letters, 25(4), 233-235.

[2] Yang, S. Y., Martin, L. W., Byrnes, S. J., Conry, T. E., Basu, S. R., Paran, D., ... & Ramesh, R. (2009). Photovoltaic effects in BiFeO3. Applied Physics Letters, 95(6).

[3] Choi, T., Lee, S., Choi, Y. J., Kiryukhin, V., & Cheong, S. W. (2009). Switchable ferroelectric diode and photovoltaic effect in BiFeO3. Science, 324(5923), 63-66.

[4] Alexe, M., & Hesse, D. (2011). Tip-enhanced photovoltaic effects in bismuth ferrite. Nature communications, 2(1), 256.

[5] Yang, S. Y., Seidel, J., Byrnes, S. J., Shafer, P., Yang, C. H., Rossell, M. D., ... & Ramesh, R. (2010). Above-bandgap voltages from ferroelectric photovoltaic devices. Nature nanotechnology, 5(2), 143-147.

[6] Nechache, R., Harnagea, C., Li, S., Cardenas, L., Huang, W., Chakrabartty, J., &Rosei, F. (2015). Bandgap tuning of multiferroic oxide solar cells. Nature photonics, 9(1), 61-67.

[7] Huang, X., Paudel, T. R., Dong, S., & Tsymbal, E. Y. (2015). Hexagonal rare-earth manganites as promising photovoltaics and light polarizers. Physical Review B, 92(12), 125201.

[8] Bhatia, S., & Singh, B. P. (2017). Ferroelectric Photovoltaics: Principles and Efficiency Limits. Materials Research Express, 4(8), 085701.

[9] Wang, K. F., Liu, J. M., & Ren, Z. F. (2009). Multiferroicity: the coupling between magnetic and ferroelectric order parameters. Advances in Physics, 58(4), 321-448.

[10] Seidel, J., et al. (2011). Efficient photovoltaic current generation at ferroelectric domain walls. Physical Review Letters, 107(12), 126805.

[11] Zhang, W., et al. (2014). Enhancing the photovoltaic effect in ferroelectric-semiconductor heterostructures. Nature Communications, 5, 3031.

[12] Grätzel, M. (2014). The light and shade of perovskite solar cells. Nature Materials, 13(9), 838-842.

[13] Snaith, H. J. (2013). Perovskites: the emergence of a new era for low-cost, high-efficiency solar cells. Journal of Physical Chemistry Letters, 4(21), 3623-3630.

[14] Young, J., & Rondinelli, J. M. (2018). Inducing spontaneous electric polarizations in double perovskite iodide superlattices for ferroelectric photovoltaic materials. Physical Review Materials, 2(6), 065406.

[15] Azarhoosh, P., McKechnie, S., Frost, J. M., Walsh, A., & Van Schilfgaarde, M. (2016). Research Update: Relativistic origin of slow electron-hole recombination in hybrid halide perovskite solar cells. Apl Materials, 4(9).

[16] Znidi, F., Morsy, M., & Uddin, M. N. (2024). Recent advances of graphene-based materials in planar perovskite solar cells. Next Nanotechnology, 5, 100061.

[17] Yu, Z., Wang, S., & Zhang, Y. (2015). Evaluation of Solar Cell Materials Using the Spectroscopic Limited Maximum Efficiency Model. Journal of Applied Physics, 117(4), 045104.

[18] Shockley, W., & Queisser, H. J. (1961). Detailed Balance Limit of Efficiency of p-n Junction Solar Cells. Journal of Applied Physics, 32(3), 510-519.

[19] Blaha, P., Schwarz, K., Madsen, G. K., Kvasnicka, D., &Luitz, J. (2001). wien2k. An augmented plane wave+ local orbitals program for calculating crystal properties, 60(1).

[20] Tran, F., & Blaha, P. (2009). Accurate band gaps of semiconductors and insulators with a semilocal exchange-correlation potential. Physical review letters, 102(22), 226401.

[21] Ahmed, S. J., Kivinen, J., Zaporzan, B., Curiel, L., Pichardo, S., & Rubel, O. (2013). BerryPI: A software for studying polarization of crystalline solids with WIEN2k density functional all-electron package. Computer Physics Communications, 184(3), 647-651.

[22] Eperon, G. E., Paternò, G. M., Sutton, R. J., Zampetti, A., Haghighirad, A. A., Cacialli, F., & Snaith, H. J. (2015). Inorganic cesium lead iodide perovskite solar cells. Journal of Materials Chemistry A, 3(39), 19688-19695.

[23] Yao, H., Zhao, J., Li, Z., Ci, Z., & Jin, Z. (2021). Research and progress of black metastable phase $CsPbI_3$ solar cells. Materials Chemistry Frontiers, 5(3), 1221-1235.

[24] Afsari, M., Boochani, A., &Hantezadeh, M. (2016). Electronic, optical and elastic properties of cubic perovskite $CsPbI_3$: Using first principles study. Optik, 127(23), 11433-11443.

[25] Nematov, D. D., Burhonzoda, A. S., Kurboniyon, M. S., Zafari, U., Kholmurodov, K. T., Yamamoto, T., & Shokir, F. (2023). The Effect of Structural Phase Changes on Fermi Level Shifts and Optoelectronic Properties of Lead-Free $CsSnI_3$ Perovskites. arXiv preprint arXiv:2310.19693.

[26] Sze, S. M., Li, Y., & Ng, K. K. (2021). Physics of semiconductor devices. John wiley& sons.

[27] Conwell, E. M. (1958). Properties of silicon and germanium: II. Proceedings of the IRE, 46(6), 1281-1300.

[28] Bockris, J. O. M., Reddy, A. K., & Gamboa-Aldeco, M. (2000). Electrodics. Modern Electrochemistry 2A: Fundamentals of Electrodics, 1035-1400.

[29] Blakemore, J. S. (1982). Semiconducting and other major properties of gallium arsenide. Journal of Applied Physics, 53(10), R123-R181.

[30] Zianni, X., Butcher, P. N., & Kearney, M. J. (1994). Semiclassical magnetothermopower of a quasi-two-dimensional electron gas. Physical Review B, 49(11), 7520.

[31] Filippetti, A., Mattoni, A., Caddeo, C., Saba, M. I., & Delugas, P. (2016). Low electron-polar optical phonon scattering as a fundamental aspect of carrier mobility in methylammonium lead halide CH 3 NH 3 PbI 3 perovskites. Physical Chemistry Chemical Physics, 18(22), 15352-15362.

[32] Giorgi, G., Fujisawa, J. I., Segawa, H., & Yamashita, K. (2013). Small photocarrier effective masses featuring ambipolar transport in methylammonium lead iodide perovskite: a density functional analysis. The journal of physical chemistry letters, 4(24), 4213-4216.

[33] Chung, I., Song, J. H., Im, J., Androulakis, J., Malliakas, C. D., Li, H., ... &Kanatzidis, M. G. (2012). CsSnI3: semiconductor or metal? High electrical conductivity and strong near-infrared photoluminescence from a single material. High hole mobility and phase-transitions. Journal of the american chemical society, 134(20), 8579-8587.

[34] Su, Y., Song, K. K., Zhong, M., Shi, L. B., & Qian, P. (2021). Stability and phonon-limited mobility for CsSnI3 and CsPbI3. Journal of Alloys and Compounds, 889, 161723.

[35] Rodina, A. V., Dietrich, M., Göldner, A., Eckey, L., Hoffmann, A., Efros, A. L., ... & Meyer, B. K. (2001). Free excitons in wurtzite GaN. Physical Review B, 64(11), 115204.

[36] De Wolf, S., Descoeudres, A., Holman, Z. C., & Ballif, C. (2012). High-efficiency silicon heterojunction solar cells: A review. green, 2(1), 7-24.

[37] Shockley, W., & Queisser, H. (2018). Detailed balance limit of efficiency of p-n junction solar cells. In Renewable energy (pp. Vol2_35-Vol2_54). Routledge.

[38] Rau, U., Blank, B., Müller, T. C., &Kirchartz, T. (2017). Efficiency potential of photovoltaic materials and devices unveiled by detailed-balance analysis. Physical review applied, 7(4), 044016.

[39] Alharbi, F. H., & Kais, S. (2015). Theoretical limits of photovoltaics efficiency and possible improvements by intuitive approaches learned from photosynthesis and quantum coherence. Renewable and Sustainable Energy Reviews, 43, 1073-1089.

[40] Yu, L., & Zunger, A. (2012). Identification of Potential Photovoltaic Absorbers Based on First-Principles Spectroscopic Screening of Materials. Physical review letters, 108(6), 068701.

[41] Heo, J., Ravichandran, R., Reidy, C. F., Tate, J., Wager, J. F., & Keszler, D. A. (2015). Design meets nature: Tetrahedrite solar absorbers. Advanced Energy Materials, 5(7), 1401506.

[42] Schade, L., Mahesh, S., Volonakis, G., Zacharias, M., Wenger, B., Schmidt, F., ... & Snaith, H. J. (2021). Crystallographic, Optical, and Electronic Properties of the $Cs_2AgBi_{1-x}In_xBr_6$ Double Perovskite: Understanding the Fundamental Photovoltaic Efficiency Challenges. ACS Energy Letters, 6(3), 1073-1081.

[43] Sharma, H., Verma, V. K., Singh, R. C., Singh, P. K., & Basak, A. (2023). Numerical analysis of high-efficiency $CH_3NH_3PbI_3$ perovskite solar cell with PEDOT: PSS hole transport material using SCAPS 1D simulator. Journal of Electronic Materials, 52(7), 4338-4350.

[44] Kibbou, M., Haman, Z., Essaoudi, I., &Ainane, A. (2023). Designing new halide double perovskite materials Rb_2AgGaX_6 (X: Br, Cl) with direct band gaps and high-power conversion efficiency. Journal of Solid-State Chemistry, 317, 123698.

[45] Resta, R. (1994). Macroscopic polarization in crystalline dielectrics: the geometric phase approach. Reviews of Modern Physics, 66(3), 899.

[46] King-Smith, R. D., & Vanderbilt, D. (1993). Theory of polarization of crystalline solids. Physical Review B, 47(3), 1651.

[47] Vanderbilt, D., & King-Smith, R. D. (1993). Electric polarization as a bulk quantity and its relation to surface charge. Physical Review B, 48(7), 4442.

[48] Cohen, R. E., & Krakauer, H. (1992). Electronic structure studies of the differences in ferroelectric behavior of $BaTiO_3$ and $PbTiO_3$. Ferroelectrics, 136(1), 65.

[49] Eerenstein, W., Mathur, N. D., & Scott, J. F. (2006). Multiferroic and magnetoelectric materials. nature, 442(7104), 759-765.

Density functional theory (DFT) calculations based on first principles are a valuable tool in materials science for predicting and analyzing the electronic and structural characteristics of materials. This quantum mechanical approach determines the electronic makeup of a material by considering the arrangement of its atoms. DFT offers valuable insights into properties such as electronic band structure, density of states, and total energy. By solving the Schrödinger equation with approximations for exchange-correlation energy, which accounts for electron interactions, these calculations are widely used to comprehend material properties, develop new materials with specific traits, and enhance existing materials for particular uses.

From density functional theory (DFT) calculations, we looked on electronic structure and related properties of perovskite materials. Our study is divided into three main sections. In the first section, we focused on lead-free halide double perovskites, specifically $Cs_2InBi(Br,Cl)_6$. These materials were found to be thermodynamically stable, as indicated by their negative formation energies, and feasible for experimental synthesis. Both materials were studied using the generalized gradient approximation (GGA) with the inclusion of TB-mBJ and spin-orbit coupling (SOC), confirming their semiconducting nature. Optical property analysis revealed their potential applications across the infrared, visible, and ultraviolet regions of the electromagnetic spectrum. Additionally, we examined the strong cation-anion covalent interactions and the significant hybridization of the s and p orbitals at the Bi/In sites with the p orbitals at the Cl/Br sites. These interactions enhance the stereochemical activity of the lone pair, leading to substantial structural distortion within the unit cell and the formation of polar geometry. To quantify spontaneous polarization, the Berry phase method, implemented using the BerryPI code, was applied. Strong spontaneous polarization values were observed: approximately 0.39 C/m^2 for $Cs_2InBiCl_6$ and -0.40 C/m^2 for $Cs_2InBiBr_6$.

The photovoltaic characteristics of $Cs_2InBiCl_6$ and $Cs_2InBiBr_6$ were analyzed using the SLME framework. We examined how the parameters Jsc, Voc, FF, and efficiency (η) vary with increasing thickness of the perovskite absorber layer. Using the TB-mBJ method, the efficiencies of the $Cs_2InBiCl_6$ and $Cs_2InBiBr_6$ absorber layers were calculated at a thickness of 50 µm, yielding values of 26.24% and 28.33%, respectively.

In the second part of this study, we explore the properties of SF_3PbI_3, a polar halide perovskite, using a first-principles DFT approach. Our findings reveal that SF_3PbI_3 is a semiconductor with unique ferroelectric and Rashba spin-splitting properties, making it a promising material for

photovoltaic and spintronic applications. This study provides a detailed analysis of the electronic band structure, optical characteristics, and ferroelectric behavior of SF_3PbI_3. The compound exhibits strong spin-orbit coupling due to the heavy elements lead and iodine, resulting in Rashba splitting near the electron band edges. This feature improves charge separation and minimizes recombination losses, enhancing its suitability for photovoltaic use. We also investigate distortion-induced polarization switching in SF_3PbI_3. At equilibrium, the material displays low ferroelectric polarization because of its pseudo-symmetric atomic structure. However, controlled distortions—caused by factors like temperature variations, external pressure, or lattice defects—can trigger a transition to a high-polarization state with an enhanced dipole moment. This transition occurs with a low energy barrier, making the material suitable for applications in memory storage, sensors, and energy harvesting. Furthermore, the Rashba parameters of SF_3PbI_3 can be tuned through structural distortions, offering a flexible platform for developing spintronic devices. By integrating ferroelectric control with spintronic functionality, SF_3PbI_3 emerges as a versatile material with significant potential for advancing photovoltaic efficiency and spintronic technology.

In the third section of this work, we examined the $(CsRb)(SnGe)I_6$ perovskite and identified its potential for advanced photovoltaic applications. Our theoretical analysis revealed that the intrinsic ferroelectric properties of $(CsRb)(SnGe)I_6$ stem from cation ordering, which facilitates enhanced charge separation—a key factor for dependable photovoltaic performance. The electronic structure of $(CsRb)(SnGe)I_6$ features a direct band gap of 0.89 eV and demonstrates strong light absorption across the visible and ultraviolet regions, making it an excellent candidate for efficient light harvesting. Based on the SLME model, we estimate that this material could achieve an efficiency of up to 25%, positioning it as a competitive alternative to existing photovoltaic materials. Further experimental studies are required to confirm these theoretical predictions and to explore practical implementations in solar cells, contributing to advancements in sustainable energy technologies.

The spectroscopic limited maximum efficiency (SLME) is a theoretical framework used to estimate the highest possible efficiency of a solar cell based on the material's light absorption characteristics. It determines the maximum efficiency achievable if all absorbed photons are converted into electrical energy, effectively setting an upper limit on the solar cell's performance based on its light absorption capability.

In this study, we utilized the SLME model to assess the efficiency of the compounds under investigation for solar energy conversion. The exceptional efficiency observed is primarily attributed to the material's outstanding light absorption capabilities, stemming from its distinctive electronic structure and chemical makeup. Consequently, our findings

underscore the potential of these perovskites as a viable and promising alternative to conventional lead-based perovskite materials for solar cell applications.